Deuterium Inventory in Tungsten After Plasma Exposure: A Microstructural Survey

Dissertation zur Erlangung des Doktorgrads
von
Armin Manhard

vorgelegt
am 30. Dezember 2011

an der Mathematisch-Naturwissenschaftlichen Fakultät
der Universität Augsburg

Universität
Augsburg
University

IPP
Max-Planck-Institut
für Plasmaphysik

Mündliche Prüfung abgelegt am 18. Juni 2012

Erstgutachter: Prof. Dr. B. Stritzker
Zweitgutachter: PD Dr. Ch. Linsmeier

Contents

1. Introduction

Tungsten is a metal that is special in many respects. It has, for example, the highest melting point of all metals and an extremely low vapour pressure even at very high temperatures. It is an excellent electrical and thermal conductor. With its high atomic mass and high atomic displacement energy, it is very durable with respect to physical sputtering. Chemically, it is also very resistant (at least at room temperature) and is not even attacked by most of the strongest acids. Its mechanical properties, being very hard and at the same time also very brittle, remind more of a ceramic material than a metal [23].

Its durability makes tungsten a promising candidate for the armour material in the harsh environment of a nuclear fusion reactor despite its brittleness, especially in intensely irradiated regions like the divertor. For this application it is only rivalled by carbon, which can tolerate even more heat load, has more favourable mechanical properties, and is significantly less expensive [95].

An important safety concern for future nuclear fusion power plants is the inventory of the radioactive hydrogen isotope tritium inside the machine [95]. While a deuterium-tritium mixture leads to the most efficient energy production by fusion, the health and environmental hazards of tritium impose severe limits on the tolerable amount of tritium that could be mobilised in the case of an accident. Here carbon has a severe drawback: It readily forms volatile, tritiated hydrocarbons when bombarded by atoms and ions from the plasma. The chemistry of carbon with hydrogen can, on the one hand, strongly increase the carbon removal rate compared to physical sputtering alone [94] and thus lead to rapid destruction of carbon armour [95]. On the other hand, the hydrocarbons formed by chemical erosion can be re-deposited in regions that are shadowed from the plasma, e.g., in gaps between armour tiles and behind the armour support structure. There they can form thick amorphous hydrocarbon layers, which can contain large amounts of tritium. This so-called co-deposition of tritium with carbon in hydrocarbon layers would soon lead to an unacceptably high tritium inventory inside the reactor vessel [95]. Here tungsten has an advantage: It does not undergo chemical

reactions with hydrogen and has a very low solubility for hydrogen and its isotopes [27]. The low solubility is, however, somewhat offset by the high diffusivity of hydrogen in tungsten: Although local concentrations of hydrogen isotopes are typically very small, it can diffuse far into the bulk of the tungsten armour [1, 82] and eventually permeate through it, especially at high temperatures as they are expected for plasma-facing components [95].

Despite decades of work by many research groups, the data base for the solubility and diffusivity in tungsten, especially for defect-rich technical material, is astonishingly uncertain: The values can vary by orders of magnitude and depend strongly on the exact type of material as well as on the experimental conditions, both for the hydrogen loading and the subsequent measurement of the hydrogen retained in the specimen. Examples can be found in the review by Causey [14]. The difficulties in accurately determining the properties of hydrogen isotopes in tungsten are due to the low solubility: On the one hand, the inventories to be measured are typically very small and require measurement techniques with a high sensitivity. Because of that, techniques such as neutron scattering or nuclear magnetic resonance, which have been successfully used for detailed, non-destructive studies of the binding states and diffusion of hydrogen particularly in metals with a high solubility for hydrogen and in metal hydrides [68, 124], are not easily applicable for tungsten. Highly sensitive ion beam analysis techniques, on the other hand, are strongly impaired by the high mass of tungsten and accordingly by the short range of ions in it.

On the other hand, hydrogen typically bonds much more strongly to crystal defects than to undisturbed sites in the tungsten lattice, i.e., the defects act as "traps" [26, 82, 88]. Because the concentrations of trap sites can easily exceed the very low equilibrium concentration of hydrogen in the undisturbed sites, most of the hydrogen inventory that is retained in a tungsten specimen, e.g., after plasma exposure, is usually located in the traps. Their density, in turn, is determined by, e.g., the chemical composition and the microstructure. It is likely that many of the discrepancies between different publications on the hydrogen isotope retention in tungsten can be attributed at least partially to differences between the investigated tungsten materials.

The aim of this thesis is to clarify the role of the microstructure of the tungsten, i.e., its grain structure and its dislocation density, for the deuterium retention in tungsten specimens exposed to a low-energy deuterium plasma. To achieve this, only specimens from a single manufacturing batch of a commercially avail-

able powder metallurgical tungsten grade were analysed. This ensured that the chemical composition (i.e., the impurity concentrations) as well as the mechanical working history and therefore the initial microstructure of all specimens was identical. These specimens were then carefully polished with a procedure that ensured that no deformation layer was present at the surface. Different grain structures and dislocation densities were produced by annealing at different temperatures. After these preparation steps, representative specimens of all types were then thoroughly characterised by scanning and (scanning) transmission electron microscopy.

Specimens of all types were exposed to deuterium plasmas in a fully quantified plasma source [65]. In order to understand the different aspects of retention and diffusivity of deuterium in these specimens, the temperature during implantation, the ion energy and the ion fluence were varied over wide ranges. After plasma exposure, degassing of deuterium from tungsten specimens can be considerable, particularly during the first few days [72]. To avoid a large scatter of the measured retention data, all specimens were stored for about two months before analysis. This ensures that the unavoidable small time differences between the analyses of the individual specimens have only a minor impact when comparing their deuterium inventories. The specimens were then analysed with a wide range of optical and electron microscopy techniques in order to study surface modifications due to the plasma exposure, particularly the formation of gas-filled cavities near the surface (so-called "blisters"). The deuterium inventory was quantified by nuclear reaction analysis (NRA), which allows non-destructive, depth-resolved measurements up to approximately 8–12 μm below the surface for tungsten (depending on the highest energy used in the ion beam analysis). The total inventory, including the bulk of the sample beyond the probing range of NRA, was also investigated by thermal desorption spectroscopy (TDS). A series of TDS measurements with varying heating rates and also interrupted temperature ramps was performed on a set of identical specimens in order to avoid the ambiguity of binding energy distribution and depth profile of the deuterium for the interpretation of thermal desorption spectra [14, 112]. This method also allows to determine the attempt frequency for desorption of bound deuterium. The influence of the plasma exposure on the defects in the tungsten was studied by *ex situ* and *in situ* transmission electron microscopy for selected specimens.

Chapter 2 first introduces the reader to the general properties of hydrogen–metal systems. The thermodynamic aspects are discussed to provide a basic understand-

ing of the interactions of dissolved hydrogen with the host metal. The diffusion of interstitially dissolved hydrogen is discussed as well as the influence of crystal defects and the effect of non-equilibrium loading conditions. Chapter 3 then focusses on the peculiarities of the tungsten-hydrogen system. It provides an overview of the existing data and discusses diffusion-trapping models, which are a common tool for the numerical simulation of hydrogen isotopes in tungsten. Based on this, the details of the model used in this thesis are explained. The device for plasma exposure of tungsten specimens and the central methods for measuring their deuterium inventory, NRA and TDS, are discussed in detail in chapter 4. This chapter also gives a short overview over the microscopy equipment used for this work, and explains the technique of differential interference contrast (DIC) microscopy. Chapter 5 is dedicated to the procedures for specimen preparation. While this may seem trivial at first, it will be shown also in experimental results in section 8.4 that the specimen preparation can indeed have a notable influence on measurement results. The thorough pre-characterisation of the investigated material is presented in chapter 6. In detail, the influence of different heat treatments on the grain size distribution and the dislocation density are investigated. Knowledge of these parameters is essential for understanding the connection between the microstructure of tungsten and the deuterium retention. Chapter 7 describes the strategy and scientific rationale of the experiments performed here. The results of the individual experiments are presented and discussed in detail in chapter 8. Chapter 9 then summarises these results and delivers a synopsis in order to combine the large amount of individual data into a global picture. This chapter also provides an outlook on possible further investigations based on the results presented here.

The variation of several key parameters of the plasma exposure, as well as of the well-characterised initial microstructure of the specimens, provides a broad data base. Rigorous standardisation of experimental procedures ensures the reproducibility and comparability of the results. This allows a more detailed understanding of the mechanisms of hydrogen isotope retention in tungsten due to plasma exposure. This thesis will try to elucidate these mechanisms and provide the basis for a better understanding of more complex systems like they will be found in a future fusion reactor, e.g., tungsten damaged by fast neutrons (see, e.g, [109, 115]) or the formation of so-called "mixed materials" [19].

2. Hydrogen in metals: general considerations

This chapter aims to give a general overview of the complex behaviour of hydrogen–metal systems. Starting from the solubility in thermal equilibrium and defect-free single crystals, the influences of defects and mutual hydrogen–hydrogen interactions are discussed. Some basic mechanisms of hydrogen diffusion in metals are explained, as well as the influence of external forces. Finally, some effects of loading a metal specimen with hydrogen in conditions far from thermal equilibrium, e.g., by an ion beam or plasma, are described.

2.1. Thermodynamics of hydrogen in metals

2.1.1. Solubility in thermal equilibrium: Sieverts' Law

From a thermodynamical point of view, one has to examine a two-phase system consisting of hydrogen in the gas phase and hydrogen dissolved in the metal. Upon entering a metal, hydrogen typically dissociates and forms an interstitial solution in a defect-free crystal. It has been experimentally verified — e.g., by ion channelling or neutron scattering experiments — that hydrogen preferentially occupies the tetrahedral interstitial sites in bcc metals, while in metals with a close packed crystal structure the octahedral sites are preferred [28]. This is also backed by model calculations (see, e.g., [33, 40, 64, 74]).

The properties of the solute hydrogen in the metal can generally be derived from its chemical potential μ_{solute}. In the tracer limit, where the occupancy of hydrogen ζ_H is much smaller than unity, it is given by

$$\mu_{solute}(\zeta_{\mathrm{H}}) = k_B T \ln(\zeta_{\mathrm{H}}) + const. \tag{2.1}$$

T denotes the temperature of the system and k_B is the Boltzmann constant. The occupancy ζ_H in this case should be understood as the ratio between the amount of dissolved hydrogen atoms n_H and of the available sites n_{sites}. The chemical potential of the hydrogen in the gas phase $\mu_{H_2,gas}$, on the other hand, is for moderate pressures given by

$$\mu_{H_2,gas} = k_B T \ln(p/p_0) + const., \tag{2.2}$$

i.e., the expression for an ideal gas, where p is the pressure of the gas and p_0 is an (in principle arbitrary) reference pressure. In equilibrium, the dissolution of hydrogen in the metal and the desorption from the metal into the gas phase balance each other. This can be expressed by the reaction equation

$$\mathrm{Me} + \frac{1}{2}x\mathrm{H}_2 \rightleftharpoons \mathrm{MeH}_x, \tag{2.3}$$

where Me stands for the metal and x is the occupancy of hydrogen times the number of available sites per metal atom. Accordingly, the equilibrium condition for the chemical potentials μ_{solute} and $\mu_{H_2,gas}$ is

$$\mu_{solute} = \frac{1}{2}\mu_{H_2,gas}. \tag{2.4}$$

Inserting equations (2.1) and (2.2) into (2.4) yields the relation between gas pressure and dissolved occupancy that is also known as Sieverts' law:

$$\zeta_H = K\sqrt{p}. \tag{2.5}$$

This relation was first derived by Sieverts and Jurisch [104] from experimental values for the absorption of gaseous hydrogen by a platinum wire. They took the $\sqrt{p}$ proportionality as evidence for hydrogen being dissolved as atoms. In fact this relation holds for many metal–hydrogen systems as long as the pressure is sufficiently low so that an ideal gas can be assumed (approximately up to 10 MPa [121]), and the hydrogen concentration in the metal is small so that hydrogen–hydrogen interactions or hydride formation do not play a role [29]. The temperature dependence of ζ_H can be found in the proportionality factor K:

$$K = \frac{1}{\sqrt{p_0}} \exp\left(\frac{\Delta S_{sol}}{k_B}\right) \exp\left(-\frac{\Delta H_{sol}}{k_B T}\right). \tag{2.6}$$

ΔS_{sol} is the entropy of solution, and ΔH_{sol} is the heat of solution. A detailed thermodynamical derivation of (2.6) can be found, e.g., in Fukai's book on the hydrogen-metal system [29]. In this book it is also shown that the entropy of solution is $\Delta S_{sol}/k_B \approx 8.2$ in the tracer limit. Experimental values compiled by Fukai [29] are of the range from -4 to -9 and thus do not vary too strongly from the theoretical value for a large variety of metals. The heat of solution, however, depends strongly on the host metal and varies roughly between -1 and +1 eV per hydrogen atom. Accordingly, metals can roughly be grouped into hydrogen-affine (where the dissolution of hydrogen is exothermic, i.e, $\Delta H_{sol} < 0$) and hydrogen-repelling metals (where dissolving hydrogen is endothermic, i.e., $\Delta H_{sol} > 0$). Figure 2.1 shows the heat of solution of hydrogen in the tracer limit in most of the transition metals as listed by [29]. It can be easily seen that ΔH_{sol} varies more or less systematically when going from left to right in the periodic system.

This already hints at a strong interaction between the electronic states of the metal and the dissolved hydrogen. A more detailed explanation is given by Ebisuzaki and O'Keeffe [20]. They assume that hydrogen exists in metals as protons, whose positive potential is screened by a local increase of the electron density. That the dissolved hydrogen contributes its electron to the conduction band of the metal has been experimentally verified by different methods [124, 122, 101]. The corresponding screening length generally decreases as the (electron) density of states at the Fermi level $\mathcal{N}_e^{Fermi}$ increases. In a simple ansatz, the enthalpy of solution ΔH_{sol} for hydrogen in a metal is made up from the following contributions:

$$\Delta H_{sol} = \frac{1}{2}\Delta H_{\mathrm{H_2 \to 2H}} + \Delta H_{\mathrm{H \to H^+ + e^-}} - \Phi + (\epsilon_{rep} + \epsilon_{pol}) + \epsilon_{lattice}. \qquad (2.7)$$

In order to dissolve one hydrogen atom, a hydrogen molecule must be dissociated, which needs half the dissociation energy of $\frac{1}{2}\Delta H_{\mathrm{H_2 \to 2H}} \approx 2.3$ eV per H atom. Then the hydrogen atom must be ionised, which requires $\Delta H_{\mathrm{H \to H^+ + e^-}} = 13.6$ eV. Both the ion and the electron enter the metal. The system gains the energy $-\Phi$, which is the electron work function (typically 3–5 eV for transition metals). The screened proton is repelled by the positive metal ion cores, which is accounted for by the positive ϵ_{rep}, while the screening by the metal electrons leads by itself to the negative contribution ϵ_{pol}. What is not mentioned in [20] is the contribution of the deformation of the crystal lattice $\epsilon_{lattice}$. Later models such as the one presented by Nordlander *et al.* [78] take also this effect into account.
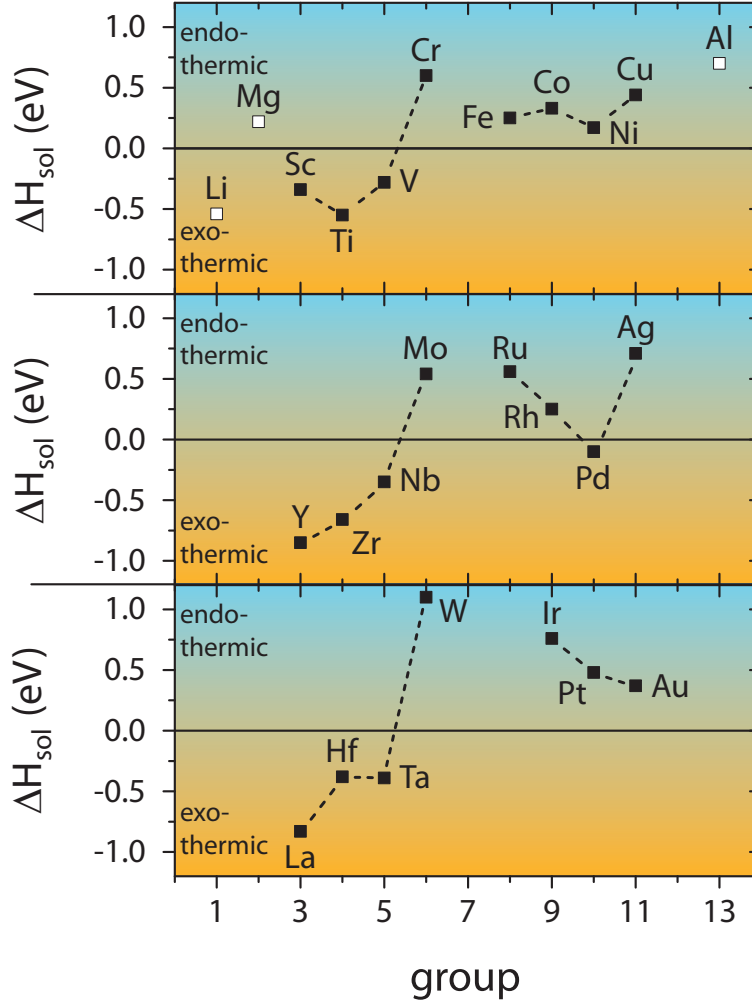
Figure 2.1. Heat of solution ΔH_{sol} for hydrogen at low occupancies in various transition metals [29]. The main group metals Li, Mg and Al are also included (white symbols). Note the mostly systematic variation from exo- to endothermic dissolution when going from left to right in the periodic system.

According to Ebisuzaki and O'Keeffe [20], ϵ_{pol} is the term that mainly balances the enthalpies for dissociation and ionisation, while ϵ_{rep} is comparatively small, but can still be important when comparing different elements. In total, the screened proton model predicts that the sum $\epsilon_{rep} + \epsilon_{pol}$ becomes more negative as $\mathcal{N}_e^{Fermi}$ increases, i.e., the heat of solution ΔH_{sol} tends towards becoming more exothermic in that case. Indeed, e.g., the vanadium group displays a high $\mathcal{N}_e^{Fermi}$ as well as exothermic ΔH_{sol}. The chromium group, on the other hand, has a low $\mathcal{N}_e^{Fermi}$ and exhibits endothermic dissolution of hydrogen.

While this relatively simple model is not sufficient to quantitatively describe the effects of hydrogen dissolution in metals (as also the authors of [20] admit), it

provides a reasonable qualitative explanation for experimental observations. One main conclusion is that the dissolution behaviour of metals for hydrogen is the result of the close balance of several large contributions. This means that even small changes in the terms listed above can have a large influence on the overall behaviour, even more so since ΔH_{sol} enters the solubility as an exponential term. Another important conclusion from the model is that although the hydrogen atom donates its electron to the conduction band of the metal, the electron density due to the shielding of the proton is comparable to that of a hydrogen atom (or in some cases even to a hydride anion).

For a more quantitative approach, *ab initio* methods such as density functional theory (DFT) are needed. Self-consistent calculations of the electronic state of hydrogen in interstitial sites were performed, e.g., by Nørskov [76]. These calculations are based on the so-called *jellium model*. This approach is actually still not too different from the screened proton model, as it also places a hydrogen atom inside a free-electron gas and then self-consistently calculates the electron density and the (electronic) density of states. However, this model already takes the full quantum-mechanical nature of the conduction electrons into account, while the screened proton model is essentially a classical model. The results include the electron density distribution around a hydrogen impurity, stating that it actually is even closer to an H^- anion than a neutral hydrogen atom. A further result is that an H_2 molecule is typically not stable in a free-electron gas at typical metal electron densities. One can conclude from this that only single hydrogen "pseudo-atoms" (respectively "anions") exist in the solute state in a metal. This backs the initial assumption that was made for deriving Sieverts' law from thermodynamics. For simplicity, hydrogen dissolved in a metal will accordingly be considered to be atomic from here on. DFT studies, however, are very complex and prone to many pitfalls. Especially the size of systems that can be computed on an atomistic scale is severely limited because such simulations require a large amount of computing power. Typical system sites that can be handled are of the order of 100 metal atoms. This inevitably leads to the question if, e.g, the assumption of an ideal dilute solution still holds, or if even a single hydrogen atom placed inside a simulation cell will interact with itself through periodic boundary conditions. Therefore, such investigations on the subject of hydrogen in metals still continue (see e.g., [40, 86]).

2.1.2. Influence of defects

As soon as one deals with a real metal, one has to consider defects, e.g., vacancies and vacancy clusters, dislocations or grain boundaries. Since crystal defects are typically more attractive to hydrogen than normal interstitial sites, they are generally referred to also as traps. The situation in a defective material is, of course, much more complex than in a perfect crystal. In metals where the solubility in interstitial sites is very low (typically those with positive ΔH_{sol}), the amount of hydrogen in trap sites can, e.g., easily exceed the amount in interstitial sites. In many cases, the exact density of interstitial and trap sites n_{sites} is not exactly known. Because of this, the *occupancy* $\zeta_H = n_H/n_{sites}$ is not easily attainable anymore. A more convenient experimental value is the *concentration* $c_H = n_H/(n_H + n_{metal})$, while ζ_H remains the better quantity for thermodynamics. Furthermore, defects can have a range of different binding energies for the dissolved hydrogen. In fact, even in a defect-free single crystal, tetrahedral and octahedral interstitial sites have different hydrogen binding energies due to their different size. For a thermodynamic treatment, a density of sites approach can be used [45]. In analogy to the electronic density of states $\mathcal{N}_e$, the density of sites for the dissolved hydrogen $\mathcal{N}_H(E)$ is defined as the number of binding sites for hydrogen atoms per energy interval dE and per unit volume. Considering that, e.g., a single trap can only bind a limited number of hydrogen atoms, it is appropriate to fill the traps in the metal in analogy to Fermi-Dirac statistics:

$$\zeta_H = \frac{1}{n_{sites}} \int\limits_{-\infty}^{+\infty} \frac{\mathcal{N}_H(E)}{1 + \exp(\frac{E - \mu_{solute}}{k_B T})} dE, \tag{2.8}$$

where μ_{solute} is, by itself, a function of ζ_H (see equation (2.1)). Equation (2.8) is therefore an implicit equation. Please note that this formulation does not impose any restriction on *how many* hydrogen atoms can occupy a certain trap, it only states that a trap can be eventually filled if the hydrogen concentration becomes high enough. Unsaturable traps, such as gas-filled voids, have to be treated separately.

Table 2.1 shows some examples for the densities of sites for a perfect crystal lattice as well as different types of defects as proposed by Kirchheim [45]. The interstitial sites in a perfect periodic lattice can be described by a delta function located at an energy E_{int} and weighted by the volume density of interstitial sites n_{int} (octahedral or tetrahedral sites, depending on the lattice) per metal. For a

lattice including point defects, e.g., vacancies or impurity atoms, in the simplest approximation a second delta function at the binding energy $E_{vac} < E_{int}$ weighted by the density of point defects n_{vac} can be added to the density of sites. It should be remembered, however, that in *ab initio* calculations vacancies have been found to be able to trap more than one hydrogen atom (see, e.g., [25, 74]).

For edge dislocations, one has to consider that the actual dislocation line is surrounded by an elastic strain field, which is compressive in the half space of the inserted lattice plane, and tensile in the other half space. Due to the elastic deformation of the lattice by the hydrogen, it is attracted to the tensile side and repelled from the compressive side. This can be described by a density of states proportional to $K^2/|E - E_{int}|^3$, where K is a constant containing the Burgers vector.

Grain boundaries contain a broad distribution of interstitial sites with different sizes and, accordingly, binding energies. One can assume that the average grain boundary interstitial site will be somewhat larger than an undistorted interstitial site, and thus attractive to hydrogen. Grain boundaries can therefore be described as a Gaussian (i.e., statistical) distribution of trap energies with the centre of weight E_{GB} below the interstitial site binding energy E_{int}, width σ_{GB} and weight n_{GB}. The bulk interstitial sites can again be treated by adding a delta function at E_{int}.

The extreme case, as opposed to the perfect single crystal, is an amorphous material, where the sizes and, accordingly, binding energies of interstitial sites are statistically deviating from the single crystal case. In this case the density of sites can be modelled by a Gaussian distribution of the width σ_{am} centred around E_{int}. This Gaussian distribution has to be normalised to contain exactly the number of interstitial sites n_{am} in the amorphous matrix. Note that n_{am} is probably close to, but not necessarily equal to n_{int}, since in a single crystal typically only one type of interstitial site, i.e., octahedral or tetrahedral, is occupied by hydrogen, whereas, strictly speaking, such a distinction is pointless in a completely amorphous matrix.

The total density of sites can then be treated as a superposition of an appropriate selection of the models discussed above. Using such a set of density-of-sites models and statistical mechanics based on a Fermi-Dirac distribution, the behaviour of hydrogen in metals can be simulated. An example for hydrogen in palladium can be found in [45].

Table 2.1. Models for the density of sites for a perfect single crystal as well as various crystal defects as proposed by [45]. Sketches of the corresponding potential trace and density of sites are included.

type of defect	density of sites model	potential trace	density of sites graph
none (perfect lattice)	$n_{int}\delta(E - E_{int})$		
point defects	$n_{int}\delta(E - E_{int}) + n_{vac}\delta(E - E_{int})$		
dislocations	$K^2/|E - E_{int}|^3$		
grain boundaries	$n_{int}\delta(E - E_{int}) + \frac{n_{GB}}{\sigma_{GB}\sqrt{\pi}}\exp\left(\frac{(E-E_{GB})^2}{(\sigma_{GB})^2}\right)$		
amorphous matrix	$\frac{n_{am}}{\sigma_{am}\sqrt{\pi}}\exp\left(\frac{(E-E_{int})^2}{(\sigma_{am})^2}\right)$		

It should not be neglected that the view that defects lower the energy of hydrogen in the metal can also be reversed, i.e, that the energy of a defect in the metal is lowered by hydrogen binding to it. One implication is that hydrogen dissolved in a metal can also lower the energy necessary for the creation of defects. For example, consider the mechanical deformation of a piece of metal containing hydrogen as well as of one free of hydrogen, but otherwise identical to the first. The hydrogen-containing metal will contain more dislocations after the deformation, as it has been shown by Kirchheim [47]. The effect can be explained by a generalisation of the Gibbs adsorption isotherm and Wagner's definition of excess solute at internal interfaces [48]. The reduction of the defect creation energy can even go so far that defects are produced *exothermically*. This can lead, e.g., to superabundant vacancies with a concentration in the range of 10–30% [30]. Please note that the exothermic defect production does not go on indefinitely if the energy necessary for defect creation rises again for large defect concentrations, but a metastable equilibrium is reached instead [47].

2.1.3. Hydrogen–hydrogen interactions

When the occupancy ζ_H of hydrogen interstitials dissolved in a metal gets higher, the H atoms can no longer be treated as completely independent. In a mean field approach, this means an interaction term μ_{H-H} has to be added to the chemical potential [45]. This interaction term can, in principle, be positive or negative, i.e., hydrogen atoms can attract or repel each other. Please note that already a concentration of the order of 1% amounts to about one hydrogen atom per $4 \times 4 \times 4$ supercell. In that case, each H atom has on average another one within a few lattice constants. At such relatively short distances interactions between hydrogen atoms could already play a role, which is a common problem for DFT calculations where often only samples of about this size are treated due to the demand on computational power.

To understand how these interactions could look like, one has to consider that each hydrogen atom in an interstitial site will slightly displace the metal atoms around it, causing the lattice to expand locally. In order to keep the surface of a finite volume of metal stress-free, the whole lattice has to expand on average, which lowers the chemical potential for the present hydrogen as well as for the dissolution of further atoms [31]. Accordingly, this can be seen an example of an attractive interaction on a global scale.

However, a single interstitial or trap site can certainly only contain only a limited number of hydrogen atoms. If this number is reached, energy must be expended to force another hydrogen atom into this site, which can be considered as repulsive interaction. This site blocking effect starts plays a role when the hydrogen concentration is comparable to the concentration of sites. Please note, that, e.g., for sparse traps this can already be the case at quite low global hydrogen concentrations.

From these examples it can already be seen that the interaction between hydrogen atoms is likely to vary both locally and with varying hydrogen concentration.

Both *ab initio* calculations and experimental approaches have been trying to estimate the hydrogen–hydrogen interactions in a metal for several decades. It is more or less generally agreed that long-range H–H interactions tend to reduce the chemical potential of the dissolved hydrogen due to the mechanism described above. The results for short-range interactions, however, appear conflicting at first. For example, Nørskov calculated that within the jellium model, a H_2 molecule is unstable and explains this by the filling of antibonding electronic states when the molecule is immersed within an electron gas of a density typical for a metal [76]. This also is confirmed by DFT studies presented in [40] for defect-free tungsten. As soon as defects enter the picture, the situation can change, however. For example, according to Kirchheim [45], there are attractive short-range interactions between hydrogen atoms close to dislocations in palladium. Recent DFT calculations for hydrogen near dislocations in nickel also point towards an attractive interaction between hydrogen atoms in nearest neighbor sites, while for second-nearest neighbor sites the interaction is repulsive [86]. Finally, for example Nazarov *et al.* [74] calculated that up to six hydrogen atoms can be trapped by a vacancy in fcc iron.

The logical conclusion from these seemingly conflicting results is that the interactions between hydrogen atoms dissolved in a metal indeed depend not only on global properties of hydrogen and metal, but also on the local environment, as it was already pointed out by Kirchheim [45].

2.2. Diffusion

Diffusion of hydrogen in metals was and is a complex problem, which is still in the focus of numerous research groups, possibly even more than the solubility alone.

One fact is that the diffusion is surprisingly fast. Even at room temperature, it can be comparable to the diffusion of ions in aqueous solution, and is in any case much faster than for any other impurity in metals. First off, this is often attributed to the small size and mass of hydrogen, but in fact the diffusion behaviour is also strongly affected by quantum mechanics. Neutron scattering experiments, for example, show discrete energy levels of hydrogen interstitials as well as a spatially extended density distribution [31].

A good overview about possible diffusion mechanisms for hydrogen in metals can be found in the review article of Fukai and Sugimoto [31]: For very low temperature, the diffusion is much faster than the extrapolation of high-temperature diffusion data suggests and, in fact, nearly independent of the temperature. The conclusion is that hydrogen moves by coherent tunnelling, i.e, the hydrogen including its elastic stress field changes its location within the crystal. This assumption is backed by a non-classical isotope dependence. For very pure and defect-free crystals even band-like propagation is occasionally postulated, but for real systems a hopping motion between adjacent sites (but nevertheless by tunnelling) is more likely. For somewhat higher temperatures, incoherent transitions dominate. This mechanism is characterised by the participation of phonons: lattice vibrations can lead to a temporary energetic levelling of adjacent sites of initially different binding energies (or to the reduction of saddle point energies). In this state, the hydrogen atom can tunnel through the barrier. This is called a non-adiabatic transition or thermally activated tunnelling. An adiabatic transition occurs if the hydrogen atom is in an excited state that extends over two adjacent sites in the common potential well of a saddle point configuration. In both cases, the hydrogen atom has a chance of being in the neighboring site when the lattice relaxes again. For adiabatic transitions, it is expected that the diffusion coefficient does not depend on the mass of the hydrogen isotope [31].

At intermediate temperatures, the transition between neighboring sites starts to become classical, and thermally activated jumps over the energetic saddle point occur. In this regime an Arrhenius-like temperature dependence is to be expected. For tungsten, DFT calculations by Heinola and Ahlgren [40] place the transition from quantum-mechanical to classical behaviour at about 200 K. If the temperature is raised further, jumps to second-nearest neighbors or multiple consecutive jumps start to occur more and more frequently. In this regime it can also make sense to describe the hydrogen as alternating between a mobile and an immobile state with different lifetimes. The validity of such assumptions for elevated

temperatures is backed by experimental evidence from quasi-elastic scattering of slow neutrons for hydrogen in palladium [63]. For very high temperatures, finally, hydrogen is more or less permanently in the mobile state. The movement can then be assumed to be gas- or fluid-like with a diffusivity that is proportional to the temperature [31]. No indication of such a behaviour has been observed for tungsten for temperatures up to 2500 K (see Figure 3.1).

Apart from these purely lattice-related effects, the conduction electrons of the metal also play a role. If one thinks back to the screened proton model in section 2.1.1, it is evident that the cloud of screening electrons has to move with the proton. The detailed theoretical framework for the interaction between a diffusing (light) impurity and the conduction electrons of the metal is laid in the Kondo theory [51, 52, 53, 54, 55].

Generally, diffusion of hydrogen in metals requires a quantum-mechanical description, and particularly at low temperatures the isotope and temperature dependence is non-classical. However, in all cases deuterium diffuses at least as fast as tritium. This means that in all experiments where the radioactive tritium is substituted by deuterium in order to minimise safety concerns (as it is done in this thesis), the measured diffusion coefficient can be seen as an upper limit for the tritium case. In the temperature range of about 300–1200 K, which is relevant for the experiments presented in this thesis, an Arrhenius-like temperature dependence of the diffusivity D hydrogen isotopes in tungsten can be expected. Using the (quantum mechanical) harmonic oscillator as an estimate for the attempt frequency for jumps of hydrogen atoms between interstitial sites, an isotope dependence like $D \propto 1/\sqrt{m}$ can be assumed, where m is the mass of the isotope [31].

Defects also do not only affect the solubility, but also the diffusivity of hydrogen in metals. Basically, there are two different possibilities: Hydrogen can be effectively trapped by defects so that the activation barrier for diffusion is increased and the effective diffusivity is, accordingly, reduced. Spatially extended defects like grain boundaries and dislocations can also *increase* the diffusivity if the saddle point energies along the extension of the defect are correlated and lower than in the undisturbed crystal. It has to be noted, however, that this leads — at least locally — to a strongly anisotropic enhancement of diffusivity. Diffusion is often faster than average parallel to the defect and hindered in the perpendicular direction. The global effect then depends strongly on the topology of the defect network, and on the possible saturation of the defects with hydrogen. Detailed

studies on the diffusivity in defective materials can, e.g., be found in [45, 46]. The special case of grain boundaries in tungsten is discussed by von Toussaint *et al.* [114]. A more detailed description of diffusion with trapping will be given in section 3.2.

2.3. Influence of external forces

All effects discussed above assumed that no other driving force for the dissolution of hydrogen and its diffusion in a metal existed than the pressure of the hydrogen gas phase and the concentration gradient in the metal, as described by Fick's first law for the diffusive flow $\vec{j}_{Fick}$:

$$\vec{j}_{Fick}(\vec{r}, t) = -D\vec{\nabla}c_{\mathrm{H}}(\vec{r}, t), \tag{2.9}$$

where D is the diffusion coefficient. But since hydrogen interstitials already interact with each other and with defects through strain fields, it is logical to assume that externally applied stress, whether tensile or compressive, will also have an influence. Furthermore, temperature gradients or electrical fields also play a role. According to Wipf [119, 120, 121], these effects add to the well-known diffusion by the concentration gradient in the following way:

$$\vec{j} = \vec{j}_{Fick} + c_{\mathrm{H}}\frac{D}{k_B T} \cdot \left(\vec{F}_{stress} + \vec{F}_{temp} + \vec{F}_{el}\right) \tag{2.10}$$

The term $D/k_B T$ is the mobility of the hydrogen, while $\vec{F}_{stress}$, $\vec{F}_{temp}$ and $\vec{F}_{el}$ stand for the forces exerted by gradients of stress, temperature and electrical potentials, respectively.

The stress gradient contribution can be written as follows:

$$\vec{F}_{stress} = v_{\mathrm{H}}\vec{\nabla}\mathrm{tr}(\sigma). \tag{2.11}$$

v_{H} is the partial volume of the dissolved hydrogen, and $\mathrm{tr}(\sigma)$ is the trace of the stress tensor, i.e., the hydrostatic stress. Since v_{H} is in most cases positive, this term leads to the migration of hydrogen from regions with compressive into regions with tensile stresses. One example for this is the accumulation of hydrogen

at crack tips, which, due to the detrimental influence of hydrogen on the mechanical stability of the metal, promotes crack propagation and material failure. It should be noted that not only stress gradients, but also gradients in plastic strain can act as a driving force for the diffusion of hydrogen [108, 113].

The force exerted by a temperature gradient is given as

$$\vec{F}_{temp} = -Q^* \frac{\vec{\nabla}T}{T}. \tag{2.12}$$

This is also known as thermodiffusion or *Soret effect*. Q^* is the heat of transport and can in principle be either positive or negative. A positive value of Q^* leads to a transport of hydrogen into cooler regions of the material. For tungsten, no definitive literature data on Q^* exists. Theoretical considerations on the heat of transport have been performed by Longhurst [61]: He derives a formula for the calculation of Q^* of the form of $Q^* = a + b \cdot T$. a is a constant that depends strongly on material parameters, particularly the heat of solution ΔH_{sol}. b depends only weakly on the material and is typically positive. Longhurst predicts a *negative* Q^* for metals with a positive (i.e., endothermic) heat of solution (such as, e.g., tungsten). Due to the typically positive sign of b, the initially repulsive effect of thermodiffusion on hydrogen at room temperature will reduce with rising temperature. Eventually Q^* will even change its sign. Using Longhurst's formula, the heat of transport for tungsten can be estimated to be of the order of roughly -0.7 eV at room temperature. The change of sign should occur somewhere around 700–1000 K. Values based on Longhurst's publication [61] that were calculated by Tamura *et al.* [107] of -2×10^{-4} J/mol are clearly wrong when compared to the experimental values of Q^* for other metals. They are typically of the order of several 10^3 to several 10^4 J/mol, i.e., 0.1–1 eV (positive or negative, depending on the metal) [61]. If the sign of the exponent of the Q^* by Tamura *et al.* were positive, it would coincide with the value calculated here.

Under low-temperature plasma loading conditions such as they will be mostly discussed in this thesis, diffusion driven by a concentration gradient will be several orders of magnitude stronger than thermodiffusion. This is because concentration gradients are usually much steeper than temperature gradients. There are, however, some cases like plasma-facing components in a steady-state fusion reactor, where the situation might be different. Here the components will probably be saturated with hydrogen isotopes, and the concentration gradient will be flat. On the other hand, the component faces a high thermal load on the plasma side and

is water-cooled on the other side. Longhurst [61] showed that under such conditions thermodiffusion could possibly drive a substantial part of the steady-state permeation flow of hydrogen isotopes through the component if Q^* is positive. This could even be the case for tungsten if the temperature is high enough for Q^* to be positive. Another effect that may play a role in a fusion reactor is an intense transient heat load due to plasma edge instabilities. In this case very steep temperature gradients could temporarily occur.

Finally, the force due to a gradient in the electrical potential Φ can be expressed as

$$\vec{F}_{el} = eZ^*\vec{\nabla}\Phi, \tag{2.13}$$

where e is the (positive) elementary charge and Z^* is the effective charge number. Please note that Z^* can be either positive or negative. It is the net effect of the electrical force acting directly on the proton and the drag force exerted on the screened proton by the electron current flowing in the metal due to the potential gradient. For hydrogen in tungsten, no value of Z^* was found in literature.

While these effects are applicable to all kinds of alloys or impurities in metals, they have an especially strong impact for hydrogen in metals due to the very high diffusivity in this system even at moderate temperatures.

2.4. Effects of non-equilibrium hydrogen loading

In the previous sections of this chapters, the behaviour of hydrogen in metals in (respectively near) thermal equilibrium was discussed. But it is also possible to create hydrogen inventories in a metal that lie far above the equilibrium solubility. One possibility to achieve this is thermal quenching after equilibrium loading at high temperatures. A very interesting alternative is the bombardment of metal samples with energetic ions, e.g., from an ion beam or a plasma. Please note that even an ion energy of only a few eV corresponds to a chemical potential that is sufficient for achieving extraordinarily high concentrations.

In such a non-equilibrium situation the corresponding equilibrium pressures as estimated by Sieverts' Law (2.5) become immense. Note that the estimation by (2.5) is somewhat mediated, e.g., because the H_2 gas becomes non-ideal at very high pressures. A more thorough calculation of equivalent pressures for oversaturated

copper is given in the report of Wipf [121].

This leads to some interesting effects. One that is observed in metals with an endothermic heat of solution H_{sol} is the precipitation of hydrogen and the formation of hydrogen molecules in internal cavities [121]. Since the equilibrium pressure is often far beyond the yield strength of the metal, the metal is displaced to make room for the hydrogen gas, and gas bubbles start to grow. A broad overview over hydrogen bubble formation in various metals is given in [17]. This article lists three main microscopic mechanisms for the nucleation and growth of bubbles: dislocation loop punching, vacancy clustering and blistering, i.e., the displacement of material near the surface, which often produces surface morphologies that can even be observed with an optical microscope. Please note that the association of blister formation with plastic deformation by Condon and Schober [17] does not conflict with recent findings [9] that blisters can, under certain conditions, collapse fully as soon as the high-pressure gas is released by puncturing the cap of the blister: The inflation of the blister has in these cases still caused a very fine crack system along grain boundaries. This decohesion at the grain boundary cannot be recovered elastically. While the term *plastic* deformation in the strictest sense is not quite applicable (the failure is actually brittle or semi-brittle), this can at least be counted as a microscopically *irreversible* deformation of the metal.

In brittle materials, such as tungsten, that are exposed to very high ion fluxes, stresses due to the oversaturation with hydrogen can become so large that the lattice is ripped apart and stress-induced cracks are formed [57, 58].

2.5. Summary of the general properties of hydrogen-metal systems

This chapter has given an overview over the general behaviour of metal–hydrogen systems. While the system is highly complex in detail, some basic properties can be identified. The most generally observed one is that hydrogen has to dissociate in order to be dissolved in a metal. Hydrogen molecules are not stable in solid solution, as has been shown by DFT modelling. The validity of Sieverts' Law — at least for dilute concentrations and moderate pressures — in a wide range of metal–hydrogen systems gives experimental backing for this.

The actual solubility of hydrogen of can vary very strongly between metals. The most general classification can be made by distinguishing metals that dissolve hydrogen either *exothermically* or *endothermically*. Please note that the heat of solution has no direct relation to the formation of a hydride phase, which can in principle occur in both types of metals at sufficiently high concentrations. The heat of solution is strongly connected to the electronic structure of the metal, as it is qualitatively described by the screened proton model. The electron density around the solute was calculated by DFT and is comparable to atomic or maybe even anionic hydrogen. Typically, hydrogen is located in tetrahedral interstitial sites for bcc and in octahedral sites for fcc metals.

Crystal imperfections such as vacancies, dislocations or grain boundaries can act as traps for hydrogen. This means they have a higher binding energy for hydrogen than regular interstitial sites. The existence of traps generally increases the absorption capacity of metals under given loading conditions. In metals where the interstitial solubility is very low, trapping can dominate the hydrogen inventory. Especially in such cases, it is helpful to consider the hydrogen inventory in the metal in a *density-of-sites* approach in analogy to the density of states in the theory of conduction electrons in metals.

Hydrogen atoms dissolved in a metal interact also with each other, especially at higher concentrations. Elastic long-range interactions imparted through the crystal lattice are assumed to be typically attractive, while short-range interactions in a defect-free crystal are repulsive in accordance with the non-existence of solute hydrogen molecules. In the vicinity of defects, especially within the tensile strain field of a dislocation, attractive nearest-neighbor interactions between hydrogen atoms can occur as well.

Diffusion of hydrogen in metals is very fast and, in particular at low temperatures, strongly influenced by quantum-mechanical effects. At very low temperatures, coherent tunnelling is believed to be dominant, although mostly for hopping between adjacent sites and usually not for band-like propagation. At slightly higher temperatures, thermally activated tunnelling as well as propagation through excited states in saddle-point configurations are the most important processes. At intermediate temperatures of the order of 300 K and above, thermally activated, classical hopping over the barrier between adjacent sites takes place. With increasing temperature, there is some evidence that long-range jumps start to occur, until at very high temperature the movement of hydrogen is gas- or fluid-like. Interaction with the conduction electrons of the metal also plays a role for diffu-

sion. This is discussed in the Kondo theory. External forces such as gradients in (hydrostatic) stress, temperature and electrical potential can also drive a diffusive flow of hydrogen.

Non-equilibrium conditions such as irradiation of a metal with a plasma or an ion beam can lead to — at least transient — hydrogen inventories far above the equilibrium solubility. This leads to enormous corresponding pressures particularly in metals with an endothermic ΔH_{sol}. As a result, hydrogen precipitates in high-pressure gas bubbles in internal cavities. If this happens near the surface, it leads to blistering.

3. Hydrogen isotopes in tungsten

While the previous chapter described metal–hydrogen systems in general, this chapter now focusses on the hydrogen–tungsten system. It addresses, therefore, a system whose hydrogen inventory is dominated by defects. After a brief review of the data published so far, a tool for the numerical simulation of a system heavily influenced by traps is introduced: so-called diffusion-trapping models. Along with a general description of the method, details of the model used in this thesis are presented.

3.1. Characteristics of the hydrogen–tungsten system

Tungsten is a metal that has only one stable modification, namely the bcc phase. Any other modifications are only metastable, e.g, the A-15 β phase, which can be created by physical vapour deposition of thin tungsten films. They decay into the bcc phase at temperatures far below the melting point of tungsten, values between room temperature and up to ≈ 900 K are reported in literature [85, 84, 102, 93]. Since nearly all the tungsten specimens discussed in this thesis are powder-metallurgical bulk tungsten that was annealed at least at 1200 K, it will be assumed from now on that only the bcc phase is present.

Since tungsten is a bcc metal, hydrogen in a perfect single crystal is expected to occupy only tetrahedral interstitial sites. This has been confirmed by ion channelling measurements [87]. DFT calculations [40] also show that tetrahedral sites are preferred and that the energetic separation between octahedral and tetrahedral sites in tungsten is 0.38 eV. These calculations yield an endothermic enthalpy of solution of $\Delta H_{sol} = +0.96$ eV per hydrogen atom and state a partial volume of hydrogen of $v_{\mathrm{H}} = 2.90$ Å^3 per hydrogen atom. The most commonly accepted experimental value for the enthalpy of solution is $\Delta H_{sol} = 1.04 \pm 0.17$ eV per

hydrogen atom [27].

The enthalpy of solution for hydrogen in tungsten is the most endothermic ones that can be found among the transition metals (see Figure 2.1). Therefore, the solubility in a tungsten single crystal is extremely low. This also has the consequence that even small concentrations of traps can easily dominate the achievable concentration and behaviour of the dissolved hydrogen. This has severe implications for attempts to measure the diffusivity of hydrogen in tungsten: as long as the temperature is low enough that the traps can still bind a considerable fraction of the hydrogen in the specimen, the diffusion barrier is governed by the traps. If one looks at diffusion barriers E_{diff} published by in literature, one finds, e.g., values of $E_{diff} = 0.39$ eV [27], $E_{diff} = 0.86$ eV [96] or $E_{diff} = 1.8$ eV [71]. In the appendix of [27] the difference between the values found by Frauenfelder [27] and by Moore *et al.* [71] are explained by a second type of "residual" site that is strongly attractive to hydrogen ($E_{trap} \approx 3$ eV). The deviations between Frauenfelder's [27] and Ryabchikov's [96] values could be explained by taking into account that the hydrogen in Ryabchikov's tungsten specimens possibly had a non-uniform spatial distribution (while Ryabchikov assumed a *homogeneous* distribution for the evaluation of the data) [27]. DFT results by Heinola *et al.* [40] state a diffusion barrier of $E_{diff} = 0.21$ eV. The authors of [40], following a suggestion in [100], also calculated a fit to the data of Frauenfelder [27] that neglects the two data points below 1500 K and arrived at a diffusion barrier of $E_{diff} = 0.25$ eV, which is rather close to the DFT result. However, the simulation cell in [40] contained 128 W and one H atom, which corresponds to a hydrogen concentration of approximately 0.8% using periodic boundary conditions. This is an extremely high value even for defect-rich tungsten, and even more so for an undisturbed crystal.

These differences in reported values show how difficult it is to determine a reliable diffusion barrier for hydrogen isotopes in tungsten. Experimental results appear to depend strongly on the temperature window and the quality of the tungsten specimen that is investigated. Similarly, the diffusion pre-factor D^0 also varies by several orders of magnitude, depending on the experimental conditions. The most extreme cases are $D^0 = 6 \times 10^{-4}$ m^2/s [123] and $D^0 = 3.5 \times 10^{-11}$ m^2/s [32]. The Frauenfelder value of 4.1×10^{-7} m^2/s is somewhere in between.

A large selection of diffusivity data from experiments and modelling are compiled into the Arrhenius plot shown in Figure 3.1. So far, the most widely accepted values are those proposed by Frauenfelder [27]:

$$D = \left(4.1^{+5}_{-2}\right) \times 10^{-7} \exp\left(-\frac{0.39 \pm 0.09\,\text{eV}}{k_B T}\right)\,\text{m}^2/\text{s}. \tag{3.1}$$

It can be clearly seen how the diffusivity drops below the extrapolation of the high-temperature data by Frauenfelder [27] at lower temperatures. This is probably an effect of the increasing influence of hydrogen trapping at lower temperatures.
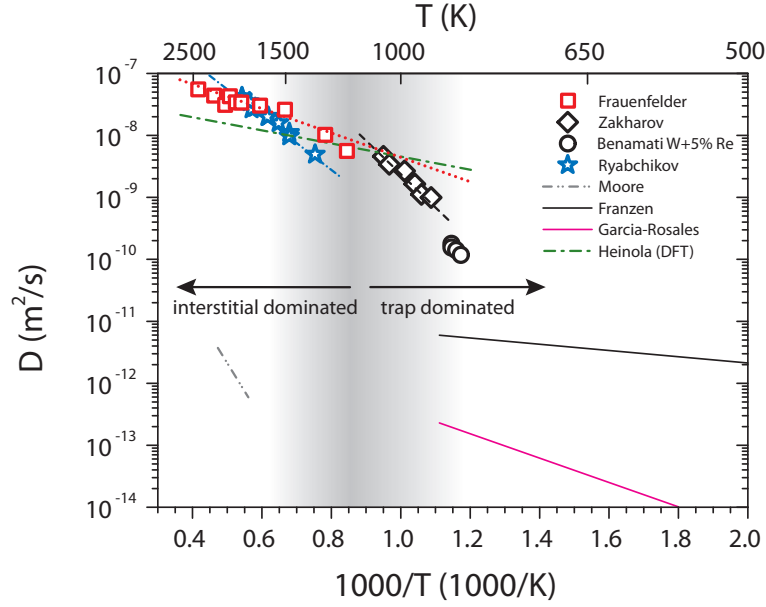

Figure 3.1. Selection of experimental [27, 123, 11, 96, 71, 26, 32] and DFT [40] data of hydrogen diffusivities in tungsten. The transition from interstitial-dominated to trap-dominated diffusion is also indicated.

3.2. Modelling of the deuterium inventory: diffusion and trapping

Typical ion beam or plasma exposure experiments, as they will be discussed in the experimental section of this thesis, are performed at temperatures between 300 and 800 K. Subsequent analysis by thermal desorption is usually performed in the temperature range up to 1200 K, with the largest part of the desorption usually occurring well below 1000 K. In this temperature range it is not sufficient to consider only jumps of hydrogen atoms between interstitial sites, and the diffusivity is not simply given by equation (3.1) anymore (see Figure 3.1). Instead, traps also have to be taken into account.

The diffusion in defect-containing tungsten at intermediate temperatures (i.e, between room temperature and up to roughly 1500 K) is often described by one-dimensional rate equation models, so-called *diffusion-trapping models*. Well-documented examples are the model by Krom and Bakker [56] and the program TMAP7 [62], but many varieties of such codes are in use. The following discussion of diffusion-trapping models refers mostly to the two models cited above.

These models typically assume that hydrogen is either dissolved in "normal" interstitial lattice sites or resides in one or several types of saturable traps with specified binding energies E_{trap}. Trapped hydrogen is considered immobile, while interstitial "mobile" hydrogen diffuses around the tungsten specimen with a diffusivity D_{mobile}. While the value of D_{mobile} is in principle arbitrary, usually a classical hopping motion is assumed, which is characterised by a pre-factor D^0 and a diffusion barrier E_{diff} [62]:

$$D_{mobile}(T) = D^0 \exp\left(-\frac{E_{diff}}{k_B T}\right).$$

(3.2)

The values for D^0 and E_{diff} are typically taken from experimental data, e.g., the work of Frauenfelder [27], but occasionally they are also regarded as free parameters.

The bound hydrogen can leave the traps in a classical, Arrhenius-like process with an attempt frequency ν_{detrap} and an activation energy E_{trap}, which is expressed by a detrapping rate coefficient α_{detrap} [56, 62]:

$$\alpha_{detrap}(T) = \nu_{detrap} \exp\left(-\frac{E_{trap}}{k_B T}\right).$$

(3.3)

Vice versa, mobile hydrogen can also be captured again by a trap. The trapping rate α_{trap} for the diffusing hydrogen is in these models expressed by the diffusive speed of the hydrogen [56, 62]:

$$\alpha_{trap} = \frac{D_{mobile}}{a^2},$$

(3.4)

i.e., the number of lattice parameters a a particle can travel in a given time interval. This expression includes two assumptions: First, the trapping probability is *independent* of the depth E_{trap} of the trap, and second, one trap site equals one lattice space. The possible spatial extension of traps is only considered as

an average, i.e., it is included into the total concentration of trap sites c_{trap}^0. Of course, this approach neglects the possibility of anisotropic, locally enhanced diffusion, which can occur due to correlated saddle point energies along a spatially extended defect (see section 2.2).

The mobile (i.e, interstitial) hydrogen concentration c_{mobile} and the trapped concentration $c_{trapped}$ are linked by a generalisation of Fick's second law [56]:

$$\frac{\partial c_{mobile}}{\partial t} + \frac{\partial c_{trapped}}{\partial t} - D_{mobile}\frac{\partial^2}{\partial x^2}c_{mobile} = \alpha_{sources} - \alpha_{sinks}. \tag{3.5}$$

The rate coefficients $\alpha_{sources}$ and α_{sinks} stand for additional local sources and sinks for hydrogen, e.g., dissolution from and desorption into the gas phase at the surface [62]. When the system is in a stationary state, the right hand side of equation (3.5) vanishes as in the model by Krom and Bakker [56], but the more general form used here includes also *non-stationary* effects. This allows studying also transient effects in dynamical processes such as ion implantation and thermal desorption experiments.

Using equations (3.3)–(3.4), the time evolution of the trapped concentration $\partial c_{trapped}/\partial t$ can be written for saturable traps as [62]

$$\frac{\partial c_{trapped}}{\partial t} = \alpha_{trap}(c_{trap}^0 - c_{trapped})c_{mobile} - \alpha_{detrap}c_{trapped}. \tag{3.6}$$

Since c_{trap}^0 stands for the total concentration of traps (filled as well as empty), $c_{trap}^0 - c_{trapped}$ is the concentration of empty traps.

Diffusion-trapping models are often semi-empirical, and several central constants such as ν_{detrap} or E_{trap} are regularly used as free parameters in order to fit experimental results. Such experiments are, e.g., loading of a specimen with hydrogen isotopes under certain conditions and subsequent thermal desorption spectroscopy (TDS; see also section 4.3) in order to probe the retained hydrogen inventory, or also permeation experiments. The simulation can then include the full experimental process, i.e, hydrogen loading along with migration from the surface into the bulk of the specimen, re-emission after the loading stops (especially for experiments at elevated temperatures) and the release of hydrogen during thermal desorption spectroscopy. This can be supplemented by depth profile measurements, e.g., by the D(^{3}He, p)^{4}He nuclear reaction (see also section 4.2) if deuterium was used for the loading of the sample. Depth profiles can serve as a further dataset

to be compared with the state of the simulated system after the loading with hydrogen, or be used to estimate trap concentrations for the simulation.

The desired results derived from diffusion-trapping simulations are often trap energy distributions $\mathcal{P}(E_{trap})$. While the simulations typically lack *ab initio* character, they can still be used to predict new experiments based on existing experimental data. This is also the ultimate test for the validity of the empirical results, and of course the assumptions of the model itself.

3.3. Modelling details

For the interpretation of experimental results presented in this thesis, a (yet unpublished) diffusion-trapping code developed by K. Schmid was used. The model is, in its central equations, similar to the models introduced in section 3.2. It is implemented in *Wolfram Mathematica® 8* and uses the *NDsolve* solver for the numerical solution of the differential equations. The *Mathematica* implementation offers a high flexibility of the code together with a powerful solver.

The numerical solution is based on the so-called *method of lines*. An overview of this technique for numerically solving partial differential equations is presented by Hamdi *et al.* [39]. The basic idea behind the method of lines is to approximate a partial differential equation by a system of ordinary differential equations by replacing the spatial derivatives with algebraic approximations, while the time derivatives are not transformed. When this is done, one can choose a well-established method for integrating ordinary differential equations. One possible approximation for the spatial derivatives are finite differences. This means that the spatial coordinate is *discretised* into a so-called *grid*, i.e., an indexed array of positions. The choice of an appropriate grid is important for success in finding a solution: If the grid is too coarse, the accuracy of the solution can be insufficient or singularities may appear. If the grid is too fine, the demand on computational resources can become excessive.

In the model used here, the initial condition at $t = 0$ is either chosen as an empty specimen for the simulation of hydrogen implantation experiments, or set as the result from a previous implantation simulation, e.g., for modelling TDS results. The boundary conditions in space are that the hydrogen concentration in any type of site vanishes at the front and the rear surface of the specimen, i.e., the desorption from the specimen is assumed to be *diffusion limited*, as suggested in

the review by Causey [14]. Hydrogen losses from the free surfaces of the specimen are the only sinks in the system. For implantation experiments, the source term in equation 3.5 is set to a Gaussian profile that is truncated by a steep Boltzmann function towards the surface. The position of the maximum and the width of the implantation profile are pre-calculated by SDTrimSP [22] (see Figure 7.1) and entered into the model as parameters. The incident ion flux is taken from measurements (see section 4.1 respectively [65]) and reduced by the reflection yield calculated by SDTrimSP. The energy distribution of the incident ions is approximated as monoenergetic.

The grid used for the numerical solution has a variable step width: The discretisation is very fine near both surfaces in order to fulfil the boundary conditions without numerical oscillations. The step width is increased following a Gaussian function towards the bulk of the specimen and is then set to a constant value throughout most of the specimen. While the specimens used for experiments were about 800 μm thick, the specimen thickness used for the simulations was set to only 200 μm because this significantly reduced the demand on computational resources. The reduced specimen thickness has no influence on the simulation of most deuterium implantation experiments since the diffusion range turned out to be typically less than about 100 μm at the implantation temperature of 370 K for which this simulation was optimised, even at high incident fluences. The reduced specimen thickness in the simulations usually only led to a larger fraction of the deuterium desorbing from the rear side of the specimen in TDS simulations.

For the movement between interstitial sites as well as from interstitial sites into traps, the values by Frauenfelder [27] were used, as suggested by Causey [14]. Since Frauenfelder's values were derived for hydrogen, the pre-exponential factor was scaled by $1/\sqrt{2}$ to account for the larger mass of deuterium. Unfortunately, measurements directly comparing the diffusivity of hydrogen isotopes in tungsten apparently do not exist, and the scatter between different published values is large (see section 3.1).

Just like most other diffusion-trapping models (e.g., TMAP7 [62]) the model used here specifies a small number of different types of traps with a precisely defined binding energy. Escape of hydrogen atoms from traps are modelled by Arrhenius laws. While an ensemble of traps with many different binding energies might be used to approximate a continuous density of sites, it would still neglect spatial and energetic correlations between trap sites, e.g, in the strain field of a dislocation or in a grain boundary. On the other hand, increasing the number of traps also

increases the stiffness of the differential equation system and thus impairs the numerical stability of the solutions. However, the model goes beyond most of its predecessors by allowing also a *time evolution* of trap density profiles. This is necessary to account for the experimentally observed production of defects due to the plasma exposure of tungsten specimens (see sections 8.2 and 8.3). The time evolution of traps is, for now, modelled by specifying empirical, explicitly time-dependent trap density functions. An implicit time dependence that is based on local hydrogen concentrations is, at present, not implemented.

Currently, three different types of trap are used in the model. Firstly, a high-energy trap with a high binding energy of 2.2 eV is used to represent displacement damage near the surface caused during plasma exposure. These defects are confined to a narrow subsurface region, and their density increases up to an empirical saturation value with time respectively fluence. The high binding energy traps give rise to a release peak at relatively high temperatures of about 800–900 K. The assignment of displacement damage with this release peak is based on observations for self-damaged tungsten [109].

Secondly, dislocation cores (and grain boundaries) are modelled as defects with an intermediate binding energy of 1.2 eV. This value is based on the analysis of TDS spectra with different heating rates. Details of this analysis will be discussed in section 8.5.1. Their density profile is the sum of a background, which is constant in time and space, and an evolving Gaussian peak within a few microns of the implanted surface, which is used to model dislocations emitted due to the growth of blisters (see, e.g, section 8.1.6). Based on measured deuterium depth profiles, the peak does not only grow in magnitude up to a certain saturation value, but also becomes broader and shifts its centre of weight towards larger depths with time respectively fluence.

The third trap at 0.7 eV is set to five times the density of the 1.2 eV trap. This trap is used as a coarse approximation for hydrogen being trapped in the strain fields of dislocations. The density relation reflects the $1/E^3$ model for the density of sites around a dislocation (see Table 2.1). This trap is responsible for the early onset of deuterium release that is observed in thermal desorption experiments. The evolution of the time-dependent trap densities is presently based on experimental depth profiles of deuterium retained in stress-relieved tungsten after plasma exposure at different fluences (see Figure 8.11). Details about these experimental results are discussed in section 8.2. Overall, the trap energies stated above all lie within the range of previously published values (for an overview see

[14]) and reproduce the main features in experimental thermal desorption spectra of deuterium from tungsten.

The detrapping attempt frequency was initially chosen at 3.3×10^{13} s^{-1}, i.e, $1/\sqrt{2}$ times the ground state vibration frequency of interstitial hydrogen calculated by Heinola *et al.* [40]. By comparison with experimental data (see section 8.5.1), this value was iteratively refined to 6.6×10^{11} s^{-1}.

So far, simulations were only performed for stress-relieved tungsten at a temperature of 370 K during implantation. The reason is that an empirical description of the trap evolution — mainly due to blistering — currently exists only for this temperature and only for this type of material. For other temperatures and microstructures, a consistent trap evolution model has yet to be developed. Considering the large amount of experimental data that was necessary to find a suitable description only for the conditions mentioned above, this has to be regarded as a long-term project.

4. Analysis methods and equipment

This chapter first introduces the device "PlaQ" that was used to expose tungsten specimens to deuterium plasmas. After that, the main analysis techniques used in this thesis are described. Both nuclear reaction analysis (NRA) and thermal desorption spectroscopy (TDS) are discussed in detail. A short overview over the electron microscopy equipment as well as an introduction to the differential interference contrast (DIC) method for optical microscopes are also presented.

4.1. Plasma exposure of tungsten specimens

For the deuterium loading of all tungsten specimens investigated for this thesis, the plasma device "PlaQ" was used. A detailed description of PlaQ can be found in [65], but the key features are reviewed here. A sketch of the set-up can be found in Figure 4.1.

In this device, a low-temperature, low-pressure plasma is ignited by electron cyclotron resonance (ECR) heating. The operating gas is D_2 at a pressure of 1.0 Pa, the nominal output power of the 2.45 GHz microwave source is set to 144 W. The main discharge is spatially separated from the sample holder. This allows setting the impact energy of ions from the plasma on the specimens by biasing the holder with a (negative) voltage V_{bias} without strongly influencing the plasma itself. The deuterium ion flux density impinging on the sample holder has been absolutely quantified using a retarding field analyser and a plasma monitor [65]. It has only a weak dependence on the bias voltage and an absolute value of $\approx 10^{20}$ D m^{-2}s^{-1}. Variations derived from measurements of the sample holder current are typically less than 5% during an implantation run. The ion flux is constant even over long periods — up to 12 consecutive days of implantation were successfully tried so far. This allows the accumulation of large deuteron fluences. The deuteron flux is mostly carried by D_3^+ ions, accompanied by small fractions of D^+ and D_2^+ ions. This means that the typical energy per deuteron
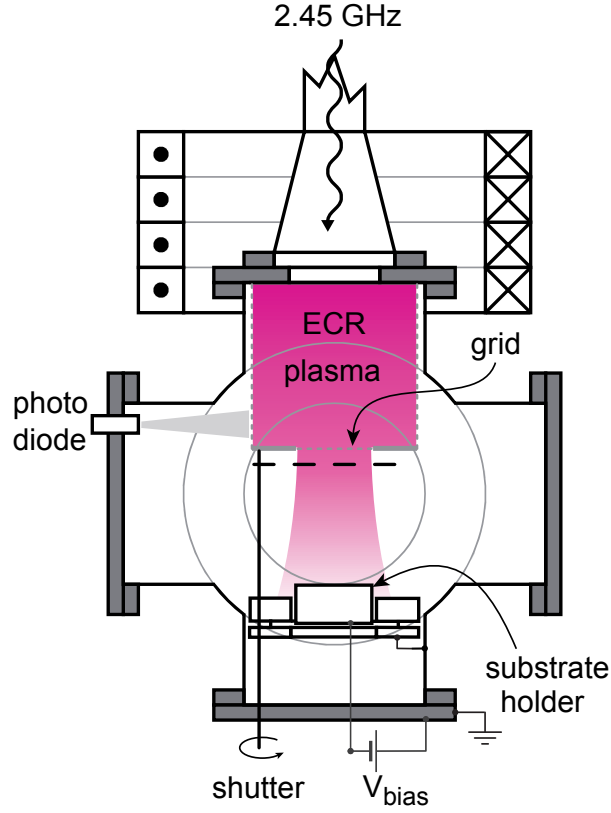
Figure 4.1. Schematic drawing of the PlaQ plasma device [65]. The main ECR discharge is confined to a stainless steel cage and monitored by a photo diode. The sample holder is hit by a freely expanding plasma beam, which can be blocked by a shutter. The holder can be biased with the voltage V_{bias} in order to adjust the ion energy. Its temperature is regulated either by radiative heating or by a liquid thermostat.

is one third of the total ion energy. The energy spectrum of the ions is peaked at $e \cdot |V_{bias}| + 15$ eV. Its shape is nearly unaffected by the sample holder bias. The offset of 15 eV is present even at floating potential and reduces only slightly towards higher values of V_{bias}. Accordingly, all ion energies E_D specified in this thesis for specimens implanted in PlaQ should be understood in this way:

$$E_D = \frac{1}{3} e \cdot |V_{bias}| + 5 \text{ eV/D}. \tag{4.1}$$

The maximum possible bias voltage is -600 V, corresponding to 205 eV/D. Typically a lower voltage of $V_{bias} = -100$ V, corresponding to 38 eV/D, is used. This reduces the sputtering as well as the heating of the specimens and the holder by the impinging ions.

It should be noted that the specimens are also bombarded by a large amount of neutral D atoms from the plasma [65]. They have approximately thermal kinetic energies (i.e., typically $\ll 1$ eV), but an about 10–100 times higher flux. It will be shown by bias variation experiments, however, that their contribution to the deuterium uptake of tungsten specimens is usually negligible compared to the effect of the energetic ions.

For all implantation experiments, the actual plasma exposure of the specimens is preceded by a phase of about 30 minutes where the direct plasma beam is blocked by a shutter. This burn-in phase is necessary to ensure that the plasma discharge is stabilised and impurities at surfaces in direct contact with the main plasma are removed [65].

The specimen temperature during loading can be adjusted by either radiatively heating a stainless steel holder from the rear side with a BORALECTRIC® heater, or by using a copper holder that is either heated or cooled by a fluid thermostat (heat transfer medium: silicon oil). Radiative heating is used for temperatures of 500 K and above, while the latter method is applicable between ≈ 300 and 450 K. Both the steel and the copper holder are coated with ≈ 1 μm of sputter-deposited tungsten to minimise sputtering by the plasma. Both types of holder can hold up to 5 specimens of the type described in chapter 5. They are firmly attached to the holder by 4 molybdenum screws each. This ensures a good thermal contact between the specimens and the holder.

For implantation at elevated temperatures, the sample holder is pre-heated to the desired temperature before the plasma exposure. When the exposure starts, the heating power of the BORALECTRIC® heater or the oil thermostat is typically slightly reduced in order to compensate for the additional power input from the plasma. When the implantation stops, the cool-down procedure is immediately started. Using the oil thermostat, the cool-down curve is approximately linear. From a temperature of 370 K, it takes about 40 minutes with a cooling rate of ≈ 1.7 K/min. If the BORALECTRIC® heater is used, the cool-down curve is exponential. For example, it takes about 50 minutes to cool to room temperature from 500 K, with a decay time constant of ≈ 11 minutes.

4.2. Nuclear reaction analysis

4.2.1. Basic description of the technique

One method used to probe the retained deuterium inventory in a tungsten specimen after plasma exposure utilises the nuclear reaction of energetic ^{3}He ions with the deuterium in the specimen:

$$D(^3He, p)^4He \quad \text{respectively} \quad D(^3He, \alpha)p. \tag{4.2}$$
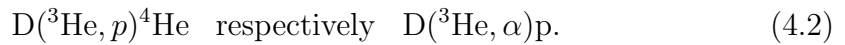
This reaction has a Q-value of 18352 keV, which is distributed to the proton and the α particle according to the laws of conservation of energy and momentum. Both particles can be detected in order to quantify the amount of deuterium within the specimen volume probed by the incident ^{3}He beam. This reaction has a resonant cross-section with a relatively broad maximum at about 620 keV projectile kinetic energy. For the work presented here, the cross-section data published by Alimov *et al.* [3] was used. The symbols in Figure 4.2 show the measured differential cross-section σ_{NRA} at a laboratory angle of 135° versus the energy of the incident ^{3}He beam E_{beam}. The line shows a fit of the data that is included in the more recent versions of the SIMNRA program package [69]. The version used here is v6.06.

By varying the energy of the incident ^{3}He beam, this maximum can be positioned at different depths below the specimen surface due to the energy loss of the ^{3}He particles. Due to the high stopping power of tungsten, the accessible information depth is limited to about 8 μm for 4500 keV ^{3}He and to ≈ 12 μm for a 6000 keV ^{3}He beam. Figure 4.3 shows simulated effective cross-sections of the D(^{3}He, p)^{4}He nuclear reaction for ^{3}He beams with different energies impinging on a tungsten specimen. These effective cross-sections are based on the data shown in Figure 4.3 and SDTrimSP [22] calculations of the stopping of the ^{3}He beam in the tungsten. The effective cross section $\sigma_{NRA} \times \eta_{beam}$ takes into account a small correction due to the range straggling of the ^{3}He beam. Calculations were made for all energies that were used in this thesis (although the highest energy of 6000 keV was only used for a few selected investigations). Please note that even at high beam energies E_{beam}, where the cross-section maximum lies deep in the specimen, there is a considerable contribution to the cross-section from deuterium close to the specimen surface.

In addition to counting the total amount of protons (or also α particles) for
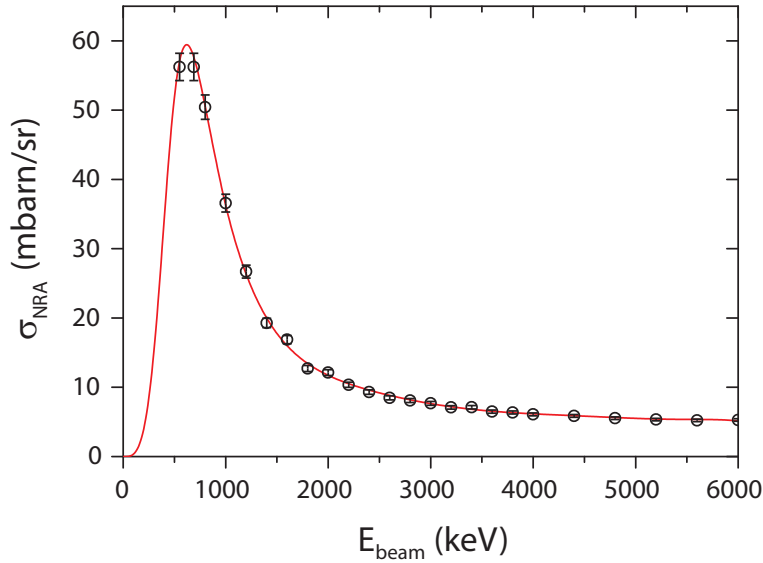
Figure 4.2. Differential cross-section of the D(^{3}He, p)^{4}He nuclear reaction as published by
Alimov *et al.* [3] (symbols). The solid line represents the fit included in the current
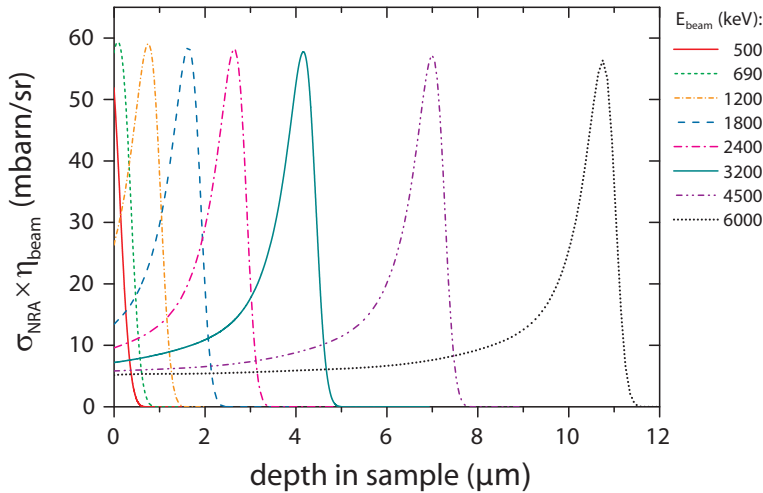versions of the SIMNRA program package [69].

Figure 4.3. Effective differential cross-sections $\sigma_{NRA} \times \eta_{beam}$ of the D(^{3}He, p)^{4}He nuclear re-
action versus beam penetration depth in a tungsten specimen. The cross-section
data by Alimov *et al.* [3] were convolved with stopping simulations for various
incident ^{3}He energies and include range straggling.

each incident beam energy, the energy spectrum of the reaction products can be
acquired. For this, a thick proton counter capable of completely stopping the high-
energy protons is necessary. A single full proton spectrum of the D(^{3}He, p)^{4}He
reaction for deuterium in tungsten yields theoretical depth resolutions that range
from slightly more than 100 nm close to the specimen surface for low incident

beam energies up to around 1–2 μm at 8 μm for 4000 keV incident ions [70]. The α particle spectra at low incident beam energies can yield a better depth resolution, but are limited to the near-surface inventory due to the limited range of the α particles in the material. Additionally, the accurate determination of deuterium depth profiles from the α particle spectrum only works well for very smooth specimens. The reason is that the α particles lose a considerable amount of energy on their way out of the tungsten specimen. Together with the relatively shallow detection angle of 102° (see below), this can lead to distortions of the energy spectrum of the detected particles due to surface roughness.

For the measurements performed for this thesis, a proton detector thick enough to stop all reaction protons was used. It was installed at a laboratory scattering angle of $135 \pm 0.5°$. The detector is equipped with a parabolic slit that limits the solid angle to 29.94 ± 0.2 msr, and with a stopping foil that allows the high-energy protons to pass but blocks the back-scattered ^{3}He particles. With this set-up an effective energy resolution of around 100 keV can be achieved. This value was obtained by measuring the NRA proton spectra of a 20 nm thick amorphous deuterated hydrocarbon (a–C:D) layer on silicon.

The alpha particles were detected with a detector under $102 \pm 0.5°$ scattering geometry in the laboratory system. This detector has rectangular aperture that leads to a solid angle of 9.16 ± 0.07 msr and has no stopper foil. Energy spectra from this detector can only be evaluated for incident beam energies below 1000 keV. For higher energies, the much larger signal from back-scattered ^{3}He particles obscures the α particle spectrum. Additionally, due to the small solid angle of the detector, its sensitivity is rather small. This is even aggravated by the dead time caused by the massive amount of backscattered ^{3}He particles impinging on the detector. Together with the typically small deuterium inventories in tungsten, this often leads to poor signal quality, which cannot be outweighed by the superior depth resolution achievable with this detector. Although α particle spectra were recorded for all analysed specimens, most of them were discarded during the data analysis due to the aforementioned problems.

The ^{3}He beam was generated by a tandem accelerator manufactured by High Voltage Engineering Europa B.V. (HVE). This accelerator has a terminal voltage of 3 MV and thus allows to generate ^{3}He$^+$ with up to 6000 keV. Due to radiation safety limits only up to 4500–5000 keV can be achieved with ^{3}He$^+$ ions, however. For higher energies, it is necessary to use ^{3}He^{2+} ions.

4.2.2. NRADC optimisation

The energy spectra from NRA were analysed with a combination of the SIMNRA software [69] for calculating energy spectra and the NRADC program [99] for the deconvolution of the data resulting from an energy variation of the incident beam. Considering the spatial overlapping of the effective reaction cross-sections shown in Figure 4.3, it is clear that all data from a beam energy scan have to be fitted simultaneously in order to get a reliable result.

The NRADC program calculates a "free-form" reconstruction of the deuterium concentration depth profile. Since it is based on SIMNRA, it has to discretise the depth profiles into layers with a constant deuterium concentration. The reconstruction uses very little prior knowledge about the depth profile to be fitted and is therefore relatively unbiased. The necessary prior information (besides the experiment parameters) is limited to the material of the specimen, a starting layout for the depth profile, the energy calibration for the detector and the regions of interest for the peaks that are to be fitted. The program then optimises the number N, thicknesses Δx_i and D concentrations c_i of the layers. The procedure for a depth profile reconstruction is shown in the flowchart in Figure 4.4.

First, a SIMNRA template file containing the experiment geometry and a simple target layout that includes all elements that are present in the target and needed for the analysis — e.g., tungsten, deuterium and, for the energy calibration, a very thin layer of carbon on the surface. Then, the energy calibration of the detector is fine-tuned for every measured spectrum by the user. The linear dispersion of the detector can best be derived from the three proton peaks originating from nuclear reactions of a ^{3}He beam and the small amount of carbon containing impurities that are nearly always present on the specimen surface. These peaks are typically very narrow and are well visible for ^{3}He energies of 2000 keV or more. The surface edge of the proton peak is also a fixed point in the energy spectrum. Quite often, the constant offset of the energy calibration has to be slightly adjusted for each spectrum in order to ensure a good agreement of the measured surface edge and the corresponding SIMNRA calculation. This is mostly due to small variations of the angle between the beam and the specimen surface normal. After that, the user has to specify the range of detector channels containing the proton (or α particle) peak for each measured spectrum. The last preparation step is the generation of the starting layout for the optimisation. This is typically done by calculating the stopping range and the position of the cross-section maximum (see Figure 4.3) for each incident beam energy in the specified target material.
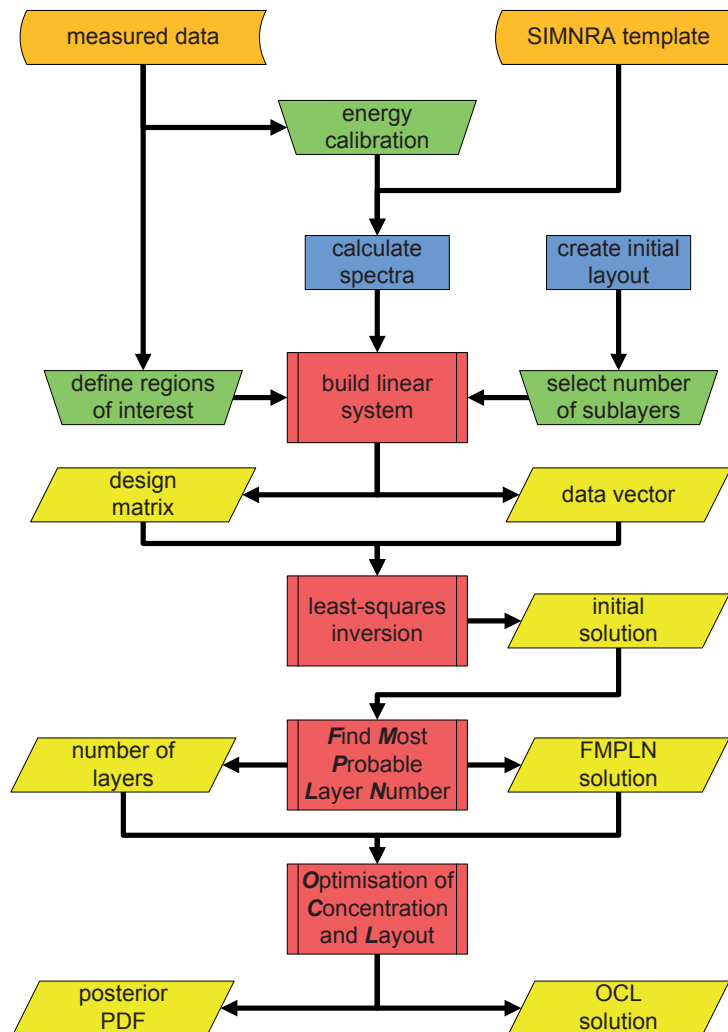
Figure 4.4. Flowchart of the NRADC optimisation procedure of a deuterium depth profile.

The program package provides an automated function for that. Each layer in this initial layout is subdivided to a certain degree specified by the user in order to allow future refinement of the layout. A typical value is 4 sub-layers per layer.

The first step of the actual calculation is the linearisation of the problem: For small deuterium concentrations (like they usually occur for tungsten specimens) it can be assumed that the stopping power of the incident ^{3}He beam depends only on the specimen material and not on the deuterium concentration. In this case the calculation of NRA spectra from an assumed deuterium depth profile can be simplified to a linear problem:

$$I_k = \sum_{i=1}^{N} \mathcal{D}_{ik} \times c_i. \tag{4.3}$$

In this equation, I_k is the kth component of the *data vector* $\vec{I}$, which contains the measured intensities of all channels in the regions of interest for all incident ^{3}He beams. The integrals over the individual regions of interest are also included as channels in $\vec{I}$. $\mathcal{D}_{ik}$ is the so-called *design matrix*, which specifies the contribution of the deuterium concentration c_i in layer i (i.e., in a certain depth in the specimen) to the data in channel k. This design matrix is built by the program by positioning a small amount of deuterium sequentially in every sub-layer of the specimen and calculating the resulting NRA spectrum with SIMNRA for each incident ^{3}He beam energy. The calculation of $\mathcal{D}_{ik}$ is often the most time-consuming part of the reconstruction process, but in turn strongly reduces the necessary computing time for the following Monte-Carlo optimisations. It even allows a first quick estimate of c_i by a simple least-squares inversion of equation (4.3), including error bars. However, the least-squares result is not always physically meaningful since it can also include *negative* concentrations c_i in the depth profile.

The next step is the optimisation of the number of layers N and their thicknesses Δx_i. For this, the parameter space is sampled for a range of N specified by the user. For each N the best solution $\mathcal{C}_{opt}(N)$ is searched by a Monte-Carlo sampling of possible layouts $\{\Delta x_i\}$ and a subsequent least-squares inversion of equation (4.3) in order to find the corresponding concentrations c_i ($i = 1...N$). For each solution the χ^2 value is computed, and the solution with the smallest $\chi^2 = \chi^2_{min}(N)$ is considered the best solution $\mathcal{C}_{opt}(N)$. Solutions containing one or more negative concentration are discarded. The solutions $\mathcal{C}_{opt}(N)$ for the different numbers of layers N are then compared using the Bayes theorem

$$\mathcal{P}(H|D,B) = \frac{\mathcal{P}(D|H,B) \times \mathcal{P}(H|B)}{\mathcal{P}(D|B)}. \tag{4.4}$$

The basic meaning of this equation is that the *posterior* probability $\mathcal{P}(H|D,B)$, i.e., the probability for a hypothesis H being true given the data D and the background information B, is given by the product of the *likelihood* $\mathcal{P}(D|H,B)$ and the *prior* probability $\mathcal{P}(H|B)$, divided by the *evidence* $\mathcal{P}(D|B)$ (which is often treated as a normalisation constant). For a more detailed introduction into data analysis with the help of Bayesian probability theory, the book of Sivia [105] is recommended to the reader.

In this case, the posterior probability of a certain number of layers N given the experimental data vector $\vec{I}$ is needed to find the most probable number of layers N^{opt}. For this, a method called *marginalisation* is needed. Marginalisation eliminates unwanted "nuisance" parameters Y from the probability $\mathcal{P}(H, Y|B)$ by integrating over them:

$$\mathcal{P}(H|B) = \int \mathcal{P}(H, Y|B) dY. \tag{4.5}$$

In this optimisation step, the exact depth profiles $\mathcal{C}(\mathcal{N}) = \{c_i, \Delta x_i\}(N)$ are the "nuisance" parameters and the measured data vector $\vec{I}$ is the parameter against which the number of layers N has to be optimised. Using a flat prior, i.e., $\mathcal{P}(N|B) = const.$ independent of N (at least for all N in the specified range), equation (4.4) yields that the posterior probability $\mathcal{P}(N|\vec{I}, B)$ is proportional to the likelihood $\mathcal{P}(\vec{I}|N, B)$. The likelihood itself is obtained by marginalisation as follows:

$$\mathcal{P}(\vec{I}|N, B) \propto \int \mathcal{P}(\vec{I}, \{c_i, \Delta x_i\}|N, B) d^N c_i d^N x_i. \tag{4.6}$$

Using the Bayes theorem (4.4) on the expression under the integral of equation (4.6) and assuming flat priors $\mathcal{P}(\{c_i\}|B)$ and $\mathcal{P}(\{\Delta x_i\}|B)$ yields

$$\mathcal{P}(\vec{I}, \{c_i, \Delta x_i\}|N, B) \propto \mathcal{P}(\vec{I}|\{c_i, \Delta x_i\}, N, B). \tag{4.7}$$

Although the likelihood $\mathcal{P}(\vec{I}|\{c_i, \Delta x_i\}, N, B)$ is actually a Poisson distribution, it can be approximated by a χ^2 distribution for this step. With this approximation the marginalisation integral in equation (4.6) is simplified to a multivariate Gaussian integral, which can be solved analytically. The posterior probability $\mathcal{P}(N|\vec{I}, B)$ is then given as

$$
\begin{aligned}
\mathcal{P}(N|\vec{I}, B) &\propto \frac{1}{[(\Delta x_i^{max} - \Delta x_i^{min})(c_i^{max} - c_i^{min})]^N} \int e^{-\chi^2/2} d^N c_i d^N x_i \tag{4.8} \\
&= \frac{1}{[(\Delta x_i^{max} - \Delta x_i^{min})(c_i^{max} - c_i^{min})]^N} \frac{N!(4\pi)^N}{\det(\nabla\nabla\chi^2)} e^{-\chi_{min}^2(N)/2}.
\end{aligned}
$$

This equation gives now the probability that the best model for the depth profile underlying the measured data $\vec{I}$ can be discretised into N layers. The exponential

term in equation (4.9) judges the quality of the fit to the measured data. $\chi^2_{min}(N)$ is, as stated above, the smallest χ^2 value found in the Monte-Carlo sampling of possible depth profiles for a certain number of layers N. $\chi^2_{min}(N)$ typically gets smaller for increasing N since the model has more degrees of freedom and can fit more details of the measured NRA spectra. The pre-factor of the exponential term serves as a so-called "Occam factor" that penalises more complicated models, i.e., those with a larger number of layers N.

The most probable solution $\{N, (\Delta x_i), (c_i)\}$ can then be selected after the posterior probability has been calculated for all numbers of layers allowed by the user. This step already yields a physically relevant result $\mathcal{C}$ including error bars for the concentration, but it is usually refined in a second Markov-Chain Monte-Carlo process.

This second step can either be a Markov-Chain Monte-Carlo (MC-MC) optimisation of only the concentrations c_i (*OC* mode) or of both c_i and Δx_i (*OCL* mode) for the previously determined optimum number of layers N (which is now kept fixed). The most probable result of the previous optimisation step also serves as the starting value for the refinement. In this second MC-MC refinement, the actual Poisson distribution, which describes a counting experiment such as the acquisition of NRA spectra, is used to calculate the likelihood $\mathcal{P}(\vec{I}|\mathcal{C}, B)$:

$$\mathcal{P}(\vec{I}|\mathcal{C}, B) \propto \prod_k \frac{\hat{J}_k(\mathcal{C})^{I_k}}{I_k!} \times \exp\left(-\hat{J}_k(\mathcal{C})\right). \tag{4.9}$$

$\vec{I}$ respectively I_k denotes the actual *measured* data, while $\hat{J}_k(\mathcal{C})$ stands for the result of the forward calculation according to equation (4.3) based on the *assumed* depth profile $\mathcal{C}$.

The prior probability $\mathcal{P}(\mathcal{C}|B)$ is, in the simplest case, flat for all relevant solutions (i.e., those with $c_i \geq 0$ and $\Delta x_i > 0$ for $i = 1..N$), but it is also possible to impose further restrictions such as a minimum and/or maximum thickness for each layer Δx_i.

After the refined solution $\mathcal{C}^{MC-MC}$ has been found by maximisation of the posterior probability $\mathcal{P}(\mathcal{C}|\vec{I}, B) \propto \mathcal{P}(\vec{I}|\mathcal{C}, B)\mathcal{P}(\mathcal{C}|B)$, a high resolution sampling of the posterior probability distribution function (PDF) $\mathcal{P}(c_i|\vec{I}, B)$ is performed for the concentration c_i in each layer. The PDF is the most general description of the system, but can in many cases be approximated reasonably well by normal

distributions. Accordingly, it can be described by conventional σ error bars. However, there are occasional cases where the PDF is strongly asymmetric or even multimodal. In these cases, while it is still possible to find the maximum of the PDF, a description of the uncertainty by conventional error bars is clearly wrong. The complete N-dimensional PDF would lead to very complicated graphs, especially when several depth profiles are to be compared. Therefore, a conservative estimate for the uncertainty, i.e., the full range of concentrations c_i where the sampling of the PDF is non-zero, will be used for simplicity in the presentation of data when the PDF deviates strongly from a normal distribution.

Figure 4.5 shows the measured proton spectra from sample A0129 for 8 different beam energies (at 690 keV, two measurements were performed). The forward calculation result for the most probable solution $\{N, (\Delta x_i), (c_i)\}$ is also included in the graph. For an easier presentation, all spectra were combined into a single data vector as it is also used by the deconvolution algorithm. They are therefore plotted not against the proton energy, but against their index k in the data vector $\vec{I}$. It can be seen that the calculated spectra are a good fit to the measured data. Figure 4.6 shows the reconstructed depth profile based on the data shown in Figure 4.5. For comparison with the standard error represented by the error bars, the full posterior probability density function (PDF) is represented by the shading of the red line. For better visibility, the PDF is normalised for each layer of the depth profile individually. As you can see, the PDF is in most cases reasonably well described by the (Gaussian) standard error. Only the error bars will therefore be shown from here on in order to make the presentation clearer. Please note that the errors given in this graph represent only the *statistical* uncertainty of the deconvolution result. Systematic errors like uncertainty of the absolute reaction cross-section or of the measurement geometry are not included here since they act in the same direction on *all* results. When trying to compare the *shape* of depth profiles measured under the same conditions, displaying the systematic errors would be obstructive. Looking at a "Round Robin" experiment comparing different analysis methods for deuterium [10], one can estimate the absolute error to be of the order of at least $\pm 15\%$, although the reproducibility of measurements performed with *one single* analysis device can be significantly better. Overall, the uncertainty in of the absolute value would scale the whole depth profile homogeneously by this value. Wherever not explicitly stated otherwise in the future, only the *statistical* errors of measurements of the deuterium inventory will be given.
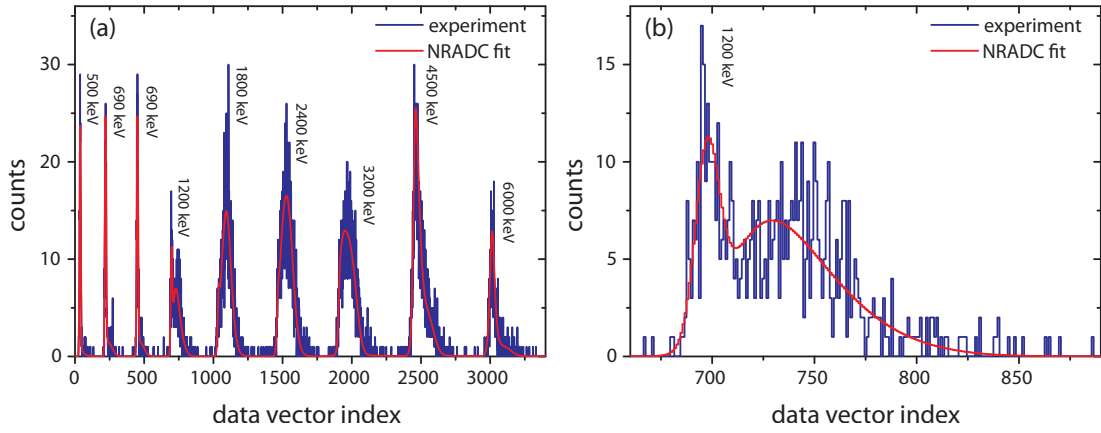
Figure 4.5. Comparison of experimental NRA data from sample A0129 and the corresponding fitted spectra by NRADC. 9 Proton spectra were measured at incident beam energies of 500, 690 (2x), 1200, 1800, 2400, 3200, 4500 and 6000 keV. The integrated beam currents were 20 μAs for 4500 keV and 6000 keV (^{3}He^{2+}), and 10 μAs for all other energies. For better demonstration, the spectra have been combined into a single data vector in panel (a). Panel (b) shows a close-up of the spectrum acquired at 1200 keV. Sample A0129 was exposed to a deuterium plasma with an ion energy of 38 eV/D to a fluence of 6×10^{24} D m^{-2} at a temperature of 370 K.
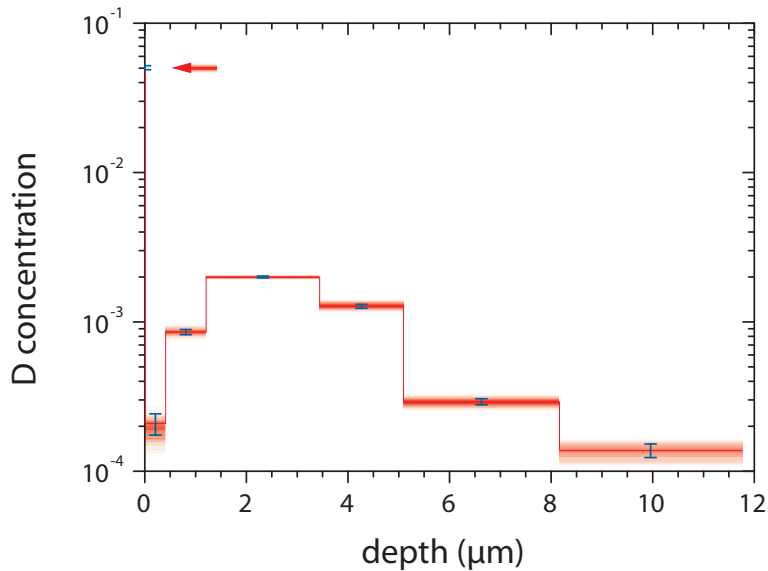

Figure 4.6. Deuterium depth profile reconstruction based on the NRA measurement data from sample A0129 shown in Figure 4.5. The arrow indicates the average deuterium concentration in an ≈ 8 nm thick surface layer. Error bars represent the statistical standard errors from the NRADC deconvolution. The shading of the red line represents the full posterior probability density function.

4.3. Thermal desorption spectroscopy

A major drawback of NRA as a method to probe the deuterium inventory of bulk tungsten specimens is its limited information depth of around ≤ 12 μm. Thermal desorption of the deuterium, on the other hand, is able to probe the whole volume of the deuterium.

For thermal desorption spectroscopy (TDS), a deuterium containing specimen is heated in ultra high vacuum with an (approximately) linear temperature ramp up to a certain temperature while the release of gases from the specimen is monitored with a residual gas analyser. An example of a thermal desorption spectra showing the deuterium-containing molecules HD, D_2, HDO and D_2O is shown in Figure 4.7. For the work presented in this thesis, this temperature was ≈ 1200 K due to technical constraints of the available measurement set-ups. However, the deuterium release rate reduced to zero before the maximum temperature was reached for nearly all investigated specimens. Subsequent analysis with NRA as well as a second TDS measurement was performed for selected specimens and showed no indication of deuterium being in the specimen anymore. This means that the remaining D inventory within the first 8 μm (for a 4500 keV ^{3}He beam) is at least below 10^{18} D m^{-2}, which would correspond to a D concentration of $\approx 10^{-6}$ evenly distributed across the probed volume. This is far below the D inventories of the order of 10^{20} D m^{-2} that were typically measured in specimens exposed to a D plasma. The inventory that would be released at temperatures of more than 1200 K can therefore be considered negligible.

The main uncertainty besides the absolute calibration of a TDS set-up is the release of deuterium-containing molecules other than D_2 from the specimen (see also Figure 4.7. While for the HD molecule sensitivity calibrations can be performed either with HD calibration gas or by interpolating between the sensitivities for H_2 and D_2, this is extremely difficult for heavy water species, i.e., HDO and D_2O. The difficulty with these molecules is that they have a high tendency to stick to any cold (i.e., room temperature) surface. Therefore, only by using heated gas lines and delivering the calibration gas directly at the specimen location it would be possible to perform an accurate calibration. For most set-ups, including the ones used for the work presented here, such an *in situ* calibration set-up with heated gas lines is technically not realisable. Additionally, the high sticking probability of water-like molecules near room temperature also means that the TDS set-up may have a "memory": Heavy water released from a specimen during a
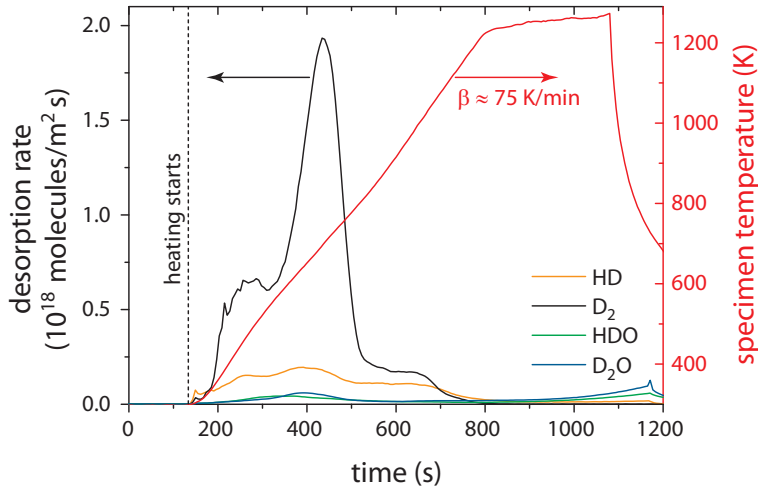
Figure 4.7. Thermal desorption of deuterium-containing molecules (HD, D_2, HDO and D_2O) from sample A0052 after exposure to a deuterium plasma (ion energy: 38 eV/D, fluence: 6×10^{24} D m^{-2}, temperature: 370 K). The heating rate β was approximately 75 K/min. The calibration factors for HDO respectively D_2O were estimated to be 50% of those for HD respectively D_2 (see below).

measurement may first adsorb at a surface and then appear during a *subsequent* measurement when the chamber walls become warm again. Because of these difficulties, the specimens were protected from oxidation as much as possible by storage in a vacuum exsiccator (see section 5.1.3) in order to prevent heavy water formation during TDS. The remaining HDO and D_2O release — in most cases much less than the D_2 release — is treated as an uncertainty of the upper limit of deuterium in the specimen. The sensitivity on HDO and D_2O is approximated as about twice the sensitivity for HD respectively D_2. This scaling is recommended by manuals on residual gas analysis (see, e.g, [41]). While by no means reliable enough for an absolute quantification due to the reasons described above, this is the best possible estimate for the uncertainty due to heavy water release.

TDS is not only capable of measuring the total deuterium inventory in bulk tungsten specimens, but also yields information about the binding states of the deuterium to trap sites in the specimen by correlation of the release rate to the temperature. With the help of, e.g, diffusion-trapping models (see section 3.2), TDS release peaks can then be assigned to binding energies [14, 82]. Even complex release spectra can, however, also be modelled solely by a depth distribution of the deuterium using only a single binding energy [14, 112]. The reason is that diffusion of the deuterium from a trap site to the surface takes a finite time. Deuterium depth profiling by NRA shows that diffusion during the implantation

results in significant concentrations at least several microns below the surface, and often even much deeper. This means that the resulting release spectrum typically is a convolution of diffusion and (de-)trapping effects, which makes the interpretation of the spectrum non-trivial. For a reliable deconvolution accurate knowledge not only of the deuterium depth profile but as well of the diffusion constant and detrapping attempt frequency is necessary. Unfortunately there is a large scatter in literature data on these values (see also section 3.1). The surface recombination rate of deuterium leaving a tungsten specimen is also not known with very much accuracy, but most publications on this subject agree that it is very fast and thus does not limit the release rate [14].

Because of the large uncertainty in the parameters necessary for the interpretation of thermal desorption spectra, a set of identical tungsten specimens was prepared and implanted with deuterium. These specimens were then analysed with different heating rates as well as with interrupted ramps. All acquired data then had to be fitted using only one single set of parameters. Since such a detailed approach is not feasible for a large number of different implantation conditions and specimen types — as it is needed for a comparison of different tungsten microstructures — this was only performed for one selected case (see section 7.6). For the rest of the specimens, TDS was mainly used to investigate the total deuterium inventory.

The TDS experiments for the majority of the specimens were performed in the "HSQ-TDS" set-up sketched in Figure 4.8. In this set-up, the specimen is held by a molybdenum frame, which also contains contacts for a K-type thermocouple. The specimen is heated from the rear side by an electron beam (acceleration voltage $V_{e-beam} = 3$ kV), with the specimen at high potential and the filament at
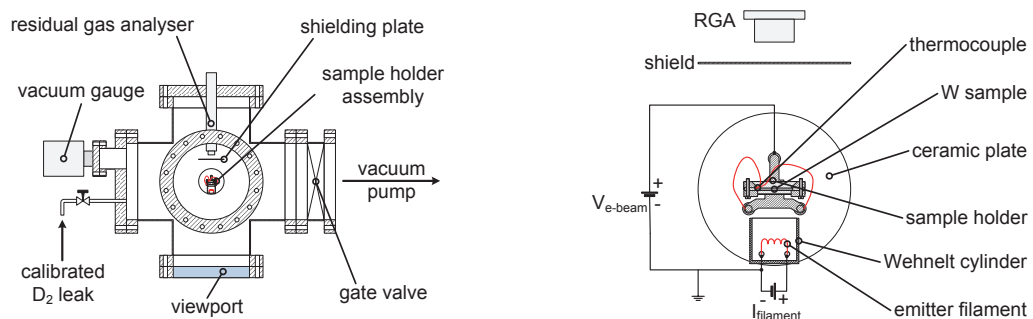

Figure 4.8. Sketch of the TDS set-up located at the Garching High Current Source ("HSQ-TDS"). The specimen is clamped in a molybdenum frame and heated by a 3 kV electron beam heater with a maximum power of 90 W. The specimen temperature is measured by a K-type thermocouple.

ground potential. The implanted surface faces towards a Pfeiffer QMG700 residual gas analyser. The ionisation chamber of the analyser is shielded from the acceleration voltage and the direct molecular beam desorption by a grounded stainless steel plate. This way, the sensitivity to desorbed deuterium is equivalent to the reference signal from a calibrated leak valve. The analysis chamber is pumped by a turbomolecular pump. For specimen exchange a load-lock chamber with an in-vacuum transfer system is used so the analysis chamber is never exposed to atmosphere. This way, the base vacuum can be maintained at less than 10^{-7} Pa. The heating rate is set by a feed-forward program of the emitter heating current and has a typical value of ≈ 70–80 K/min, which allows a relatively quick analysis with a high sensitivity. A typical temperature ramp is shown in Figure 4.10. Together with the short pump-down time due to the load-lock and the small heated mass (i.e., only the specimen and its holder) this is well-suited for quick surveys over a large number of specimens.

Some measurements, e.g., those described in section 7.6, were performed in the TESS set-up [98]. The layout of TESS is sketched in Figure 4.9. Here typically six specimens are loaded into a quartz tube, which is pumped for approximately 4 hours before it is connected to the main analysis chamber. After another ≈ 10 hours of pumping the base vacuum of the order of 10^{-8} Pa is reached. For the analysis one specimen is moved to the measurement position by a magnetic transfer mechanism while the other specimens remain in the storage position. The specimen in the measurement position is then radiation-heated by a tube furnace, which is programmed for a linear temperature ramp. The specimens in the storage position are not heated significantly during a measurement. The desorption signal is monitored by a Pfeiffer Vacuum DMM 422 residual gas analyser, which is calibrated by deuterium leak valves. For slow ramps (3 K/min and less), the specimen temperature follows the furnace temperature ramp accurately with only a small offset. For faster ramps, there is a significant delay between the furnace temperature ramp and the specimen temperature. This is due to the relatively high heat capacity of the tungsten specimen together with its very low emission respectively absorption coefficient for infrared radiation. For very fast temperature ramps (300 K/min and faster) the furnace is pre-heated to a certain temperature and then pushed over the glass tube. This results in a linear temperature increase of the specimen approximately up to about two thirds of the final temperature, followed by an asymptotic approach. The results of calibration measurements for several heating rates between 0.3 and 600 K/min are shown in Fig. 4.10.
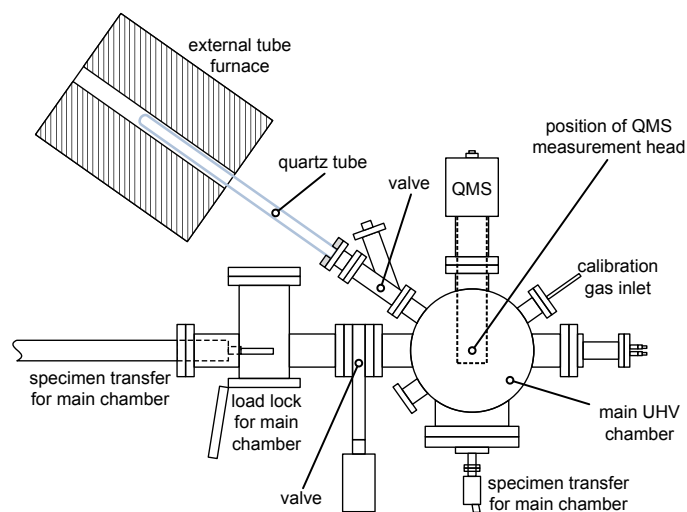
Figure 4.9. Sketch of the TESS set-up. The specimens are placed in a quartz glass tube and radiation-heated by an external tube furnace. The thermal response of the specimens to the linear temperature ramp of the furnace was calibrated by a K-type thermocouple for each heating rate.
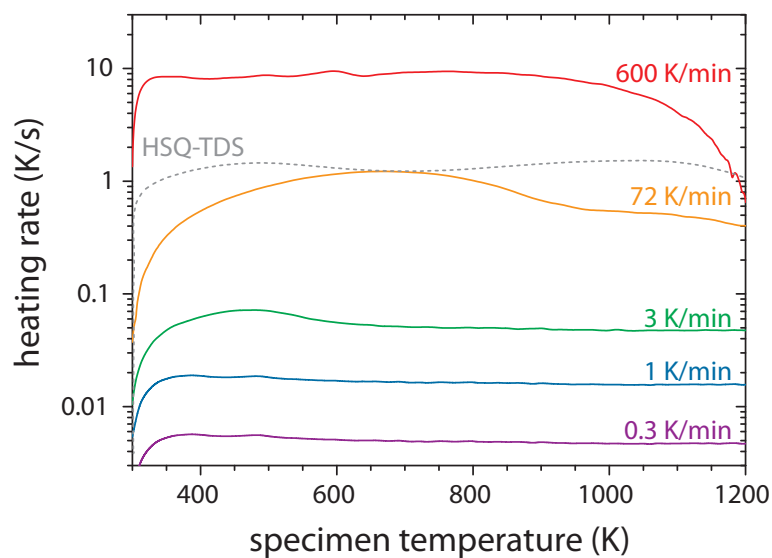

Figure 4.10. Thermal response of a tungsten specimen in TESS for different heating rates. The plot shows the rate of specimen temperature increase versus temperature. The values indicated at each graph are the heating rates at ≈ 600–700 K, i.e., the approximate location of the main desorption peak. For comparison, the typical heating rate achieved in the "HSQ-TDS" apparatus is also included (dashed line).

The TESS set-up provides more flexibility in terms of the heating program and a better base vacuum than the "HSQ-TDS". Due to the long pump-down time and the thermal inertia of the furnace, it allows only a much slower specimen throughput, however.

4.4. Electron microscopy

Electron microscopy was an important tool for analysing the surface and sub-surface morphology of the tungsten before and after plasma exposure. Besides that, backscattered electron (BSE) contrast in scanning electron microscopes as well as (scanning) transmission electron microscopy ((S)TEM) were used to investigate the microstructure of the specimens.

For scanning electron microscopy, a Philips XL30 ESEM and a FEI HELIOS NanoLab 600 were available. Both microscopes use acceleration voltages up to 30 keV. The XL30 microscope uses a LaB_6 cathode, while the HELIOS uses a Schottky thermal field emitter (FEG). Together with an immersion lens mode for high resolution, this allows point resolutions down to ≈ 1 nm. For the XL30, the resolution is limited to 6 nm. Both microscopes are equipped with secondary electron (SE) and BSE detectors.

The HELIOS NanoLab 600 is furthermore equipped with a Ga^+ focused ion beam (FIB) with acceleration voltages up to 30 kV. This allows, e.g., to prepare micro-cross-section cuts *in situ* in the electron microscope. The cross-sections can then be imaged with the electron beam without having to transfer or reposition the specimen. The FIB was also used to apply markers to the surface of a number of specimens.

Besides surface analysis by scanning electron microscopy, the HELIOS system is also equipped with a multi-segment solid-state STEM detector. It consists consists of a bright-field (BF) segment with a collection semi-angle of 7.1°, a concentric annular dark field (DF) detector and a high-angle dark field (HADF) detector. The latter is made up of 12 segments, which can be combined into a high-angle annular dark field (HAADF) detector. The segments can also be read out individually or in arbitrary combinations (HADF-P mode). This directional selectivity allows in some cases to enhance the diffraction contrast in dark-field mode.

TEM investigations were also carried out using the Jeol JEM-2010F TEM at the

University of Augsburg, Germany, and the FEI Titan E-Cell 80-300ST environmental TEM (ETEM) at the DTU–CEN facility in Copenhagen, Denmark[1].

Technical specifications of the microscopes as well as drawings of the arrangement of beams and detectors in the XL30 and HELIOS scanning electron microscope can be found in the appendix in section A.2.

4.5. Differential interference contrast microscopy

Since scanning electron microscopes (SEMs) have become widely available, they have been replacing optical microscopes more and more in the field of materials science. Nowadays, optical microscopy is mostly used in life sciences and biology, especially for transparent specimens. A highly specialised technique for specimens that have only poor contrast is the differential interference contrast microscopy (DIC). The most common set-up for this is based on the design by Nomarski [77] and integrated in a microscope with Köhler illumination. An excellent review of the working principle of the Nomarski-type DIC microscope was written by Murphy *et al.* [73]. A brief excerpt will be given here. Technical details of the equipment used for the work presented in this thesis can be found in the appendix in section A.3.

Basically, DIC microscopy is closely related to both phase contrast and interferometric imaging. In short, the image is formed by the interference of two parallel beams separated by a distance of the order of the radius of an Airy disk. The image is thus a map of local phase differences. In a DIC set-up, linearly polarised light is separated into two beams of orthogonal polarisation by a birefringent prism, in the simplest case a Wollaston prism. It consists of two wedges of calcite that are glued together at the hypotenuse, e.g., with Canada balsam. The optic axes of both wedges are parallel to the flat surfaces of the Wollaston prism, but perpendicular to each other. The polarisation vector of the incident light lies exactly between the orientation of both optic axes. This shears the light into two polarised beams (i.e., ordinary and extraordinary beam) that are polarised perpendicularly to each other and also have a certain phase shift. This makes the incorporation of such a prism into a microscope difficult because it has to be integrated into the condenser and objective lenses. A modification of the Wollaston

---

[1]DTU–CEN: Centre for Electron Nanoscopy, Danmarks Tekniske Universitet, Copenhagen.
http://www.cen.dtu.dk

prism is the Nomarski prism: Here one wedge is cut like in the Wollaston prism, but the second one has its optic axis at an oblique angle to the flat surface of the prism, while it is still oriented perpendicular to the optic axis of the first wedge. This causes the ordinary and the extraordinary beam to form a focal point outside the volume of the prism. This allows much easier integration into the optical set-up of the microscope since no special lens construction is needed anymore. Sketches of a Wollaston and a Nomarski prism are shown in Figure 4.11.
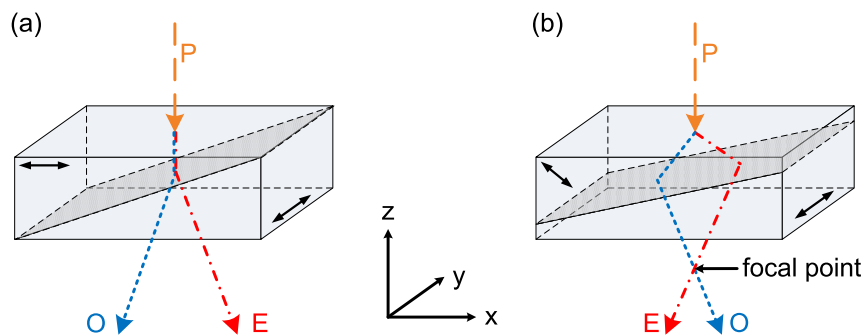

Figure 4.11. Sketches of a Wollaston prism (a) and a Nomarski prism (b). Both consist of calcite wedges that are joined at the hypotenuse and whose optical axes are perpendicular to each other. In the Wollaston prism both optical axes are parallel to the prism surface, while in the Nomarski prism one optical axis is inclined towards the surface. This produces a focus of the ordinary and extraordinary beam.

The ordinary and extraordinary beam are projected onto the specimen by the condenser lens with a spatial separation of approximately one Airy disk radius, i.e., depending on the numerical aperture (NA) of the condenser. Due to the shear, they can experience a slightly different phase shift when passing through the specimen. A second Nomarski prism placed behind the objective lens recombines the two beams and exactly compensates the phase shift of the condenser prism. Only the phase difference introduced by the specimen remains. A second polarisation filter oriented perpendicular to the one in the illumination system removes all linearly polarised light and allows only circularly polarised light to interfere in the image plane.

The image then represents the *local* phase difference between two beams that are separated by a diffraction-limited distance. In other words, it is a map of the local gradient of optical path length trough the specimen. In case of a plane-parallel cut of the specimen, this translates to a gradient in refractive index. If the refractive index is constant (and different than that of the ambient air), the image repre-

sents the local thickness of the specimen. In all cases, minimum light intensity corresponds to a locally flat profile. By displacing the compensator prism (i.e., the one behind the objective lens) along the shear direction and relative to the optical axis of the microscope, the compensation of the phase shift introduced by the condenser prism is not exact anymore. This is also occasionally called "introduction of bias retardation". In that case, the image appears brighter than average in areas where optical path length increases along the shear direction, and darker where it decreases. This can be reversed by displacing the compensator prism in the opposite direction with respect to the microscope optical axis. The result of DIC with bias retardation is a pseudo-relief image with an apparent shadow-casting in the direction of the shear caused by the condenser Nomarski prism. Some instructive examples can be found in the article of Murphy *et al.* . [73]. A further possible modification of the image can be achieved by introducing a compensator plate (e.g., a full-wavelength plate) after the compensator prism together with white light illumination. This will lead to all interference fringes beyond the principal minimum not being dark anymore, but rather displaying interference colours. This can be used for so-called optical staining of the specimens (for details see [73]).

DIC microscopy is best known in transmission geometry as in the original set-up by Nomarski. However, it also works very well in a reflection geometry, e.g., for surface analysis in materials science. In fact, reflection geometry even makes the system simpler and more robust, because the same lens-prism combination is used both for illumination and imaging. Brandmaier *et al.* [12] describe this variant of the DIC technique in detail. The actual working principle is very similar to the classical transmission DIC described above, as it still uses the local shearing and subsequent recombination of the light by the birefringent Nomarski prism. However, the phase shift between ordinary and extraordinary beam is now no longer caused by transmission through areas with different refractive index respectively thickness. It rather corresponds to the local distance between specimen and objective lens. Accordingly, the image now represents a map of the local *slope* of the specimen surface. For zero bias retardation (i.e, an undisplaced Nomarski prism), dark areas are perpendicular to the optical axis and, accordingly, flat. For a finite bias retardation, a similar relief image as described above is formed, where bright areas ascend along the shear direction and dark areas descend, or vice versa.

Since basically, DIC is an interferometric method, it is sensitive even to very small changes in the optical path length, respectively specimen height, typically

of the order of 1% of the wavelength of the incident light, i.e., a few nanometres. Therefore, even very small steps respectively very gentle slopes can be imaged with a clear contrast. It has to be noted, however, that DIC microscopy still suffers from the physical constraints of optical microscopy, i.e., the Abbe limit for lateral resolution and the small focal depth for objectives with a high numerical aperture. In summary, optical DIC microscopy is a valuable addition to scanning electron microscopy in terms of surface analysis, especially if surveys over many specimens and large areas are needed.

4.6. Summary of the analysis techniques for tungsten specimens

This chapter gave an overview over the different tools and techniques used for the analysis of tungsten specimens. Nuclear reaction analysis as well as thermal desorption spectroscopy are used in combination to probe the deuterium inventory of plasma-exposed specimens. NRA yields the depth-resolved, absolutely quantified deuterium inventory in the near-surface volume (up to 12 μm below the exposed surface). TDS allows to measure the total deuterium content in the specimen and gives insight into the binding energy distribution of trapped deuterium. A broad set of optical, scanning and transmission electron microscopy as well as focused ion beam techniques is used to study the surface topology, grain structure and dislocation density of specimens. These methods are used to characterise specimens before exposure and to reveal changes induced by the plasma exposure. The combination of all these analysis methods is necessary to give an as complete as possible picture of the mechanisms of deuterium retention in tungsten due to plasma exposure.

5. Specimen preparation

This section describes the preparation procedures for the specimens investigated in this thesis. It will be shown in detail how high-quality specimen surfaces without any visible distortion layer were produced with a sophisticated mechanical polishing procedure (for the influence on the deuterium retention see section 8.4). Apart from that, heat treatment procedures for producing the different microstructures described in chapter 6 are addressed, as well as the issue of specimen storage. Finally, the preparation of tungsten TEM specimens by electrochemical thinning is discussed.

5.1. Bulk specimen preparation

For a thorough comparison of the deuterium retention under different loading conditions and for different microstructural modifications, it is indispensable to work with a well-defined base material. To ensure this, all tungsten specimens discussed in this work were procured from one single manufacturing batch. The samples were manufactured by PLANSEE. The material had a purity of 99.97 wt.%. The tungsten was hot-rolled into a sheet of 0.8 mm thickness and subsequently ground to a coarse, plane-parallel finish. Finally it was cut into pieces with the dimensions $12 \times 15 \times 0.8$ mm^3 by the manufacturer. The impurity concentrations specified by PLANSEE can be found in Table A.3 in the appendix.

5.1.1. Polishing procedure

While the technical finish of the tungsten by the manufacturer guaranteed an even thickness of all specimens, the surface of the as-received samples was still very rough. In order to be able to observe changes to the microscopic surface morphology and to ensure a well-defined surface condition before loading, the specimens were mechanically polished to a mirror-like finish. This was done by first grinding

the samples with increasingly more fine-grained silicon carbide grinding paper (P400 up to P4000) and subsequent polishing with a diamond suspension. However, it must be taken into account that this kind of mechanical polishing can also introduce defects into the polished surface, up to completely obscuring the bulk grain structure to a depth in the micrometre range. Therefore, it was necessary to derive a polishing procedure that removes this damaged layer in the final polishing step. One way to do this is to apply a chemo-mechanical polishing method after grinding and diamond polishing. As an alternative, electrochemical polishing can also be used. For most specimens discussed here, the chemo-mechanical treatment was chosen because it proved to be a quicker and more reliable method than electrochemical polishing. Only a small number of specimens were electropolished for comparison. In order to optimise the polishing procedure, several specimens were polished at the same time. After certain steps, i.e., after grinding, after diamond polishing and after different durations of chemo-mechanical polishing, specimens were successively removed from the process in order to assess the quality of the polished surfaces.

The polished surfaces were investigated with a FEI HELIOS 600 dual-beam scanning electron microscope (SEM) with a focussed ion beam (FIB) for cross-section preparation. Both the plan-view surface and a FIB cross-section were analysed for each specimen. The exact polishing procedure is listed in Table 5.1 along with the sample numbers associated to each polishing steps. It can be clearly seen in the plan-view image in Fig. 5.1a that after grinding the grains at the surface of sample A0025 appear very small. The cross-section view in Fig. 5.1b makes it clear that the actual bulk grain structure is much coarser, but in a top layer of about 0.5 μm the grains have fragmented. The near-surface region also contains many small pores, cracks and craters. After diamond polishing this fragmentation is strongly reduced, but the grains near the surface still appear distorted as it can be seen both in the plan-view and cross-section images of sample A0026 in Fig. 5.2. The sample surface also still contains cracks, pores and craters. This makes it clear that diamond polishing alone is not sufficient to remove preparation damage from the sample surface. Therefore, the remaining specimens A0027, A0028 and A0029 were chemo-mechanically polished with an alkaline colloidal silica suspension[1] for 10, 20 and 30 minutes. The plan-view and cross-section imaging of these specimens showed a gradual reduction of the distortions as well as of the density of cracks, pores and craters. Only after a long chemo-mechanical polishing time of 30 minutes the grains next to the surface were indistinguishable from grains

---

[1]Logitech SF1, "Syton"

in the bulk as the cross section-image in Fig. 5.3b shows. The grains in the plan-view image in Fig. 5.3a are clearly visible with only occasional distortions and a small number of scratch traces. For comparison, plan-view and cross-section images of sample A0091 are shown in Fig. 5.4. This specimen was electrochemically polished with 2.5 wt.% NaOH solution in water. The polishing voltage was 25 V, the duration was 2–3 minutes. The electrolyte was stabilised at a temperature of approximately 293 K. Because the electropolishing usually leaves a residual oxide layer with a thickness of the order of up to several 10 nm on the surface, the specimen was subsequently annealed for 60 minutes at 1200 K in a high vacuum oven. During this treatment, the oxide fully evaporates respectively decomposes. The grain structure remains unchanged. The effects of annealing are discussed in more detail in chapter 6. Sample A0091 exhibits a grain structure very similar to sample A0029, which was chemo-mechanically polished for 30 minutes. In the plan-view image Fig 5.4a the grains are clearly visible, with the same occasional distortions as for A0029. The main differences are that the contrast of some grain boundaries of A0091 is slightly enhanced due to superficial etching, and that no scratch traces are visible at all. The cross-section image shows the same grain structure near the surface and in the bulk.

Table 5.1. Polishing steps and associated sample IDs for the specimen preparation procedure applied in this work.

Finish	Force	Polishing pad	Sample ID	Figure
SiC paper P4000	20 N	hard	A0025	Figure 5.1
diamond suspension, 10 min	35 N	textile	A0026	Figure 5.2
Logitech SF1, 10 min	30 N	felt (SubaX)	A0027	
Logitech SF1, 20 min	30 N	felt (SubaX)	A0028	
Logitech SF1, 30 min	30 N	felt (SubaX)	A0029	Figure 5.3
Electropolishing			A0091	Figure 5.4

This analysis shows that (chemo-)mechanical polishing can produce specimens of similar quality as electropolishing. The main advantage of the mechanical preparation is that once the polishing recipe was optimized, large numbers of samples could be prepared quickly and with excellent reproducibility. Getting stable results from electropolishing proved much more tedious in comparison. A reproducibly good quality could only be achieved when the samples were embedded in epoxy resin prior to grinding and electropolishing. Otherwise there was a high risk of electrolyte spilling to the anode conductor, which produced local galvanic
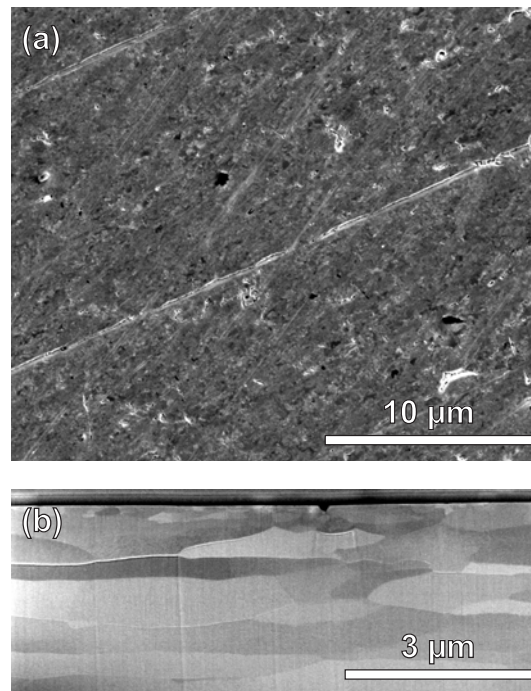
Figure 5.1. Plan-view (a) and cross-section (b) SEM images of the surface of sample A0025 after grinding with SiC paper up to P4000.
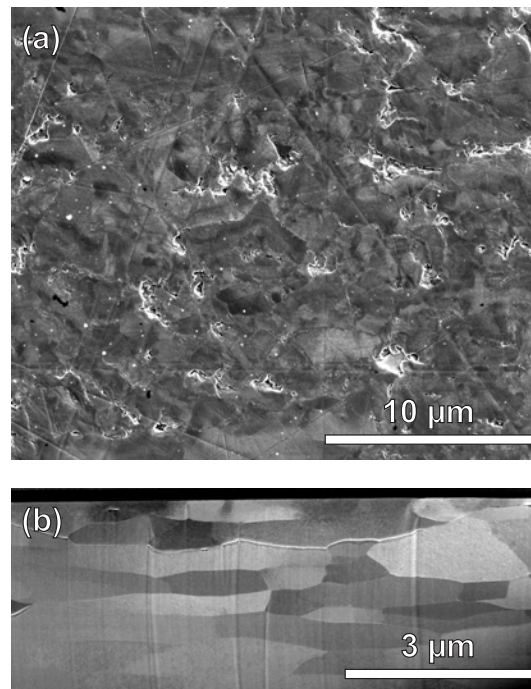

Figure 5.2. Plan-view (a) and cross-section (b) SEM images of the surface of sample A0026 after grinding and 10 minutes of diamond polishing.
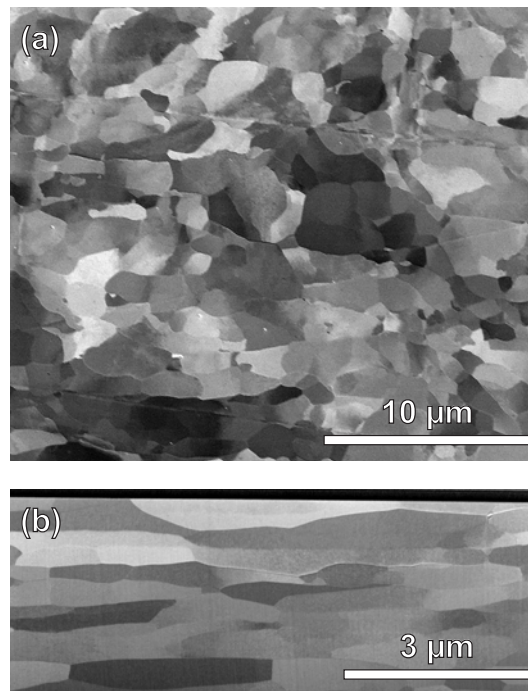
Figure 5.3. Plan-view (a) and cross-section (b) SEM images of the surface of sample A0029 after grinding, diamond polishing and 30 minutes of chemo-mechanical polishing.
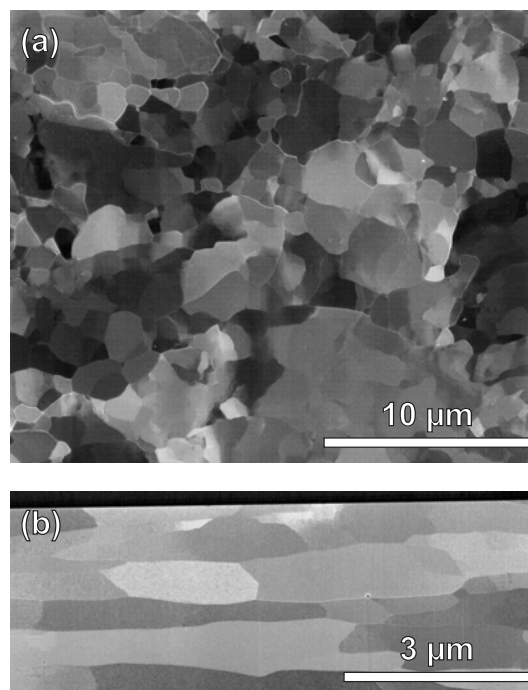

Figure 5.4. Plan-view (a) and cross-section (b) SEM images of the surface of sample A0091 after grinding and 2–3 minutes of electrochemical polishing with 2.5% NaOH. The specimen was also annealed for 60 minutes at 1200 K in a high vacuum oven in order to evaporate the residual oxide layer from electropolishing.

elements. This in turn led to severe damage of the sample surface, e.g., numerous etch pits or strong preferential etching at grain boundaries. After electropolishing the epoxy resin had to be dissolved in acetone.

5.1.2. Heat treatment

After polishing of the surface and thorough cleaning of the specimens, they were annealed at different temperatures in order to selectively create specimens with different well–defined grain and defect structures. All in all, four different annealing procedures were used: stress relief at 1200 K, partial recrystallisation at 1500 K and full recrystallisation at 1700 K as well as at 2000 K. The result of these heat treatment procedures is discussed in detail in chapter 6.

The stress relief at 1200 K was performed in a custom-built high–vacuum oven ("MoMo") where the hot zone is constructed entirely from molybdenum. A drawing of the oven is shown in Figure 5.5. After pumping for at least four hours, the base vacuum before heating was typically several 10^{-5} Pa. At the maximum temperature the vacuum was still better than 10^{-3} Pa. The specimens were held at 1200 K for 60 minutes. After the holding time, the heating power was set to zero in order to let the specimens cool to room temperature as quickly as possible. Apart from relieving residual stress from the manufacturing and preparation processes, this heat treatment served the purpose of decomposing and evaporating any oxide layers on the specimens, and to remove the hydrogen introduced during the manufacturing. 1200 K is also the maximum temperature that is reached during analysis by thermal desorption spectroscopy (TDS), so it can be expected that the specimen microstructure does not change significantly during TDS.

Heating of specimens to 1500 K and higher was performed under a protective gas atmosphere at 150 kPa in a commercial graphite oven manufactured by Thermal Technology LLC ("HORST"). A drawing of this oven can be seen in Figure 5.6. For 1500 and 1700 K, argon (purity: 4.8) was used, for 2000 K helium (purity: 5.0) was necessary due to oven specifications. The specimens were enclosed in a tantalum box or an envelope made of tungsten foils. Blocking all direct lines of sight to the graphite parts of the oven in such a way prevented carbide formation on the specimen surface. The oven was brought to the annealing temperature as quickly as possible. The holding time was 30 minutes in each case. Cool-down was also performed as quickly as possible after the specified holding time by setting the heating power to zero.
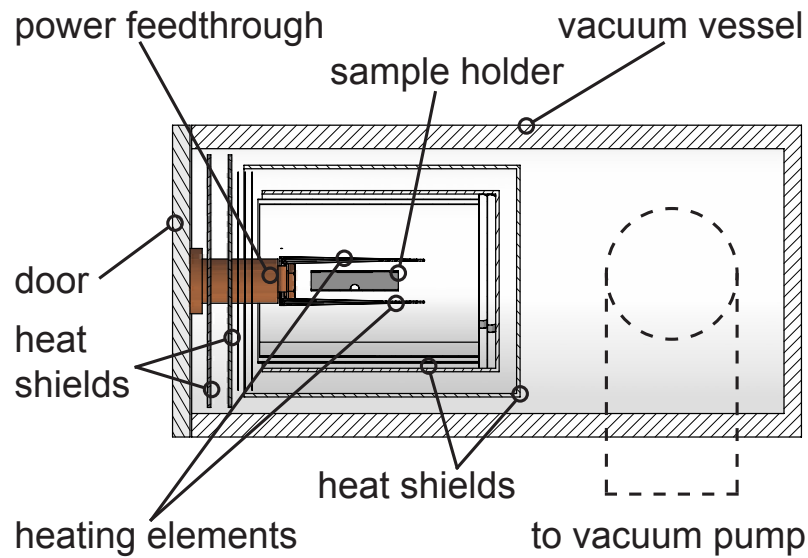
Figure 5.5. Drawing of the high-vacuum oven "MoMo". The entire hot zone including heating elements, sample holder and heat shields is constructed from molybdenum. The water-cooled vacuum vessel is evacuated to $\leq 10^{-4}$ Pa by a turbomolecular pump.
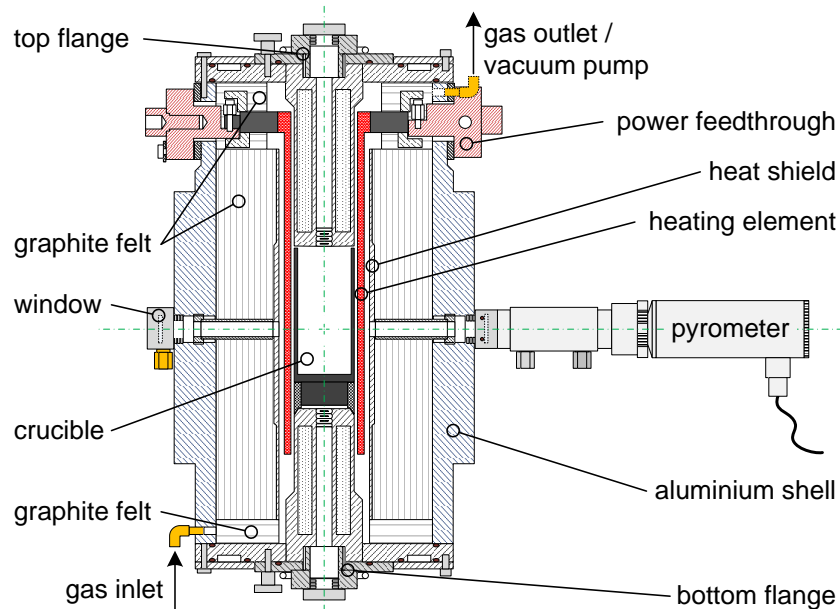

Figure 5.6. Drawing of the high-temperature oven "HORST". All interior components are fabricated from graphite, the water-cooled external shell is aluminium and the flanges are nickel-plated copper. The oven is operated under a protective gas atmosphere (Ar or He) at 150 kPa. A rotary pump providing a vacuum of ≤ 1 kPa is used for removing the air prior to filling with the protective gas.

5.1.3. Storage

The heat treatments described in section 5.1.2 remove all surface oxide layers from the specimens. After heating, excessive oxidation particularly of the polished surfaces has to be prevented. Although tungsten is generally assumed to be resistant against oxidation in air at room temperature, this is mostly due to a passivating oxide layer forming at the surface. During the first attempts at finding a suitable preparation technique for the tungsten specimens for this thesis, it was discovered that highly polished tungsten surfaces can suffer severely from air exposure. While some test surfaces appeared clean and shiny even after more than two years of storage in ambient air, others visibly changed to a dull gray appearance already after a few weeks. However, this uncontrolled modification of the polished surface can be effectively suppressed by storing the samples in a dry vacuum environment, e.g., a vacuum exsiccator equipped with a desiccant.

It is even more important to suppress the uncontrolled oxidation process in ambient air for specimens that are implanted with deuterium. Investigations performed by Moshkunov *et al.* [72] have shown that even after less than 24 hours of ambient air exposure, deuterium-containing water fractions detected in TDS, i.e., HDO and D_2O, were increased significantly compared to a specimen that was stored in vacuum all the time between implantation and analysis. This was explained by the formation of surface oxide on the specimen exposed to air. Formation of heavy water fractions during TDS, however, is problematic because the absolute calibration of the sensitivity of a TDS setup to water molecules is not possible with reasonable effort. A large heavy water fraction therefore means a large error in the determination of the deuterium inventory of a specimen (see also section 4.3). Fortunately, the storage of specimens in a vacuum exsiccator for the time between implantation and analysis has also proven to be sufficient to suppress excessive heavy water formation during TDS. All specimens analysed for this thesis were therefore only exposed to ambient air when this was unavoidable for analysis and otherwise stored in a vacuum exsiccator with a filling of silica gel desiccant.

5.2. TEM specimen preparation

In order to understand the deuterium retention in specimens with different heat treatment prior to plasma exposure, a thorough characterisation of the microstructure is necessary. While the grain structure can be studied by SEM anal-

ysis of well-polished bulk specimens, the dislocation density can only be revealed by transmission electron microscopy (TEM). It was therefore necessary to develop a thinning procedure for TEM samples that introduces as little preparation artifacts as possible into the material. So far, only electrochemical thinning has proven to fulfil these requirements. The thinning process that produced the best and most reliable results is described in this section.

After cutting a disc with 3 mm diameter from a bulk specimen, the disc was first mechanically pre-thinned to a thickness of 0.1 mm. The electrochemical thinning was then performed with a custom-built set-up, which is sketched in Fig. 5.7. In this set-up, the specimen is mounted upside-down above a thin stainless steel needle, which delivers the electrolyte and serves as the cathode for the electrochemical process. The electrolyte flow is set by a drip. The specimen disc is placed on a stainless steel holder. It is fixed to the holder by a PTFE cap with a 2 mm aperture. The cap also largely prevents spilling of electrolyte to the sample holder. This is necessary because it has been observed that contact between electrolyte and sample holder leads to the formation of local galvanic elements, which in turn leads to a strong roughening of the specimen, which renders it useless for TEM analysis. To increase the reliability of the thinning process, the surface of the holder that is in contact with the specimen was also PVD-coated with tungsten in order to prevent electrochemical reactions between specimen and holder in case of small electrolyte leaks through the PTFE cap.

Specimens were usually electropolished on both surfaces in order to remove any roughness or damage introduced from the mechanical pre-thinning. For this, the specimen is first electropolished from one side, typically for between one third and half of the time required to achieve a small perforation. The specimen is then removed from the holder, cleaned, and re-mounted with the already polished surface facing towards the holder. The electrochemical thinning is then continued until a small perforation appears near the centre of the specimen.

For the detection of this perforation, the sample holder contains a central hole of 1.5 mm diameter, which allows observation of the rear side of the specimen during the thinning process. The front side is illuminated through the cathode needle by a white LED. As soon as the perforation appears, the light from the LED is registered by an electro-optical detection circuit, which then disconnects the polishing voltage. With this automatic detection mechanism perforations as small as 30 μm can be achieved. The best thinning results were achieved with a 2.5. wt.% NaOH dissolved in water as the electrolyte. The polishing voltage

was 19 V. The electrolyte flow was adjusted to a small drip rate corresponding to an etching current of approximately 5–10 mA. After ≈ 5 minutes on one side the thinning was interrupted. After washing, the thinning was continued on the other side of the specimen. Under these conditions perforation of a ≈ 0.1 mm thick specimen is typically achieved after approximately 15 minutes of cumulative thinning time, which corresponds to a total charge of roughly 5–8 C. After perforation is achieved, the sample is carefully washed alternatingly in de-ionised water and ultra-clean acetone and subsequently stored in a vacuum exsiccator until it is analysed.
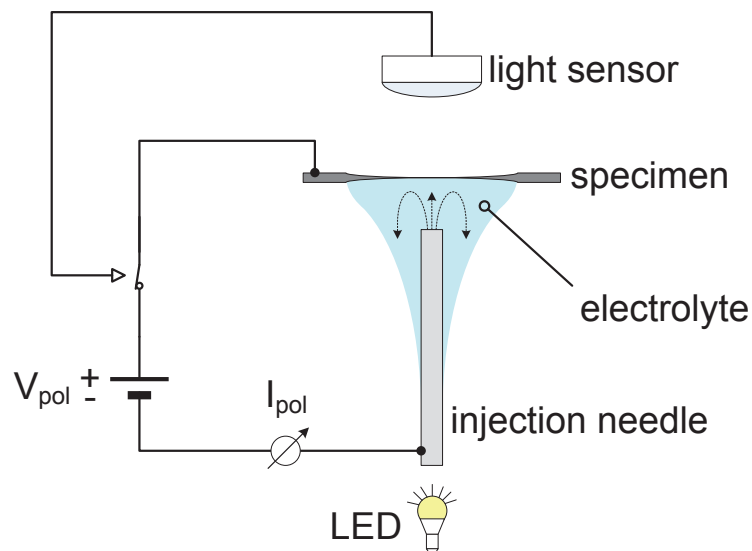

Figure 5.7. Sketch of the set-up for TEM sample thinning. The electrolyte (2.5 wt.% NaOH in water) is supplied from a drip and applied to the specimen with a stainless steel injection needle. The light of a white LED placed coaxially with the needle is detected by a phototransistor as soon as a small ($\varnothing \approx 30~\mu$m) perforation appears. This immediately disconnects the polishing voltage.

6. Microstructural properties of the material

In order to correlate the results for deuterium retention and surface modifications of tungsten specimens that will be discussed in the following chapters, it is first necessary to characterise the material *before* plasma exposure as thoroughly as possible. Therefore, after the preparation steps described in section 5.1, a selection of specimens with different heat treatment were analysed by a scanning and transmission electron microscopy. Part of the results presented here were already published in [66], but will be shown here in more detail along with previously unpublished investigations. The quantitative data on grain size and dislocation density are summarised in Tables 6.1 and 6.2.

6.1. Initial material and stress relief at 1200 K

The initial material is powder metallurgical tungsten with a nominal purity of 99.97 wt.% manufactured by PLANSEE. It is hot-rolled to 0.8 mm and cut into pieces of $12 \times 15 \times 0.8$ mm by the manufacturer. Figure 6.1 shows a backscattered electron (BSE) micrograph of a specimen after mechanical polishing and subsequent stress-relief annealing for 60 minutes at 1200 K. The grains have typical dimensions between ≤ 1 and 5 μm. The grain structure is virtually identical for the stress-relieved and the initial, hot-rolled material. Although no explicit mechanical testing was performed on the material, its basic mechanical properties still became apparent while handling it. Particularly thin foils without heat treatment or after stress relief — albeit much more brittle than most other metals — are still quite sturdy and can even be plastically deformed to a limited extent. This made it possible to use such foils for protecting the actual specimens during annealing in the graphite furnace for temperatures of 1500 K or more (see section 5.1.2).

A more detailed statistical analysis shows that the mean grain area is

$\overline{A_{grain}} = 1.99 \pm 0.08\ \mu\text{m}^2$. The statistical error is calculated under the assumption of a Gaussian error distribution. The mean of the equivalent square side length (as a measure for the grain size) $\overline{s_{equiv}} = \overline{(A_{grain})^{1/2}}$ of the grains is $1.17 \pm 0.02\ \mu\text{m}$. The average grain boundary surface per unit volume $\overline{S_V}$ is correlated to the average number of intercepts per length $\overline{N_l}$ of an arbitrary straight line with grain boundaries on a micrograph as follows [92]:

$$\overline{S_V} = 2\overline{N_l}. \tag{6.1}$$

The quantity $\overline{N_l}$ is in turn equivalent to the inverse square root of the mean grain area, so

$$\overline{S_V} = 2 \cdot \left(\overline{A_{grain}} \right)^{-1/2}. \tag{6.2}$$

For the initial respectively stress-relieved tungsten as investigated here, $\overline{S_V} = 1.42 \pm 0.03\ \mu\text{m}^2/\mu\text{m}^3$.

Many grains have a non-uniform greyscale contrast in this imaging mode, which points towards deformations of the lattice that affect the channelling and backscatter diffraction of the electrons. These deformations are due to the rolling process. In the plan-view image in Figure 6.1, the elongation of the grains in the rolling direction (horizontal in this image) is very difficult to see. Images of cross-section cuts along the rolling direction, such as shown in Figure 6.2, clearly show that the grains are strongly flattened. Cutting in the perpendicular direction reveals that the grains are indeed primarily elongated parallel to the rolling direction.

In order to quantify the dislocation density in a STEM micrograph such as it is shown in Figure 6.3, the image was first converted into a binary image showing only the dislocations. For this, the dislocations were traced by hand in the image. Semi-automatic filtering turned out to be usually just as time consuming, but not quite as accurate. The dislocation density was then determined by first measuring the total projected surface of dislocations in the binary image. The projected surface was divided by the line width used for tracing in order to obtain the total length of dislocations in the image. This value was then divided by the image area times the average sample thickness, which yields the dislocation density. In order to improve the statistical relevance of the measured dislocation density, several different images from the initial material as well as from a stress relieved
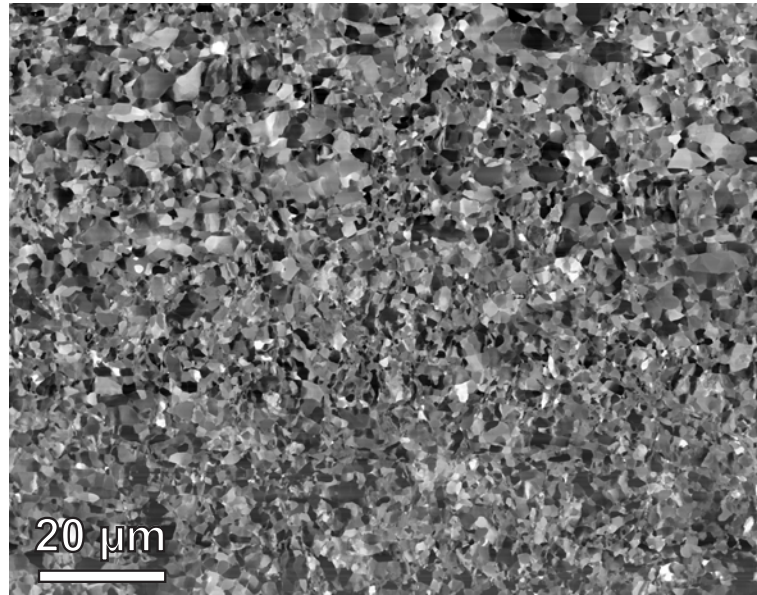
Figure 6.1. BSE micrograph of a tungsten specimen stress-relieved at 1200 K for 60 minutes in vacuum. The average grain size is 1.17 ± 0.02 μm. Many grains show deformations due to the production process. The elongation of the grains in the rolling direction (horizontal) is difficult to see in the surface is difficult to see. The grain structure is identical to that of a specimen without heat treatment.
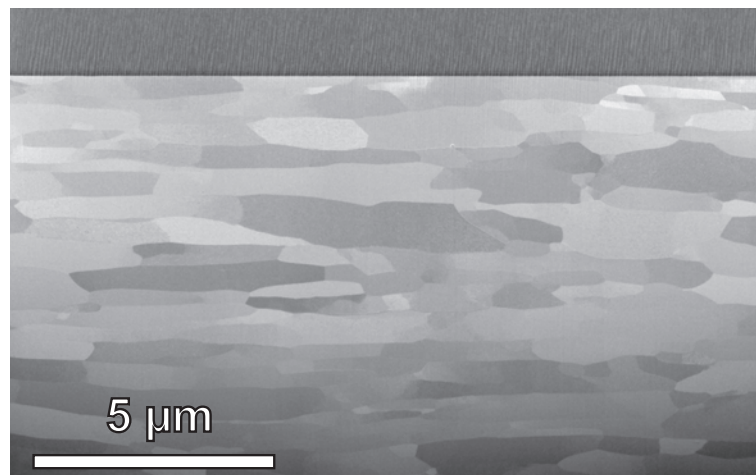

Figure 6.2. Scanning electron micrograph of a cross-section through a piece of the initial material. The cross-section was prepared by focused ion beam. The surface is protected by a Pt-C layer. The image clearly shows the elongation of the grains in the rolling direction (left to right).

sample were analysed. This showed that the measured dislocation density can vary significantly from image to image, which leads to statistical uncertainties of $\pm 15\%$ for stress-relieved material, which still has a comparatively homogeneous
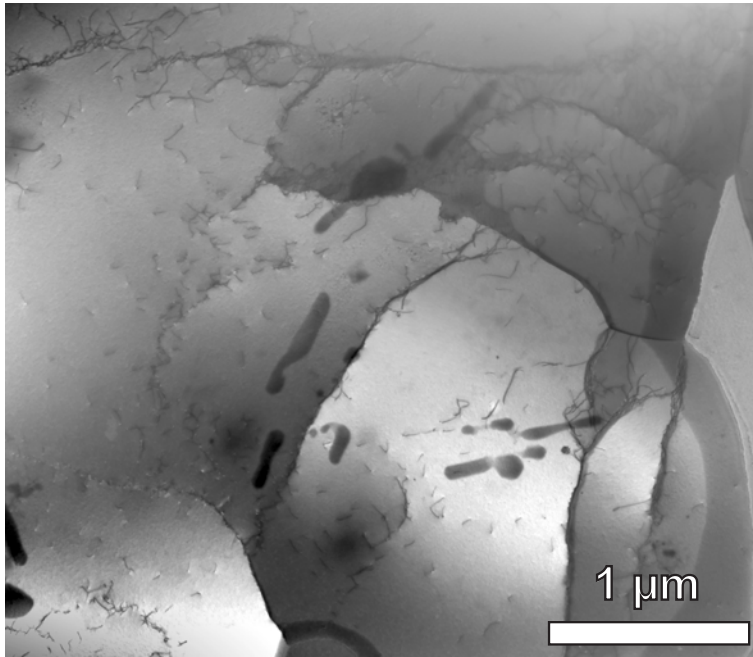
Figure 6.3. Bright field (BF) STEM micrograph of tungsten stress-relieved for 60 minutes at
1200 K. A dense network of dislocations can be seen as well as several grains.
Grain boundaries and dislocation arrays or tangles can barely be separated. The
elongated dark patches in the image are residue from thinning that could not be
removed.

distribution of dislocations. For recrystallised material, which has very few and
inhomogeneously distributed dislocations, it can go up to over $\pm 50\%$. In most
cases the most uncertain value in the calculation of dislocation densities from the
STEM images is the sample thickness, however. Unfortunately, commonly used
methods for determining the sample thickness in a TEM, like tilting experiments
or the comparison of elastic and inelastic contributions to the EELS spectrum,
are not applicable in the HELIOS NanoLab 600 microscope that was used for
most of the analysis. Taking into account the acceleration voltage of 30 kV and
an acceptance semi-angle of $\approx 7.1°$ of the bright field detector, the NIST database
on electron elastic scattering cross-sections [42] yields an elastic mean free path
of ≈ 21.5 nm. In order to acquire a clear diffraction contrast image, the sample
thickness must not be thicker than about one or two mean free paths. Addition-
ally, the thickness typically varies also across a single image. All in all, since the
images were usually acquired in areas of intermediate thickness some distance
from the thin edge, the average thickness is estimated to be about 35 nm $\pm 50\%$.

The STEM images also show that a large fraction of the grain boundaries can

be easily resolved into arrays of dislocations. In fact, in many cases it is not easily possible to distinguish between grain boundaries and dislocation arrays respectively tangles of dislocations. Therefore all features that can be resolved into individual dislocations are also counted as dislocations. The occurrence of these — often rather loosely spaced — dislocation arrays also points towards another property of the initial respectively stress-relieved material: namely that a large fraction of the grain boundaries are *small angle* grain boundaries. This is deduced from the relation between the tilt angle θ between two adjacent grains, and the spacing d of dislocations constituting the boundary [92]:

$$\sin(\theta/2) = \frac{b}{2d}. \tag{6.3}$$

In this equation b is the magnitude of the Burgers vector. Although equation (6.3) is directly applicable only to simple pure tilt boundaries, its underlying principle is rather general: the larger the distance between the dislocations in an array, the smaller the misorientation between the grains. In other words, many of the grains visible in Figure 6.1 are actually sub-cells originating from polygonisation during the hot-rolling process and to some extent possibly also during the subsequent annealing. A similar strong tendency towards polygonisation and sub-grain formation has also been investigated recently for molybdenum [90], which has many similarities to tungsten. In this publication the sub-grains were assigned a key role in the recrystallisation behaviour of the metal.

The result is an average dislocation density of $\rho_\perp = 3.2 \pm 1.7 \times 10^{14}$ m^{-2} for the stress relieved material, corresponding to a dislocation length of 320 μm/μm^3. There is no significant difference between the initial hot-rolled and the stress-relieved material. This is about 20 times lower than the dislocation density of 7.8×10^{15} m^{-2} measured by Debye-Scherrer X-ray diffraction of tungsten filings produced at 290 K, but coincides within the measurement accuracy with the value of 2.1×10^{14} m^{-2} found after annealing these filings without recrystallisation [118]. It is to be expected that the material analysed in this thesis is more similar to the annealed powder since it was deformed at high temperatures, which generally leads to a lower dislocation density than cold working such as filing.

Since the initial and stress-relieved material are very similar, both in terms of grain structure and dislocation density, both terms will be usually used synonymously from now on.

6.2. Partial recrystallisation at 1500 K

The recrystallisation temperature of tungsten, i.e., the temperature at which total recrystallisation takes one hour, is reported to be about 1500–1600 K [23]. Annealing a tungsten specimen for 30 minutes at 1500 K should accordingly lead to partial recrystallisation. Indeed such a heat treatment produces a rather fine grain material that looks not very different from the initial material at first glance, as it can be seen in Figure 6.4. However, partially recrystallised foils turned out to be already much more brittle and delicate than stress-relieved ones, respectively than those without heat treatment.
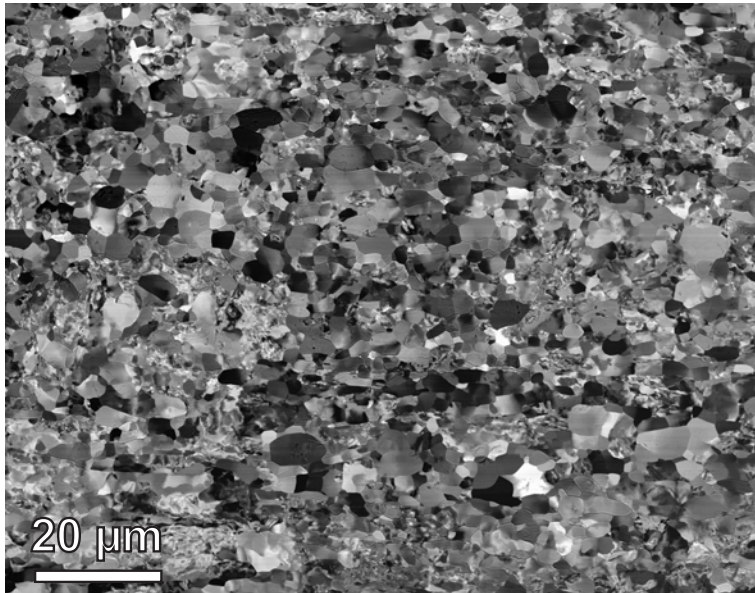

Figure 6.4. BSE micrograph of a tungsten specimen partially recrystallised at 1500 K for 30 minutes under Ar atmosphere. The average grain size has slightly increased to 1.54 ± 0.02 μm compared to the initial material. While many grains still show deformations, there are already many new grains with nearly uniform orientation contrast.

If one takes a closer look, many grains already show a much more uniform greyscale contrast than in the initial material, which is a clear indication for the beginning formation of new, more or less strain-free grains, i.e., recrystallisation. Also, grain growth, especially of these new grains, has already begun, leading to a slightly larger average grain size of $\overline{s_{equiv}} = 1.54 \pm 0.02$ μm, respectively a mean area of $\overline{A_{grain}} = 3.77 \pm 0.11$ μm. Accordingly, the partial grain boundary surface is reduced to slightly less than 3/4 compared to the initial material and is now $\overline{S_V} = 1.03 \pm 0.01$ μm^2/μm^3. Especially for the larger, strain free grains, ther-

mal grooving at the intersections of grain boundaries with the surface is already starting. This effect becomes much more pronounced for the fully recrystallised material (see sections 6.3 and 6.4). In short, grain boundary grooving is due to the relaxation of surface tension when a grain boundary meets a free surface. More details can be found, e.g., in [92]. Please note that nevertheless, grain growth can be assumed to be not significantly affected by free-surface effects since the specimen thickness is much larger than the grain size [92].

The partial recrystallisation after annealing for 30 minutes at 1500 K is also clearly visible in (S)TEM images. An example is shown in Figure 6.5. Overall, the dislocation network appears less dense and more fragmented than in the initial material. The arrangement of dislocations into strands and sub-grain boundaries also appears to be continuing. Besides these recovery effects, some grains that are nearly free of dislocations are appearing. Many of these grains are even smaller than the dislocation-rich grains and occasionally have thick dislocation walls around them. These are most probably new grains that have just nucleated. An example for such a grain can be seen roughly in the centre of Figure 6.6.
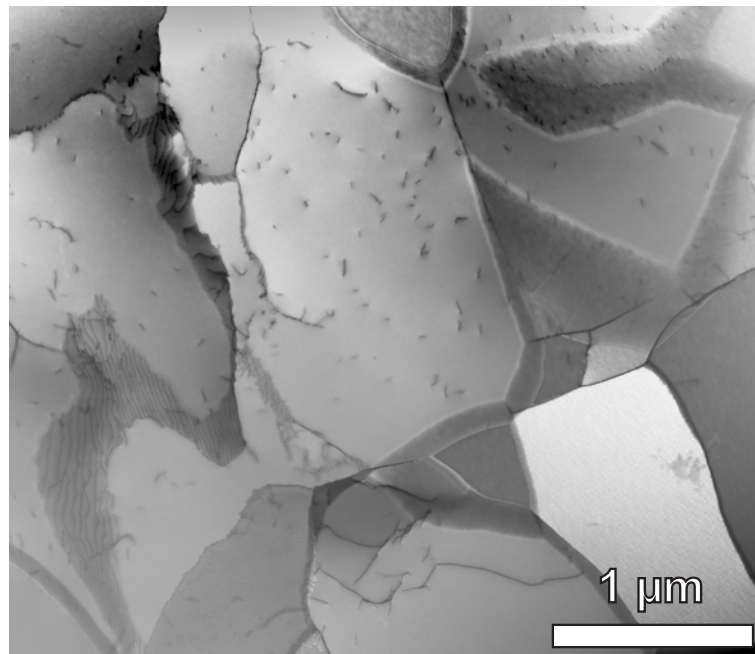

Figure 6.5. BF STEM micrograph of tungsten after annealing for 30 minutes at 1500 K. The dislocation network is slightly less dense than in the initial or stress-relieved material. Several new, practically dislocation-free grains have already formed. An increasing number of grain boundaries cannot be resolved into individual dislocations anymore.
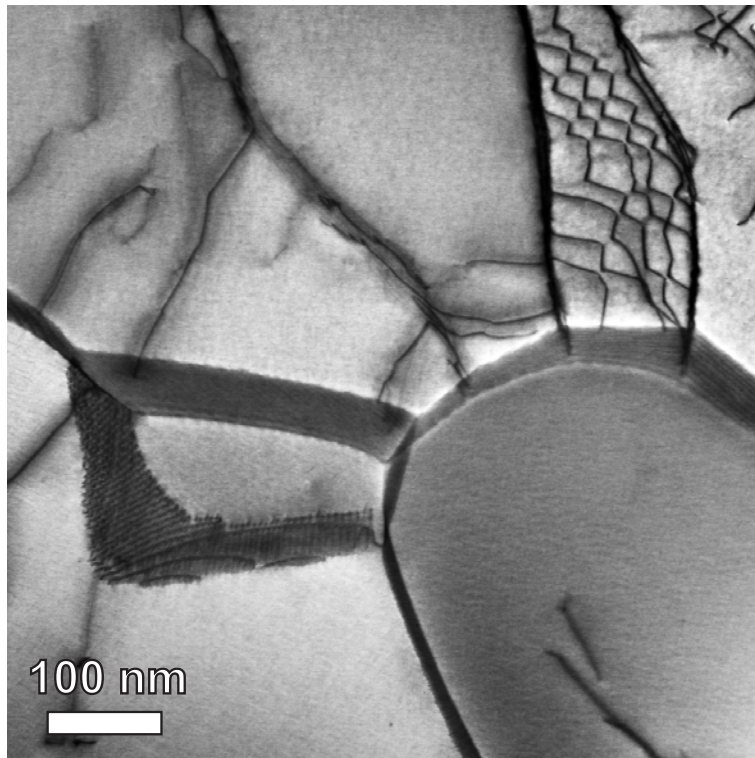
Figure 6.6. BF STEM micrograph of tungsten after annealing for 30 minutes at 1500 K. Note the small grain without dislocations roughly in the centre of the image. This grain has probably just nucleated in the recrystallisation process.

Other grains with a very low local dislocation density are have already reached a considerable size. These grains have most likely already nucleated very early after the annealing started and therefore have had sufficient time to grow.

All in all, the average dislocation density has reduced by roughly three times to $\rho_\perp = 9.8 \pm 5.3 \times 10^{13}$ m^{-2} compared with the initial material. Due to the presence of larger areas without dislocations, the dislocation density also becomes more inhomogeneous, which is reflected by the larger relative uncertainty of the dislocation density.

The appearance of the grain boundaries is also gradually changing. Compared with the initial material, a larger fraction of the grain boundaries cannot (or only barely) be resolved into individual dislocations. This points towards grain boundaries changing their nature from small-angle to large-angle grain boundaries. It is likely that this, as well as the reduced dislocation density, affects also the mechanical behaviour of the tungsten and contributes to the increased brittleness. This would be in agreement with observations on the cracking behaviour

of tungsten bi-crystals by Liu and Shen [59]: According to that study, cracks propagate along the grain boundary rather than crossing it for misorientations of more than 10°. The grain boundaries are generally believed to be the weak points in polycrystalline tungsten [23].

6.3. Full recrystallisation at 1700 K

Tungsten recrystallised for 30 minutes at temperatures of 1700 K can be considered fully recrystallised in the sense that the grain structure of the initial material is not recognisable anymore. This is also predicted by literature data [23]. The material has practically no ductility at all, as it is typical for recrystallised tungsten. This requires great care especially when handling thin foils, such as TEM specimens. The grain structure is significantly coarser, as it can be seen in Figure 6.7. There is already a significant number of grains with sizes of 10 μm or more. However, areas with small grains in the micron range can also be found in patches between these big grains. The coarsening of the grain structure also becomes apparent when one looks at the average grain size: $\overline{s_{equiv}}$ has nearly doubled to 2.92 ± 0.13 μm compared to the partially recrystallised material. $\overline{A_{grain}}$ is now 18.7 ± 2.4 μm^2, and correspondingly $\overline{S_V}$ has reduced to 0.46 ± 0.03 μm$^2/\mu$m^3, i.e, about one third of the initial value.

Another feature of specimens annealed at 1700 K is the apparently strongly corrugated surface. This is due to grains that have formed grooves at the intersections of their boundaries with the surface shortly after nucleation, but were subsequently consumed by grains with a faster growth rate. Note that the cells outlined by these residual grooves have roughly the same size as the remaining small grains that can be distinguished by channelling contrast.

The recrystallisation also has a strong effect on the dislocation structure of the tungsten. As Figure 6.8 shows, the initially long strands and dense networks of dislocations have often fragmented into many short lines. Their arrangement sometimes still hints at the former layout. Besides that, there are now many large areas nearly devoid of dislocations. Note also the numerous bright, angular shapes in the image. These result most likely from preferential etching of some dislocations during the electrochemical thinning. The resulting pits then appear bright due to thickness contrast. These pits are not prominent for the initial or partially recrystallised material. Only at high magnifications can similar, but
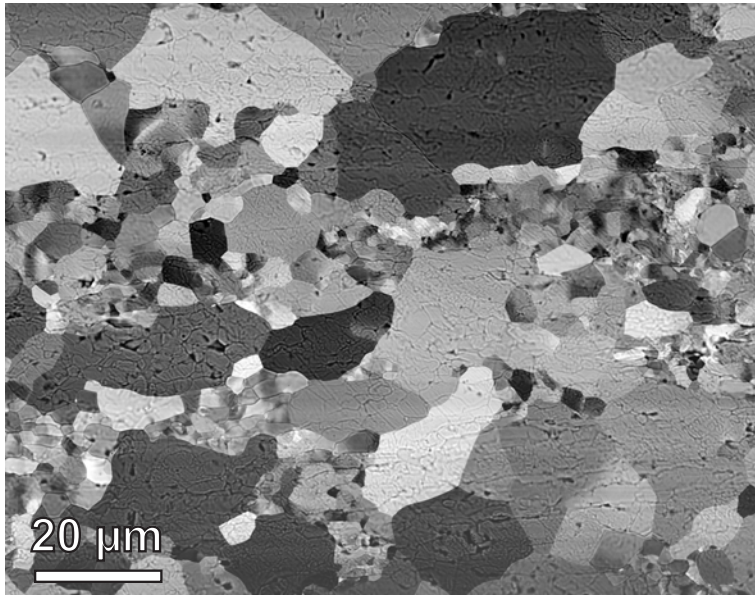
Figure 6.7. BSE micrograph of a tungsten specimen recrystallised at 1700 K for 30 minutes under Ar atmosphere. While still patches with small grains remain, grain growth has produced large areas covered by large grains. The average grain size is now 2.92 ± 0.13 μm, with some grains as large as 30 μm. The specimen surface appears corrugated due to thermal grooving at grain boundaries and subsequent grain growth.

much smaller features be distinguished at the intersections of dislocations with the specimen surface.

Since usually there is no sign of the typical diffraction contrast signature of dislocations around the etching pits in the fully recrystallised material, it is assumed that the dislocations were perpendicular (or at least steeply inclined) to the specimen surface. The exact appearance of the etching pits also depends on the crystallographic orientation of the grain they occur in. Etching pits are also counted as dislocations. Because of their orientation, each one of them is assigned a length corresponding to the average sample thickness. All in all, this results in an average dislocation density of $\rho_\perp = 5.2 \pm 3.0 \times 10^{12}$ m^{-2}. This is almost two orders of magnitude lower than the dislocation density of the initial, hot-rolled material, and matches well with the value of 3.0×10^{12} m^{-2} found by X-ray diffraction of recrystallised tungsten powder [118].

The appearance of grain boundaries has also changed significantly compared to the initial material. They typically cannot be resolved into individual dislocations anymore, which means that large-angle grain boundaries are now dominant. Some
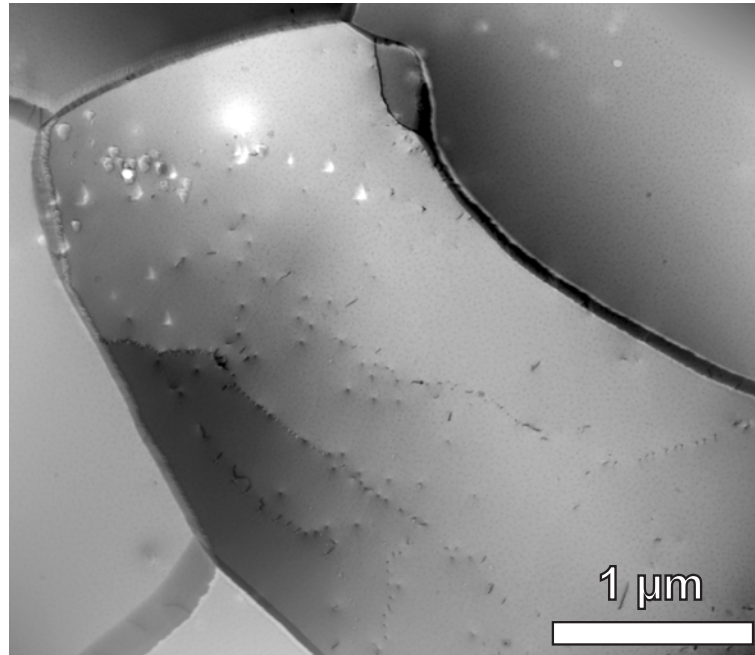
Figure 6.8. BF STEM micrograph of tungsten after annealing for 30 minutes at 1700 K. There are large areas free of dislocations. The dense dislocation networks have fragmented into short individual dislocations or even completely disappeared. The bright angular features in the images are etching pits due to end-on dislocations. Grain boundaries typically cannot be resolved as individual dislocations anymore.

grain boundaries also show distinct traces of preferential etching. This effect, like the prominent etching pits at end-on dislocations, is not found in tungsten annealed at 1200 or 1500 K.

6.4. Full recrystallisation at 2000 K

Annealing the material for 30 minutes at 2000 K also leads to full recrystallisation of the tungsten, like already at 1700 K. Again, the material becomes extremely brittle after the annealing. However, the resulting grain structure is quite different, as Figure 6.9 shows. It is now even coarser with grains up to 50 μm, and does not show patches of small grains between the larger ones anymore. The small and large grains are now much more evenly distributed. Also, residual grooves inside large grains are usually not found like after recrystallisation at 1700 K. Only occasional traces of grain boundary movement, or of the disappearance of small grains, are visible, e.g., on the right hand side of Figure 6.9. Occasionally also small amounts of carbon-rich precipitate can be found, mostly inside the grooves

at grain boundaries. Deuterium plasma exposure was typically able to completely
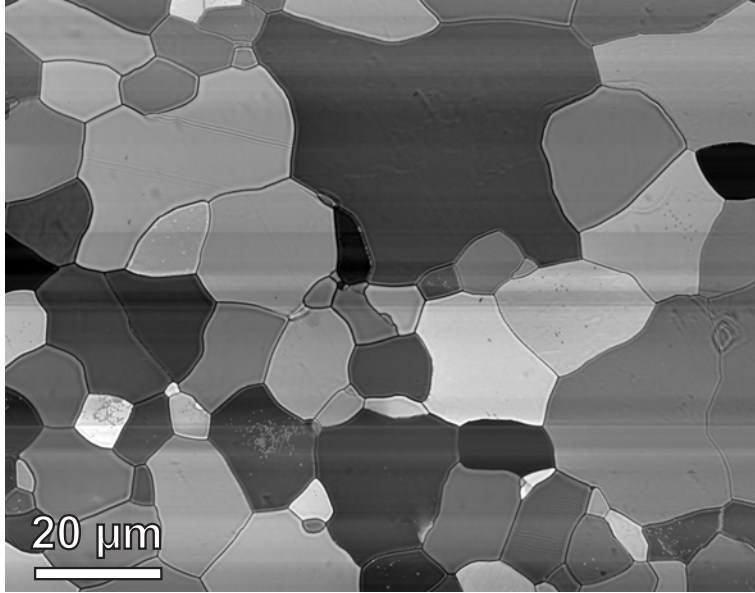remove this kind of contamination.

Figure 6.9. BSE micrograph of a tungsten specimen recrystallised at 2000 K for 30 minutes
under He atmosphere. The grain structure is dominated by large grains of up to
50 μm, with an average size of 12.1 ± 0.3 μm. The grains can be well distinguished
by channelling contrast as well as by thermal grooving.

Because of the small number of grains visible in Figure 6.9, this image was not
suitable for grain size statistics, but it is shown here for better comparability with
the other BSE-SEM images. The actual statistical analysis was performed for an
image at one quarter of the magnification. The results were an average grain size
$\overline{s_{equiv}} = 12.1 \pm 0.3$ μm, an average grain area of $\overline{A_{grain}} = 216 \pm 10$ μm^2 and a
corresponding grain boundary fraction of $\overline{S_V} = 0.136 \pm 0.003$ μm$^2/\mu$m^3. This is
again by more than a factor of three less than for the tungsten recrystallised at
1700 K.

The dislocation density is very low after annealing at 2000 K, just as for the heat
treatment at 1700 K. Also, large areas practically without any visible dislocations
exist, and etching pits are also observed. Fragments of former dislocation networks
are only very rarely found. Instead, dislocations rather appear as isolated, straight
lines with lengths of up to a few 100 nm, as Figure 6.10 illustrates. The average
dislocation density of $\rho_\perp = 1.9 \pm 1.4 \times 10^{12}$ m^{-2} is even slightly lower than
for recrystallisation at 1700 K, but the large statistical uncertainty due to the
inhomogeneous distribution of dislocations makes it hard to tell. Compared to

the initial and partially recrystallised material, both fully recrystallised materials have a dislocation density close to zero.
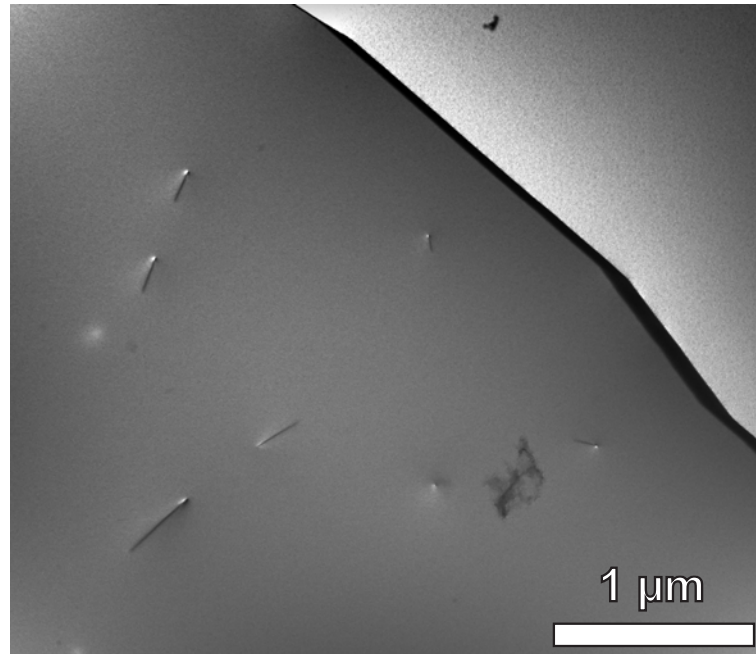

Figure 6.10. BF STEM micrograph of tungsten after annealing for 30 minutes at 2000 K. Dislocations typically appear as well-separated, straight lines. Etching pits are also occasionally present. Large areas are free of dislocations. Grain boundaries typically cannot be resolved into individual dislocations.

6.5. Summary of the tungsten microstructure analysis

The annealing of tungsten at different temperatures between 1200 and 2000 K produces a wide range of different microstructures, both in terms of the grain size and the dislocation density. The quantitative results for the grain structure and the dislocation density are summarised in Tables 6.1 and 6.2. While annealing for 60 minutes at 1200 K barely changes the microstructure, heat treatment 2000 K for 30 minutes causes full recrystallisation. The grain size increases by one order of magnitude, which leads to a corresponding reduction of the grain boundary surface area per volume. At the same time, the dislocation density is reduced by about two orders of magnitude. Annealing for 30 minutes at 1500 K leads to partial recrystallisation and produces a still fine-grained material whose dislocation

density is reduced by about three times compared to the initial material, but is still relatively high. Tungsten annealed for 30 minutes at 1700 K can be considered fully recrystallised, like for annealing at 2000 K. The initial grain structure is more or less completely transformed, and the dislocation density is similarly low. The grain structure, while including already a notable number of grains larger than 10 μm, is still not as coarse as for the highest annealing temperature used here.

Table 6.1. Results of the grain size analysis of tungsten specimens after different heat treatment. The table lists the statistical averages for the equivalent square side $\overline{s_{equiv}}$ as a linear measure for the grain size, the grain area $\overline{A_{grain}}$ and the grain boundary surface per volume $\overline{S_V}$.

Heat treatment	s_{equiv}	A_{grain}	S_V
none / 1200 K	1.17 ± 0.02 μm	1.99 ± 0.08 μm^2	1.42 ± 0.03 μm^2/μm^3
1500 K	1.54 ± 0.02 μm	3.77 ± 0.11 μm^2	1.03 ± 0.01 μm^2/μm^3
1700 K	2.92 ± 0.13 μm	18.7 ± 2.4 μm^2	0.46 ± 0.03 μm^2/μm^3
2000 K	12.1 ± 0.3 μm	216 ± 10 μm^2	0.136 ± 0.003 μm^2/μm^3

Table 6.2. Average dislocation density $\rho_\perp$ in tungsten specimens after different heat treatment, based on a sample thickness estimation of 35 nm $\pm 50\%$. Particularly for high annealing temperatures the dislocation density is highly inhomogeneous on typical TEM analysis scales.

Heat treatment	evaluated images	total image area	$\rho_\perp$
none / 1200 K	5	57.8 μm^2	$3.2 \pm 1.7 \times 10^{14}$ m^{-2}
1500 K	6	172 μm^2	$9.8 \pm 5.3 \times 10^{13}$ m^{-2}
1700 K	7	388 μm^2	$5.2 \pm 3.0 \times 10^{12}$ m^{-2}
2000 K	7	495 μm^2	$1.9 \pm 1.4 \times 10^{12}$ m^{-2}

Figure 6.11 shows histograms of the grain size distribution for all four heat treatments of the tungsten. Note that the bin size is increased for the larger and accordingly less frequent grain sizes. To compensate for this, the histogram is normalised to the bin size so that the *area* of a bin accurately represents the

relative abundance of grains of a specific size. It can be clearly seen how the abundance of large grains increases steadily with the annealing temperature.
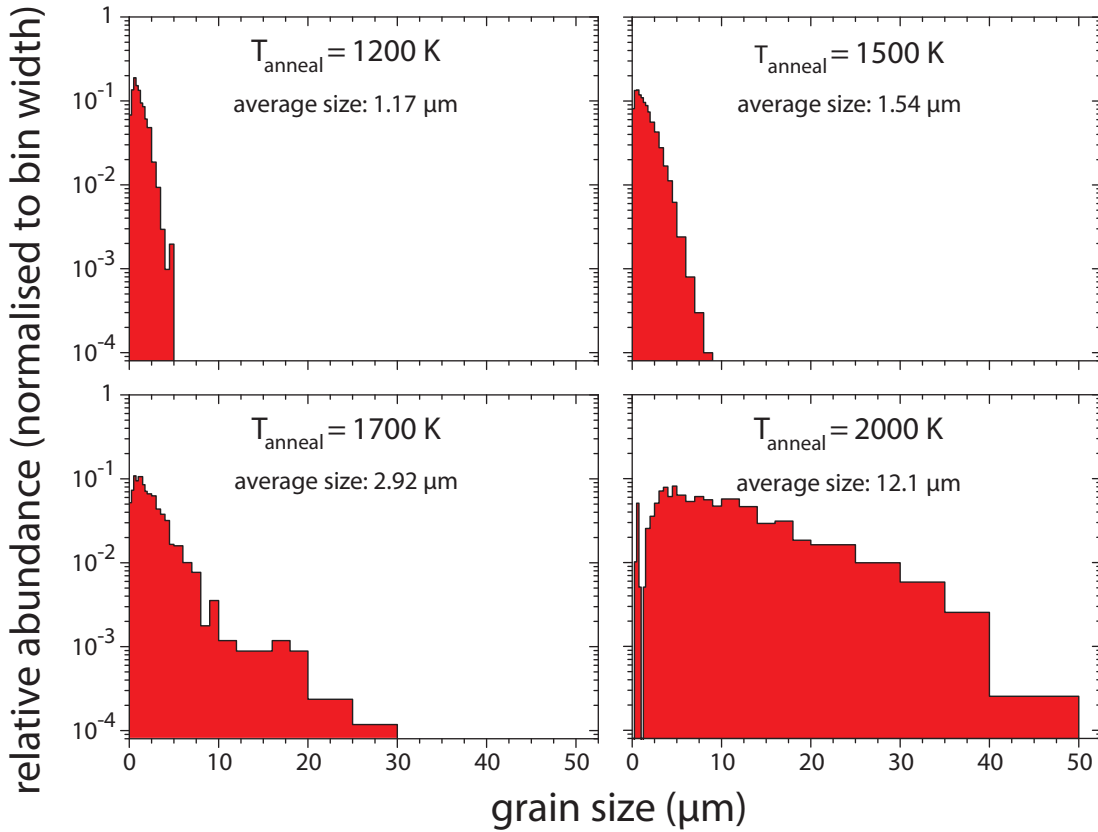

Figure 6.11. Grain size ($\overline{s_{equiv}}$) distributions of tungsten stress-relieved for 60 min at 1200 K and (partially) recrystallised for 30 min each at 1500, 1700 and 2000 K. The relative abundance of grains in each size bin is normalised to the bin width.

Figure 6.12 visualises the variation of the dislocation density $\rho_\perp$ and the grain boundary surface per volume $\overline{S_V}$ with the annealing temperature. It can be clearly seen that both $\rho_\perp$ and $\overline{S_V}$ decrease significantly for higher annealing temperatures. However, the dislocation density is nearly equal and close to zero for both fully recrystallised materials, while $\overline{S_V}$ decreases steadily. This should allow distinguishing between the influence of grain boundaries and dislocations on the deuterium retention after plasma exposure.

The different heat treatment procedures applied here also lead to a pronounced change in the mechanical behaviour of the material, as it becomes apparent especially when handling thinner foils used for protective wrapping during the annealing, respectively TEM specimens. While the initial material displays at least some ductility, even partial recrystallisation makes the material much more brit-

tle. While this is to be expected for tungsten (see, e.g., [23]), it makes the material very difficult to handle, especially in the form of TEM samples. This increased brittleness is probably related to the transition from many small-angle to dominantly large-angle grain boundaries. This can be deduced from the misorientation angle dependence of the fracturing behaviour of tungsten bi-crystals [59]. The reduced dislocation density might also play a role. In experiments, a pre-deformed polycrystalline specimen exhibited a higher fracture toughness than specimens without such pre-treatment [34].
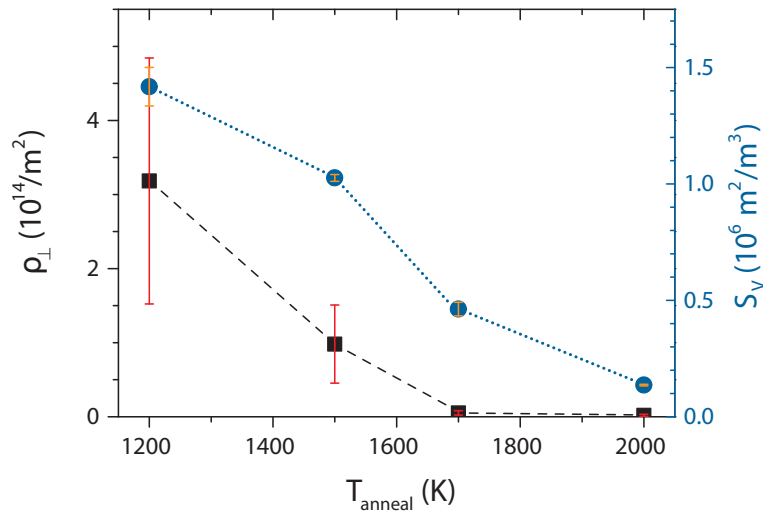

Figure 6.12. Dislocation density $\rho_\perp$ (squares, left y-axis) and grain boundary surface per volume $\overline{S_V}$ (circles, right y-axis) in tungsten for different annealing temperatures.

7. Strategy and motivation of the experiments

This chapter presents an overview of the experimental studies performed for this thesis. It describes the scientific rationale and summarises the key parameters for each experiment. The crossing point of the parameter variations introduced in this chapter is an ion energy of 38 eV/D, an incident fluence of 6×10^{24} D m^{-2} and a specimen temperature during plasma exposure of 370 K. These exposure conditions will from here on be termed as "reference conditions". A detailed interpretation of the results from the experiments described here will be given in chapter 8 and will be summarised in chapter 9.

7.1. Temperature variation

As it was already explained in detail in chapter 3, the deuterium inventory in a tungsten specimen is governed to a large extent by diffusion and trapping, i.e, by thermally activated processes. This makes a series of experiments at different specimen temperatures crucial for the understanding of deuterium retention in tungsten. For these experiments, the ion energy was kept constant at 38 eV/D. A fluence of 6×10^{24} D m^{-2} was chosen since own preliminary investigations showed that the deuterium inventory accessible by NRA is more or less saturated at this fluence [66] (see also section 8.2.1). Based on the results from these own investigations [66] as well as from literature, five different temperatures were chosen: 300, 370, 450, 500 and 750 K. The first four temperatures were selected because they cover the region of the typically observed desorption maxima with good resolution. A broad overview of published values was compiled by Causey [14]. Furthermore, the maximum of deuterium retention varies typically between about 300 and 600 K depending on the experiment conditions [4, 5, 13, 38]. The highest temperature of 750 K is of interest because it lies beyond the typically

observed desorption maximum: This means that the deuterium can be expected
to be able to escape from most traps and, accordingly, to be highly mobile. Also,
it was reported that blistering effects can be suppressed at such high temperatures [57]. For each temperature listed above, four specimens were mounted and
exposed at once, one of each microstructure described in chapter 6.

7.2. Fluence variation

Observing the variation of the retained deuterium inventory with the implantation
fluence allows to study the effective diffusion of deuterium from the implantation
zone into the bulk of the sample. In particular for small fluences, NRA is invaluable because it allows direct observation of the deuterium depth profile. For high
fluences, where the diffusion front has already moved beyond the range of NRA
analysis, thermal desorption completes the picture. The experiments in this campaign were all performed at a specimen temperature of 370 K, where diffusion is
expected to be measurable, but most trap sites reported in literature [15] can still
be expected to bind deuterium in significant quantities (see also section 8.5). An
ion energy of 38 eV/D was selected because sputtering and displacement damage
to the specimens due to plasma impurities (see also section 7.3) can be considered moderate. Still, the energy of the impinging ions is already far above the
enthalpy of solution of $\Delta H_{sol} = 1.04$ eV [27] for hydrogen in tungsten. The fluence was varied by more than three orders of magnitude from 3×10^{22} to about
5×10^{25} D m^{-2}. This corresponds to implantation times between 5 minutes and
6 consecutive days. For each fluence, four specimens, one of each microstructure
described in chapter 6, were exposed simultaneously.

Assume that the retention of hydrogen is determined solely by diffusive transport
to traps with a homogeneous distribution and without any temporal variation
(apart from saturation). Then one can expect the retained amount of deuterium
R_D to scale with the fluence Φ (which is proportional to the implantation time
for a constant ion flux) according to

$$R_D \propto \Phi^{1/2}. \tag{7.1}$$

Any deviation of the fluence dependence of R_D from such a power law with an
exponent of 1/2 points towards additional effects besides diffusion. Such effects

could be, e.g., the creation of additional traps during implantation or the existence of diffusion barriers at specific depths below the surface of the specimens.

7.3. Ion energy variation

Implantation experiments at different ion energies are of interest for various reasons. First of all, the ion energy determines the range an impinging ion can penetrate into a specimen before its kinetic energy is reduced to thermal energies. From then on, it can only travel by diffusion. For all investigated energies, the thermalisation range is small: SDTrimSP [22] calculations predict an average range of about 1.2 nm for 8 eV deuterons, and up to 6.4 nm for 205 eV. Nevertheless, this could strongly change the re-emission probability of an implanted and thermalised deuteron. The reflection yield for energetic particles is only weakly affected by the incident energy in this energy range and lies roughly between 60 and 70%. For this experiment series, bias voltages of -10, -100, -300 and -600 V were used. This corresponds to energies per deuteron of 8, 38, 105 and 205 eV/D (see section 4.1). Figure 7.1 shows the calculated particle stopping profiles for these energies.
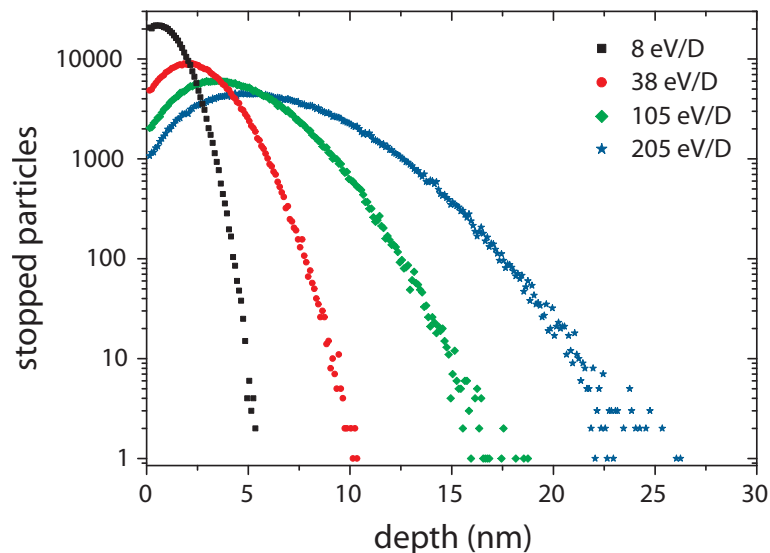

Figure 7.1. Particle stopping profiles for deuterium ions with incident energies between 8 and 205 eV/D. All profiles were calculated with the simulation package SDTrimSP using 10^6 incident particles.

A plasma practically always contains impurities from the background gas or from reactions with plasma-facing surfaces. A notable effect of background impurities

was even reported for experiments using a mass-separated ion beam [89]. In the experiments performed here, particularly the quartz plate through which the microwave for plasma generation is coupled in (see section 4.1) is slowly eroded by the deuterium plasma. This produces, e.g., D_2O molecules and their corresponding ions. Presently the formation of deuterated silane molecules cannot be excluded. However, the exposure of SiC to deuterium ions showed no indication of SiD_4 formation, only CD_4 [8]. Similarly, it is assumed that mainly oxygen is removed in form of D_2O from SiO_2 by the deuterium plasma. There is also no indication for SiD_4 in residual gas mass spectra at PlaQ, i.e., silane is assumed to be only a minor erosion product, if at all. While the sputter threshold for deuterium on tungsten is quite high at 250 eV/D (the threshold for directly producing displacement damage is even higher), the threshold for heavier impurity ions such as oxygen is much lower. Already at $V_{bias} = -100$ V, where all deuterium ion species are well below the sputter threshold, a D_2O^+ ion delivers an oxygen atom with 80 eV, which is already well above the sputter threshold of ≈ 50 eV [21]. For this reason it can be expected that even a small impurity ion flux of less than 1% (corresponding to the typical background gas composition during a discharge [65]) will cause significantly more damage than the deuterium ions. Varying the sample holder bias and accordingly the ion energies will allow to get a better picture of these effects. Applying a very low bias of only -10 V means that no ion from the plasma will have enough energy to produce sputtering or displacement damage. Experiments at such a low ion energy also allow to estimate the influence of low-energy particles like, e.g., neutral atoms with thermal energies. The advantage of a small bias over experiments at floating potential is that the ion flux is higher and can be monitored by measuring the current to the sample holder.

The experiments on the influence of ion energy were performed at a fluence of 6×10^{24} D m^{-2} and at a specimen temperature of 370 K. For each ion energy, all four specimen types described in chapter 6 were exposed to the plasma simultaneously.

7.4. Influence of the specimen preparation

7.4.1. Surface finish

The typical specimens investigated in this thesis were all carefully polished to a metallographic finish without any visible distortion layer at the surface, as described in chapter 5.1.1. But it is also interesting to see what effect an *imperfect* surface has on the deuterium retention. Also, it is necessary to check if the even slightly better surface quality produced by electropolishing leads to notable differences of the behaviour of specimens with respect to plasma exposure.

To study this, stress-relieved samples with the as-received technical surface finish were exposed at the same time as electropolished samples and samples with the standard polishing. The plasma exposure was performed under the reference conditions at a specimen temperature of 370 K with an ion energy of 38 eV/D to an incident fluence of 6×10^{24} D m^{-2}.

7.4.2. Comparison of stress-relieved and initial material

In chapter 6 it was shown that the microstructure of the initial and the stress-relieved specimens is more or less indistinguishable. However, annealing a specimen for 60 minutes at 1200 K in a vacuum of 10^{-4} Pa can be expected to produce changes that cannot be detected by electron microscopy, mainly the release of *hydrogen* (i.e., the ^{1}H isotope) from the specimen. This hydrogen is introduced during the manufacturing of the material: Typically, all processes at elevated temperatures, e.g., sintering or hot-rolling, are performed under H$_2$ atmosphere to prevent oxidation. This means that the hydrogen is literally *worked into* the tungsten. The manufacturer guarantees a hydrogen content of ≤ 5 μg/g, which corresponds to a concentration of about 10^{-3} H/W. This is comparable to the values of deuterium concentrations reached by D plasma loading of tungsten (see, e.g., section 8.1 or [5]).

Such a high concentration of "natural" ^{1}H can be expected to significantly impede the uptake of deuterium in a tungsten specimen: since practically all hydrogen isotopes retained in a tungsten specimen are bound to traps, a D atom has to swap places with a trapped H atom before itself can be bound by the trap. This isotope exchange process can be expected to be significantly slower than the filling of empty traps.

TDS experiments usually show that the release of deuterium from D implanted tungsten specimens subsides at temperatures $\leq$ 1200 K (see, e.g., [50, 82, 109] or section 8.5). Accordingly, annealing for 60 minutes at 1200 K (compared to $\leq$ 20 minutes for TDS experiments) should be able to drive out a large amount of hydrogen. Also, using Frauenfelder's value for the diffusion coefficient at this temperature [27], one arrives at a time of little more than 1 minute necessary for a hydrogen atom to diffuse through the whole specimen thickness of 0.8 mm. However, this fast diffusion speed also means that all the hydrogen in the specimen will be in thermal equilibrium with the hydrogen background in the vacuum during the annealing process. This will lead to a finite hydrogen concentration after the annealing, regardless of the holding time. The release of *deuterium*, on the other hand, usually is not affected in this way since the D_2 partial pressure in the vacuum is much lower due to the small natural abundance of deuterium.

It is quite difficult to get a handle on the "natural" hydrogen content in tungsten specimens. It is only possible to probe for hydrogen in very shallow depths with ion beam analysis techniques (e.g., NRA with ^{15}N or ERDA), and TDS spectra of *hydrogen* release from tungsten are often obscured by the H_2 in the background gas. Therefore, non-annealed and stress-relieved specimens, both polished and unpolished, were exposed to a D plasma under the reference conditions at 370 K and 38 eV/D to a fluence of 6×10^{24} D m^{-2}. The D inventories in these specimens were subsequently investigated by NRA, and in several cases also by TDS to investigate the release of H_2, D_2 and HD molecules.

7.5. Investigation of blisters and related surface modifications

As it was explained in section 2.4, metals with an endothermic heat of solution for hydrogen isotopes, such as tungsten, can be easily oversaturated, e.g., by plasma loading. This can lead to the formation of gas bubbles in the material. A special case are blisters, i.e., gas-filled cavities near the exposed surface that are visible as a protrusion on this surface. Blistering is frequently reported in literature (e.g., [103, 82, 57, 116, 50]) and occurred for many of the exposure conditions mentioned above, but the blisters varied considerably in terms of their size, shape and abundance. Blistering effects also depend strongly on the microstructure of the specimen (see sections 8.1.6, 8.2.3 and 8.3.3).

Understanding these dependencies and the connection between blistering and the retained amount of deuterium in a specimen is an important step towards understanding deuterium retention in tungsten as a whole. Therefore, the surfaces of most specimens were investigated, mainly by optical DIC microscopy. It could be recently demonstrated that blisters are not purely plastic deformations, but can vanish due to degassing of the specimen during TDS [66] or when their cap is punctured by a focussed ion beam [9]. Because of this, blisters were usually investigated before TDS and in some cases additionally afterwards. For the experiment series on the influence of specimen temperature during deuterium loading, markers were applied to the specimen surface by FIB in order to compare the identical area before and after the plasma exposure as well as after TDS (see section 8.1.6). For some selected cases, cross-sections were also prepared by FIB and imaged by SEM in order to investigate the cavities corresponding to the blisters.

7.6. "Ramp-and-Hold" experiments

In order to deconvolve the effects of the depth and binding energy distributions on the release temperature of deuterium from a specimen (see section 4.3 and [14, 112]), one set of identical specimens was prepared and loaded with deuterium specifically for a detailed investigation by TDS. All these specimens were mechanically polished and stress-relieved. Deuterium implantation was performed under the reference conditions, i.e., at a specimen temperature of 370 K, an ion energy of 38 eV/D and to a fluence of 6×10^{24} D m^{-2}. The temperature of 370 K is also below the typical release temperatures reported in literature [14], so all traps can be expected to bind at least some deuterium. Finally, for these parameters the largest deuterium inventory was found in this thesis, which ensures a good signal-to-noise ratio in the TDS. The specimens for the "Ramp-and-Hold" TDS experiments that are described in this section were stored for two months in a vacuum exsiccator before analysis, like all the other specimens investigated here (see section 5.1.3). The depth distribution of the deuterium in these species was investigated in a detailed NRA study.

The specimens described above were degassed in TESS (see Figure 4.9) with heating rates varying over more than three orders of magnitude between 0.3 and 600 K/min. This variation of heating rates allows a decoupling of the binding energy and the attempt frequency for the escape of deuterium from a certain type of binding site. Two different methods for this are discussed in detail in

section 8.5.1 [24, 91]. Both of them require as much variation of the heating rate as possible to yield accurate results. In detail, the specimens were degassed with heating rates of 0.3, 1, 3, 30, 72, 300 and 600 K/min. A spectrum acquired in the "HSQ-TDS", with a heating rate similar to that of the 72 K/min program in TESS (see also Figure 4.10), is also included in the dataset. Since some heating programs lead to a non-linear specimen temperature response, the values stated here correspond to the rate of temperature increase at ≈ 600 K, i.e., at the approximate temperature of the main D_2 release peak.

In addition to the degassing at different heating rates, several samples were also subjected to interrupted temperature ramps. One variant of these experiments was to heat up the specimen to a certain temperature at 30 K/min and then retract the tube furnace from the glass tube of TESS in order to cool the specimen to room temperature as quickly as possible. The second variant was to heat the tube furnace to a temperature that — after a sufficiently long time — results in a specimen temperature equal to that reached in the pull-off experiment. The specimen was then held at this temperature for about 90 minutes in order to allow the mobilised deuterium to be released from the specimen. This asymptotic-heating method was chosen in order to prevent overshoots of the temperature. After either of these first heating steps, the specimen was allowed to cool down to room temperature. Then a second, uninterrupted temperature ramp at 30 K/min was applied in order to release the deuterium that remained in the specimen after the first step. This is a method to determine in how far diffusion and binding energy distribution contribute to the release spectrum: Deuterium that remains in the specimen after a pull-off experiment, but is released during an equivalent asymptotic heating, must have had a similar binding energy, but have been trapped deeper inside the specimen. These experiments were performed for holding (respectively interruption) temperatures for 470 and 660 K, which is in both cases close to one of the release peaks at ≈ 450 and ≈ 680 K (see section 8.5.2).

The deuterium depth profile before TDS was determined for a representative specimen (ID: A0129) by NRA. Additionally, this specimen as well as a second one (ID: A0144) were re-analysed by NRA after partial degassing due to pull-off experiments. This was done to study the redistribution of deuterium inside specimens during TDS experiments. Prior to the pull-off experiments, sample A0129 was also analysed two days after the plasma exposure in addition to the reference NRA measurement after the standard two months resting time in order to investigate the degassing during storage.

The results from this chapter are interpreted on the basis of the diffusion-trapping model introduced in section 3.3. The model was iteratively refined to match the observations of the experiments. The comparison of the model with a whole set of TDS spectra acquired with different heating rates is needed to compensate the fact that most methods for the analysis of these spectra were developed for the desorption of *surface adsorbates* [24, 91] and do not include diffusion from larger depths. Only with the model taking into account the full depth distribution of the traps as well as of the deuterium the influences of trap energy, detrapping attempt frequency and depth profile on the temperature of the desorption maximum can be resolved. Comparison with interrupted TDS ramps allows to study the redistribution of deuterium inside the specimen due to annealing, and to explore the limits of the strongly simplified model.

7.7. Hydrogen isotope exposure of transparent TEM specimens

As it was already briefly mentioned in section 2.1.2, the presence of hydrogen isotopes in a metal can significantly reduce the energy for the formation of defects. This can go so far that defects are even produced exothermically [48]. Also, the mobility of dislocations can be *enhanced* by hydrogen through shielding of their stress fields [86]. Therefore, it was tried to study these effects also for the tungsten-hydrogen system.

The most commonly used tool to study crystal defects, particularly dislocations, is the transmission electron microscope. However, preparation of specimens is always involved with the risk of introducing artifacts. Although the electrochemical preparation method described in section 5.2 is commonly believed to be damage-free, it still leaves the difficulty of not removing the most interesting layers when preparing plan-view TEM samples from an implanted bulk specimen. Unfortunately, the method does not work for cross-section preparation. Furthermore, it is highly valuable to be able to study exactly the same part of a specimen before and after exposure. Because of that, it was decided to perform these experiments on already transparent TEM specimens.

One specimen was prepared from partially recrystallised tungsten (see section 6.2) and exposed to a deuterium plasma at an ion energy of 38 eV/D. The specimen holder was kept at ≤ 300 K during the exposure. The loading time was about

30 minutes, which corresponds to a fluence of $\approx 1.5 \times 10^{23}$ D m^{-2}. For this, an adapter was constructed that allowed clamping a TEM specimen to the specimen holder of the PlaQ device for the best possible temperature control. It must be said, however, that there is no way of measuring (respectively accurately controlling) the temperature of the transparent areas during the deuterium loading. They receive considerable energy input from the energetic ions, which are fully stopped even within the thickness of the specimen. This may lead to a significant heating of the thin areas because heat diffusion away from the thin edge can be expected to be significantly lower than in bulk material. For obvious reasons, the thin areas themselves cannot be clamped directly.

Before and after plasma exposure, the specimen was thoroughly investigated in the JEOL JEM-2010F TEM at the University of Augsburg. This instrument was chosen because it offered, besides high-quality TEM and STEM imaging at intermediate magnifications, also the possibility of achieving lattice resolution by HRTEM imaging.

Two more TEM specimens, one from stress-relieved (see section 6.1) and one from partially recrystallised tungsten (see section 6.2) were investigated in a so-called "environmental TEM" (ETEM). This kind of instrument features a differentially pumped specimen chamber and allows the introduction of gases, among others H_2 at pressures up to about 0.7 kPa. These experiments were made possible by Mr Martin Deutges and Prof. Reiner Kirchheim from the University of Göttingen. They offered to expose these specimens along with their own material during their experiment time at the DTU–CEN facility in Copenhagen, Denmark[1]. The experiments carried out consisted of acquiring TEM image series ("videos") while varying the pressure of the H_2 gas in the specimen chamber, and of trying to damage the specimen with a high-intensity electron beam in STEM mode while the specimen was exposed to hydrogen. These experiments allowed a direct investigation of the reaction of the specimens to the presence of an H_2 atmosphere while irradiated by high-energy electrons.

---

[1]DTU–CEN: Centre for Electron Nanoscopy, Danmarks Tekniske Universitet, Copenhagen. http://www.cen.dtu.dk

8. Discussion of the experimental results

This chapter discusses the detailed results from the experiments introduced in chapter 7. Each parameter variation is first examined separately in order to identify the key tendencies of deuterium retention and blister formation. Some of the experimental results are also interpreted based on a diffusion-trapping model (see section 3.3). Because of the large amount of data presented here, chapter 9 is dedicated to deliver a synopsis and correlate the individual experiments.

8.1. Temperature dependence of D retention

Generally, the retained amount of deuterium after exposure to a plasma with an ion energy of 38 eV/D was of the order of 10^{-5} to 10^{-4} of the incident fluence of 6×10^{24} D m^{-2}. Overall, the retained D inventories measured here are of the same order of magnitude as values reported for comparable fluences by other researchers (see, e.g., [1, 37, 79]), although in detail there are also notable differences between those results and the ones presented in this thesis. They will be discussed in the course of this chapter and in chapter 9.

Generally, the balance between diffusion of the implanted deuterons deeper into the bulk and losses through the specimen surface changes considerably as the temperature rises. Consequently, the deuterium retention strongly depends on the temperature during plasma exposure, as Figure 8.1 illustrates. The following sections 8.1.1–8.1.5 will discuss in detail the retention in tungsten specimens with different microstructures due to implantation at temperatures between 300 and 750 K.
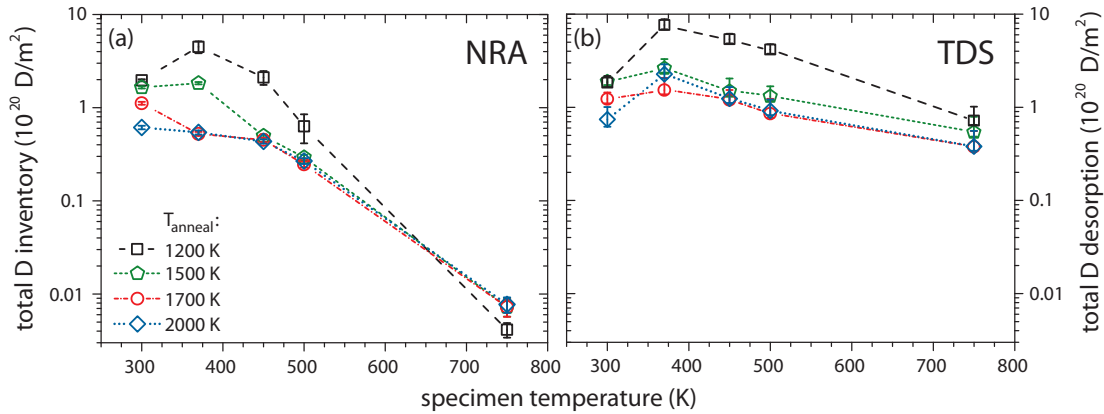
Figure 8.1. Total deuterium inventory in tungsten specimens exposed to deuterium plasmas
with an ion energy of 38 eV/D up to a fluence of 6×10^{24} D m^{-2} at various
specimen temperatures. (a) shows the total D inventory accessible by NRA, (b)
shows the corresponding value as determined by TDS. The symbols refer to the
same type of specimen for both panels.

8.1.1. Implantation at 300 K

The retained amount of deuterium, as well as its depth distribution in the tung-
sten specimens, varies strongly within the temperature range between 300 and
750 K. At 300 K, the deuterium inventory determined by NRA is already quite
large (for tungsten) and ranges between 0.7×10^{20} D m^{-2} for the material annealed
at 2000 K, and 1.9×10^{20} D m^{-2} for the stress-relieved tungsten (see Figure 8.1).

Because diffusion is still comparatively slow at this temperature, the amount of
deuterium released by TDS matches the NRA value for the defect-rich, stress-
relieved material. For the partially and fully recrystallised specimens the situation
is similar. The deuterium depth profiles of all materials are shown in Figure 8.2a.
In all cases a high concentration of several 10^{-2} (i.e, several atomic percent) was
found in a very narrow zone at the specimen surface. Considering the low solu-
bility of hydrogen in tungsten, this is a very high value. Since the analysis takes
place about two months after the plasma exposure, this is no transient super-
saturation effect but permanent. The extension of this zone roughly corresponds
to the stopping range of the implanted ions. The deuterium concentration then
sharply drops by one to two orders of magnitude and subsequently decays down
to concentrations of $\approx 10^{-5}$ towards the depth range limit of the NRA measure-
ment. For the recrystallised material the initial drop of the concentration after
the surface maximum is steeper, but the subsequent decay into the bulk is slightly
flatter compared to the stress-relieved material. This points towards diffusion be-

ing generally slow, but already slightly faster in material with a smaller defect density. Overall, NRA and TDS are consistent that the deuterium retention is highest in the stress-relieved material, followed by the partially recrystallised and finally the fully recrystallised tungsten.

8.1.2. Implantation at 370 K

If the temperature during implantation is increased to 370 K, the D inventory of the stress-relieved material increases strongly. NRA results range from 4.5 to 5.4×10^{20} D m^{-2}, TDS yields even larger inventories of up to 7.7×10^{20} D m^{-2}, as illustrated by Figure 8.1. For the other materials, this increase of the deuterium inventory is less pronounced. It is barely detectable by NRA for the partially recrystallised tungsten and does not show in NRA results for the fully recrystallised materials. The results from TDS indicate a significant increase for all materials. In all cases, TDS yields also a higher total deuterium inventory than NRA. This means that a significant amount of deuterium (roughly up to one third of the total inventory) has already diffused beyond the detection range of NRA.

While the D depth profiles of all types of specimen were not too different for implantation at 300 K, at 370 K remarkable differences between the materials become apparent as Figure 8.2b shows: The surface maximum is comparable to implantation at 300 K for all materials, but the depth profile in stress-relieved material now shows a local concentration minimum directly beyond the surface maximum. In this minimum the concentration reduces to a few 10^{-4}. This minimum is followed by a strong secondary maximum of up to 2×10^{-3} in a depth range between 0.5 at 5 μm. The highest values are reached between about 2 and 4 μm. Towards larger depths, the concentration decays down to values of about 10^{-4}. For the partially recrystallised tungsten, the local minimum and secondary maximum are also visible, but much less distinctive.

Both fully recrystallised materials do not display this structure in the depth profile. Instead, the depth profile becomes even flatter than at 300 K. Also, the bulk concentration typically becomes smaller for higher pre-annealing temperatures. As a result, the stress-relieved material shows significantly higher retention than all other materials, again followed by the partially recrystallised specimen. The fully recrystallised materials have the lowest retention. Both of them show very similar inventories in the NRA measurement. This is somewhat surprising considering the significant difference between the grain sizes of these two materials.

The TDS results show some variation, but in general the reproducibility of NRA is better than for TDS, so this could also be due to experimental uncertainties.

8.1.3. Implantation at 450 K

The temperature of 450 K roughly corresponds to the first release peak of deuterium found in literature (see, e.g., [4, 82]) and also in own preliminary work [66]. For a detailed discussion of the features in thermal desorption spectra see also section 8.5. At this temperature, it is expected that significant amounts of deuterium can already escape from low-energy traps. Accordingly, the diffusivity of deuterium in the material should already be considerable. At the same time, desorption losses from the surface are also expected to increase. Indeed, the depth profiles of deuterium in tungsten of all the microstructures described in chapter 6 become flatter (see Figure 8.2c).

For stress-relieved tungsten, the secondary concentration maximum is still clearly visible, but lower in magnitude at about 7.3×10^{-4}. At the same time, the bulk concentration is slightly higher. The surface maximum is practically unaffected by the higher temperature, but the following local minimum becomes even deeper and is now slightly below 10^{-4}. This could be due to deuterium re-emission while the specimen cools down (see section 8.5.2). The depth profile in partially as well as in fully recrystallised tungsten is now practically flat beyond the surface maximum. The bulk concentration in tungsten pre-annealed at 1500 K is a bit higher at 3×10^{-5} than that of both fully recrystallised materials, which is at 2×10^{-5}. The maximum itself, like in the other materials, is not strongly affected by the higher temperature during implantation.

Both TDS and NRA measurements of the total inventory displayed in Figure 8.1 show that the retention of deuterium is smaller than at 370 K. However, the reduction is less pronounced in the TDS result. In fact, the inventory determined by TDS is now more than 2.5 times larger than the inventory accessible by NRA in the case of stress-relieved tungsten. For the other materials the difference is not quite as large, but still considerable. Comparing the different microstructures, the same tendency as for the lower implantation temperatures can be seen: The stress-relieved material retains the most deuterium, and the fully recrystallised material the least — again the materials annealed at 1700 and 2000 K show very similar retention. The partially recrystallised material lies in between the stress-relieved and fully recrystallised materials.

8.1.4. Implantation at 500 K

For implantation at 500 K, the depth profiles of all specimens, even of the stress-relieved one, are more or less flat beyond the surface peak (see Figure 8.2d). The surface maximum itself is of the same order of magnitude as for the lower implantation temperatures, i.e., the concentration in this thin layer is still several 10^{-2}. For the stress-relieved material a shallow minimum followed by a slight increase of the concentration towards larger depths can be seen. This could be interpreted as a low, broad secondary maximum whose spatial extension cannot be fully probed by NRA, but with the available data this cannot be said with certainty. Looking at Figure 8.1 you can see that the bulk concentrations and, accordingly, the total inventories are again lower than at 450 K, both for the NRA and the TDS measurement. The amount of deuterium detected by TDS is now for all specimens much larger than the amount within the detection range of NRA. Again, the total retention shows the same dependence on the microstructure as for the other implantation temperatures.

8.1.5. Implantation at 750 K

The implantation temperature of 750 K is beyond the main desorption maximum that has been previously observed for a similar material [66], respectively for the lower implantation temperatures. Because of this, the total retained amount of deuterium is very low for all specimens. In fact, it is just barely detectable by NRA. Only the surface concentration peak, which has now reduced by about one order of magnitude to $\approx 10^{-3}$, is still discernible and about the same for all specimens. Beyond that, the concentration is too low to be detected within reasonable measurement times. However, TDS still shows a small, broad but nevertheless well-discernible desorption peak starting roughly at the implantation temperature. At lower temperatures the desorption is — not surprisingly — practically zero. The total retained amount measured by TDS is significantly larger than the amount contained within the surface maximum, and shows the same systematic variation with the microstructure as for the other temperatures. This means that the deuterium has probably permeated through the whole thickness of the specimens. Accordingly, the concentration is very small throughout, but sums up to a well-measurable total amount.
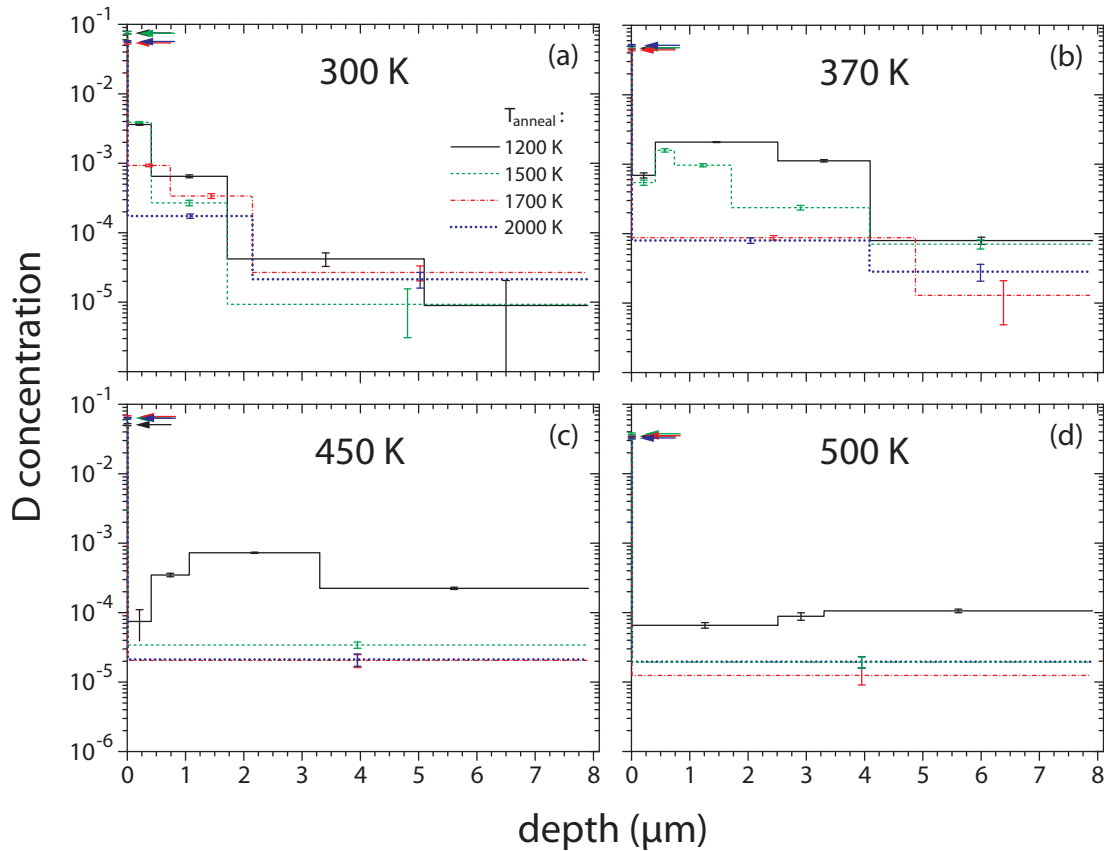
Figure 8.2. Deuterium depth profiles in tungsten specimens pre-annealed at various temperatures after plasma exposure at 38 eV/D to a fluence of 6×10^{24} D m^{-2}. The temperatures during exposure were (a) 300, (b) 370, (c) 450 and (d) 500 K. At 750 K only a D concentration of $\approx 10^{-3}$ in the surface layer could be measured, but apart from that the concentration was too small for depth profiling. Tungsten specimens of the same type are represented by the same line style in each panel. Arrows indicate the D concentration at the surface. The maximum ^{3}He beam energy for this analysis was 4500 keV, which allows to probe a depth up to 8 μm.

8.1.6. Effect of the implantation temperature on blistering

The size and density of blisters vary just about as strongly with the implantation temperature as the retained deuterium inventory, and also show a strong dependence on the microstructure that goes in the same direction: Blisters appear at all implantation temperatures between 300 and 500 K on the surface of the stress-relieved material. On the partially recrystallised material, some small, sporadic blisters can be found in surface regions without grain boundary grooving at temperatures of 300 and 370 K, while the fully recrystallised material does not show any blisters at any temperature. The blisters on the stress-relieved material

often have nearly circular and sometimes elliptic outlines and a rounded dome. At temperatures above 300 K, elliptical or even irregular shapes become slightly more common. This is most likely due to overlapping and/or coalescence of neighboring blisters. This domed type of blisters with diameters between 1 and up to over 100 μm is regularly found on hot-rolled tungsten irradiated with hydrogen isotope ions [1, 50, 79, 110], while the exact shape, size and density varies considerably depending on the exact experiment conditions. Additionally, occasional small, flat, angular shapes can be found at 370 and 450 K. These are discussed in more detail in section 8.3.3. While they are much scarcer than the round type, they can usually be found when a sufficiently large area is searched.

Figure 8.3 shows images of blisters on stress-relieved tungsten acquired by optical DIC microscopy for implantation temperatures between 300 and 500 K. An image of the specimen implanted at 750 K is not shown because no blisters were found on this specimen. Alimov *et al.* also reported that blistering can be suppressed at temperatures above $\approx 700\ K$ [1]. The reason is probably that at such high temperatures, the deuterium concentration is already very low, and the diffusivity is very high. Accordingly, local accumulations of deuterium that are sufficient to initiate blistering — whether by supersaturation stress or by precipitation of D_2 — are no longer possible. "T"-shaped markers were applied by FIB to the surface of all specimens to compare the same area before and after implantation as well as after TDS. All images have the same magnification. One can clearly see that the blisters increase in size for increasing temperatures, but their density and surface coverage decreases. At 500 K the blister density is already so low that no blisters were found in the same area around the markers as for the other temperatures, so a different spot is shown instead for this temperature.

The marked areas were investigated again after TDS. Figure 8.4 shows the same areas as in Figure 8.3 for comparison. Please note that contrast changes due to different illumination and DIC prism settings are generally very difficult to avoid.

Most blisters on the specimen implanted at 300 K vanished during TDS (as already published [66]). Mainly blisters with a strong bright-dark contrast, i.e., those with steep flanks and accordingly a strong deformation of the material in the cap, remained recognisable (Figure 8.3a).

For the material loaded with D at 370 K, things are different: Now a large fraction of the blisters were still visible after TDS (Figure 8.3b). For this specific specimen also a 3D analysis using a confocal optical microscope could be performed directly
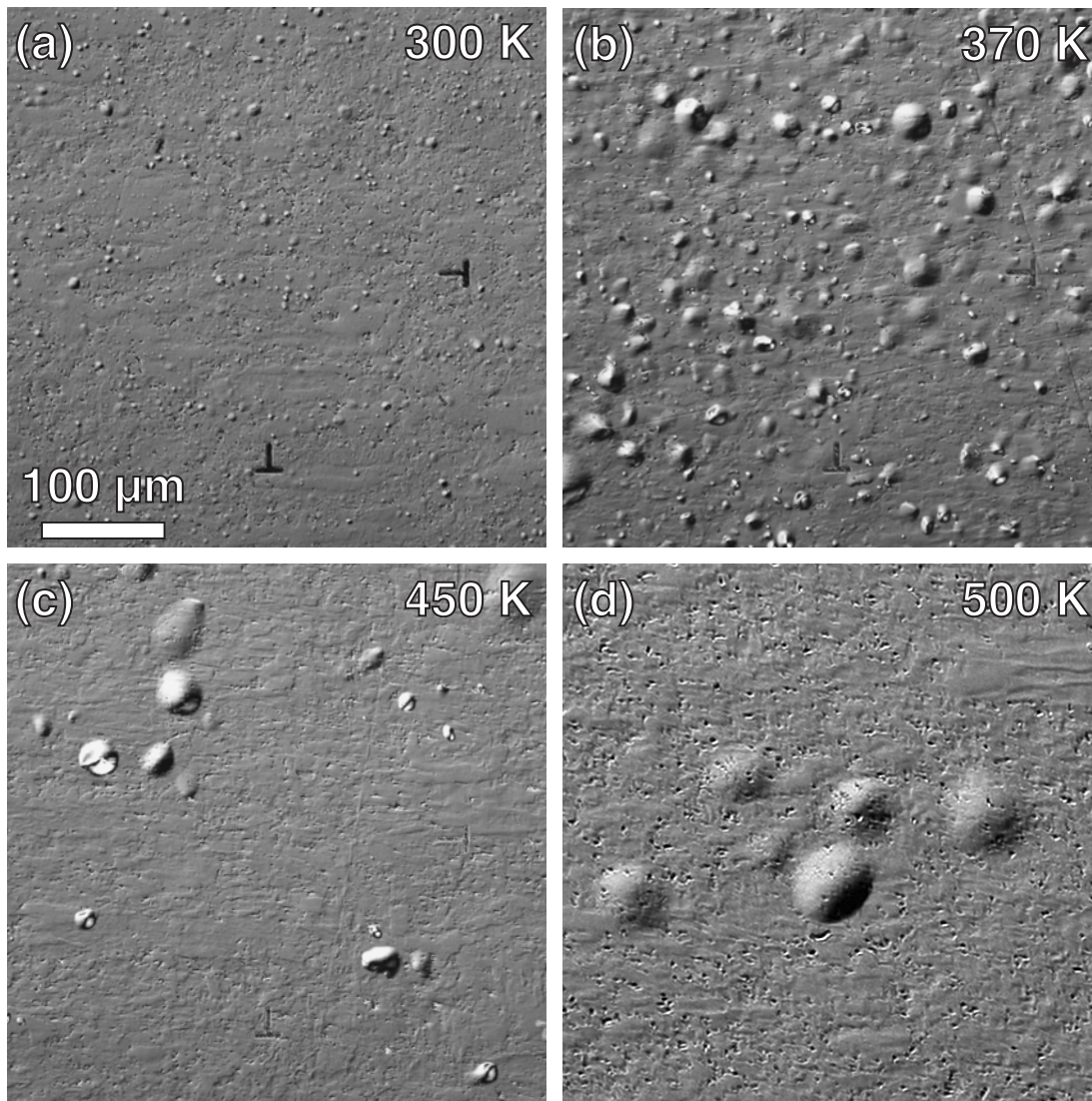
Figure 8.3. Optical DIC micrographs of blisters on stress-relieved tungsten *before* TDS on stress-relieved tungsten for various temperatures during implantation at 38 eV/D to a fluence of 6×10^{24} D m^{-2}: (a) 300, (b) 370, (c) 450 and (d) 500 K. At 750 K, the surface remained unchanged apart from a small amount of sputtering due to plasma impurities. "T"-shaped markers were used to compare the same area before and after implantation and after TDS.
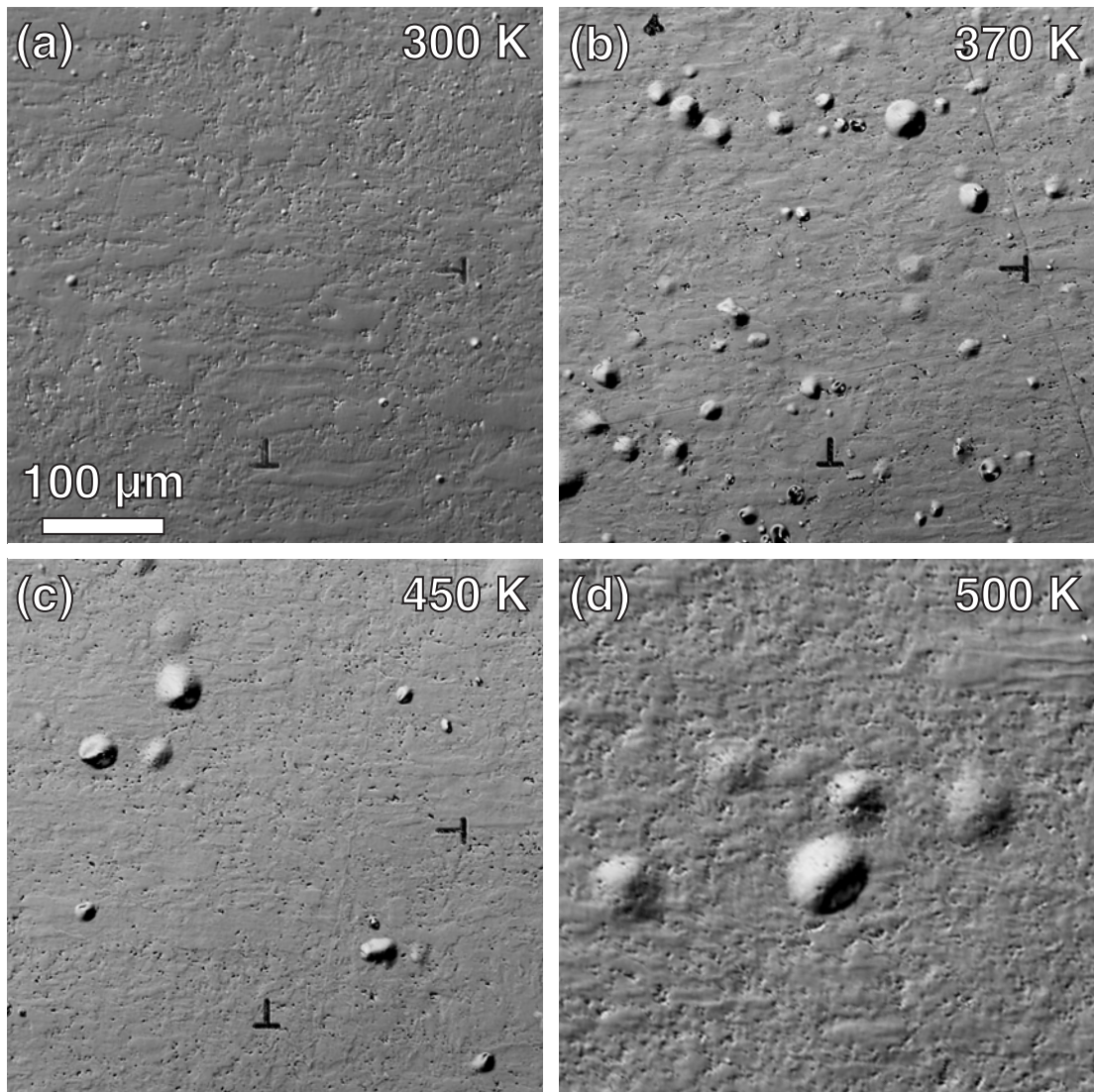
Figure 8.4. Optical DIC micrographs of blisters on stress-relieved tungsten *after* TDS up to 1200 K for various temperatures during implantation at 38 eV/D to a fluence of 6×10^{24} D m^{-2}: (a) 300, (b) 370, (c) 450 and (d) 500 K. The micrographs shown here depict the same areas as those in Figure 8.3.

before and after TDS. This showed that still a significant number of blisters, particularly those with a small bulge height, deflated like the blisters created at 300 K. This could also be clearly seen by comparing the DIC images. Others deflated only partially or barely changed their appearance at all. The fraction of this group of blisters was much larger than for implantation at 300 K. One blister within the investigated surface area even grew in size during TDS due to the thermal expansion of the contained D_2 gas.

It is likely that all blisters that collapsed at least partially were emptied at an early stage of the TDS, either by permeation of D through thin caps or by rupturing. Blisters that do not show any discernible change during TDS might have been emptied already during the plasma exposure. A likely mechanism for this is that the blisters can grow to a size where their cavity intersects with a crack connected with the surface, respectively that the expanding cavity itself follows a grain boundary that leads to the surface. The blister that increased in size held its D_2 inventory until a high temperature of the TDS ramp. After the TDS ramp is completed, however, all blisters can be considered to be empty since neither NRA nor a second TDS analysis reveal any further deuterium in the specimen.

For the higher implantation temperatures, the blisters change their appearance less and less during TDS (see panels (c) and (d) in Figure 8.3). Only very few blisters vanish more or less completely, and some more appear to have undergone a rather strong partial relaxation. In any case, most blisters are unambiguously recognisable in the DIC images acquired before and after TDS. They can therefore be considered to be mostly plastic deformations. For the specimen implanted at 500 K, there were not enough blisters around the "T" markers for a reasonable analysis, but due to the low overall density of blisters it was relatively easy to find a particular group of blisters again after TDS. Most blisters in this group had barely changed at all. One particularly flat blister appears to have vanished, another one is still just barely visible. Overall, it can be said that the fraction of mostly plastically deformed blisters increases significantly for higher specimen temperatures during plasma exposure.

For the specimens exposed to a deuterium plasma at 300 and 370 K, cross-section cuts were prepared *in situ* by FIB and imaged by SEM in the HELIOS NanoLab 600 dual-beam microscope. The caps of some blisters were also punctured by FIB before cross-sectioning in order to observe the relaxation of the blisters. The relaxation was typically complete for the blisters on the specimen exposed at 300 K, and often only partial for 370 K. Figure 8.5 shows one example of a cross-section

through a blister created by D implantation at each of these two temperatures. In both cases the cavity is a crack system following grain boundaries running parallel to the surface. For 300 K, the crack system is typically located about 1 μm beneath the surface, as already reported in [66]. However, the crack does not necessarily appear at the *first* grain boundary below the surface.

For 370 K, the blister cavities are often located much deeper at depths up to about 4 μm. In these cases, there are several layers of grains between the cavity and the free surface. Nevertheless, some blister cavities also come very close to the surface at some points. Generally, the geometry of the cavities is complex: at grain boundary junctions, it can follow either the grain boundary leading closer to the surface or deeper into the bulk, and in some cases it also branches to follow both. In many cases, the cavity tends to propagate towards the surface near the perimeter of the blister and in some cases is also found to intersect with it. In fact, DIC images also occasionally reveal fine cracks following the circumference of the blister. Cracks at the apex of the blister are only rarely found and not clearly identifiable. Apparently the preferred mode for the rupturing of a blister is not bursting of the cap, but the eventual intersection of the cavity with the free surface at the rim of the blister. It can also be seen from the cross-section images that blisters do indeed overlap, i.e., there can be multiple cavities within the projected area of a larger blister. These cavities are located at different depths below the surface and often do not intersect with each other, although coalescence is occasionally also found. One can conclude that the irregular blister shapes found in DIC micrographs often are such overlapping structures, and that small blisters in particular often "stack" upon larger ones. It is therefore usually correct to treat these blisters as individual objects in a statistical analysis.

The typical location of the blister cavities found in cross-sections coincides rather well with the secondary D concentration maximum found by NRA depth profiling. On the other hand, it could recently be shown by the analysis of individual blister bursts visible in TDS experiments at slow heating rates that the amount of deuterium stored as D_2 gas inside blisters is only a few percent of the total retained amount [67]. This small fraction cannot by itself explain the secondary concentration maximum observed by NRA.

To clarify if the observed D_2 bursts indeed represent all (or at least most) of the blisters, a stress-relieved specimen that had been implanted with 38 eV/D up to 3×10^{24} D m^{-2} at 300 K [66] was investigated again. As it is typical for a specimen loaded with deuterium under these conditions, most of the blisters vanished

completely during degassing in a TDS experiment up to a temperature of 1200 K. This specimen was implanted again up to 6×10^{24} D m^{-2} at the same ion energy and temperature. The blisters on the specimen were subsequently re-analysed by optical DIC microscopy. The result was that blisters that disappeared during TDS did not reappear after the second plasma exposure. One must therefore assume that the emptying of the blisters is *irreversible*, most probably because the cavity is open to the surface after TDS. Furthermore, TDS one day after the implantation yielded the same deuterium inventory in the re-implanted specimen and in a fresh specimen that had been implanted at the same time. The shapes of both release spectra also matched. Since the number of blisters on the re-implanted specimen was much smaller than on the fresh one, this means that the D$_2$ gas stored in the cavities indeed does not contribute significantly to the total D inventory. Consequently, the observed D$_2$ release from blister bursts can be considered to represent at least the majority of the D$_2$ gas stored in blisters.

The interplay between blisters and deuterium retention, on the other hand, must be dominated by other effects than the D$_2$ gas contained in the blisters themselves, as opposed to the suggestion of Causey *et al.* [16]. A likely mechanism is that the fracturing of the material due to expansion of the blister cavities causes the emission of dislocations. This is supported by the crack-tip plasticity for tungsten single crystals, which was observed, e.g., by Gumbsch *et al.* [35]. Crack-tip plasticity means that dislocations are emitted in the concentrated stress field at the crack tip and then move away from it. It should be noted, however, that the situation discussed here is cracking along a grain boundary, i.e., a somewhat different case. Still, finite element continuum mechanical simulations of blisters like those described here point towards stresses far beyond the yield strength of tungsten [9], which should lead to the emission of dislocations. These "dislocation halos" created due to blister growth, in turn, trap the majority of the deuterium in the blister region and remain in the specimen even after the blister cavities are opened and the D$_2$ gas released. This theory will be discussed further in the following sections.

Automatic detection of blisters such those as shown in Figure 8.3 is not trivial. Brightness threshold filters fail due to the bipolar intensity distribution that is typical for DIC and makes the blisters so easy to discern by eye. Edge filters also suffer from this and have additional problems due to image noise and due to contrast variations originating from surface roughness. This roughness is due to the polishing and also to sputtering during the implantation.
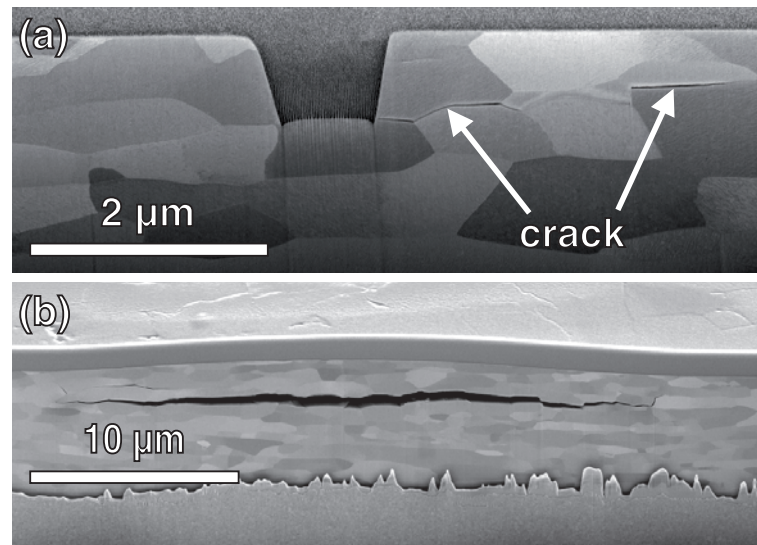
Figure 8.5. SEM images of cross-sections prepared by FIB of blisters due to plasma exposure at 38 ev/D to a fluence of 6×10^{24} D m^{-2}. (a) shows a blister created at 300 K that collapsed as soon as the cap was punctured by FIB. Only a fine crack system remains. The central crater is where the cap was perforated. (b) shows the cavity of a significantly larger blister created at 370 K that relaxed only partially upon perforation. In both images the specimen is tilted by 52° and the surface is protected by an amorphous Pt:C layer. The structure in the lower half of (b) is an artifact of the FIB preparation.

For implantation at 300 K, where the vast majority of the blisters have a circular outline and very similar brightness distribution, a more sophisticated automatic detection mechanism was tried: The bipolar brightness distribution with its fixed orientation was exploited to calculate a quantity analogous to a dipole moment (i.e, the strength of the bright-dark contrast). Using that, a disk radius and centre position could be derived that described the size and location of the blisters rather well. Unfortunately this method is not applicable anymore for the higher implantation temperatures. One thing is the increasing amount of (at least nearly) overlapping or coalescing blisters. Probably even more problematic is the occurrence of a significant number of blisters with steep flanks: These show interference fringes in the DIC image save for high magnifications — where in turn the image area is not statistically relevant anymore. It might be that sophisticated shape recognition algorithms such as those used for face detection and recognition could be modified and trained to detect blisters, but currently there is no expertise in applying these programs to blister analysis.

In order to gain some statistical information on blistering at various temperatures,

the blisters were therefore marked by hand in some selected images. In order
to keep the necessary amount of time tolerable, blisters were represented by a
straight line following the largest lateral extension of the blister (i.e., the diameter
for circular and the longer half-axis for elliptical outlines). The lengths of these
lines were taken as measures for the blister size. Approximate blister areas were
calculated assuming only circular shapes. Therefore the derived values for the
average size and the surface coverage must be considered as upper limits for the
actual values. On the other hand, this marking method has the advantage that
blisters whose outlines touch, or small blisters sitting on top of larger ones, can
still be easily separated. Accordingly, "pile-up" effects leading to a statistical
over-representation of very large blisters are reduced.

Figure 8.6 shows the results of the statistical evaluation described above. The
number of blisters per area is huge at about 4.7×10^4 mm^{-2} for 300 K — to a large
extent due to many very small blisters — and decays approximately exponentially
for higher temperatures, until at 500 K the areal density is down to a few dozen of
blisters on the entire specimen surface. For comparison, Ueda *et al.* [110] found a
blister density of 450 mm^{-2} for pure tungsten irradiated by a hydrogen plasma at
653 K and a bias voltage of 1 kV. At the same time, the average size of the blisters
increases strongly, from less than 2 μm at 300 to over 40 μm at 500 K, with some
blisters reaching over 100 μm. Reports of blisters with comparable sizes as well as
of the increase of their size with temperature can also be found in literature (see,
e.g., [1, 50]). The surface coverage is already quite high at over 15% for 300 K and
reaches a maximum of about 27% for 370 K. For higher temperatures it reduces
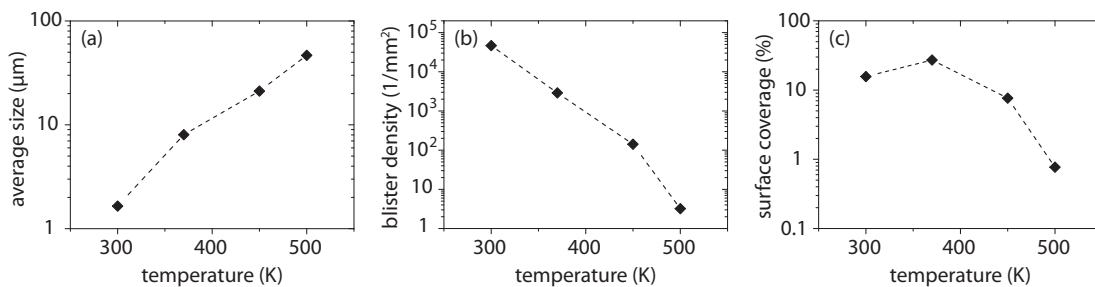down to less than 1% at 500 K.

Figure 8.6. Statistical evaluation of blister parameters after plasma exposure at 38 eV/D to a
fluence of 6×10^{24} D m^{-2} for temperatures between 300 and 500 K. For 750 K no
blisters occurred. (a) shows the average size of blisters, (b) displays the number
density and (c) the surface coverage.

Figure 8.7 shows an Arrhenius plot of the average blister size versus the inverse

temperature. There is no data point for 750 K (corresponding to 1.33 on the $1000/T$-axis) because no blisters were found at this temperature anymore. As one can see, the dependence of the average size on the temperature can be very well described by an Arrhenius law, i.e., a function proportional to $\exp\left[-\frac{E_A}{k_B T}\right]$ (E_A: activation energy, T: temperature) within the range of temperatures where blisters were observed. This points towards blister growth being a thermally activated process. Considering that the blister cavities are typically located far beyond the stopping range of the implanted ions and can only be reached by deuterium by means of diffusion (which is also thermally activated), this appears reasonable. The activation energy E_A resulting from a fit of the data points is 0.21 ± 0.01 eV. This is lower than Frauenfelder's activation energy for interstitial diffusion of hydrogen in tungsten of 0.39 ± 0.09 eV, but coincides with the lowest published value of 0.21 eV by Heinola *et al.* [40]. This suggests that the growth of blisters is to a large extent governed by diffusion of deuterium to the cavities. Still, other temperature-dependent processes probably also play a role. For example, the softening of tungsten as it approaches the ductile-to-brittle transition temperature (BDTT) could promote the growth of blisters as well. For single crystalline tungsten, values of the BDTT as low as 370–470 K were reported [35]. The lower purity and high dislocation density of the specimens discussed here will most probably lead to a somewhat higher BDTT, but even then a gradual softening within the temperature range discussed here is likely.

8.1.7. Summary of effects related to the specimen temperature

The deuterium retention in the investigated tungsten specimens of different microstructures (see chapter 6) was observed to depend strongly on the temperature during D plasma exposure. Considering that the behaviour of hydrogen isotopes in tungsten is assumed to depend predominantly on thermally activated processes, i.e., diffusion and (de)trapping of dissolved atoms at defects, this appears reasonable. The present study does not only show the detailed evolution of the deuterium depth distribution with temperature, but also shows its connection to the defect structure. At room temperature (≈ 300 K), the uptake of deuterium is predominantly affected by the (yet) slow diffusion. The depth profiles for all microstructures are qualitatively similar, and the deuterium does not diffuse beyond the range of ≈ 8 μm that is accessible by NRA (with a maximum incident ^{3}He beam energy of 4500 keV) in significant amounts. The total retention is no-
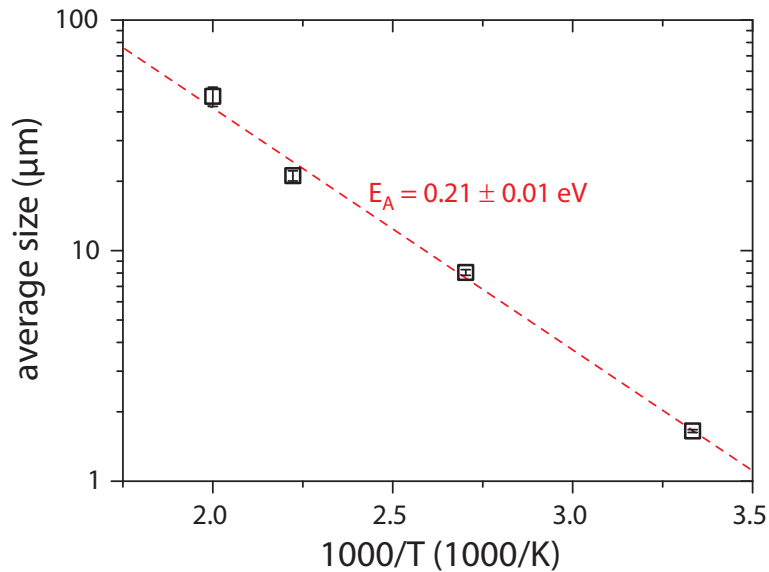
Figure 8.7. Arrhenius plot of the average blister size versus the inverse temperature. The data
can be well described by an Arrhenius law, i.e., by thermally activated behaviour.
There is no data point for 750 K ($\hat{=}1.33$ on the $1000/T$-axis) since no blisters were
observed at this temperature.

ticeably smaller for recrystallised materials with a low dislocation density, as it
can be seen in Figure 8.1. Blisters are only observed for stress-relieved specimens.
They are numerous, but relatively small.

Looking back at Figure 8.1, 370 K appears to be the temperature where most deu-
terium is retained after implantation under the conditions applied here (38 eV/D,
6×10^{24} D m^{-2} at 10^{20} D m^{-2}s^{-1}; see also section 4.1): Diffusion into the bulk
of the specimens is already strong, but not yet outweighed by losses through the
surface. For all types of specimen, the total retention observed by TDS displays
a maximum, which is most distinct for the stress-relieved material. The D depth
profiles measured by NRA show a clear secondary maximum for stress-relieved
and partially recrystallised tungsten, but become flat for fully recrystallised tung-
sten.

A significant amount of deuterium has already diffused beyond the detection range
of NRA and is only accessible by TDS. The secondary D concentration maxi-
mum observed for stress-relieved and partially recrystallised tungsten appears to
be connected to blistering. The blistering activity is maximal for stress-relieved
specimens, and weak but at least detectable for partially recrystallised material.
The typical location of blister cavities coincides with the secondary concentration
maximum, although the amount trapped in gaseous form (see [67]) is not sufficient

to explain the observed maximum. The cavities always form at grain boundaries parallel to the specimen surface. This could be due to some grain boundaries acting as trapping centres respectively diffusion barriers, which lead to a local pile-up and subsequent precipitation of deuterium. Particularly the comparison of stress-relieved and partially recrystallised tungsten — which both have similar average grain sizes — gives some indication of *small-angle* grain boundaries being likely blister nucleation points. They are abundant for stress-relieved material, which shows strong blistering. During partial recrystallisation they are partially replaced by *large-angle* boundaries (see also chapter 6). This coincides with a significantly lower blistering activity, in particular on surface areas that show signs of recrystallisation (i.e, grain boundary grooving).

For higher temperatures of 450 and 500 K diffusion into the bulk of all specimens is very strong: The depth profiles become increasingly flatter, and the amount of D retained beyond the range of NRA starts to dominate. At the same time, desorption losses increase even more strongly with temperature. This leads to a reduction the total retained amount of deuterium with increasing temperature for high implantation temperatures (see Figure 8.1). As before, it is highest for the stress-relieved material, followed by the partially recrystallised one and finally both fully recrystallised materials, which show nearly identical retention. Blisters are only observed for stress-relieved material. They become larger, but also less numerous, and the surface coverage reduces significantly with higher temperature. Overall, the average blister size was found to correlate to the temperature according to an Arrhenius law with an activation energy that is comparable to that for interstitial diffusion. This points towards diffusion of deuterium to the blister cavities being a key factor in blister growth, but other effects like softening of the tungsten probably also play a role.

For 750 K, the deuterium is distributed throughout the specimen at a local concentration that is too low to be detected by NRA within reasonable acquisition times, apart from a small amount very close to the surface. TDS, however, still shows a small but well-measurable amount of deuterium, which is released from the specimens predominantly at high temperatures. This is the reason why in Figure 8.1 the total amount measured by NRA is orders of magnitude lower than the amount measured by TDS. The dependence on the microstructure is similar as for lower temperatures. This consistent behaviour suggests that dislocations are more important for the retention of deuterium than grain boundaries: The fully recrystallised specimens have significantly different grains sizes, but similar

dislocation densities and also similar deuterium inventories. Blisters are not observed on any material for this high temperature. This can be attributed to the overall low deuterium concentration as well as to the deuterium being able to effortlessly cross any diffusion barriers where blisters might otherwise nucleate.

8.2. Fluence dependence

8.2.1. Evolution of the deuterium inventory

Contrary to the simplest possible assumption of ideal diffusion-limited retention (see section 7.2), the deuterium inventory after plasma exposure at 38 eV/D and 370 K does *not* vary with the incident fluence Φ according to a $\Phi^{1/2}$ power law, as Figure 8.8 shows. At high fluences, the increase of the deuterium retention is considerably flatter than $\Phi^{1/2}$ and more or less saturates, while at very low fluences, the curve is *steeper*. From this one can already conclude that the uptake of deuterium is governed by more complex processes than simply diffusion to time-independent trap sites.

Nevertheless, the dependence of the retention on the microstructure is very clear: regardless of the fluence, the stress-relieved material retains the most deuterium, followed by the partially recrystallised one. Both fully recrystallised materials have a nearly identical retention that is considerably lower than for stress-relieved tungsten. This gives further credit to the assumption made in section 8.1 that the dislocation density has the strongest influence on the deuterium retention, while the grain size plays a minor role.

The total amount of deuterium released from stress-relieved specimens during TDS in the TESS set-up is significantly flatter than a power law with an exponent of 1/2 at high fluences (see Figure 8.9), similar to the NRA results.

At low fluences, the steep increase of the retention with the fluence that was found by NRA is also clearly visible. The error bars in this graph are to be understood in the way described in section 4.3. The data point at 6×10^{24} D m^{-2} appears significantly higher than the surrounding ones. This would mean that the retention actually *reduces* towards very high fluences, which is considered rather unlikely. Looking at the release spectrum from the specimen corresponding to this data point, a significantly larger high-temperature shoulder than for all specimens from the fluence variation campaign is visible. At this point, it cannot be said
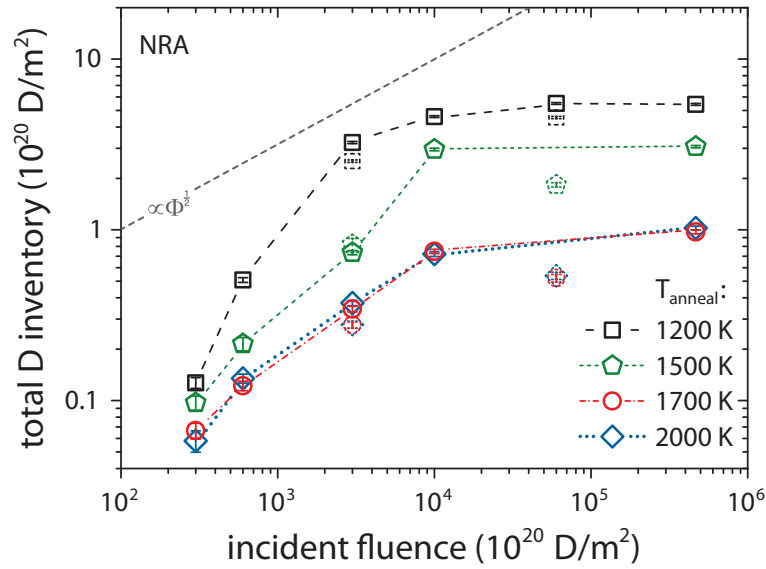
Figure 8.8. Variation of the deuterium retention in tungsten of different microstructures with the incident fluence Φ for plasma exposure at 38 eV and 370 K. The dashed grey line represents ideal diffusion limited ($\propto \Phi^{1/2}$) retention. Dotted symbols not connected by lines show the effect of a slower cool-down after implantation.
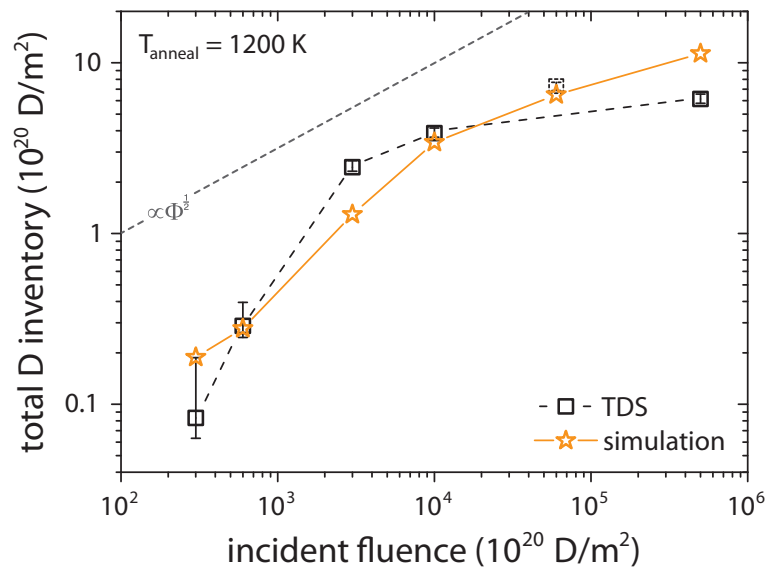

Figure 8.9. Variation of the total amount of deuterium released from stress-relieved specimens during TDS with the incident fluence Φ at 38 eV/D and 370 K. The data point with the dotted outline was acquired in a different experimental campaign. For comparison, the total deuterium inventory resulting from diffusion-trapping simulations is also shown. The simulation results have been downscaled to 2/3 to account for losses during storage of the specimens.

definitely if *this* data point is the exception: It was acquired in the course of the "Ramp-and-Hold" experiments (see section 7.6) and was well in agreement with other measurements taken during that measurement campaign. Therefore it must be for now assumed that the observed deviation shows the limits of reproducibility between experimental campaigns. The reproducibility within a *single* campaign is significantly better, however. The total amounts of D_2 released from identical specimens implanted all under the same reference conditions (ion energy: 38 eV/D, fluence: 6×10^{24} D m^{-2}, temperature: 370 K) in the "Ramp-and-Hold" experiments (section 7.6) showed a standard deviation of only $\pm 5.1\%$ (which is included in the error bars in Figure 8.9).

The only way to explain the steep increase of the retention at the lowest fluences discussed here (corresponding to several minutes of plasma exposure) is the creation of additional traps during plasma exposure. One such type of trap is connected with the concentration peak that is observed at the surface of the specimens (see also section 8.1). As it will be explained in more detail in section 8.3, it is due to the amorphisation (and possibly also doping) of the implantation zone by plasma impurities — mainly nitrogen- and oxygen-containing molecular ions. For all investigated microstructures, the surface peak shows a very similar dependence on the fluence (see Figure 8.10). In fact, its magnitude is practically independent of the microstructure of the material before plasma exposure. The magnitude $R_{surface}$ of this peak grows quickly at low fluences and then saturates: It can be reasonably well approximated by a simple exponential saturation law:

$$R_{surface} = A \cdot \left[1 - exp(-\Phi/\tilde{\Phi}) \right]. \tag{8.1}$$

A is the saturation value of the inventory in the surface layer. A fit of the data in Figure 8.10 yields $\tilde{\Phi} \approx 8 \times 10^{23}$ D m^{-2}.

A second mechanism for the production of traps is the growth of blisters. If one looks carefully at Figure 8.8 again, one notices that for the stress-relieved material the initial increase of the deuterium retention with the fluence is even a bit steeper than for the other materials. As it was already mentioned in section 8.1.6, blister growth most likely leads to the production of additional dislocations in the vicinity of the blister cavities. These "dislocation halos" are believed to be the reason for the enhanced retention in the depth region where the blisters occur. In fact, the secondary concentration peak, which was already associated with the blisters in the previous section, becomes higher and broader with increasing fluence, as it

can be seen from the depth profiles in Figure 8.11. The position of the maximum also moves towards larger depths. This can be interpreted as the result of the blistering zone extending over a larger depth range.

The observed saturation of the total deuterium retention at high fluence was also reported before, e.g., by Haasz *et al.* [37]. It could, in theory, have several reasons: Firstly, all traps in the specimen could be filled at sufficiently high fluences. Secondly, a diffusion barrier could present at a certain depth. Ogorodnikova *et al.* [82] introduced a fluence-dependent diffusion coefficient due to stress fields caused by the ion implantation in order to describe saturation effects. The first option can be ruled out because even when the diffusivity is calculated using the Frauenfelder values [27], which certainly overestimates the diffusion at low temperatures, the time necessary for permeation of a 0.8 mm thick specimen at 370 K would take nearly 90 hours, while the actual implantation only took 18.5 hours. Using the values published by Franzen *et al.* [26], which were determined for temperatures comparable to the implantation temperature used here, permeation would even take about 3000 hours. In any case, the deuterium cannot have permeated all the way to the rear side of the specimen. Accordingly, the specimen cannot be *fully* saturated. The limited range accessible by NRA (≈ 8 μm for 4500 keV ^{3}He), however, is indeed more or less saturated at high fluences: between a fluence of 6×10^{24} and 5×10^{25} D m^{-2}, the depth profile barely changes (see Figure 8.11), and the total retention is the same within the error margins (Figure 8.8). Even if the ^{3}He beam energy is increased to 6000 keV to extend the depth range to ≈ 12 μm, no significant difference between the depth profiles at 6×10^{24} and 5×10^{25} D m^{-2} is visible. On the other hand, the total D retention determined by TDS also exhibits a trend at high fluences that is significantly flatter than a $\Phi^{1/2}$ power law (Figure 8.9). The fact that the slow uptake of deuterium is not only observed by NRA but also by TDS shows that this is not only an artifact of the limited observation depth of NRA. This only leaves the reduction of diffusivity — either by an already existing diffusion barrier, or by a stress field [82] — as a possible explanation.

Figure 8.9 also contains the fluence dependence of the total deuterium retention in a stress-relieved specimen obtained from diffusion-trapping simulations as described in section 3.3. To account for deuterium losses during storage (see section 8.5.2), the simulation results were downscaled to two thirds. Both the steep increase of retention at the low fluences as well the slower uptake than a $\Phi^{1/2}$ power law at high fluences is — at least qualitatively — captured by the model,
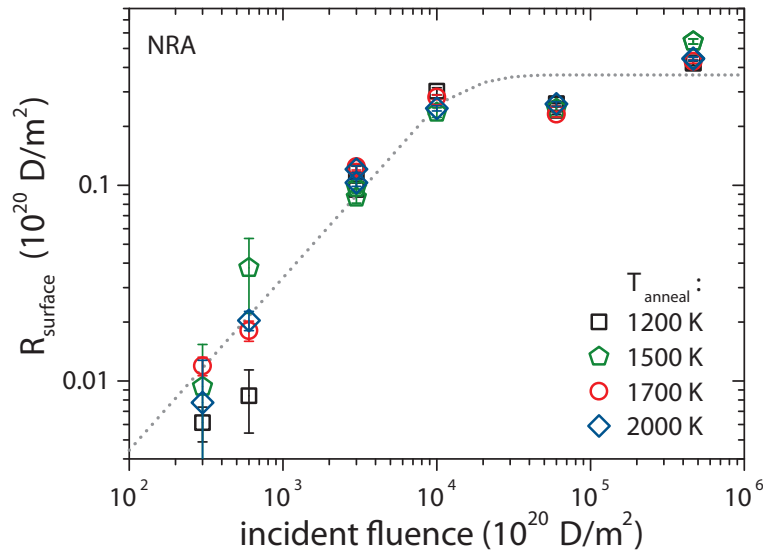
Figure 8.10. Variation of the deuterium retention $R_{surface}$ at the implanted surface with the incident fluence Φ for plasma exposure at 38 eV/D and 370 K. The magnitude of this surface peak is independent from the initial tungsten microstructure. It grows with the fluence according to an exponential saturation law (dotted line).
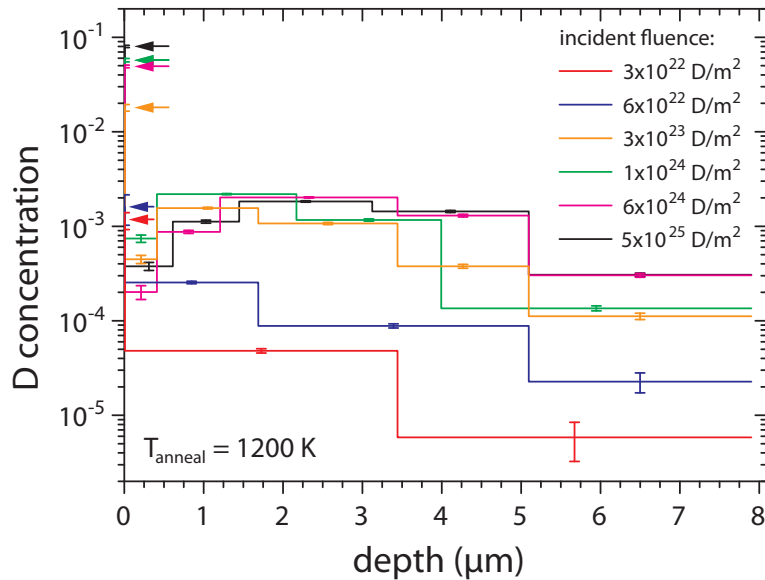

Figure 8.11. Evolution of the deuterium depth distribution in stress-relieved tungsten with the incident fluence at a constant ion energy of 38 eV/D and a temperature of 370 K. Arrows indicate the deuterium concentration at the surface.

which includes evolution of the trap density at the surface as well as in the blister region. The absolute values of the retention are also reasonably well reproduced. The model is primarily adapted to reproduce the deuterium depth profiles, release temperature and retention at higher fluences. It should be mentioned that trap evolution at very low fluences could only be extrapolated because of the comparatively poor depth profile resolution for very small deuterium inventories.

The simulated dependence of the retention on the fluence shows that a local increase in trap density over a depth of several microns can indeed qualitatively explain the observed retention curve. In contrast, simulations with *flat* concentration profiles show the expected $\Phi^{1/2}$ dependence of the retention. Simulations with a trap profile resembling the observed one at high fluence, but *without* trap evolution, show a similar slower uptake of deuterium at high fluence as with evolving traps, but exhibit a "normal" $\Phi^{1/2}$ behaviour for low fluences. Therefore, only a model including *evolving* traps can describe the experimentally observed behaviour. Still, dynamic effects of the ion implantation (i.e., stress fields) such as proposed by Ogorodnikova *et al.* [82] might produce a synergistic effect. Further studies on stress fields during deuterium implantation and their effect on the deuterium uptake would be desirable. Their results should then also be included in future simulations.

8.2.2. Evolution of thermal deuterium release with the fluence

The stress-relieved tungsten specimens implanted at different fluences were degassed at a heating rate of 3 K/min in the TESS set-up (see section 4.3) in order to investigate deep diffusion at high fluences and to provide a broader data base for the interpretation of the "Ramp-and-Hold" measurements described in section 7.6). The slow heating rate was chosen for two main reasons: First, the temperature increase of the tungsten specimens is nearly linear under these conditions. This makes the interpretation of TDS spectra — which are furthermore expected to be strongly influenced by a depth distribution varying with the fluence — easier. Second, D_2 bursts due to rupturing blisters are best visible at a slow heating rate.

All the specimens whose release spectra are displayed in Figure 8.12 were loaded at once into TESS to reduce reproducibility problems due to changing of the glass tube (see section 8.2.1. As it can be seen, the main desorption peak at ≈ 600 K not only grows in magnitude, but also broadens and shifts towards higher tempera-

tures with increasing fluence. This can be mainly attributed to diffusion: The peak shift can be interpreted as the centre of weight of the deuterium depth distribution being located deeper in the specimen. Diffusion-trapping simulations confirm this. The broadening is, accordingly, due to the deuterium being distributed over a larger depth range. At intermediate fluences, a minor release peak at a lower temperature than the main peak is clearly visible. This peak is obscured at high fluences due to the broadening of the main peak. The nature of this peak is not completely clear since this region is not accurately reproduced by the diffusion-trapping model introduced in section 3.3. The reason is that the binding energy distribution in a real specimen is more complex than in the simulations. Spatially extended traps like dislocation networks or grain boundaries that provide "shortcuts" for desorption could also play a role.

In the high temperature part of the spectrum — i.e., between the main desorption peak and the maximum temperature of about 1200 K — a broad, flat shoulder extending nearly to the highest temperatures is visible. This shoulder also becomes more pronounced at higher fluence. Simulations show that this shoulder is made up from two contributions: One is the release of deuterium from point defects with a high binding energy that are created at the irradiated surface as discussed in the previous section. The second contribution comes from deuterium not being released from the implanted surface, but diffusing all the way through the specimen and leaving from the *rear* surface. Both contributions are expected to increase with fluence: As shown in Figure 8.10, the amount of deuterium retained at the surface increases with fluence, up to a certain saturation value. At high fluences, the deuterium has also reached larger depths and is therefore closer to the rear side, which increases the fraction of deuterium leaving the sample on that route.

Mainly in the low-temperature part of the release spectrum — i.e., from 300 K up to the release maximum — sharp bursts of D_2 release are visible. They are the result of pressurised D_2 gas being released from rupturing blisters, as it could recently be shown [67]. The bursts increase in magnitude and frequency towards higher fluences. This is in accordance with the development of blister size and abundance, which will be discussed in detail in the following section. The sporadic bursts visible at high temperatures are also due to rupturing blisters, albeit not from the specimen being currently investigated: The specimens in the storage position also heated up slightly towards the end of the temperature ramp. This leads to the release of a small amount of deuterium from these specimens as well as

to the rupturing of some blisters. As it was discovered during the experiments in TESS, some blisters are extremely sensitive to any disturbance of the specimen, and occasionally even rupture when a specimen is moved to the measurement position.
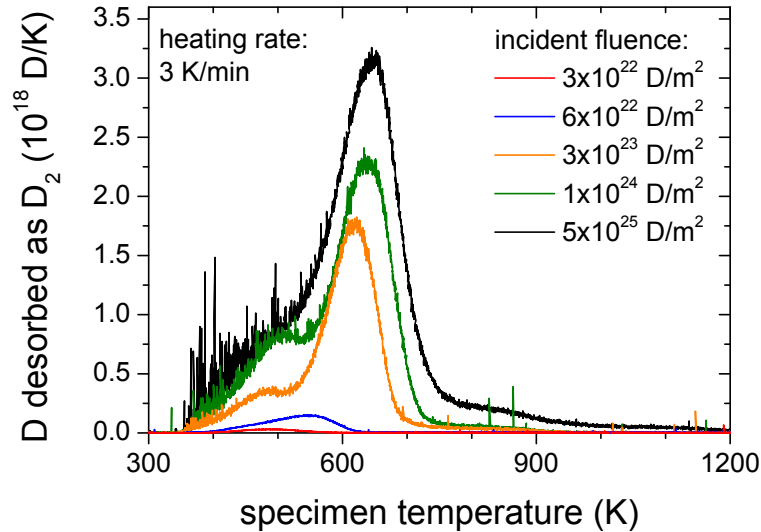
Figure 8.12. Evolution of the D_2 release spectra from stress-relieved specimens with the incident fluence at 38 eV/D and 370 K. The main release peak broadens and shifts to higher temperatures for higher fluences, mainly due to deep diffusion. The minor low-temperature peak visible at intermediate fluence is obscured by the broad main peak at high fluences. Bursts on the low-temperature flank of the main peak correspond to rupturing blisters.

8.2.3. Blister evolution with fluence

It is an ongoing discussion if blisters occurring due to ion beam or plasma loading of specimens with hydrogen isotopes are the result of supersaturation and the accompanying stress, or of the gas pressure inside cavities. However, recent investigations gave strong support to the internal gas pressure being responsible at least for expanding the blister cavities [9]. Also, it was shown in section 8.1 that the average blister size depends on the temperature, which indicates a filling of the cavities by deuterium diffusing into them. It is now also highly interesting to study the kinetics of blister growth at a fixed temperature, i.e., the abundance and size of the blisters depending on the incident fluence. For this, the blisters in DIC images of stress-relieved specimens from the fluence variation experiments were marked in the same way as on the specimens from the temperature varia-

tion. It should be noted that again, no blisters were found on the recrystallised tungsten, not even at the highest fluence. The fluence of 5×10^{25} D m^{-2} is already comparable to fluences achieved in high-flux experiments such as those reported on by Alimov *et al.* [6, 2] as well as by Lindig *et al.* [57, 58]. That those researchers *did* find blister-like structures also on recrystallised tungsten can therefore not simply be attributed to the fluence, but probably has other reasons such as the ion flux and the detailed properties of the material. Figure 8.13 shows the results of the statistical analysis of the blisters. At the lowest fluence of 3×10^{22} D m^{-2}, no blisters were found, which indicates a fluence threshold for blistering. Both the number density and the surface coverage then grow with the incident fluence until the values stagnate at a fluence of 1×10^{24} D m^{-2}. For the highest fluences first the number density and then also the coverage apparently become smaller again. This could be due to several reasons: After six days of continuous plasma exposure corresponding to the highest fluence of 5×10^{25} D m^{-2}, the specimen surface is rather strongly corrugated due to sputtering by plasma impurities. This might have destroyed many of the smaller blisters by eroding away their caps. Also, the smaller blisters might simply be not recognisable anymore on the rough surface. A third possibility is the coalescence of small blisters into larger ones at high fluences. This would be consistent with the average blister size continuing to grow up to the highest fluence. It is likely that a combination all these effects leads to the observed results.

In any case, the analysis of the blisters depending on the incident fluence indicates that blisters are not spontaneously created, but rather grow with the incident fluence. This is consistent with the conclusion in section 8.1 that blisters grow due to deuterium diffusing into their cavities. From the absence of blisters exposed only to a very small fluence of 3×10^{22} D m^{-2}, respectively for a very short time (≈ 5 minutes), it can be concluded that a minimum concentration of deuterium must be present in order to nucleate blisters. Since the blister cavities were always observed at grain boundaries parallel to the surface, this concentration must also be reached at a location sufficiently deep within the specimen. Therefore, both a minimum fluence and a sufficient time for diffusion to the grain boundaries are necessary to create blisters.

From the recent statistical analysis of D$_2$ gas bursts during TDS it can be concluded that the blister size distribution should follow an exponential distribution [67]. This can now be explicitly tested by looking at the detailed blister size histograms derived from image analysis. Figure 8.14 shows the size distributions of
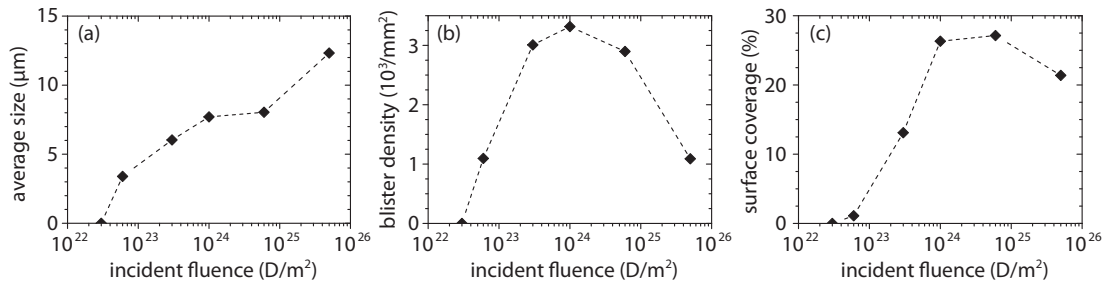
Figure 8.13. Statistical evaluation of blister parameters for fluences between 3×10^{22} and 5×10^{25} D m^{-2} at 38 eV/D and 370 K. Blisters were, apart from sporadic occurrences on partially recrystallised material, only found on stress-relieved tungsten. (a) shows the average size of blisters, (b) displays the number density and (c) the surface coverage.

the blisters for all fluences where blisters were observed. Because very large blisters are comparatively rare, the bin width for the computation of the histogram was increased for larger sizes. In order to conserve the correct relative weight with respect to the smaller bins for the smaller sizes, the abundance per bin was normalised to the bin width.
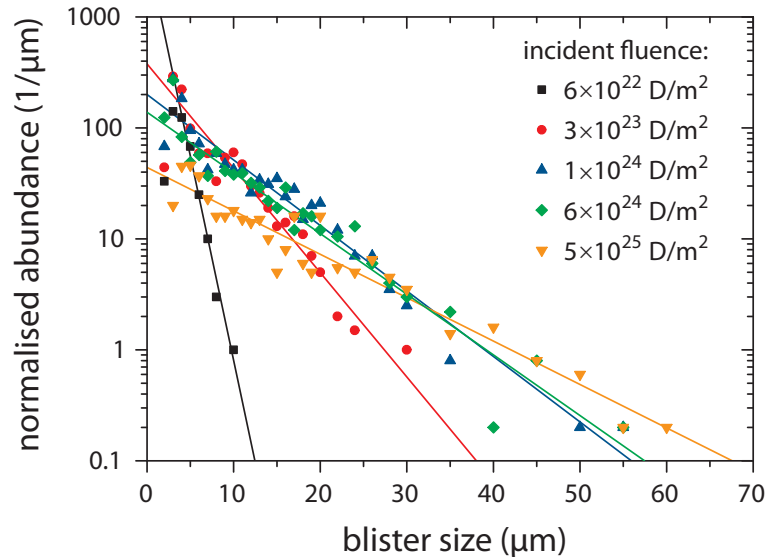

Figure 8.14. Blister size distributions on stress-relieved tungsten for various fluences between 6×10^{22} and 5×10^{25} D m^{-2} at 38 eV/D and 370 K (symbols). The abundance of blisters in a certain size class is normalised to the bin width. The straight lines represent exponential fits to the size distributions.

For all fluences shown in Figure 8.14, the blister size distribution can indeed be well described by exponential distributions. This is illustrated by the straight

lines representing exponential fits to the individual size distributions. The size distributions become flatter for large fluences, probably due to coalescence and maybe also due to destruction of smaller blisters, as already discussed above. The matching distribution functions for both burst sizes and lateral blister dimensions support the assumption that the size distribution of blister bursts indeed represents the size distributions of the blisters themselves. For an accurate computation of the pressure inside the blisters, it is necessary to analyse not only the lateral dimensions of the blisters, but the actual *volume* of the blisters. For this, 3D surveys by confocal laser scanning microscopy would be ideal. However, such equipment was only available for some first, sporadic investigations.

8.3. Influence of ion energy

8.3.1. Deuterium retention

The depth profiles of deuterium implanted into tungsten specimens of the four different microstructures described in chapter 6 at a temperature of 370 K and a fluence of 6×10^{24} D m^{-2} all exhibit a common characteristic when the bias voltage, and therefore the ion energy, is increased: The concentration peak at the surface — which was already ascribed to damage caused by impurity ions in the plasma in the previous sections — grows significantly. As it can be seen in Figure 8.15, the amount of deuterium retained in this peak shows a nearly linear dependence on the bias voltage and has no pronounced dependence on the initial tungsten microstructure. This increase could be due to a higher damage potential of the impinging impurity ions, or due to a deeper penetration range of these ions. In all cases, the deconvolution of the measured proton spectra yielded the minimum allowed width (due to the depth discretisation of the specimen) of approximately 8 nm for this layer (i.e., the equivalent of a delta function at the surface). The average deuterium concentration that corresponds to the amount of deuterium retained in this 8 nm thick layer reaches surprisingly high values of more than 20% for the highest bias of -600 V. It should be noted that the depth resolution of the present NRA analysis using the D(^{3}He$, p$)^{4}He reaction [70] is not sufficient to clarify whether the deuterium concentration increases within a layer of fixed thickness, or if the thickness of the layer increases while the concentration stays constant. Maybe highly surface sensitive techniques such as ERDA could be applied to investigate this surface peak in more detail as a follow-up project.
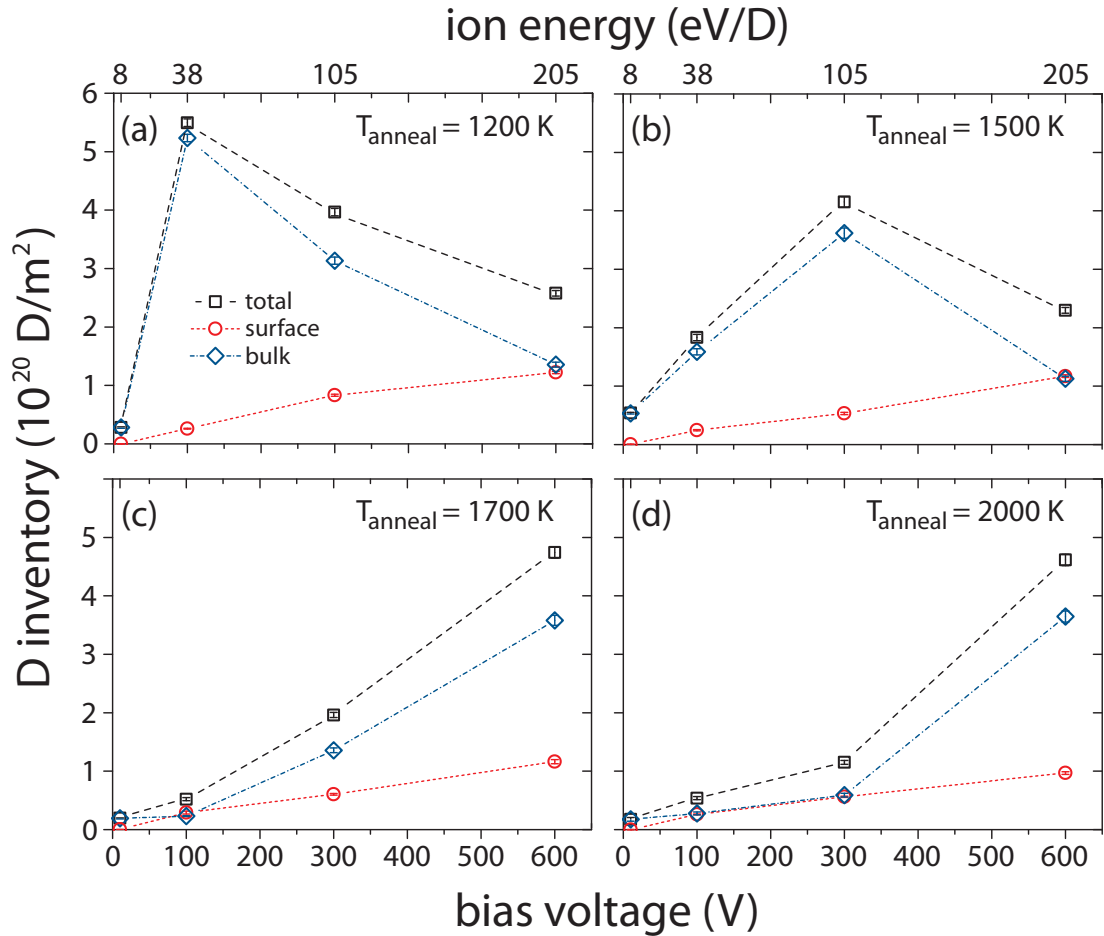
Figure 8.15. Deuterium retention measured by NRA in tungsten specimens of different microstructures depending on the applied bias voltage, respectively ion energy for a fluence of 6×10^{24} D m^{-2} and a temperature during exposure of 370 K. (a) shows the total amount of deuterium together with the amount retained at the surface and in the bulk up to ≈ 8 μm for specimens stress-relieved at 1200 K. (b), (c) and (d) show the same for specimens pre-annealed at 1500, 1700 and 2000 K.

At -10 V bias, corresponding to 8 eV/D, the amount of deuterium retained in any of the specimens is very small. The concentration profile is practically flat, and a concentration peak near the surface cannot be identified. There is no obvious systematic variation with the microstructure, but this is most likely due to the experimental uncertainties under these conditions. The deuterium inventory is very small, and due to the low energy, even minor differences in the surface quality of the specimens could have a comparatively strong effect. In any case, the very small deuterium uptake at these low ion energies shows that the large amount of low-energy neutral deuterium atoms in the plasma can only have a negligible effect on the deuterium retention at higher ion energies.

Rather surprisingly, the effect of higher ion energies on the deuterium retention in the bulk of the specimen (up to ≈ 8 μm) is quite different from the behaviour of the near-surface region, as Figure 8.15 shows. At 38 eV/D, the deuterium retention is significantly higher than at 8 eV/D, but shows the pronounced differences in the total retention for different microstructures that were discussed in the previous sections of this chapter. For stress-relieved and partially recrystallised tungsten, the largest part of the deuterium inventory is contained in the bulk of the specimen, although the surface peak is clearly visible. For both fully recrystallised materials, the bulk inventory accessible by NRA (i.e., up to ≈ 8 μm) is about equal to the amount retained in the surface peak, and the total retention is considerably lower than for the other two specimens.

At 105 eV/D, the deuterium retention in the stress-relieved specimen is *smaller* than at 38 eV/D, while it increases by different amounts for the other specimens. The partially recrystallised specimen now contains approximately as much deuterium as the stress-relieved specimen. For tungsten recrystallised at 1700 K, the retained amount is about half as much, and for material annealed at 2000 K only about one quarter of the amount in stress-relieved specimens. The bulk retention detectable by NRA dominates the total retention at this energy for all specimens except for the specimen recrystallised at the highest temperature. Here the amounts of deuterium contained in the bulk and in the surface peak are about equal. The implantation at 105 eV/D is one of the rare cases where the specimens recrystallised at 1700 and 2000 K show significantly different behaviour.

At the highest investigated ion energy of 205 eV/D, the deuterium retention in stress-relieved tungsten decreases further to about half of the maximum retention observed at 38 eV/D. The amounts found by NRA in the bulk and in surface peak are now nearly equal. For partially recrystallised tungsten, a similar total retention as well as the same distribution between bulk and surface are observed. Both fully recrystallised specimens, however, show again a strong *increase* of the deuterium retention. The inventory is now nearly as large as for stress-relieved tungsten implanted at 38 eV/D and about the same for both specimens. Contrary to the stress-relieved and partially recrystallised specimens, much more deuterium is retained in the bulk of the fully recrystallised specimens than in the surface peak.

The observed changes of the total deuterium retention as well as of the distribution between bulk and surface are, at first, quite surprising. The maximum of the retention is found at different energies for different microstructures, but is

in every case comparable in the absolute magnitude. The distribution between bulk and damage zone also depends strongly on the microstructure for different energies. For stress-relieved tungsten, the abundant defects at the surface apparently act as a diffusion barrier preventing migration of deuterium into the bulk of the specimens at higher ion energies. For partially recrystallised tungsten, the diffusion into the bulk is first enhanced and then again reduced as the ion energy increases. For fully recrystallised tungsten, the diffusion into the bulk is, paradoxically, apparently the highest when the near-surface region suffers the most damage from the plasma.

8.3.2. Surface damage

Because of the pronounced dependence of the retention within the damage zone on the bias voltage respectively ion energy, this is an ideal parameter for studying the nature and origin of the damage in this region. Two different investigation methods, which were both performed in SEMs, were applied for this. One method was energy-dispersive X-ray spectroscopy (EDX). Impurities, mainly ions from the plasma containing oxygen or nitrogen, are suspected to be the cause of the damage near the specimen surface. Accordingly, one can expect to find some oxygen and nitrogen implanted into the specimen at very shallow depths. At the most commonly used acceleration voltages in SEMs of 20–30 kV, thin layers of these light elements are nearly invisible against a thick, heavy background target such as tungsten. By decreasing the acceleration voltage to 5 kV, the EDX analysis becomes much more surface sensitive. Together with long integration times of 1–2 hours per spectrum, the K_α X-ray lines of N and O can be clearly identified, as the example in Figure 8.16 shows. At an electron energy of 5 keV, the M lines of tungsten are still excited and can be used for normalisation of the X-ray spectra from different specimens. It should be noted at this point that traces of silicon on tungsten (from hypothetical silane molecules in the plasma) cannot be distinguished by EDX because the Si K_α line overlaps with the W M_α line.

As Figure 8.17 shows, the intensity of the N and O K_α lines exhibit a very clear dependence on the bias voltage applied during plasma exposure. For the unexposed reference specimen only a small oxygen peak, probably due to a superficial oxide skin and some oxygen impurities in the bulk, is visible. With increasing bias, the intensity of the O K_α line increases linearly from its background level.

With increasing bias voltages, also the N K_α becomes clearly visible. Its intensity increases at a similar, albeit slightly lower rate than that of the O K_α line. This is clear evidence that the near-surface damage on the specimens is indeed caused by impurities in the plasma. These are present in practically *any* plasma. In nuclear fusion experiments, impurities are even intentionally introduced into the plasma boundary layer in order to reduce the heat load on the plasma-facing components due to concentrated particle fluxes [43, 44]. As it was shown in section 8.3.1, a combination of intense deuterium fluxes with heavier impurity ions can have a pronounced effect on the deuterium retention at energies where the hydrogen by itself is not yet able to cause displacement damage.

The second analysis method applied to these specimens was electron backscattering diffraction (EBSD), a tool otherwise often used for orientation mapping. This technique is usually difficult to apply because the quality of EBSD patterns is very sensitive even on thin contamination or amorphisation layers on the investigated surface. Here, this sensitivity was exploited to observe the damage caused by the plasma in a narrow near-surface zone of the tungsten specimens. In order to have as clear EBSD patterns as possible, the material recrystallised at 2000 K was selected for this analysis. It can be seen as representative for all specimens because, as described above, the retention in the damage zone does not depend on the microstructure. For the EBSD analysis, an acceleration voltage of 20 kV and a specimen tilting angle of 70° were used. The working distance was 5.5 mm. From each specimen, at least two arrays of 22×19 points evenly distributed over an area of about 10^5 μm^2 (corresponding to an image width of 64 μm) were acquired to gather statistically significant information. Figure 8.18 shows EBSD patterns acquired from specimens exposed to deuterium plasmas with ion energies between 8 and 205 eV/D, as well as from an unexposed reference specimen. All patterns were recorded with the same camera settings and acquisition time. Both the reference specimen and the specimen exposed at 8 eV/D showed very clear, detailed and contrast-rich patterns. There was some variation in pattern contrast due to electron channelling effects, but on average the pattern quality was excellent. Accordingly, nearly all recorded patterns could also be solved by the EBSD software (Channel 5 HKL Flamenco). Only a few grains on the reference specimen showed unsolvable patterns of comparatively poor quality. Closer inspection of these grains showed a small-scale roughness and an increased carbon signal in EDX spectra. This means that these grains were contaminated by a thin layer of tungsten carbide during the recrystallisation in the graphite furnace. Such grains were not found on the specimen exposed at 8 eV/D. The conclusion is that the
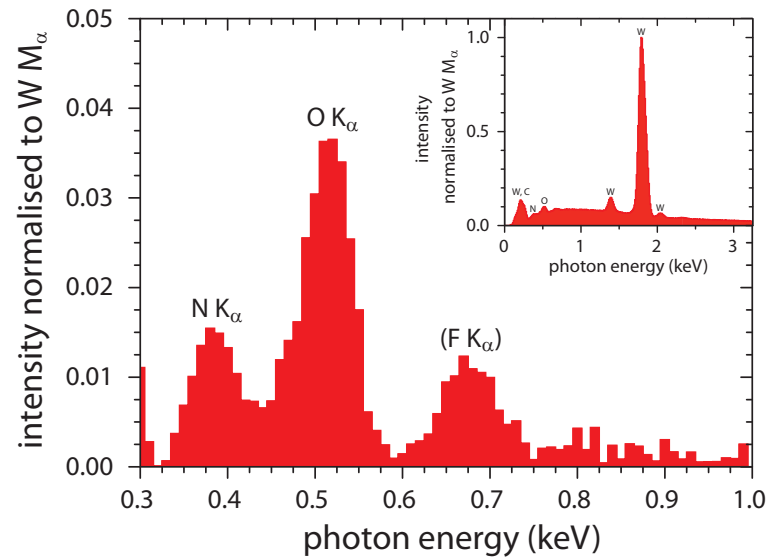
Figure 8.16. Low-energy detail of an EDX spectrum acquired at an acceleration voltage of 5 keV. The specimen was implanted at -600 V bias voltage, corresponding to 205 eV/D (fluence: 6×10^{24} D m^{-2}, temperature: 370 K). The background due to the bremsstrahlung was subtracted from the spectrum. Both N and O K$_\alpha$ lines are clearly visible. The small F K$_\alpha$ line is present on all specimens and is therefore considered a background impurity. The inset shows the full spectrum (including the background).
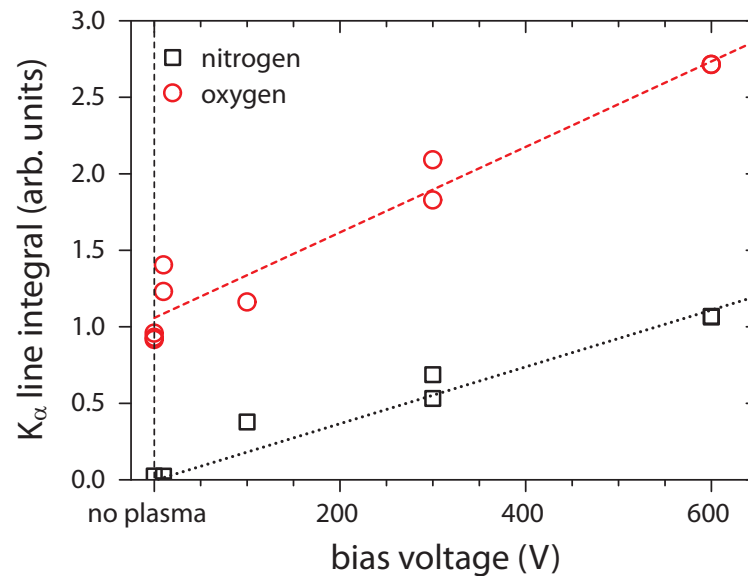

Figure 8.17. Integral intensity of the N and O K$_\alpha$ lines depending on the bias voltage applied during plasma exposure to a fluence of 6×10^{24} D m^{-2} at 370 K. The intensities were normalised to the tungsten M$_\alpha$ line for each spectrum. Both N and O intensities increase nearly linearly from their base levels on an unexposed specimen ("no plasma") with the bias voltage.

surface contamination was completely eroded during plasma exposure. On both specimens, the orientation contrast between different grains is strong and clear in BSE images.

The EBSD patterns from the specimen exposed at 38 eV/D are still recognisable and in many cases solvable by the analysis software. However, the pattern quality is markedly worse than on the reference and low-energy exposed specimens. The orientation contrast between different grains is fainter, but still visible. This points towards a beginning destruction of the ordered tungsten lattice in the near-surface region.

For specimens exposed at higher energies of 105 and 205 eV/D, the EBSD patterns are barely visible anymore. Most images recorded by the EBSD detector are a near-uniform gray. Only very faint and diffuse traces of some Kikuchi bands can be seen. Consistently, also the orientation contrast on these specimens has faded to a point where it is barely visible anymore. On these specimens, the near-surface layer is practically completely destroyed. Together with the extremely high concentrations of deuterium — and accordingly defects — measured in this zone, one comes to the conclusion that the specimen surface is practically amorphised at higher incident ion energies.
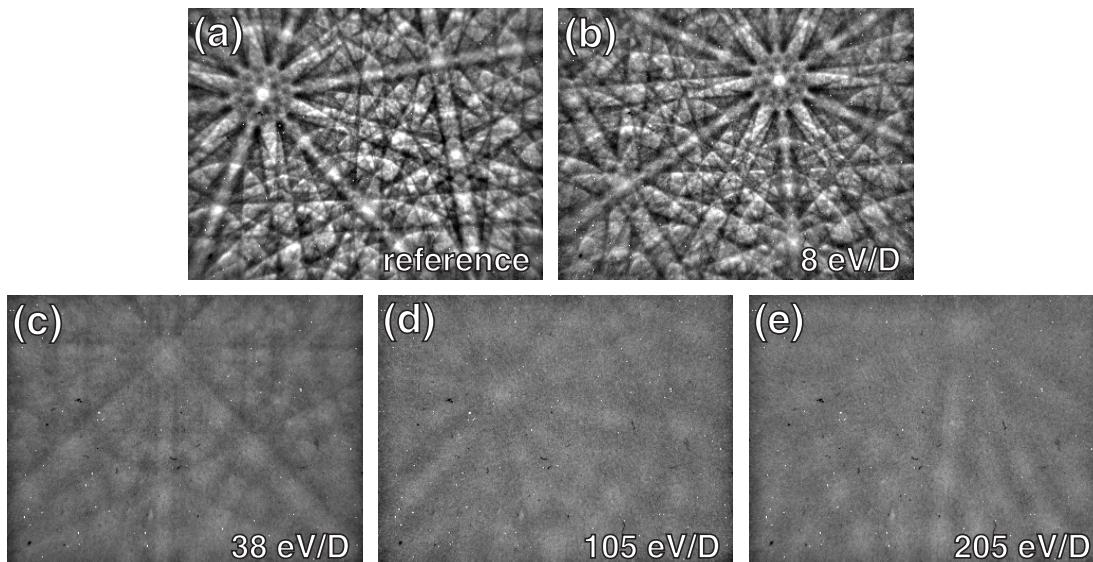

Figure 8.18. EBSD patterns from recrystallised tungsten specimens exposed to deuterium plasmas (fluence: 6×10^{24} D m^{-2}, temperature: 370 K) with different energies. (a) shows a pattern from an unexposed reference specimen. (b), (c), (d) and (e) show patterns from specimens exposed at ion energies of 8, 38, 105 and 205 eV/D. Note how the pattern quality deteriorates for increasing bias.

Assuming Frenkel pairs, respectively vacancies, as the dominant trap for deuterium in the surface layer, one comes to defect concentrations similar to superabundant vacancies reported in hydrogen-loaded Pd and Ni [30]. As mentioned above, only the *average* concentration of deuterium respectively traps in an 8 nm thick layer could be measured. Accordingly, it could not be distinguished between an increase of the trap concentration in a layer of fixed thickness and an increase of the layer thickness on the nanometre scale at a fixed concentration. However, the stopping range of the ions also increases with the ion energy, so the latter explanation appears more plausible.

8.3.3. Blisters and other surface modifications

The intensity of blister formation at different incident ion energies (respectively bias voltages) appears to be tightly correlated to the deuterium retention. Whenever the deuterium retention, particularly the fraction *beyond* the damage zone, is at its maximum, so is the blistering activity. In contrast to all other parameter variations performed for this thesis, blister-like structures are even found on *fully recrystallised* tungsten at a bias voltage of −600 V (corresponding to 205 eV/D), where the maximum retention is observed for this material. Likewise, a low blistering activity always coincides with a comparatively small deuterium inventory.

At an incident energy of 8 eV/D, none of the specimens show any blisters or similar structures. Sputtering of the specimen surface is also not observed. The only apparent effect on the specimen surface is the removal of superficial carbide contamination, as discussed in section 8.3.2. As shown in Figure 8.15, the retained deuterium inventory is also very small and rather evenly distributed in within the depth range accessible by NRA.

At 38 eV/D, the blistering activity is at its maximum on stress-relieved tungsten. The details were already discussed in sections 8.1.6 and 8.3.3 (see, e.g., Figure 8.3). For partially recrystallised material only occasional, small blisters are observed. On both types of tungsten, most blisters have a circular or elliptical circumference and a domed cap as panels (a) and (c) of Figure 8.19 show. There are no blisters on either of the fully recrystallised materials. Slight traces of sputtering are visible mainly on stress-relieved tungsten, e.g., when comparing surface areas covered by the mounting screws and exposed areas. On the other materials, sputtering traces are more difficult to see due to strong thermal groov-

ing at grain boundaries: The grooves make it difficult to observe steps between neighboring grains caused by preferential erosion.

At 105 eV/D, the picture changes, as Figure 8.19 illustrates: On stress-relieved tungsten, which is depicted in panel (b), sputtering traces are now clearly visible. Blisters are still numerous, but their density is slightly lower and the largest blisters are missing in comparison to specimens implanted at 38 eV/D. On the other hand, partially recrystallised tungsten (Figure 8.19e) now shows a much *higher* number of round blisters than the same material exposed at 38 eV/D. They are quite small compared to blisters on stress-relieved tungsten exposed at 38 eV/D and 370 K, on average about 2.5 μm in diameter. These blisters are almost only found in areas that show little to no thermal grooving, i.e., that are more or less still in the initial, non-recrystallised state. On the recrystallised areas, i.e, on those showing grooves at the grain boundaries, a *different* type of blister-like protrusion shows up in large numbers. These features are very small, on average around 2 μm. In contrast to the blisters observed on stress-relieved tungsten, they are flat, plateau-like protrusions with an angular outline. While they were occasionally also found at 38 eV/D, these features are now at least as abundant as the round blisters on partially recrystallised tungsten. Another difference between the recrystallised and non-recrystallised areas is that the non-recrystallised areas appear to be rather uniformly and slightly more strongly eroded than the recrystallised ones. On fully recrystallised tungsten, no round blisters appear, but some isolated features of the second, angular type are found.

After exposure at the highest energy of 205 eV/D, blistering on stress-relieved tungsten is significantly reduced compared to 38 and 105 eV/D. Figure 8.19c shows that blisters are now small and have roughly the same size as for exposure at 38 eV/D and 300 K (see Figure 8.3), although the specimen temperature here was 370 K. The blister density is also much lower than in the other cases. On the other hand, sputtering of the surface is now considerable. At the bias voltage of -600 V applied here, impurity ions as well as the small fraction of D$^+$ ions with the full energy of about 600 eV/D from the plasma can erode the tungsten surface. On partially recrystallised tungsten (Figure 8.19f), the situation is similar. Blisters are rare and difficult to find due to the strong roughening of the surface by sputtering. Of the few blisters found after exposure at the highest energy, almost all have rounded bulges, but are rather flat. The outlines of the blisters vary between nearly circular features and strongly elongated, ridge-like shapes.
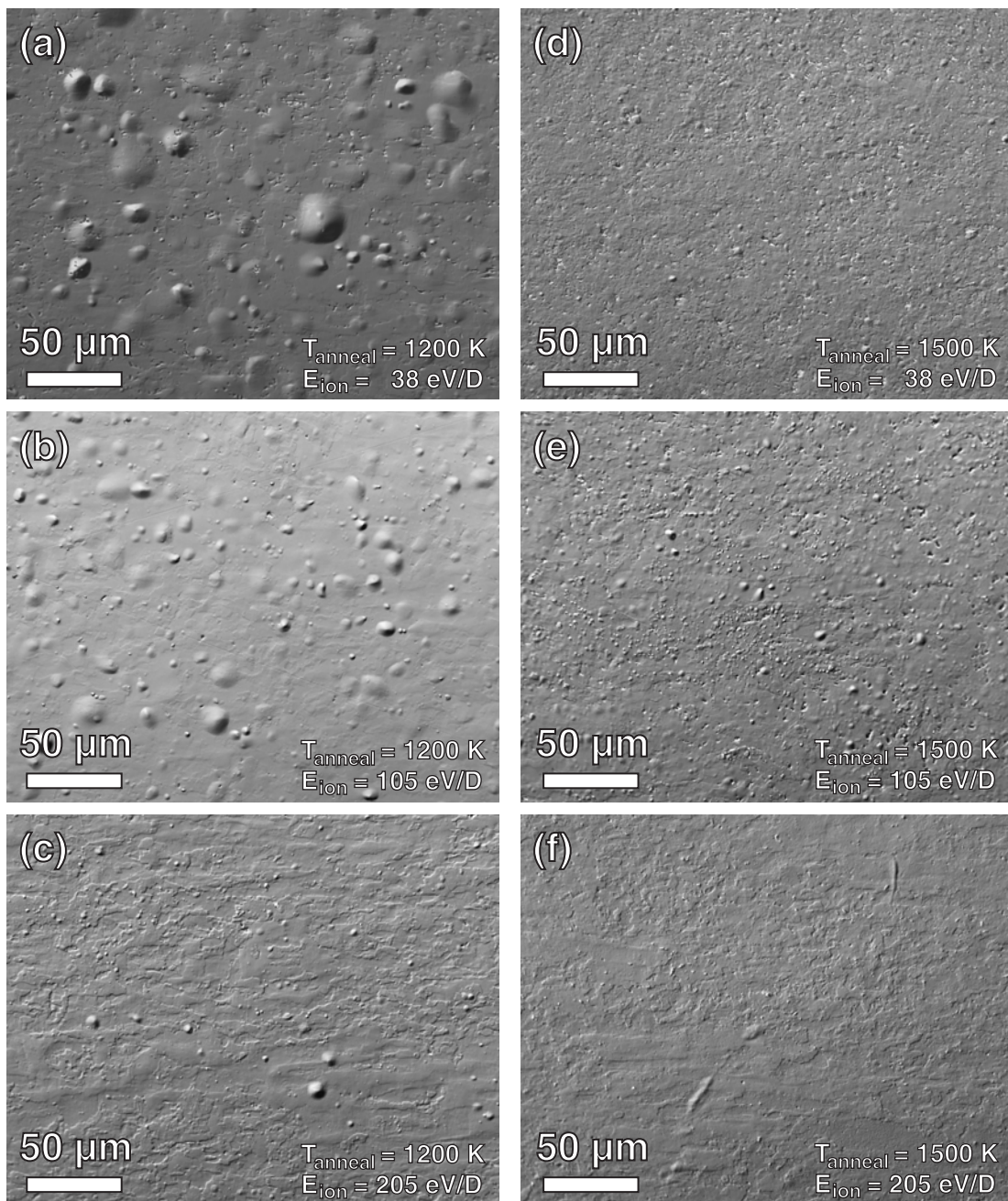
Figure 8.19. Optical DIC micrographs of stress-relieved (a–c) and partially recrystallised (d–f) tungsten after plasma exposure to a fluence of 6×10^{24} D m^{-2} at 370 K at various ion energies. At 38 eV/D (a, d) nearly all blisters have a circular or elliptical circumference and a domed cap. At 105 eV/D the density and size of blisters on stress-relieved tungsten (b) is reduced, while partially recrystallised tungsten (e) shows many blisters as well as small, flat, angular protrusions. At 205 eV/D the size and density of the blisters on the stress-relieved specimen (c) is significantly reduced compared to lower ion energies. The partially recrystallised specimen (f) shows only very few, isolated blisters and ridge-like features.

On the other hand, fully recrystallised material now shows a high density of the small, flat, angular features such as in Figure 8.20a. With a mean size of about 1.2 μm, they are a bit smaller than those found on partially recrystallised tungsten at 105 eV/D, but look otherwise very similar. Such surface features were also found by Ogorodnikova *et al.* [81] after irradiation of recrystallised tungsten with a 3 keV D^+ ion beam. On FIB cross-sections, as shown in Figure 8.20b, one can find short, intragranular cracks in a depth around 1 μm. They are typically inclined towards the specimen surface. Due to the large average grain size, they are typically far away from grain boundaries and can therefore not be seen as material failure at distinguished weak spots. Around and between the cracks, the SEM image shows varying greyscale contrast within the otherwise uniform grains. This is due to severe plastic deformation of the material, particularly in the vicinity of crack tips, which is visible as (mis-)orientation contrast. The cracks and distortion fields are coincident with a secondary deuterium concentration peak that is found in NRA depth profiles.

These features observed on recrystallised tungsten at high incident ion energies are remarkably similar to features observed on recrystallised tungsten at a similar exposure temperature by Lindig *et al.* [57, 58]. In this case, however, the base material was different and the grain size was significantly larger. The plasma exposure was performed with a lower ion energy of 38 eV/D, but with a 100 times higher particle flux. Nevertheless, very similar flat, angular features were observed, also with similar subsurface cracks and distortion fields. This suggests that there is at least some degree of equivalence between plasma exposures at high ion energies (205 eV/D respectively -600 V bias) but low flux ($\approx 10^{20}$ D m^{-2}s^{-1}), and those at high flux ($\approx 10^{22}$ D m^{-2}s^{-1}) but low energy (38 eV/D).

The strong correlation between blistering and deuterium retention beyond the surface peak backs up the hypothesis that retention is enhanced by dislocations that are emitted when the material fails locally and cracks appear. Particularly for recrystallised tungsten, the volume of the cavities is very small, but the distortion fields in their vicinity are clearly visible. These fields might be due to the semi-brittle fracture mechanism associated with crack-tip plasticity for tungsten in this temperature range [35]: This process is controlled by the emission and movement of dislocations near the crack tip. Furthermore, the dislocation density was low before plasma exposure, so the increase in dislocation density due to cracking is even more pronounced than in initially dislocation-rich material. Judging from the magnitude of the deuterium retention in the cracked region, the dislocation
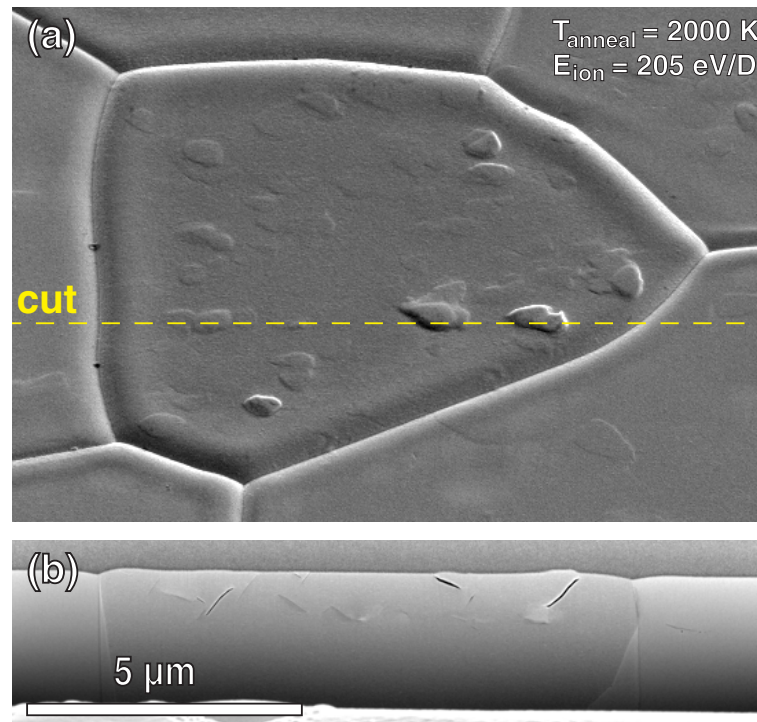
Figure 8.20. SEM micrographs of fully recrystallised tungsten after plasma exposure at 205 eV/D and 370 K. (a) shows a view of the surface at a specimen tilt of 52°. (b) shows a FIB cross-section of the same region. The cut is located at the line indicated in (a). The surface was protected by an amorphous Pt:C layer for cutting. Note also the changing greyscale contrast around the cracks indicating distortion fields.

density can be expected to be comparable to that in the blister region of stress-relieved specimens implanted at lower ion energies.

The reason for intragranular cracks appearing in recrystallised tungsten at high incident ion energy is probably at least partially due to a higher transient supersaturation of the material with deuterium during the plasma exposure. Simulations (for defect-free tungsten) indeed show that the interstitial solute concentration in the subsurface region is higher for a higher ion energy, respectively penetration depth of the ions, although the effect is not as pronounced as for a higher ion flux. As already mentioned in section 7.3, the direct reflection yield of energetic deuterium ions depends only weakly on the incident energy. It is nevertheless a striking coincidence that high-energy deuterium implantation at an intermediate particle flux produces very similar surface features to those resulting from a low-energy but high-flux exposure, where also a high supersaturation is expected [1, 2, 57, 58]. Furthermore, the extremely high deuterium concentration

and the amorphisation of the tungsten matrix in the damage zone at the surface can be expected to exert a considerable stress on the underlying material due to dilatation of the surface layer. This would also promote cracking.

On the other hand, the question comes up why non-recrystallised material does *not* fail in the same way. This might be due to the different mechanical properties of the material: Non-recrystallised tungsten shows at least some residual ductility, while it is very brittle when recrystallised (see also chapter 6). The appearance of cracks can be expected to be accompanied by the emission of dislocations due to crack-tip plasticity, as also indicated by the well-visible distortion fields in Figure 8.20. The suddenly increased defect density then effectively acts as an attractive potential drawing deuterium from the implantation region into the bulk and binding it there. Grain boundaries, which are assumed to act as weak points in bulk material, are typically too far away from the stressed region to play a decisive role due to the large grain size. In already dislocation-rich material, however, it might be easier to relax stress by moving *existing* dislocations than by initiating a fracture and creating new ones. A similar opinion is expressed by Alimov *et al.* [2], who assumes that a deformation layer at the specimen surface might act as a damper to implantation stresses. Indeed, edge dislocations in tungsten are quite mobile with an activation energy of 0.2–0.5 eV [35]. On the other hand, the core energy of an edge dislocation in tungsten is 16.9 eV/nm according to Liu *et al.* [60]. It is therefore possible that the increased stress does not lead to a significant increase in dislocation density, but rather to a rearrangement of the existing dislocations. So contrary to the recrystallised material, the defect density is not significantly enhanced beyond the implantation region, albeit it is still higher than in recrystallised specimens without cracks. Furthermore, experiments by Ogorodnikova *et al.* [82] also showed the seemingly paradox effect of lower total retention at high incident ion energy (i.e., above the damage threshold) for polycrystalline tungsten irradiated with mass-filtered deuterium ion beams. As mechanisms for this, the reduction of the diffusivity into the bulk by a stress field caused by the incident ion flux was suggested. It is possible that a similar mechanism reduces the bulk concentration of deuterium and accordingly the precipitation into blisters at grain boundaries in stress-relieved tungsten.

On partially recrystallised specimens, both effects can be observed right next to each other: The yet untransformed regions behave similar to stress-relieved material, while the already recrystallised parts of the specimen behave more like fully recrystallised tungsten. This shows that even local variations of the dislocation

density (and probably also of the grain boundary type) on a microscopic scale can have an immediate effect on the blistering behaviour of the material.

8.4. Effects due to specimen preparation

As mentioned in section 7.4, the influence of the specimen preparation, i.e., polishing as well as degassing during stress-relief annealing were also investigated. Figure 8.21 shows the deuterium inventories in stress-relieved tungsten specimens with unpolished, mechanically polished (see section 5.1.1) and electropolished surfaces. All specimens were exposed in a single plasma discharge with a specimen temperature of 370 K and an ion energy of 38 eV/D. The incident fluence was 6×10^{24} D m^{-2}. The specimen with the unpolished surface retains significantly more deuterium than the other two specimens. Its surface has received only a coarse mechanical grinding by the manufacturer. It is very rough with height differences of the order of 10 μm and more, and can be expected to contain very much mechanical damage from the grinding in the whole depth range accessible by NRA. Therefore, it is not very surprising that this specimen contains the most deuterium, even though blisters were not found on its surface. It should be noted, however, that this may also be due to blisters being simply undetectable on the corrugated surface. On the other hand, experiments by Nishijima *et al.* [75] also led to the conclusion that blisters do not appear on rough, distorted surfaces. The deconvolution of the NRA measurements on this specimen shows less detail than for the polished specimens. Since the surface contains height differences that are comparable to the range of the ^{3}He ions used for analysis, it must be expected that this significantly blurs the depth resolution.

As it was shown in section 5.1.1, the distortion layer on the surface of a specimen is effectively removed by the mechanical polishing procedure applied here (see section 5.1.1, and the defect concentration should accordingly be close to the bulk level. Indeed, the mechanically polished specimen shows about 10% less deuterium in the depth accessible by NRA than the unpolished one. The lower defect density compared to the heavily deformed surface layer is probably partially offset by the appearance of blisters on the polished surface. As it was discussed in the previous sections of this chapter, it is likely that the expansion of blister cavities produces new defects during plasma exposure.

The electropolished specimen has again about 10% less deuterium inventory. Al-

though both electrochemical and mechanical polishing looked virtually the same in surface and cross-section SEM images (see section 5.1.1), this points to some residual damage being present in mechanically polished specimens. The formation of blisters is at first glance not very strongly affected by that, as Figure 8.22 shows. However, a detailed statistical analysis, such as in sections 8.1.6 and 8.2.3, reveals some differences: For example, small blisters are more abundant on the electropolished surface. This is at least partially due to the better visibility of these small features on a very smooth surface. Still, this may also be due to small blisters typically having their cavities closer to the surface, so these are most likely to be more affected by any residual surface roughness or porosity. Also, large blisters are slightly more common on mechanically polished tungsten. This may be due to weakening of grain boundaries near the surface by shear stresses occurring during the polishing. On electron micrographs, it is difficult to make out any differences in the microstructure. The effect must therefore be rather subtle. Overall, the average size of blisters is slightly higher on mechanically polished tungsten (8 μm compared to 6.9 μm), and the surface coverage is smaller (27% compared to nearly 35%). Because of the larger number of small blisters found on electropolished tungsten, the number density of blisters is about twice as high on this material. However, it should be noted that the influence of the fluence and particularly of the temperature on blistering is much more pronounced than that of the polishing method (see sections 8.1.6 and 8.2.3). Therefore, the blistering behaviour of mechanically and electrochemically polished tungsten can still be considered rather similar.

In Figure 8.23 it can be seen that the deuterium inventory in specimens that were *not* annealed prior to plasma exposure systematically have a more than 20% lower deuterium inventory than their stress-relieved counterparts. Despite the high defect density, the unpolished and non-annealed specimen even has a lower deuterium inventory than the polished and stress-relieved specimen. Please also keep in mind that stress-relief practically does not change the defect density in the material (see section 6.1).

The explanation for the behaviour observed here is that, as suspected (see section 7.4.2), the specimen indeed contains a large amount of hydrogen due to the production process. This hydrogen occupies the available trap sites and has to be replaced by deuterium. At the exposure temperature of 370 K, the rate for thermally activated detrapping is still low, as TDS spectra show. Accordingly, the isotope exchange process necessary for binding deuterium in a trap site occupied
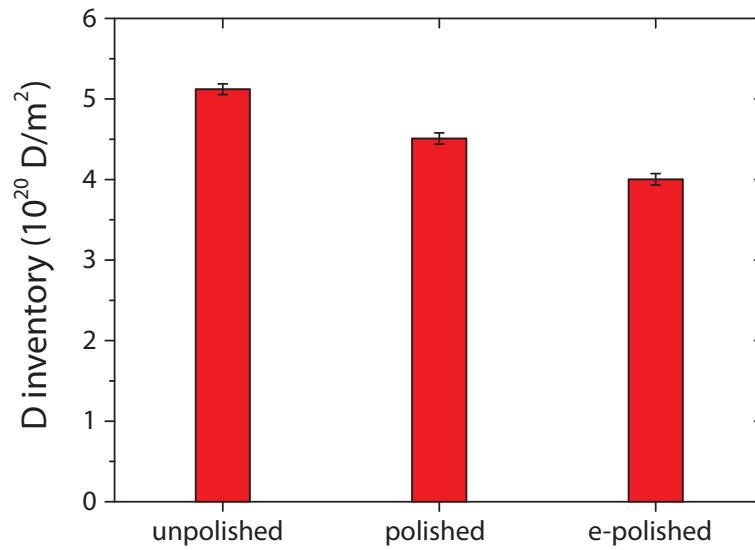
Figure 8.21. Deuterium inventories in stress-relieved specimens with different surface quality after plasma exposure at 38 eV/D and 370 K. The fluence was 6×10^{24} D m^{-2}. The inventories were measured by NRA.
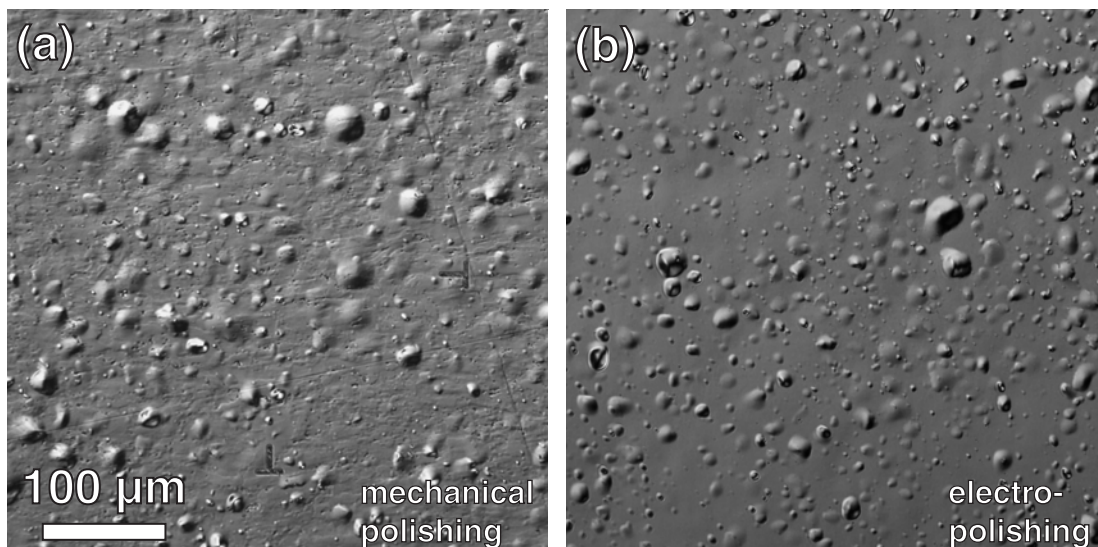

Figure 8.22. Optical DIC micrographs of blisters on (a) mechanically and (b) electrochemically polished specimens. Both specimens were stress-relieved and implanted under the same conditions (ion energy: 38 eV/D, fluence: 6×10^{24} D m^{-2}, temperature: 370 K). Blistering is only weakly affected by the polishing method.

by hydrogen is slower than filling of empty traps with deuterium. At the incident fluence of 6×10^{24} D m^{-2} that was used for this experiment, diffusion-trapping simulations (see section 3.3) predict the diffusion front at about 35 μm below the surface. Considering that the NRA measurements probed only about 1/4 of
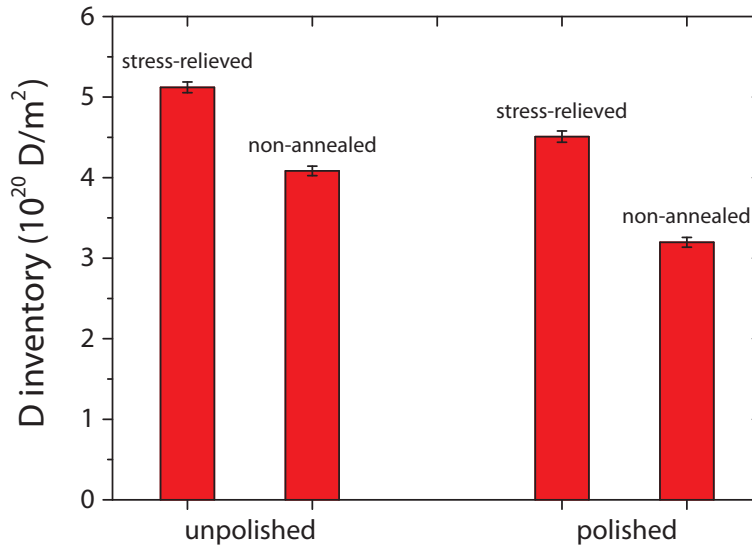
Figure 8.23. Deuterium inventories in mechanically polished and unpolished specimens with
and without stress-relief for 60 minutes at 1200 K in vacuum prior to plasma
exposure (ion energy: 38 eV/D, fluence: 6×10^{24} D m^{-2}, temperature: 370 K).
The inventories were measured by NRA. Non-annealed specimens systematically
have a lower inventory than the corresponding stress-relieved ones.

that depth, the measured difference of deuterium retention in stress-relieved and
non-annealed specimens is already quite remarkable.

The influence of the initially present hydrogen was also studied by TDS. While
the hydrogen background pressure in ultra high vacuum makes it much more
difficult to directly measure the hydrogen release from a tungsten specimen, this is
nevertheless possible. Of course, the release of the deuterium-containing molecules
D_2 and HD was also observed. Particularly the release of HD is a very useful
indicator for interactions between H and D: If H and D atoms reach the surface
simultaneously and in similar amounts, one can expect much more HD to desorb
from the sample compared to H_2 and D_2. The reason is that hydrogen isotopes are
dissolved in the tungsten as atoms and have to recombine at the surface before
they can desorb as molecular gas. This process is considered to be very fast for
tungsten [14], but the laws of combinatorics still dictate that the probability to
form HD is twice as high as for the isotopically pure molecules.

When one looks at the desorption spectra of unexposed tungsten specimens with
and without heat treatment in panels (a) and (b) of Figure 8.24, one can imme-
diately see that much more H_2 desorbs from the non-annealed specimen. There
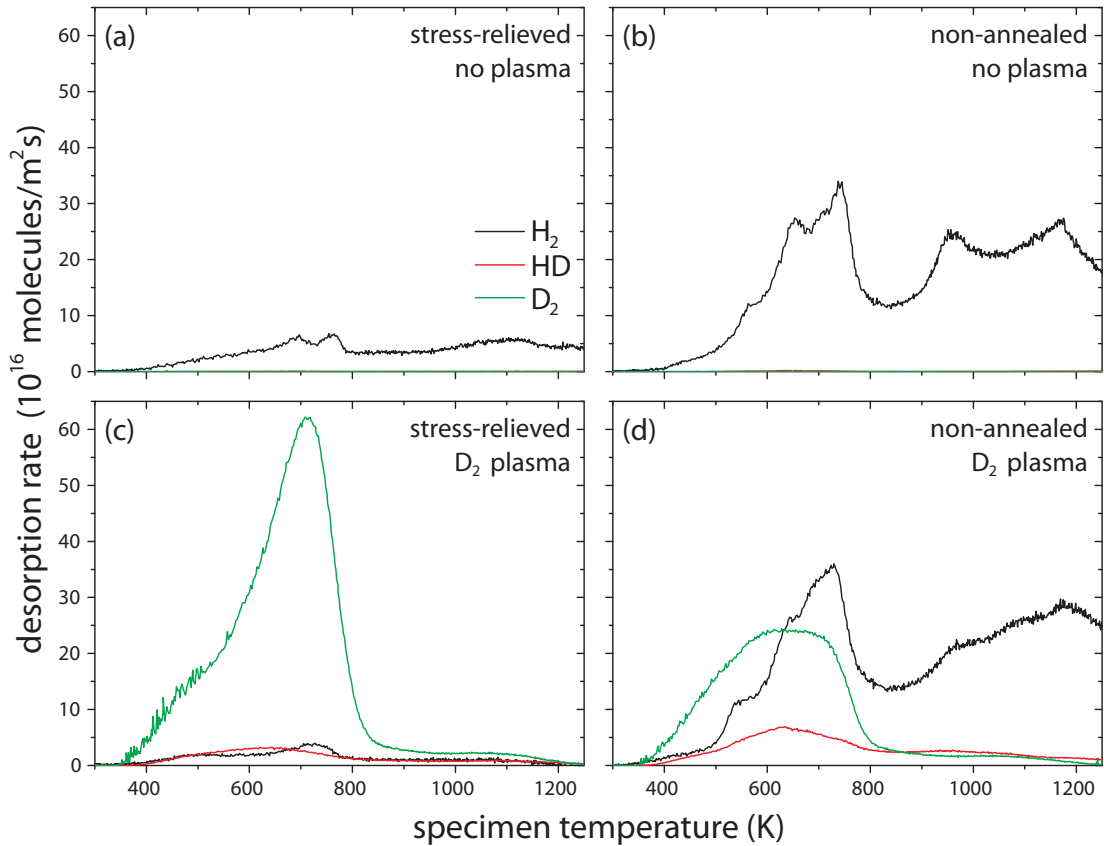is also a strong H_2 peak at around 600–700 K where the main D_2 release peak

Figure 8.24. TDS spectra of mechanically polished tungsten specimens (a) with and (b) without stress-relief for 60 minutes at 1200 K in vacuum. For comparison, spectra of (c) stress-relieved and (d) non-annealed specimens that were exposed to a D_2 plasma (38 eV/D, 6×10^{24} D m^{-2}) at 370 K are also shown. The spectra were recorded in TESS at a heating rate of 30 K/min. Non-annealed specimens release significantly more H_2, while D_2 release after plasma exposure is reduced. The release of HD molecules is only slightly increased if the specimen is not annealed before plasma exposure.

is typically found. Additionally, a large amount of H_2 is released at a late stage of the TDS run, i.e, at high temperatures. The background H_2 emission from the glass tube that contains the specimens is already subtracted from the spectra shown in Figure 8.24. As expected, D_2 and HD are practically not released from specimens not exposed to a deuterium plasma.

After exposure to a deuterium plasma, both the stress-relieved and non-annealed specimen (see panels (c) and (d) in Figure 8.24) release a significant amount of D_2 and also some HD during TDS. The H_2 release spectrum is similar in shape and magnitude for both non-annealed specimens, whether exposed to a deuterium plasma or not. On the other hand, the specimen that was not annealed

before plasma exposure released only about half as much D_2 as the corresponding annealed specimen. The release of HD from the non-annealed specimen, which released significant amounts of both D_2 and "natural" H_2, is somewhat larger than for the stress-relieved specimen, which released more D_2 but only very little H_2. Yet, the release of HD is much *smaller* than that of both H_2 and D_2. This means that H and D atoms reaching a free surface of the specimen predominantly recombine with atoms of the same isotope. This can be explained by assuming that the tungsten is initially more or less homogeneously saturated with H. When one surface of the specimen is bombarded by D ions, they gradually replace the trapped H in an isotope exchange process driven by the large excess of D. As mentioned before, this process is slower than the uptake of D by empty traps, which explains the significantly smaller D inventory in a non-annealed specimen. When the plasma exposure stops, H has been largely replaced by D up to a certain depth (at most about 35 μm judging from diffusion-trapping simulations) below the exposed surface. Still, H saturates the rest of the specimen. During TDS, D_2 is released predominantly from the *front* surface that was exposed to the plasma, since the trapped D is concentrated close to this surface. H atoms, on the other hand, detrap throughout the bulk of the specimen, save for the region where they have been displaced by D. Accordingly, H_2 can be expected to detrap first from the unexposed *rear* side of the specimen. At the exposed surface, the mobilised H atoms have to travel a longer distance before they can recombine and desorb than the D atoms. Most H even originates from deep inside the bulk of the specimen, which explains the large high-temperature tail of the H_2 release. The consequence of this model is that most H and D atoms cannot recombine into HD because in a first stage, they leave the specimens through opposite surfaces. A large part of the H_2 desorption is also delayed to a point where almost all D has already left the specimen because most H atoms are trapped deep inside the bulk and have to travel a long way to the surface.

8.5. Results of the "Ramp-and-Hold" experiments

8.5.1. Variation of the heating rate

Figure 8.25 shows measured TDS spectra of stress-relieved tungsten specimens implanted with a fluence of 6×10^{24} D m^{-2} at an ion energy of 38 eV and at a temperature of 370 K for different heating rates. Since the desorption rate is

much lower for slow heating rates, it was normalised to the heating rate for all spectra. This renormalisation is necessary to yield the same total amount of deuterium when integrating over the temperature axis as when integrating over time. Accordingly, the unit of the release rate is transformed from $D/(m^2s)$ to $D/(m^2K)$.

It can be clearly seen that the desorption spectrum shifts towards higher temperatures for faster heating rates. Redhead proposed a method to derive the energy barrier for the release of gases from this peak shift [91]. For a first-order process and a constant heating rate β, the temperature T_{peak} at which the desorption peak is observed and the energy barrier E_b are related as follows:

$$\frac{E_b}{k_B T_{peak}^2} = \frac{\nu}{\beta} \exp\left(-\frac{E_b}{k_B T_{peak}}\right). \tag{8.2}$$

ν is the frequency pre-factor for the desorption process. Redhead then suggests plotting β against T_{peak} on a double logarithmic graph and obtaining E_b from the slope $\mathfrak{m}$:

$$\mathfrak{m} = \frac{d\left(\ln\beta\right)}{d\ln\left(T_{peak}\right)} = 2 + \frac{E_b}{k_B T_{peak}}. \tag{8.3}$$

It should be noted this original notation is, in a strict sense, not correct since the arguments of the logarithms are not unitless, but it will yield the correct result if β is entered in K/s and T_{peak} in K. While with this relation E_b can be determined *independently* from ν, it has the problem that T_{peak} appears on the right hand side of the equation, i.e., the slope of the curve depends on T_{peak}. Because the range of peak shifts is usually only of the order of 10% of T_{peak}, the points still lie close to a straight line. Nevertheless, the problem remains which value of T_{peak} to choose when solving equation (8.3) for E_b.

Falconer *et al.* [24] suggest an elegant alternative to Redhead's method for deriving E_b from the peak shift due to heating rate variations: When plotting $\ln(\beta/T_{peak}^2)$ against $1/T_{peak}$ — with the same caveat for the units as in equation (8.3) — the data points ideally lie on a straight line with the slope $\mathfrak{m} = -E/k_B$. This can be seen by transforming equation (8.2) into

$$\ln\left(\frac{\beta}{T_{peak}^2}\right) = -\frac{E_b}{k_B}\frac{1}{T_{peak}} + \ln\left(\frac{k_B}{E_b}\nu\right). \tag{8.4}$$

and calculating the derivative

$$\mathfrak{m} = \frac{d\left(\ln(\beta/T_{peak}^2)\right)}{d\left(1/T_{peak}\right)} = -\frac{E_b}{k_B}. \tag{8.5}$$

This relation also yields E_b without knowledge of the frequency pre-factor ν. Falconer *et al.* even showed that equation (8.5) is valid for *any non-negative reaction order* [24]. In a comparative survey of methods for the analysis of thermal desorption spectra, de Jong *et al.* [18] credited the method with an adequate accuracy for E_b. Its main merit is that it requires only very little prior knowledge about the investigated system and is easy to apply once a set of TDS spectra acquired at different heating rates is available.

Strictly speaking, Redhead's as well as Falconer's method were developed for the desorption or decomposition of gases directly from a thin adsorbate layer and do *not* consider diffusion at all. Because of that, TDS spectra were also simulated using the diffusion-trapping model discussed in section 3.3 to cross-check the results from the Falconer method. The simulations used exactly the same temperature ramps (including all non-linearities) as in the experiments. The resulting spectra are shown in Figure 8.26 and are re-normalised like the measured spectra. To account for deuterium losses during specimen storage, the simulated spectra have been downscaled to two thirds. The effect of specimen storage is discussed in more detail in section 8.5.2. The main desorption peak at around 600 K is reproduced well.

Figure 8.27 shows a Falconer plot for the positions of the main desorption peaks of the spectra shown in Figure 8.25. The resulting energy barrier is $E_b = 1.25 \pm 0.11$ eV. Peak positions extracted from simulated TDS spectra with binding energies of 0.7, 1.2 and 2.2 eV (with the 1.2 eV trap retaining most of the deuterium) and different detrapping attempt frequencies ν_{detrap} are also included into the plot.

While the experimental peak positions showed quite some scatter, the positions of the main desorption peaks derived from simulated spectra lie almost perfectly on a straight line in the Falconer plot. Applying equation (8.5) yields $E_b = 1.22 \pm 0.02$ eV. This is only minimally higher than the binding energy of 1.2 eV of the main trap that entered into the model, and also matches the result from the experimental data within the measurement accuracy. The small deviations can be due to the non-linearities of the temperature ramps as well as to the
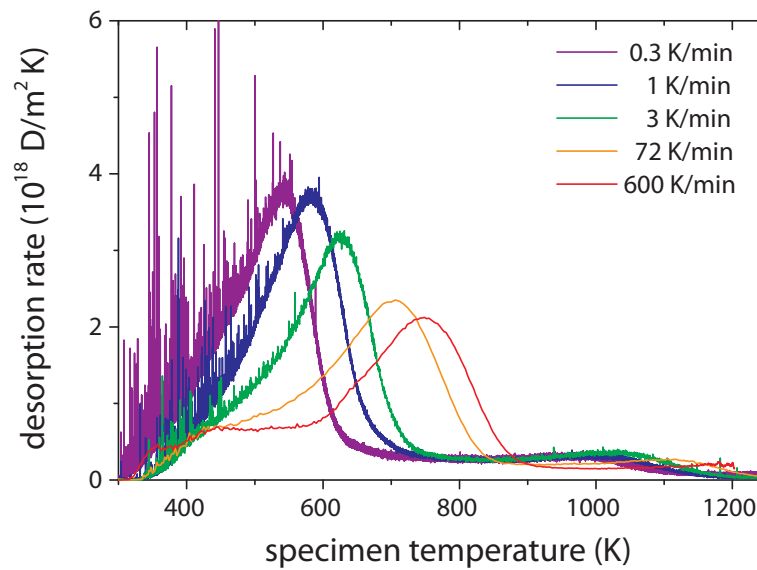
Figure 8.25. Selection of D_2 release spectra from stress-relieved tungsten implanted with 38 eV/D ions up to 6×10^{24} D m^{-2} at a temperature of 370 K. The legend indicates the heating rate in the vicinity of the main desorption peak (i.e., at ≈ 600 K). Spikes in the low-temperature part of the spectrum are due to rupturing of blisters filled with D_2 gas.
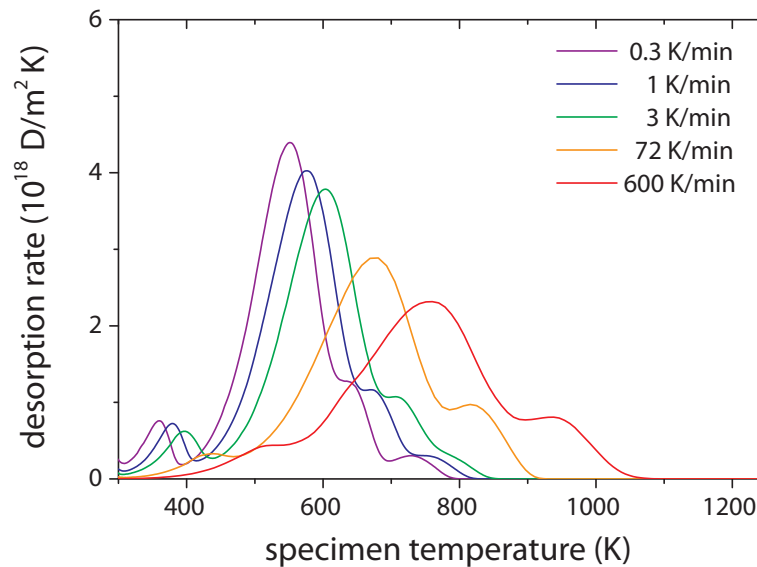

Figure 8.26. Selection of D_2 release spectra simulated with a diffusion-trapping model for the same conditions as indicated in Figure 8.25. All spectra have been downscaled to 2/3 to account for deuterium losses during storage. Please keep in mind that the specimens in the simulation have only 1/4 of the total thickness of real specimens and a strongly simplified density of sites model.

intrinsic inaccuracy of the method, which was investigated by de Jong *et al.* [18]. Therefore, one can conclude that for the present system of hydrogen in tungsten, the Falconer method yields a good estimate of the main trap energy even in a system that includes diffusion from the bulk to the surface, while eliminating the uncertainty of the frequency pre-factor ν and the order of the desorption reaction.

Looking at equation 8.4, it should be possible to calculate ν from the intercept of the straight line with the y-axis once E_b is known. Applying this to simulation results where the attempt frequency for detrapping ν_{detrap} is a known parameter, the resulting values for ν are always several orders of magnitude too low. In contrast to the trap energy, the attempt frequency for detrapping ν_{detrap} accordingly cannot be directly determined by this method. It is likely that the frequency pre-factor ν calculated with equation (8.4) is instead an *effective* value that includes the time lag due to diffusion. By iterative variation of ν_{detrap}, while keeping the trap energies and concentrations constant, experimental and simulated data points could be brought to a good agreement, as Figure 8.27 shows. By this method, ν_{detrap} was determined to be very close to 6.6×10^{11} s^{-1}, and certainly within the range of 3.3×10^{11}–1.0×10^{12} s^{-1}. This set of parameters, i.e., a main trap energy of 1.25 ± 0.11 eV and $\nu_{detrap} = 6.6 \pm 3.3 \times 10^{11}$ s^{-1}, is *unique* thanks to the determination of the binding energy independently from the attempt frequency, and simultaneously fits the main desorption peak of *all* TDS spectra.

On closer inspection of the experimental spectra in Figure 8.25 and of the simulated ones in Figure 8.26, a surprising detail becomes apparent: The small peak on the low-temperature flank of the main desorption peak that is clearly visible for fast heating rates *disappears* at slower heating rates in experimental spectra. In simulations, on the other hand, this peak is nearly obscured by overlap with the main peak at fast heating rates and becomes more clearly visible as the heating rate *decreases*. Intuitively, one would expect the behaviour seen in the simulations: At fast heating rates, peaks become broader because of the time lag of deuterium being trapped deeper inside the specimen, while at slow heating rates the shape of the desorption spectrum should approach a representation of the true binding energy distribution. A possible explanation for the counter-intuitive behaviour of the low-temperature peak can be found in the large desorption bursts that become visible at slow heating rates. As discussed in section 8.2.2, these are due to the rupturing of blisters. It could recently be shown that this is a stochastic process with a constant burst rate per temperature interval, independent of the heating
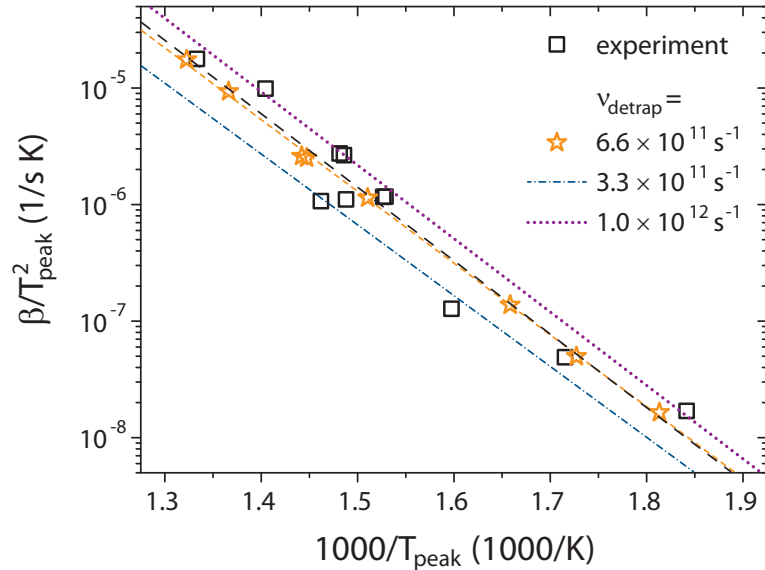
Figure 8.27. Falconer plot of $\ln(\beta/T^2_{peak})$ versus the inverse of the main desorption peak temperature $1/T_{peak}$. Data points extracted from both experimental and simulated spectra are shown. The main trap binding energy of 1.2 eV used in the model is close to E_b derived by equation (8.5) for all simulated results and matches the value derived from the experimental data points within the measurement accuracy.

rate, and that the size distribution of the bursts follows an exponential distribution [67]. This allowed also the simulation of these bursting events at different heating rates and for different integration times of the measurement equipment. As Figure 8.28 illustrates, a fast heating rate of, e.g, 15 K/min together with a slow acquisition rate and a long integration time can lead to the overlapping of individual bursts. The result is a significant offset of the desorption signal, which is only perturbed by fluctuations with a much smaller amplitude than the bursts themselves. This can in principle go so far that one has the impression of an additional, noisy desorption peak. Indeed, a close look at the low-temperature part of the measured desorption spectra shows an apparent noise level that is much higher than one would expect at the average signal level in this temperature range. This is the residual signature of the bursts that were clearly visible for the slower heating rates.

Therefore, one can conclude that the true binding energy distribution of deuterium trapped in stress-relieved tungsten is in fact rather represented by a roughly triangular shape, like it can be seen for the slowest heating rates in Figure 8.25. The small but clearly distinguishable low-temperature peak in the sim-
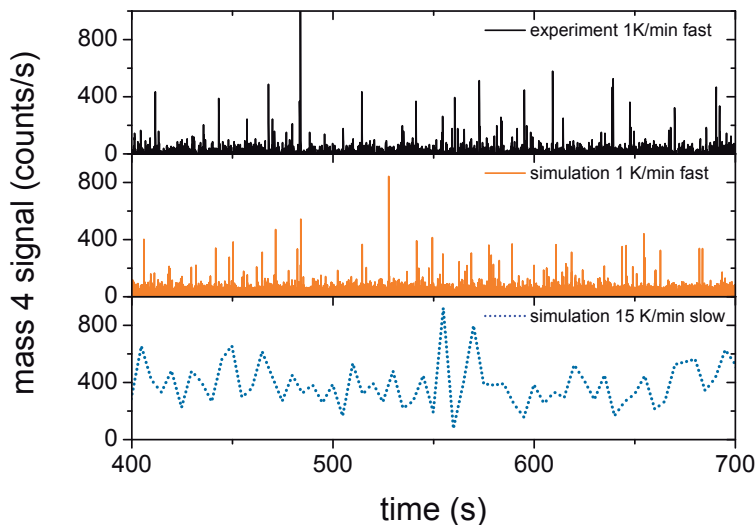
Figure 8.28. Measured and simulated D_2 bursts due to rupturing blisters [67]. The measurements in the top panel were taken at a heating rate of 1 K/min with a high acquisition rate of more than 10 Hz and a short integration time of 50 ms. The simulation in the middle panel was performed for the same conditions. The bottom panel shows the effect of overlapping blister bursts at a faster heating rate of 15 K/min and a slower acquisition rate of about 0.2 Hz with a long integration time of 1 s. The same acquisition conditions were used for the measurements presented here.

ulated spectra shown in Figure 8.26 is most likely too narrow, since the diffusion-trapping model approximates all the binding sites for deuterium in the strain fields of dislocations with one single, monoenergetic trap with a low binding energy of 0.7 eV (see section 3.3).

For a similar reason, the high temperature shoulder of the spectra is also not modelled as well as the main peak. The reason is that the binding energy of the traps in the amorphised surface layer is in reality not one discrete value, but rather a broad distribution of binding energies. A much better model for the density of sites distribution in this zone would be a Gaussian distribution, as suggested by Kirchheim [45] (see also Table 2.1). Unfortunately, this cannot be treated in current full-scale diffusion-trapping models, including the one used here (see section 3.3). Another issue in the high temperature part of the desorption spectrum is the desorption from the rear side of the specimen, i.e., the side that was not exposed to the plasma. In order to keep computation times manageable while preserving the accuracy and stability of the numerical solution, the specimen thickness was reduced from about 800 to 200 μm for the simulations. Because of that, desorption from the rear side occurs earlier and more strongly compared to

actual specimens. Besides these deviations due to necessary simplifications made for the diffusion-trapping model, the simulated spectra match the experimental ones quite well in terms of the absolute magnitude as well as of the peak positions.

8.5.2. Interrupted temperature ramps

As described in section 7.6, TDS experiments were also performed with interrupted temperature ramps in order to deconvolve the influence of the binding energy and of the depth distribution of the deuterium in the specimens. As Figure 8.29 shows, pull-off experiments at 470 K have little influence on the main desorption peak in a subsequent full TDS run. Only about up to about 400 K a nearly complete depletion of the trapped deuterium is observed. For asymptotic heating up to 470 K, i.e., holding at this temperature for approximately 90 minutes, the spectrum in the second TDS run looks remarkably similar to the one after the pull-off experiment. The main peak position is still at the same temperature, but the peak is about 10% lower. Also, the depletion at temperatures below 470 K is slightly stronger, but still a measurable amount of deuterium is released between 400 and 470 K in the second TDS run. In diffusion-trapping simulations this behaviour is quite well reproduced in many aspects. The main difference is that in simulations, mainly the onset of desorption during the second, full TDS run is significantly retarded for asymptotic heating: desorption does not start before 470 K. On the other hand, the reduction of the peak desorption is noticeably smaller in the simulation than in the experiment. From these differences the following conclusions can be drawn: The 1.2 eV trap is barely depleted at 470 K in simulations. The retardation of the onset of desorption is therefore due to depletion of 0.7 eV traps deeper below the surface. On the other hand, the experimental observations that the main peak is depleted while the onset of desorption is barely affected indicate a loss channel of deuterium from higher-energy traps at surprisingly low temperatures.

Figure 8.30 shows that after a pull-off at 660 K, i.e, approximately at the temperature of the main desorption peak, desorption starts at about 450 K in the second TDS run. Below this temperature, the traps are practically completely depleted. Also, the traps in the main peak itself are depleted to about one third of the initial value at the pull-off temperature. Beyond the main peak, again virtually no traps are depleted. Asymptotic heating to 660 K with subsequent holding at that temperature for 90 minutes practically completely depletes the main desorp-
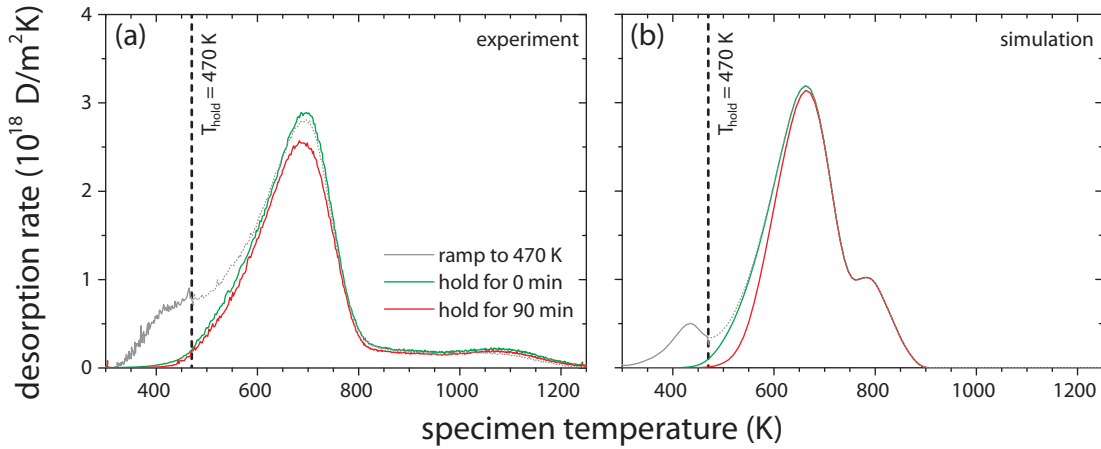
Figure 8.29. Experimental (a) and simulated (b) TDS spectra with temperature ramps inter-
rupted at 470 K. The heating rate was 30 K/min around the main desorption
peak. Each panel compares a pull-off (0 min holding time) and an asymptotic
heating (90 min holding time) experiment. Simulated spectra have been down-
scaled to 2/3 to account for losses during storage.

tion peak. Only the high-temperature shoulder remains and is nearly unaffected.
A similar qualitative behaviour is seen in diffusion-trapping simulations of these
experiments: A significant part of the deuterium in 1.2 eV traps is still retained
in the specimen after a simulated pull-off experiment. However, the onset of deu-
terium release in the second, full ramp starts about 100 K later in the simulation
than in the experiment. After asymptotic heating and holding for 90 minutes, the
1.2 eV trap is nearly completely depleted, while the high-energy trap at 2.2 eV
has only lost about 1.5% of its deuterium inventory during the holding. The small
high-temperature peak during the second TDS run is then to a large part made
up from release from the 2.2 eV trap, as indicated by the dashed line in Fig-
ure 8.30b. There is still a remarkable contribution from deuterium that has been
redistributed to 1.2 eV traps far below the implanted surface during the holding
at 660 K, which is now predominantly released from the rear side of the speci-
men. These results indicate that the high-temperature shoulder seen in measured
TDS spectra is at least partly due to a distribution of high-energy traps, but may
also contain a non-negligible fraction of rear-side release from lower-energy traps.
Due to the larger thickness of the real specimens, this contribution is distributed
over a larger time span and, accordingly, temperature range, but with a smaller
amplitude.

Interrupted heating ramps also offer the possibility to investigate the depth dis-
tribution of the deuterium remaining in the specimen by NRA. Figure 8.31 shows
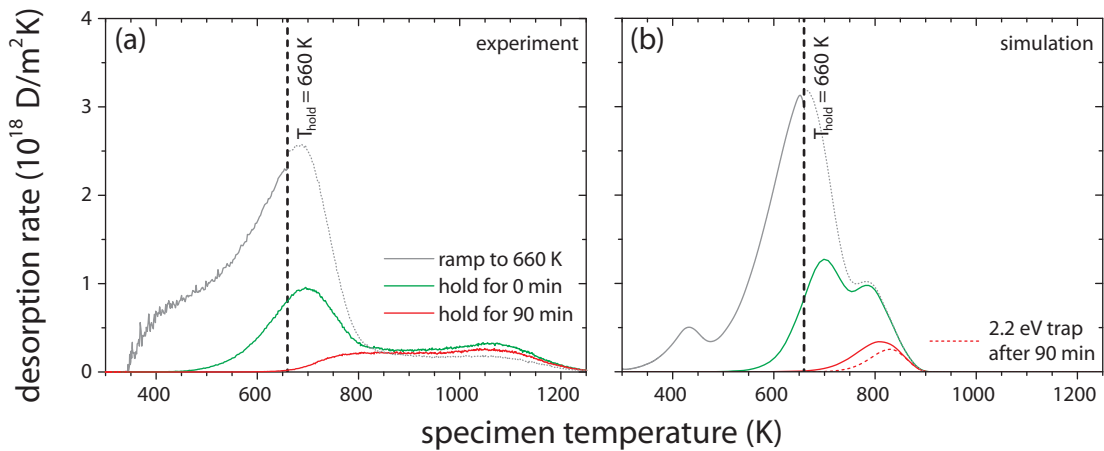
Figure 8.30. Experimental (a) and simulated (b) TDS spectra with temperature ramps interrupted at 660 K. The heating rate was 30 K/min around the main desorption peak. Each panel compares a pull-off (0 min holding time) and an asymptotic heating (90 min holding time) experiment. Simulated spectra have been downscaled to 2/3 to account for losses during storage. The dashed line in panel (b) indicates the fraction of D released from high-energy traps.

such depth profiles acquired after pull-offs at 470 K and 660 K. For comparison, depth profiles measured two days after plasma exposures and after two months of storage in vacuum at room temperature, i.e., the state before TDS, are also shown. Remarkably, the effect of the storage time is nearly the same as that of partial TDS runs: In each case, the shape of the depth profile beyond the surface peak is practically conserved, only the absolute magnitude is reduced. The surface peak itself only starts to deplete significantly at 660 K. For the partial TDS runs, this could be qualitatively reproduced by diffusion-trapping simulations, as panel (b) in Figure 8.31 illustrates. The underlying mechanism is that the deuterium concentration profile closely follows the trap concentration profiles. While these evolve during implantation, they are kept constant for the simulation of TDS. The surface peak starts depleting at higher temperatures than the bulk inventory because of its high binding energy. The simulation also allows to study the deuterium depth profile beyond the range of NRA. This shows that while the deuterium concentration gradually depletes within the first 12 μm due to annealing, the deuterium at the same time diffuses far into the bulk at higher temperatures: In the initial state, the deuterium has diffused up to 35 μm below the implanted surface. After a pull-off experiment at 660 K, it reaches an almost three times larger depth, although at a considerably lower average level.

The experiment and the simulation also differ from each other in some aspects.

For annealing up to 470 K, the measured depletion of the deuterium inventory is significantly stronger than the simulated one. The reason is that the 1.2 eV traps, which bind most of the deuterium in the simulation, barely release any deuterium at this temperature. This coincides with the conclusion drawn from the analysis of the TDS spectra shown in Figure 8.29 that in real specimens, there is a depletion channel for high-energy traps also at low temperatures. Also, while the measured and simulated depth profiles after annealing up to 660 K match rather well for depths beyond about 1 μm, there are some notable differences in the near-surface region: The surface peak already starts to deplete in the experiment, while it is yet unaffected in the simulation. Furthermore, the measured depth profile shows signs of the local minimum after the surface peak becoming shallower at 660 K. In the simulation, on the other hand, this region is depleted preferentially and the minimum deepens.
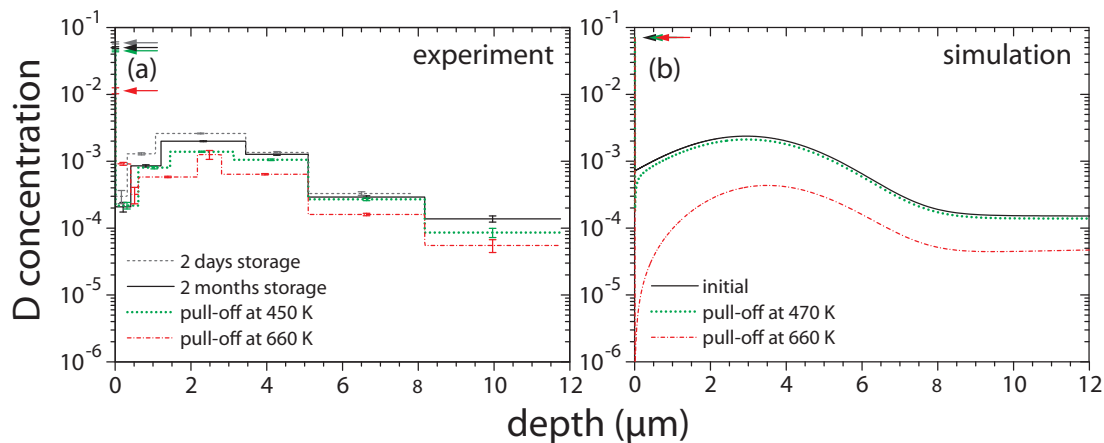

Figure 8.31. Measured (a) and simulated deuterium concentration depth profiles in stress-relieved tungsten implanted at 370 K with an ion energy of 38 eV/D to a fluence of 6×10^{24} D m^{-2}. Panel (a) shows depth profiles measured 2 days and 2 months after plasma exposure, as well as after pull-off experiments at 470 and 660 K. Panel (b) shows the initial state after a simulated D implantation as well as the result of pull-off experiments at 470 and 660 K.

While the diffusion-trapping model can at least qualitatively explain the stiffness of the concentration profile during annealing, it fails to reproduce the losses during long-term storage for two months at room temperature: At 300 K, the 0.7 eV traps can be practically fully depleted, but they contain less than 10% of the total inventory in simulations. The 1.2 and 2.2 eV traps, on the other hand, do not change their population during simulated storage. A real specimen stored for two months at room temperature only contains two thirds of the deuterium inventory measured two days after implantation, i.e, the loss is three times as much as in

the simulations (see Figure 8.31a). This means that at least the 1.2 eV trap must also lose a significant amount of deuterium. Indeed, the investigation of storage time effects on TDS spectra by Moshkunov *et al.* [72] also showed that the high-energy traps are depleted and agree on the magnitude of the total deuterium loss, too.

Like the observations made above for a specimen annealed up to 470 K, this effect cannot be explained by uncorrelated traps as they are assumed in diffusion-trapping models. A mechanism that could explain the observed behaviour is that interstitial solutes in metals tend to form so-called "dislocation atmospheres" [92] due to trapping of solute atoms in the tensile strain field particularly of edge dislocations. These aggregates of solute atoms are called "atmospheres" because they are in a dynamic equilibrium with the surrounding lattice: In a stationary state the rate of solute atoms entering the atmosphere balances the rate of particles leaving it, while the average solute density in the atmosphere is higher than in the surrounding lattice by a ratio that depends on temperature. At higher temperatures, the evaporation rate increases and the atmosphere becomes thinner. In this sense, a fitting analogy to the deuterium release observed here is, in fact, the atmosphere of a planet: Gas molecules in the upper layers are only weakly bound by gravity and can easily escape into space. This evaporation slowly reduces the *average* density of the atmosphere, i.e., also the density near the ground where the gravitational force is stronger. If the energy input by solar irradiation would increase, the evaporation would become faster. Eventually even gas molecules close to the ground would receive enough energy to overcome gravity and the planet would completely lose its atmosphere. On the scale of the lattice constant of tungsten, the strain field of a dislocation leads to correlated saddle points between interstitial sites: A site inside the strain field is not surrounded by "normal" interstitial sites, but by sites with similarly reduced potential for the deuterium (see also the potential trace for a dislocation shown in Table 2.1). One can therefore expect that the energy barrier for transition between such sites is also lower than between isolated traps of the same binding energy.

Looking again at Figure 8.8, particularly at the fluences of 3×10^{23} and 6×10^{24} D m^{-2}, one finds data points (with dashed outlines) with a noticeably lower retention. It was already mentioned in section 8.2.1 that this is due to a slower cool-down to room temperature after the plasma exposure had stopped. The effects of a finite cool-down time are closely related to interrupted TDS runs as they were described above — the main difference is that the temperature ramp

is reversed, i.e., its slope is negative. Based on the parameter set found by help of the "Ramp-and-Hold" experiments described above, cooling of a specimen after exposure could also be simulated.

In these simulations, deuterium is lost predominantly from low-energy traps in regions near the surface for exposures performed at 370 K. Using the model parameters determined in section 8.5.1, the fraction of the total inventory that escapes from the specimen during cool-down is of the order of a few percent. Looking at how much deuterium is lost from a specimen even during storage at room temperature, one can expect that the total magnitude of the deuterium loss during cool-down is also somewhat underestimated by the model. The experimentally observed magnitude of the loss due to slower cooling suggests the same.

At higher implantation temperatures, one can expect the amount of deuterium leaving the specimen while it cools to room temperature to be considerably higher, since also higher-energy traps can then release deuterium at significant rates. This means that great care has to be applied when trying to measure the deuterium retention at elevated temperatures, because the cool-down process probably must be considered as one of the main sources of error. Fortunately, the uncertainties due to cool-down could be avoided for the comparison of different microstructures under the same loading conditions since the specimens were exposed and, accordingly, also cooled simultaneously. Afterwards, the specimens were stored together and analysed within a comparatively short time.

8.6. TEM investigations of defect evolution due to hydrogen exposure

The partially recrystallised TEM specimen exposed to a deuterium plasma with an ion energy of 38 eV/D was still very well transparent afterwards and had not suffered any significant loss of thin areas due to sputtering or overheating. In fact, as the STEM images in Figure 8.32 illustrate, the dislocation and grain structures of the specimen did not change at all due to the plasma exposure. All dislocations found in images that were taken before plasma exposure were still found in the same place afterwards. New dislocations also had not formed. The most obvious differences between images taken before and after plasma exposure were due to differences in the orientation of the specimen: The orientation contrast of

the grains is different in some cases, and there is also a small perspective distortion due to different tilt angles, which were necessary to achieve good diffraction contrast.
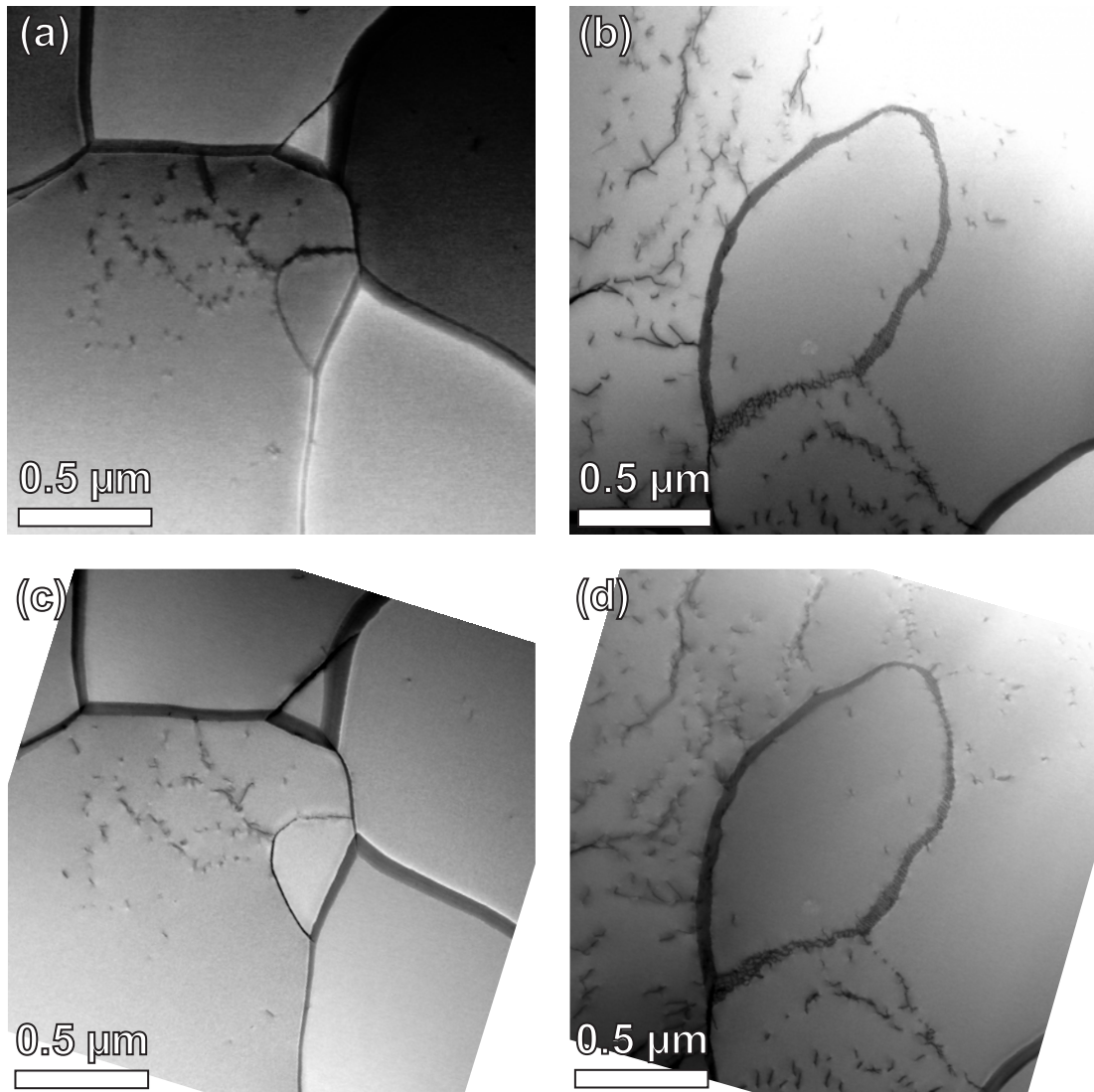

Figure 8.32. STEM images of a partially recrystallised specimen acquired before and after exposure to a deuterium plasma with an ion energy of 38 eV/D to a fluence of $\approx 1.5 \times 10^{23}$ D m^{-2}. The specimen holder was cooled to ≤ 300 K during the exposure. (a) and (c) respectively (b) and (d) depict the same area before and after exposure. The only differences in the images are due to re-orientation of the specimen.

A subtle difference was found in HRTEM images acquired right at the edge of the perforation. As Figure 8.33 shows, the lattice fringes of the tungsten specimen extend almost right to the edge. After exposure, however, a broad amorphous

rim is visible. This could be an indication of the thin amorphised layer created
by energetic impurity ions from the plasma, as discussed in section 8.3.2. This
layer should only be visible in areas that have a comparable thickness. In thicker
areas, the tungsten lattice fringes from the undisturbed material would obscure
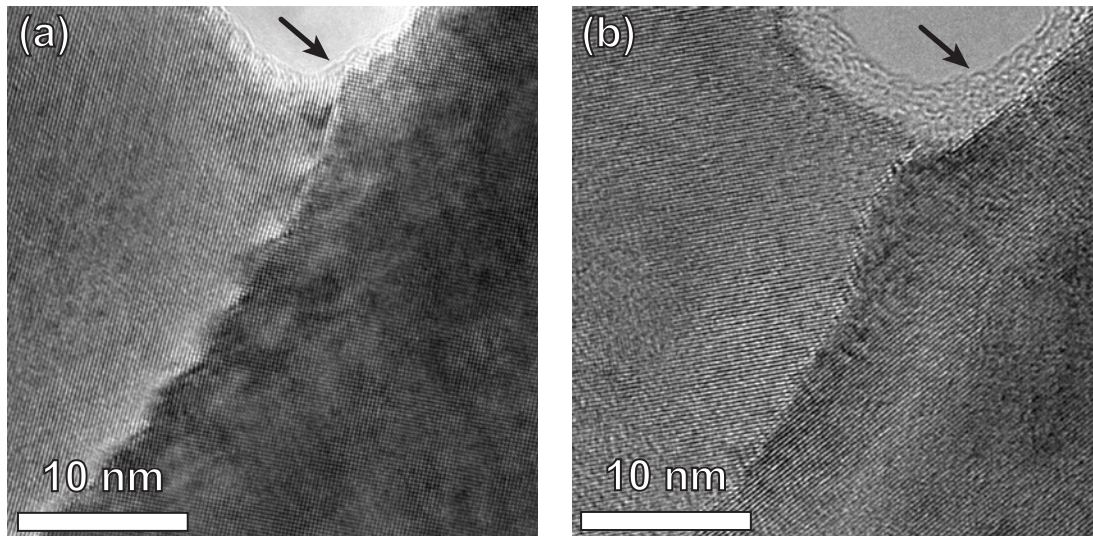the amorphous layer.

Figure 8.33. HRTEM images of partially recrystallised tungsten (a) before and (b) after exposure to a deuterium plasma with an ion energy of 38 eV/D to a fluence of $\approx 1.5 \times 10^{23}$ D m^{-2} at ≈ 300 K. The micrographs depict similar regions at the thin edge of the specimen. Note the width of the amorphous rim that is indicated by the arrows.

Exposure of stress-relieved and partially recrystallised tungsten to a hydrogen
atmosphere in an ETEM yielded very similar results to the plasma exposure:
Dislocations neither appeared, disappeared nor moved at all when up to 0.7 kPa
of hydrogen gas were introduced into the specimen chamber. This is shown representatively by the image pairs in Figures 8.34 and 8.35. The only reaction of the
specimen to the H$_2$ atmosphere was that it started bending when the hydrogen
pressure began to rise. The bending stagnated when the hydrogen pressure stabilised at its final value, and reverted back to the initial state when the hydrogen
was pumped away. The bending was a little stronger for the stress-relieved tungsten. Continuous irradiation of the specimen with a strongly focused STEM probe
under H$_2$ atmosphere for one hour also did not have any effect on dislocations.

One could interpret the observed bending effect as an indication of hydrogen
being absorbed by the specimen, possibly assisted by the high-energy electron
beam. On the other hand, introduction of He gas, which is virtually insoluble in

any metal, also produced a bending effect, so this could also be due to a pressure difference between the front and the rear side of the specimen. In that light, the difference in bending between the stress-relieved and partially recrystallised specimens could also be simply due to a different mechanical stiffness.

One can conclude from both types of TEM experiments that the mere *presence* of hydrogen or deuterium does not lead to the emission of dislocations and not even to any changes of the dislocation network in a thin, electron-transparent TEM specimen made of tungsten under the conditions investigated here. It should be noted, though, that irradiation with protons at energies of several keV (i.e., above the displacement threshold) *are* able to produce defects — particularly dislocation loops — in tungsten [97].

For the case of low-energy deuterons, which is presented here, there are some fundamental differences between an electron-transparent thin foil and a bulk specimen: One is that any stress due to implanted (respectively absorbed) hydrogen or deuterium might be redistributed differently in the thin foil. The other difference is that there are only very few grain boundaries parallel to the exposed surface of the foil because its thickness (several 10 nm) is much smaller than the average grain size (more than 1 μm). However, the investigation of blisters forming on stress-relieved bulk specimens at 38 eV/D showed that these always form at such grain boundaries (see, e.g., Figure 8.5). This prevents the formation of such blisters on the thin areas of TEM specimens.

The results presented in this section can be seen as strong evidence that dissolved hydrogen isotopes do not produce dislocations in tungsten *directly*. Accordingly, additional effects such as the expansion of blister cavities are necessary to produce these defects. So far, it was not possible to verify this directly by cross-sectional TEM of the blister zone in plasma-exposed specimens. To date, all well-established methods for the production of TEM cross-sections failed to produce specimens of sufficient quality from tungsten.
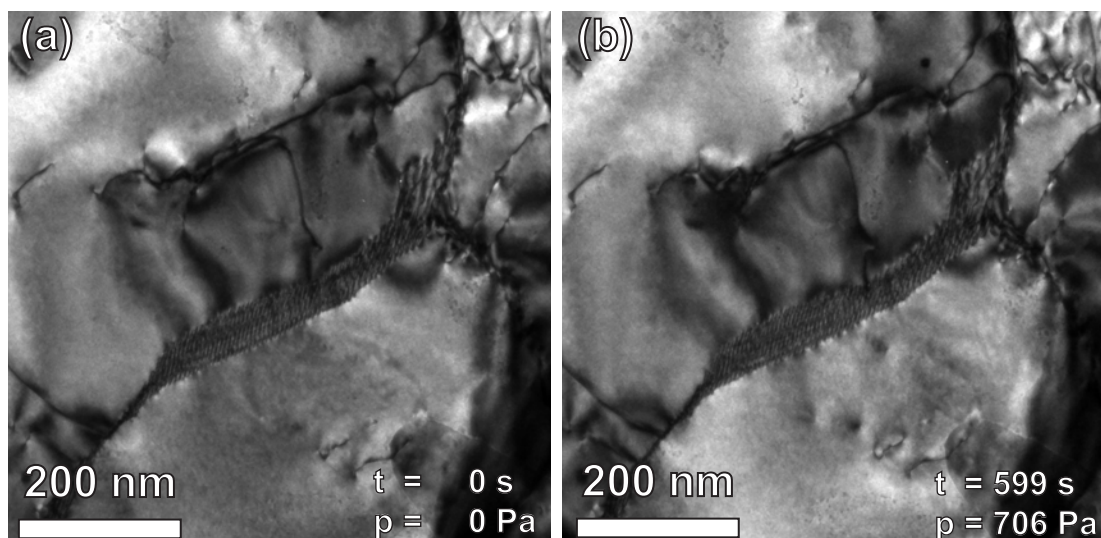
Figure 8.34. TEM specimen prepared from stress-relieved tungsten imaged in an environmental TEM. (a) shows the specimen before introduction of H_2 gas. (b) shows the same area after increasing the H_2 pressure to 706 Pa within 6 minutes and holding the pressure for further 4 minutes. During the ramp-up of the pressure, the specimen bent, but remained otherwise unchanged.
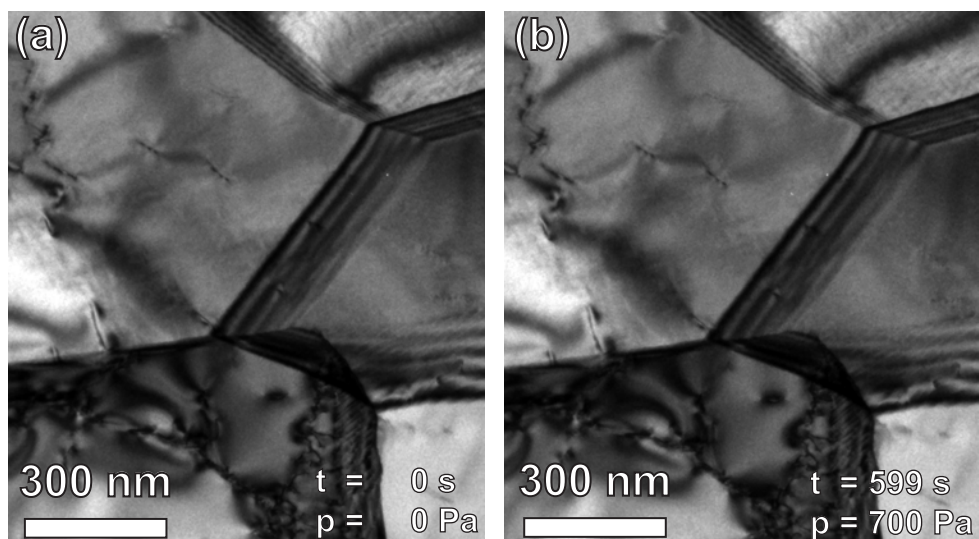

Figure 8.35. TEM specimen prepared from partially recrystallised tungsten imaged in an environmental TEM. (a) shows the specimen before introduction of H_2 gas. and (b) shows the same area after increasing the H_2 pressure to 700 Pa within 4 minutes and holding the pressure for further 6 minutes. Apart from bending, the specimen did not undergo any visible changes.

9. Synopsis and outlook

This chapter brings together the results of the individual experiments introduced in chapter 7 and discussed in chapter 8. It will be shown how and why the tendencies of deuterium retention and blistering correlate with the experimental parameters such as temperature, fluence and ion energy, as well as with each other. Together with the knowledge of the microstructure of the specimens (see chapter 6), some of the key mechanisms of deuterium retention in tungsten due to plasma exposure will be elucidated. Where appropriate, a brief outlook on possible further investigations based on the findings gained in this thesis is also given.

9.1. Balance of bulk diffusion and surface losses

As it was described in section 8.1, the variation of the deuterium inventory with temperature is considerable. In the temperature range between 300 and 750 K, the total inventory determined by thermal desorption measurements varies by up to about one order of magnitude: The maximum value for tungsten stress-relieved at 1200 K of up to nearly 8×10^{20} D m^{-2} is reached at 370 K for an ion energy of 38 eV and an incident fluence of 6×10^{24} D m^{-2}. At this temperature, all specimens showed a maximum of retention. At 750 K, the retention in stress-relieved tungsten was down to 7×10^{19} D m^{-2} at the same fluence. Throughout the whole temperature range, stress-relieved tungsten retained the most deuterium, while fully recrystallised tungsten displayed the smallest retention. Both types, i.e., annealed at 1700 or 2000 K, had approximately the same inventory. It was 2–5 times smaller than in stress-relieved tungsten. The values for tungsten partially recrystallised at 1500 K were found in between those for stress-relieved and fully recrystallised tungsten.

The deuterium inventories within the first ≈ 8 μm as determined by NRA (for a maximum ^{3}He energy of 4500 keV), i.e., the average local concentrations, vary

over up to about three orders of magnitude with the temperature. This is even more than the variation of the total inventories (see Figure 8.1). For stress-relieved tungsten, a clear maximum was also found at 370 K, while for the other materials the inventory was about equal or even slightly larger at 300 K. At 750 K, the deuterium was only barely detectable by NRA anymore, regardless of the microstructure.

The large difference between the deuterium found within the first couple of microns below the plasma-exposed surface and the total inventory at elevated temperatures points out the importance of deep diffusion for deuterium retention in tungsten. This is expected and was also observed by various other researchers (e.g., [1, 37, 82]).

The equilibrium concentration is close to zero for an undistorted tungsten lattice — at the plasma working pressure of 1.0 Pa and temperatures below 1000 K it is less than 10^{-9} according to Frauenfelder's values [27]. Accordingly, the achievable concentration is practically fully determined by the local density of traps. These are quickly saturated close to the surface, so further ones can only be reached by diffusion. The temperature dependence of interstitial diffusion is governed by the energy barrier between interstitial sites, which is overcome by classical, thermally activated jumps at temperatures above 200 K [40]. Using Frauenfelder's value of 0.39 eV for this barrier, one finds a variation of almost 4 orders of magnitude between little more than 10^{-13} and nearly 10^{-9} m^2/s within the temperature range of 300–750 K investigated here. On the other hand, traps release the deuterium bound to them also in a thermally activated process. Using a binding energy of 1.2 eV with a pre-factor of 6.6×10^{11} s^{-1} (see section 9.6), one finds an increase of the detrapping frequency by about 12 orders of magnitude, from $\approx 5 \times 10^{-9}$ (i.e., practically zero) to about 5×10^3 s^{-1}. Looking at these numbers, it is evident that at the same time as diffusion increases and transports the deuterium deeper into the bulk of a specimen, traps lose their ability to bind the deuterium. In other words, the balance of losses and diffusion determines the final deuterium inventory.

However, one parameter, which also affects this balance, was not investigated in this thesis: the ion flux. In the experiments performed here, it was about 10^{20} D m^{-2}s^{-1}. Significantly higher fluxes could not be reached with the PlaQ device (see section 4.1 and [65]), while at lower fluxes, high fluences are no longer attainable within reasonable time. However, one can still compare the temperature dependence of the deuterium retention observed here with values of other

researchers. The more recent results published by Alimov *et al.* (e.g., [5]) were performed at the same ion energy of 38 eV/D that was used here, but at a 100 times higher flux. Indeed, Alimov finds the maximum of deuterium retention at a higher temperature of about 480 K.

In order to investigate in detail the flux dependence of deuterium retention in tungsten (and correlated phenomena like blister formation) under otherwise identical conditions, a joint experimental campaign has been proposed: Several facilities for plasma exposure of tungsten specimens are supposed to expose tungsten specimens of the same type at fluxes between 10^{20} (PlaQ) and 10^{24} D m^{-2}s^{-1} (Pilot-PSI or Magnum-PSI[1]; see also [117]). The ion energies will be 20–40 eV/D. The target fluence will be 10^{26} D m^{-2} at a specimen temperature of 500 K. The joint experiment is necessary since no single existing facility can cover the whole flux range. These parameters are a compromise with respect to the range of ion fluxes: At very high flux, cooling of the specimen to approximately room temperature becomes extremely difficult. On the other hand, retention at low fluxes becomes very small at temperatures above 500 K, as it was shown here (see Figure 8.1). At fluxes in the range of 10^{22} D m^{-2}s^{-1}, 500 K is close to the temperature for maximum retention [5]. The high fluence of 10^{26} D m^{-2} is necessary so that the specimen can approach steady-state loading conditions under ion fluxes in the 10^{24} D m^{-2}s^{-1} range. Even then it will take only of the order of 100 seconds to reach this fluence. At 10^{20} D m^{-2}s^{-1}, this takes about 12 days of continuous plasma operation. Such a plasma exposure was only recently successfully performed at PlaQ, but the results are not yet evaluated.

9.2. Evolution of the specimen with fluence

9.2.1. Near-surface displacement damage by plasma impurities

It was shown in section 8.2 that the trap concentration in a tungsten specimen under deuterium plasma irradiation is not necessarily constant, but can evolve with the ion fluence. The most obvious example for this is the surface concentration maximum, which is barely visible at very low fluences in the 10^{22} D m^{-2} range, and saturates at very high deuterium concentration levels of the order of 1–10 at.% for high fluences at an energy of 38 eV/D and a temperature of

---

[1]FOM Institute for Plasma Physics, Rijnhuizen, The Netherlands

370 K during exposure. Similar concentration maxima near the surface were also frequently reported before (see, e.g., [1, 3, 13, 82]). Here, this concentration maximum was ascribed to displacement damage caused by energetic impurity ions from the plasma. These could also be detected in the specimen surface afterwards.

As it was shown in section 8.3.2, the amount of damage and accordingly the deuterium retention depends linearly on the bias voltage that is applied to the specimen during plasma exposure, respectively on the ion energy. Deuterium concentrations of more than 20 at.% were observed, which would correspond to similar defect concentrations as observed for so-called superabundant vacancies in, e.g., Pd and Ni [30]. Due to the limits of depth resolution achievable with the $D(^3He, p)^4He$ nuclear reaction [70], it is not yet clear if the increase of the deuterium concentration in the surface layer is actually due to more damage within a layer of constant thickness, or due to an increase of the thickness of the damaged layer. As discussed before, the latter explanation appears more likely because the ion stopping range also increases with the energy of the ions. It should be noted at this point that the effect of impurity ions could also depend strongly on their concentration in the plasma. In the case of intentional impurity seeding, the concentration can be sufficient to form a closed surface layer with a significantly different chemical composition than the bulk material (e.g., tungsten nitride or a similar compound). These layers can act as diffusion barriers preventing the re-emission of implanted deuterium [83].

Nevertheless, the defect concentrations near the surface must be very high in order to produce the observed results. It is likely that such high defect concentrations in tungsten can only exist with hydrogen reducing the defect formation energy, as suggested by Kirchheim [48], respectively by stabilising the defects. On the other hand, it could also be that such high defects are only stable as thin surface layers. It would therefore be very interesting to investigate the formation of radiation damage by fast neutrons, such as they are produced in nuclear fusion reactions, under simultaneous hydrogen loading. In this case, the damage would not only be produced in a thin surface layer, but evenly distributed throughout the bulk of the material. As a substitute for neutron irradiation (which inevitably leads to the complication of radioactive specimens), also self-implantation with multi-MeV tungsten ions, which have at least penetration ranges of the order of microns, could be used [109].

9.2.2. The role of blisters

Whenever blisters were found on the surface of a specimen, a distinct secondary maximum of the deuterium concentration was found in the same depth as the cavities corresponding to the surface features, which are depicted in Figures 8.5 and 8.20. Also, the maximum of blistering activity was always coincident with a maximum of the deuterium retention. Blistering on stress-relieved tungsten specimens was found to increase with fluence and stagnate at high fluences, as did the shape and magnitude of the secondary deuterium concentration maximum observed by NRA (see Figure 8.11). Together, these observations provide strong evidence that the formation of blisters locally increases the trap density.

On the other hand, only a few percent of the deuterium are found to be released as D_2 bursts due to rupturing blisters during TDS with sufficient time resolution [67]. Considering that blisters that collapsed during TDS are not re-inflated when the specimen is loaded with deuterium a second time, but the deuterium retention barely changes, one has to assume that these bursts indeed represent all (or at least most) of the D_2 gas stored in the cavities. This means that the deuterium is not primarily retained in gaseous form inside the blister cavities, as suspected, e.g., by Causey *et al.* [16], but in traps in the deformed material around them.

This would also help to explain the comparatively low pressure of the order of 100 MPa or less that was estimated from the opening of individual blisters by FIB and continuum mechanical calculations of the inflation and relaxation process [9]. Applying Sieverts' law (2.5) with Frauenfelder's solubility constant [27] of $9 \times 10^{-3} \exp[-1.04\text{eV}/(k_B T)]$ to the observed deuterium concentrations of the order of 10^{-4} to 10^{-3} at 370 K, the equilibrium pressure should be at least 14 orders of magnitude higher! This unrealistically high value can only be alleviated by traps reducing the occupancy of "normal" interstitial sites down to nearly zero. The importance of the mechanical deformation of the material associated with blistering for the production of lattice defects — i.e., traps for deuterium — was also pointed out by Alimov *et al.* [6]. The *direct* production of dislocations due the stress caused by the implantation of deuterium — i.e., *without* fracturing of the material — was suspected, e.g., by Ogorodnikova *et al.* [82]. However, this can be now considered rather unlikely because the experiments on hydrogen loading of transparent TEM specimens discussed in section 8.6 showed no indication for such a process.

It remains to be proven which type of lattice defect is responsible for the accumu-

lation of deuterium in the blister zone. Based on the correlation of the dislocation density with the deuterium retention (for details see section 9.5), dislocations are the most likely candidate. Most deuterium loading experiments were performed at 370 K, i.e., at elevated temperatures but below the BDTT. In this semi-brittle regime, crack-tip plasticity occurs [35]. This leads to the emission of dislocations particularly at the edges of blister cavities.

On the other hand, in Alimov's opinion [6] vacancies and vacancy clusters as well as voids, such as the blister cavities themselves, are responsible. At least the significant retention in the cavities seems rather unlikely based on the results presented here. To finally resolve the issue of the type and density of traps being produced in the vicinity of blisters, the direct observation of the dislocation density around blister cavities both in stress-relieved and recrystallised tungsten is necessary. As mentioned before, the preparation of cross-sectional TEM specimens of sufficient quality was not yet successful. A way out could be electron channelling contrast imaging (ECCI). Gutierrez-Urrutia *et al.* [36] have shown the potential for high-resolution imaging of dislocations with this method. The main advantage of this method for the present problem is that although a high-quality surface comparable to that of a TEM specimen is necessary to achieve this, the specimen does not need to be electron transparent. While electrochemical polishing was found to be unsuitable for the thinning of cross-section specimens, it works well for a *thick* cross-section. A recent first attempt to use ECCI for the imaging of dislocations in a thick region of an electropolished tungsten TEM specimen was already successful.

In order to understand the evolution of blisters and their associated trap sites, an integrated multi-scale model including the diffusion and trapping of tungsten coupled with the nucleation and expansion of blister cavities and a model for the production of the associated defects would be helpful. Such a model would probably have to bridge the gap between microscopic molecular dynamics (MD) simulations and meso- to macroscopic mechanical calculations such as finite element simulations.

9.2.3. Fluence dependence of deuterium retention

The evolution of the trap density with fluence is necessary to explain the experimentally observed fluence dependence of deuterium retention. At small fluences up to about 10^{23} D m^{-2}, the deuterium inventory increases *faster* than the square

root of the fluence, which can only be caused by increasing the trap density with the fluence. At fluences of 10^{24} D m^{-2} and higher, the trap evolution begins to stagnate and the enhanced trap concentration near the irradiated surface reduces diffusion into the bulk, up to the point where the deuterium inventory increases *slower* than the square root of the fluence, i.e., than undisturbed diffusion. A slower deuterium uptake at high fluence was also observed before, e.g., by Haasz *et al.* [37].

Ogorodnikova *et al.* [82] stated that an increased trap density within the implantation range of a 3 keV D$^+$ ion beam could not explain saturation effects at high fluences, and ascribed it to a fluence-dependent diffusion coefficient due to a transient, evolving stress field during the implantation instead. While such a mechanism is by no means denied — it might even be of considerable importance in the case of deuterium implantation at high incident ion energies (see section 8.3) — the results presented here clearly show that trap evolution has a major effect under the conditions discussed here. Simulations with traps that do not evolve with the fluence could not reproduce the observed behaviour across the whole range of fluences, whereas an empirical trap evolution model based on deuterium depth profiles measured at different fluences qualitatively reproduced both the steep increase of the deuterium retention at low fluences and the slower uptake at high fluences. Because of these findings, the description of trap evolution should be considered a central issue in any new models for the deuterium uptake of tungsten due to plasma exposure. Please note that although Ogorodnikova *et al.* [82] ascribe saturation of the deuterium retention to a stress-induced change of the diffusion coefficient rather than to defect evolution, they also point out that trap production during deuterium irradiation of tungsten specimen nevertheless needs to be considered in simulations (see also [80]).

9.3. Influence of the surface preparation

It was shown in section 8.4 that the quality of the surface finish of a tungsten specimen can have a marked influence on the deuterium retention. Particularly specimens with only a rough "technical" finish show an increased retention due the mechanical damaging of the surface (see Figure 8.21). Similar observations were made by Sugiyama *et al.* [106] for tungsten specimens exposed to the divertor plasma of the fusion experiment ASDEX Upgrade. Electropolished specimens show a lower retention than even high-quality chemo-mechanically polished spec-

imens. Still, chemo-mechanical polishing is deemed a good compromise for the large-scale surveys performed for this thesis because it is a much faster and more reliable preparation method.

In terms of blister formation, there was only little difference between mechanically and electrochemically polished surfaces, but on the rough surface of an unpolished specimen no blisters were found. This apparent suppression of blistering on a rough surface was also suggested as a measure to counter blister formation on fusion reactor plasma facing components by Nishijima *et al.* [75]. Considering the results presented here, this would not reduce the deuterium retention in tungsten components, but rather increase it slightly. Intentional roughening would, however, probably be not applicable to components in fusion reactor environment because the surfaces are typically exposed to very large fluxes of ions at shallow incident angles, which leads to smoothing of surfaces [106]. Together with the erosion of material, this will inevitably lead to the removal of any artificially applied surface morphologies over a prolonged operation period. All in all, the initial surface quality is probably not relevant to any fusion reactor component exposed to the plasma, but can have a strong influence on the results of laboratory experiments, particularly with respect to blister formation.

9.4. Isotope exchange with "natural" hydrogen

The initial inventory of ^{1}H in as-received tungsten specimens was also addressed in section 8.4. It was shown by means of TDS of initial and stress-relieved material that this "natural" hydrogen inventory can be considerable, but can also be significantly reduced by pre-annealing of the specimens (see Figure 8.24). The deuterium retention in specimens still saturated with the ^{1}H isotope was significantly reduced compared to specimens degassed before plasma exposure. TDS of non-annealed, plasma-exposed specimens showed that nevertheless only a small fraction of deuterium desorbs in the form of HD molecules. This indicates a spatial separation of H and D in the specimen, which is achieved by replacement of H by D atoms near the surface exposed to the plasma. The influence of the "natural" ^{1}H content shows that for reliable investigations of the hydrogen isotope uptake of tungsten specimens, it is necessary to reduce the initial hydrogen content as far as possible, or at least accurately determine it prior to the loading experiment.

The observed effects of the "natural" hydrogen content also indicate some possibilities to reduce the tritium inventory in plasma-facing components of a future fusion reactor. One is that pre-loading of these components with other hydrogen isotopes could significantly slow down the uptake of the radioactive tritium. Since it is not yet clear if the displaced isotopes migrate deeper into the bulk or are released from the surface, it would probably be safer to use deuterium so that the D-T fuel mixture of the reactor is not diluted by H. Second, the irradiation of components with pure H or D plasmas after exposure to tritium might be used to "flush out" the radioactive isotope. Some dedicated experiments towards isotope exchange by subsequent plasma irradiation with D and H have also been recently performed by Alimov *et al.* [7].

9.5. Correlation of deuterium retention in tungsten with the microstructure

Looking at the whole set of data gathered for this thesis, particularly the results from the variation of temperature and incident fluence described in sections 8.1 and 8.2, one trend becomes clear: Except for high ion energies, where other effects take over, stress-relieved tungsten always retains the most deuterium, followed by tungsten partially recrystallised at 1500 K. Both fully recrystallised materials, whether annealed at 1700 or 2000 K, nearly always have remarkably similar deuterium inventories, which are significantly smaller than those of the other two materials. In the light of the large number of consistent results presented here, the large difference between specimens recrystallised at 1700 and 2000 K that was found in a preliminary study [66] must be regarded as an exception, or at least as a peculiarity of plasma exposure at room temperature (to a smaller extent it was also observed here for D implantation at 300 K). The observation that the deuterium retention is reduced in recrystallised tungsten was also made, e.g., by Ogorodnikova *et al.* [81]. On the other hand, Alimov *et al.* [2] found nearly the same inventory after high-flux irradiation of stress-relieved and recrystallised material over a wide range of temperatures, but this is probably due to the strong blister formation enhancing the D retention (particularly for the recrystallised tungsten) under these conditions (see section 8.3).

Looking back again at Figure 6.12, it becomes apparent that the deuterium inventory follows the trend of the dislocation density rather than that of the grain

boundary surface per unit volume: Compared to the dislocation densities of stress-relieved and partially recrystallised tungsten, the dislocation densities of the fully recrystallised materials are equal, namely effectively zero. The grain boundary surface per volume, on the other hand, is markedly different for tungsten recrystallised at 1700 and 2000 K because even when most dislocations are consumed by the recrystallisation process, grain growth still takes place if the temperature is sufficiently high. It is therefore proposed that dislocations (and possibly also small-angle grain boundaries, which can be resolved into individual dislocations in the TEM) are the primary trap for deuterium in the materials investigated here. This fits well with the observation that unpolished tungsten with a strongly deformed surface layer shows increased deuterium retention compared to well-polished specimens. It is also consistent with the theory that the traps produced by the growth of blisters are, in fact, dislocations emitted due to the large stresses associated with cracking.

The residual traps density that is present in fully recrystallised (i.e., dislocation-poor) tungsten specimens could be to a large part due to impurities. The nominal purity of the base material of 99.97 wt.% corresponds to about 99.7 at.% taking into account the atomic weight of the impurities listed in Table A.3. Since the surface of the grain boundaries per unit volume is already fairly low for the large grains found in recrystallised tungsten, their influence might be obscured. This would explain the very close match of both types of fully recrystallised materials under nearly all loading conditions discussed here. A higher effective diffusivity in a material with larger grains exactly cancelling the effect of a lower trap density is considered improbable, particularly since both NRA (probing a fixed volume) and TDS (probing the total deuterium inventory) showed coincident deuterium retention for both materials.

Blister formation due to deuterium plasma exposure also showed a strong dependence on the microstructure. On stress-relieved tungsten, round, domed blisters were found under nearly all exposure conditions (see, e.g., Figure 8.3). Only at the highest specimen temperature of 750 K, very low ion energies of 8 eV/D or at the smallest fluence of 6×10^{22} D m^{-2} no blisters were found on this material. In all these cases the local deuterium concentration was very low. The round, domed blisters were always correlated to crack systems along grain boundaries such as those shown in Figure 8.5. The deformation of the blister cap was in many cases at least partially reversible (see also [9, 66]). Many of these blisters contain D$_2$ gas at a pressure of approximately 0.1 GPa [9]. This gas is responsible for the

final observed shape of the blister [9], but makes only a small contribution to the total deuterium inventory (see also [67] and section 8.1.6). A much larger effect is ascribed to the dislocation halos created during the expansion of the blister cavity.

Occasionally blisters of this type were also found on partially recrystallised tungsten. Their occurrence was usually confined to those areas on the specimen surface that showed little to no thermal grooving and are therefore considered to be still close to their initial state. On fully recrystallised tungsten, on the other hand, these domed blisters were never found. Instead, small, flat, angular features correlated to intragranular subsurface cracks and distortions such as those shown in Figure 8.20 were found for implantation at high ion energies. They are also remarkably similar to features produced by high-flux irradiation at comparable ion energy and temperature [57].

At 105 eV/D, these "blister-like" features were found in large numbers in already transformed surface areas on partially recrystallised specimens, and sporadically also on fully recrystallised tungsten. At 205 eV/D, they were abundant on fully recrystallised material, while any type of blistering was strongly reduced on the other specimens. The blister-like features on recrystallised tungsten had a very similar effect on the deuterium retention as the domed blisters on stress-relieved material. This effect is also believed to be caused by the emission of dislocations due to crack-tip plasticity at the cavities corresponding to the surface features. It is strong enough to even cause a reversal of the dependence of the deuterium retention on the initial microstructure (see section 8.3). In all cases, a strong occurrence of blisters or blister-like features was equivalent to a high deuterium retention, and vice versa, scarce or absent blisters went together with a small inventory. This shows the importance of blistering phenomena for the deuterium retention in tungsten. Because in most cases the blistering activity is affected by pre-annealing (and therefore the microstructure) in the same direction as the dislocation density, the net effect on the deuterium retention is even amplified.

The final proof for assigning a certain defect as the primary trap for deuterium in tungsten would be a linear scaling of the deuterium retention with the density of that defect, but it is difficult to find such a scaling law based on the data presented in this thesis. It would require a fixed sampling volume to compensate for the higher effective diffusivity at lower defect densities. This *could* be achieved by using NRA data, which intrinsically only include the deuterium inventories up to the depth that can be probed by the ^{3}He ion beam. This, however, leads im-

mediately to the problem that this volume near the implanted surface is strongly affected by blistering, which was already shown to have a large influence on the deuterium retention and also depends strongly on the specimen microstructure. Suppressing blistering by a high specimen temperature during the plasma exposure is also problematic since then the defects are already far from saturation. Therefore, it would be desirable to find deuterium loading conditions that do not lead to blistering on any type of specimen or any other damage while the temperature is kept preferably near room temperature.

Such a method could be, e.g., electrochemical loading like it is well-proven for other materials such as palladium [49] or also steels [101]. This is usually performed with thin foils, so the specimen can be completely saturated. Current integration during loading, NRA and TDS would then provide three independent methods to determine the deuterium uptake. Another method to ascertain the assignment of deuterium trapping to a certain type of crystal defect would be the direct detection of deuterium and the correlation with the spatial distribution of defects. Some first attempts at probing the deuterium inventory with a high lateral resolution have been made using a NanoSIMS device, i.e., a secondary ion mass spectrometry set-up capable of spatial resolutions of the order of 50–100 nm [58]. These investigations pointed towards at least *some* attraction of hydrogen to grain boundaries in recrystallised tungsten. This research is ongoing.

9.6. Density of sites in stress-relieved tungsten

In addition to identifying dislocations as a likely candidate for the dominant trap particularly in stress-relieved tungsten, the density of sites in this material was investigated in more detail. This was done by the analysis of thermal desorption spectra of identical tungsten specimens exposed to a deuterium plasma under the reference conditions, i.e., with an ion energy of 38 eV/D to a fluence of 6×10^{24} D m^{-2} at a temperature of 370 K. The spectra were acquired with different heating rates and with interrupted temperature ramps. From the shift of the main desorption peak temperature due to variation of the heating rate, a dominant binding energy of 1.25 ± 0.11 eV and a detrapping attempt frequency of $6.6 \pm 3.3 \times 10^{11}$ s^{-1} was determined by combining the analysis method proposed by Falconer [24] and numerical diffusion-trapping simulations using the model described in section 3.3. The evaluation of measured and calculated spectra was shown in Figure 8.27.

The central properties of the model are interstitial diffusion based on the values by Frauenfelder [27] and three types of traps whose density evolves with fluence based on empirical laws derived from fluence variation experiments. Traps with binding energies of 0.7 and 1.2 eV are used to represent the extended stress fields respectively the cores of dislocations and therefore share the same time evolution. They are present throughout the specimen. Traps at 2.2 eV are confined to a thin surface layer and are used to model radiation damage caused by energetic impurity ions. Large differences between the attempt frequency used in the model and the frequency pre-factor resulting from the Falconer analysis for coinciding peak positions between simulations and experiments stress the considerable effect of diffusion from larger depths on thermal desorption spectra of deuterium, which was also recognised by other researchers [14, 112].

The trap energies used here lie within the same range as those published by other researchers (see, e.g., [82, 88]), but are interpreted differently by these: The lowest-energy trap (E_b = 0.65 eV [88] respectively E_b = 0.85 eV [82]) is assigned to dislocations (and also grain boundaries [82]) and identified with a low-temperature release peak at between 400-500 K. Binding energies between 1.07 and 1.45 eV are assumed to correspond to vacancy-type defects [82, 88] or pores [82] and are stated to give rise to a desorption peak roughly around 600 K. High-energy traps (E_b = 2.1 eV [88]) are assigned to atomic hydrogen adsorbed at the internal surfaces of voids (see also [82]) and identified with high-temperature deuterium release at $\approx$ 900 K. Particularly the intermediate trap (here: E_b = 1.2 eV) is interpreted differently in this thesis and is assigned to dislocations instead, based on the comparison of tungsten materials with different microstructures (see section 9.5). Please keep in mind that the term "voids" as it is used by Poon *et al.* [88] refers to nano-cavities consisting of 30–50 vacancies [111], whereas, e.g., Tyburska *et al.* [109] identify essentially the same trap with "vacancy clusters". Basically, both terms are used to describe agglomerations of vacancies, which are, in both cases, produced by ion irradiation. In this thesis, the term "radiation damage" is used to simply describe the origin of these defects and makes no further assumption about their actual nanoscopic structure. In addition to traps with a high binding energy, rear-side release of deuterium is also found to contribute to the high-temperature release peak (or rather shoulder) for the specimens investigated here.

Please keep in mind when comparing the different models and the interpretation of the traps as certain crystal defects that the experimental data on which they

are based were acquired under very different conditions. Poon *et al.* [88] irradiated annealed tungsten single crystals with an ion energy of 500 eV/D, whereas Ogorodnikova *et al.* [82] exposed recrystallised polycrystalline tungsten to ions with energies of 200 eV/D and 3 keV/D. In both cases a low initial dislocation density is assumed. In contrast, the model introduced in this thesis was developed for hot-rolled and stress-relieved (i.e., dislocation-rich) tungsten exposed to a low-energy (38 eV/D) deuterium plasma. The different interpretations are therefore not necessarily contradictions, but probably rather the result of different experimental conditions.

While the model used here describes the observed shift of the spectra with the heating rate well, its deviations from experimental observations, especially when applied to interrupted temperature ramps, hint at a more complex density of sites than a set of three monoenergetic traps. In particular, considerable losses of deuterium for TDS ramps interrupted at 470 K and for long-term storage at room temperature can only be explained by a (slow) low-temperature loss channel for the main 1.2 eV trap. This is in agreement with observations and conclusions made by Moshkunov *et al.* [72]. Such an additional loss channel could be due to correlated trap sites or to the "evaporation" of dislocation atmospheres. In order to describe such effects, a new type of numerical model beyond the simplified one-dimensional rate-equation approach of diffusion-trapping models needs to be developed. The challenge of such a new model would be that it needs to include correlations between traps on the scale of the tungsten lattice while at the same time describing also the hydrogen isotope retention in macroscopic specimens.

10. Summary

In order to investigate the correlation between the deuterium retention in tungsten after exposure to a low-energy deuterium plasma and the microstructure of the material, a large set of specimens with four different microstructures based on a common initial material was prepared. These specimens were thoroughly pre-characterised by scanning and transmission electron microscopy to asses the grain size and dislocation density of each type of microstructure. These specimens were then exposed under a variety of different conditions: The temperature, the incident ion fluence and the ion energy were each varied individually while keeping the other parameters constant. The common point in parameter space for all parameter variations was at an ion energy of 38 eV/D, an incident fluence of 6×10^{24} D m^{-2} and a specimen temperature during exposure of 370 K ("reference conditions"). The ion flux was $\approx 10^{20}$ D m^{-2}s^{-1} for all experiments presented here. To minimise any errors due to reproducibility of the plasma discharge when comparing the different microstructures, all four specimen types were exposed simultaneously. Possible complications due to the surface quality and the initial hydrogen inventory of the specimens were identified and consequently avoided. Particular attention was also paid to identical storage of all specimens in vacuum to avoid inconsistencies of the measured deuterium inventories due to the effects of room-temperature degassing and specimen oxidation that were described by Moshkunov *et al.* [72]. This strict standardisation of the specimens and the experimental procedure allowed to gather a large set of consistent data on the deuterium retention in these specimens.

It was found that the most obvious correlation exists between the *dislocation density* of the initial specimen and the deuterium retention. In all but a few exceptional cases where other mechanisms were dominant, the highest deuterium retention was found in stress-relieved specimens, which had the highest dislocation density. Fully recrystallised specimens, which had a much lower dislocation density, also displayed a low deuterium retention. Partially recrystallised specimens showed intermediate values for both dislocation density and retention. Based on

the present data, the trapping of deuterium at grain boundaries is considered of minor importance because two types of fully recrystallised tungsten showed nearly the same deuterium retention under a broad range of loading conditions although the grain size in these specimens was significantly different.

Blistering was also found to considerably increase the deuterium retention. Blisters predominantly occurred on stress-relieved specimens and occasionally on partially recrystallised specimens under most of the exposure conditions applied here. On fully recrystallised specimens, blister-like features were only found for high ion energies and not under any other conditions investigated in this thesis. In many cases, blistering amplifies or even dominates the microstructure dependence of the deuterium retention described above. The large impact of blister formation becomes most obvious for the highest ion energy of 205 eV/D: While blister-like features are abundant on fully recrystallised specimens, blistering of the other specimen types is strongly reduced. At the same time, the order of the materials with respect to their deuterium retention is reversed, i.e., recrystallised tungsten retains *more* deuterium than stress-relieved material under these conditions.

The enhanced deuterium retention associated with blisters and blister-like features is predominantly caused by crystal defects created due to the expansion of the blister cavity. A likely candidate are dislocations emitted due to crack-tip plasticity. The deuterium stored as D_2 gas inside the blister cavities is only of minor importance for the total inventory in a specimen (see also [67]). However, the pressure of this gas is the key mechanism for expanding the cavities at least of round, domed blisters [9].

For the case of stress-relieved tungsten exposed at 38 eV/D and 370 K, the binding energy of the dominant trap was found to be 1.25 ± 0.11 eV with a detrapping attempt frequency of $6.6 \pm 3.3 \times 10^{11}$ s^{-1}. These values were found by comparison of thermal desorption spectra acquired at different heating rates with simulated spectra calculated with an iteratively refined diffusion-trapping model with discrete trap energies, and by independently determining the binding energy and the detrapping attempt frequency with the Falconer method [24]. They comprise a unique, consistent parameter set and fully account for the influence of the measured depth distribution of the deuterium. By that, the non-uniqueness of trap parameters derived from a single desorption spectrum [14, 112] is avoided. The diffusion-trapping model used here includes trap evolution due to blister growth and surface damage due to energetic impurity ions from the plasma. With that it is capable of at least qualitatively reproducing the experimentally observed flu-

ence dependence of the deuterium retention: For large fluences, this dependence is slower than the square root of the fluence, respectively the implantation time, while at small fluences the uptake of deuterium is faster. It also yields absolute deuterium inventories close to the measured ones. Differences between modelled and simulated thermal desorption spectra point towards a more complex, probably continuous density of sites function. Deuterium losses from high-energy traps particular during long-term storage at room temperature and for annealing at temperatures below the observed release maximum at approximately 600 K, suggest an — albeit slow — additional low-temperature release channel from these traps.

Many of the individual observations presented in this thesis were also made by other researchers before, but in most cases isolated from each other and each under different experimental conditions. Because of this they often seemed contradictory. Performing all these experiments on a set of strictly standardised, thoroughly characterised specimens and under standardised experiment conditions reveals many connections between the observed phenomena. This shows that the behaviour of the tungsten-hydrogen system needs to be recognised as being the result of a number of complexly interacting effects. These effects may either be synergistic or counteracting. Their interplay can even reverse under certain conditions, such as for the reversal of the dependence of the deuterium retention on the initial microstructure at high ion energies. All in all, the new, consistent data set presented here allows new, valuable insights into the complex interaction of low-energy deuterium ions from a plasma with tungsten and provides a solid basis for further experiments and modelling concerning this topic.

A. Appendix

A.1. Empirical models for trap density evolution

Please note: The models shown here are empirical descriptions of the observed evolution of the observed trap (respectively deuterium) concentration depth profiles with the incident fluence. Although they are associated with certain types of traps and their production mechanisms, their exact realisations are presently not based on physical models of these mechanisms. Please keep in mind that the deuterium concentration in a certain trap at a given temperature is a function of both the trap concentration and its binding energy.

The following functions are used to describe the time evolution of the trap depth profiles for the surface peak:

$$
\begin{aligned}
\rho^{surface}(\mathbf{x}, \mathbf{t}) &= \mathcal{B}(c^{surface}(\mathbf{t}), s^{surface}, x_s^{surface}; \mathbf{x}) && \text{(A.1)} \\
c^{surface}(\mathbf{t}) &= c_{max}^{surface} \cdot \mathcal{S}(\tau^{surface}; \mathbf{t}),
\end{aligned}
$$

as well as for dislocation cores respectively strain fields:

$$
\begin{aligned}
c_\perp^{core,strain}(\mathbf{x}, \mathbf{t}) &= c_{\perp,0}^{core,strain} + \theta(\mathbf{t} - t_0) \cdot \mathcal{G}(A(\mathbf{t}), w(\mathbf{t}), x_c(\mathbf{t}); \mathbf{x}) && \text{(A.2)} \\
A(\mathbf{t}) &= c_{\perp,max}^{core,strain} \cdot \mathcal{S}(\tau_A; \mathbf{t} - t_0) \\
w(\mathbf{t}) &= w_0 + w_{max} \cdot \mathcal{S}(\tau_w; \mathbf{t} - t_0) \\
x_c(\mathbf{t}) &= x_{c,\perp,max} \cdot \mathcal{S}(\tau_{x_c}; \mathbf{t} - t_0).
\end{aligned}
$$

The symbols $\mathcal{B}$, $\mathcal{G}$ and $\mathcal{S}$ are in the above equations are defined as follows:

$$\mathcal{B}(A, s, x_s; \mathbf{x}) \quad = \quad \frac{A}{1 + \exp\left[\frac{\mathbf{x} - x_s}{s}\right]} \tag{A.3}$$

$$\mathcal{G}(A, w, x_c; \mathbf{x}) \quad = \quad A \exp\left[-\frac{(\mathbf{x} - x_c)^2}{w^2}\right] \tag{A.4}$$

$$\mathcal{S}(\tau; \mathbf{t}) \quad = \quad 1 - \exp\left[-\frac{\mathbf{t}}{\tau}\right]. \tag{A.5}$$

$$\tag{A.6}$$

$\theta(\mathbf{t} - t_0)$ is the Heaviside theta function, i.e., 1 for $\mathbf{t} - t_0 > 0$, and 0 otherwise.

Figure A.1 shows trap concentration profiles calculated with equations (A.2) and (A.3) exactly like they were used for the diffusion-trapping simulations presented in this thesis. Please note that because of their low binding energy, only a small fraction of the 0.7 eV traps are populated at the reference temperature of 370 K (for which all simulations were performed), whereas the 1.2 and 2.2 eV traps are saturated up to a certain depth (≈ 35 μm under the reference conditions, i.e, an ion energy of 38 eV/D and a fluence of 6×10^{24} D m^{-2}). Beyond the diffusion front, all traps are still empty.
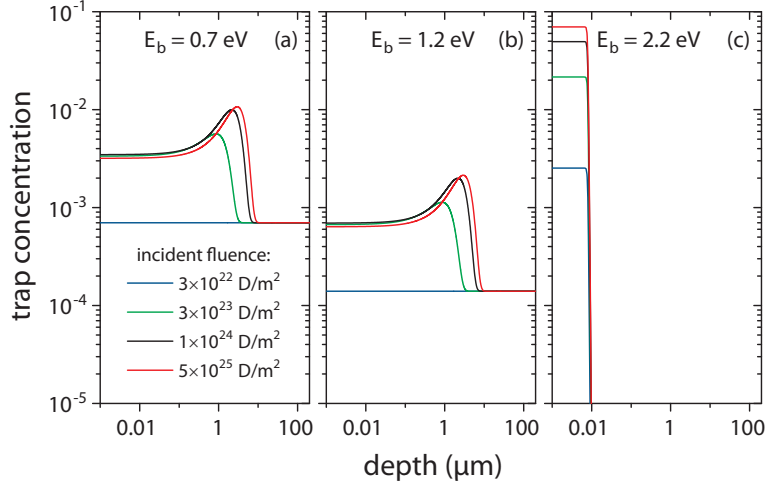
Figure A.1. Evolution of trap concentrations with time (respectively fluence) as it is used in the diffusion-trapping model described in section 3.3. The time-dependent concentration profiles of traps with $E_b = 0.7$ eV and $E_b = 1.2$ eV, which are used to represent the cores and strain fields of both intrinsic and blister-induced dislocations, are shown in panels (a) and (b). Panel (c) shows the concentration profile of the trap with a binding energy of $E_b = 2.2$ eV, which corresponds to the surface peak.

A.2. Electron microscopes

Table A.1. Properties of the electron microscopes used for the work presented in this thesis.

microscope	acceleration	resolution	detectors
Philips XL30 ESEM	1–30 kV	6 nm	ETD (SE)
		6 nm	annular BSE
			EDX (EDAX)
HELIOS NanoLab 600	0.35–30 kV		ETD (SE, BSE)
		≈ 1 nm	in-lens SE/BSE
		0.8 nm	STEM (BF, DF, HADF)
			CBS (annular BSE)
			EDX (Oxford Instr.)
			EBSD (HKL)
Jeol JEM-2010F	200 kV	lattice	GIF (TEM, EELS)
		≈ 1 nm (W)	STEM (BF, HAADF)
			EDX (EDAX)
Titan E-Cell 80–300ST	80–300 kV	< 0.08 nm	(HR)TEM
		< 0.14 nm	STEM
			EDX (Oxford Instr.)
			EFTEM
			environmental cell
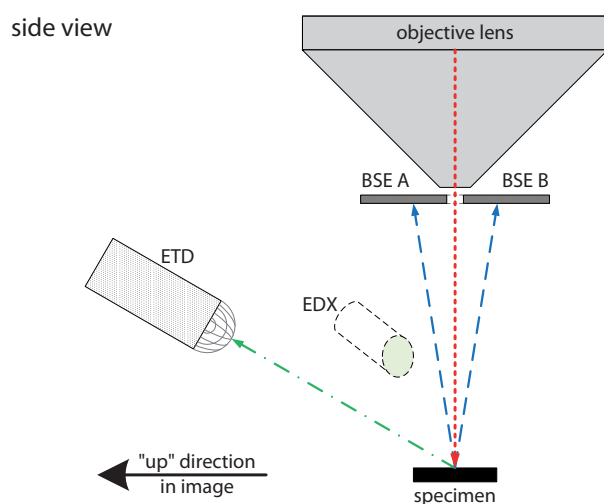
Figure A.2. Detector positions in the XL30 microscope. Images can be acquired with an Everhart-Thornley detector (ETD) or with an annular backscattered electron detector (BSE). An energy-dispersive X-ray detector is also present.
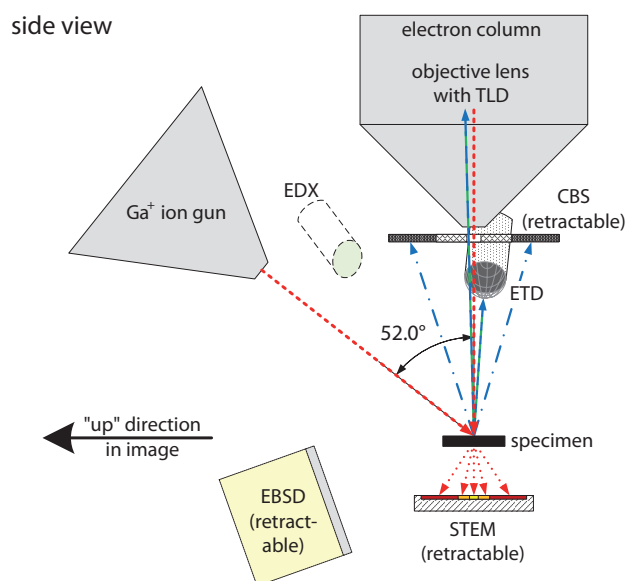
Figure A.3. Detector and beam positions in the HELIOS NanoLab 600 microscope. SE and BSE images can be acquired both with a conventional Everhart-Thornley detector (ETD) and an in-lens detector (TLD). Several additional retractable detector are also present: a concentric solid-state backscattered electron detector (CBS) and a scanning transmission electron microscopy detector (STEM). Furthermore, an EDX system and an electron backscattering diffraction (EBSD) system are present. A focused Ga^+ beam intersects the electron beam ≈ 4 mm from the objective lens. The angle between electron and ion beam is $52°$.

A.3. Optical microscope

For the work presented here, an Olympus BX60MF5 upright microscope with Köhler illumination and infinity-corrected plan semi-apochromat objectives (Olympus UMPlanFl) was used. The objective revolver contains a slot for an adjustable Nomarski prism with a compensator plate (Olympus U-DICR). The illumination and observation optical pathways are equipped with slots for retractable polarisation filters. The Nomarski prism was usually operated with bias retardation close to the neutral point, i.e., in the range where interference colors do not yet appear. The bias retardation was adjusted so that the apparent illumination comes from the top left corner of the image, and the shadows point towards the lower right corner. Since optical staining by interference colors was not used, a green interference filter (Olympus U-IFF550-2) was used to produce monochromatic light for illumination, which minimises chromatic aberration. A Nikon DS-2Mv CCD camera with 1600×1200 pixels (sensor format: 1 1/8") was used for image acquisition, usually in monochrome mode. The specifications of the microscope system for all used objectives are listed in Table A.2.

Table A.2. Properties of the objectives used in the Olympus BX60MF5 optical microscope.

objective	NA	magnification	Abbe resolution	pixel equivalent
5×	0.15	50×	1.83 μm	1.76 μm/px.
10×	0.30	100×	0.92 μm	0.88 μm/px.
20×	0.46	200×	0.60 μm	0.44 μm/px.
50×	0.80	500×	0.34 μm	0.18 μm/px.
100×	0.90	1000×	0.31 μm	0.09 μm/px.

A.4. Chemical purity specification of the tungsten material

Table A.3. Impurity concentrations in the tungsten material from PLANSEE with 99.97 wt.% nominal purity. The listed values are guaranteed maximum concentrations.

Impurity	weight %	atomic %
Ag	0.0010	0.0017
Al	0.0015	0.0102
As	0.0005	0.0012
Ba	0.0005	0.0007
C	0.0030	0.0459
Ca	0.0005	0.0023
Cd	0.0005	0.0008
Co	0.0010	0.0031
Cr	0.0020	0.0071
Cu	0.0010	0.0029
Fe	0.0030	0.0099
H	0.0005	0.0912
K	0.0010	0.0047
Mg	0.0005	0.0038
Mn	0.0005	0.0017
Mo	0.0100	0.0192
N	0.0005	0.0066
Na	0.0010	0.0080
Nb	0.0010	0.0020
Ni	0.0005	0.0016
O	0.0020	0.0230
P	0.0020	0.0119
Pb	0.0005	0.0004
S	0.0005	0.0029
Si	0.0020	0.0131
Ta	0.0020	0.0020
Ti	0.0005	0.0019
Zn	0.0005	0.0014
Zr	0.0005	0.0010

A.5. Parameter space of the experiments
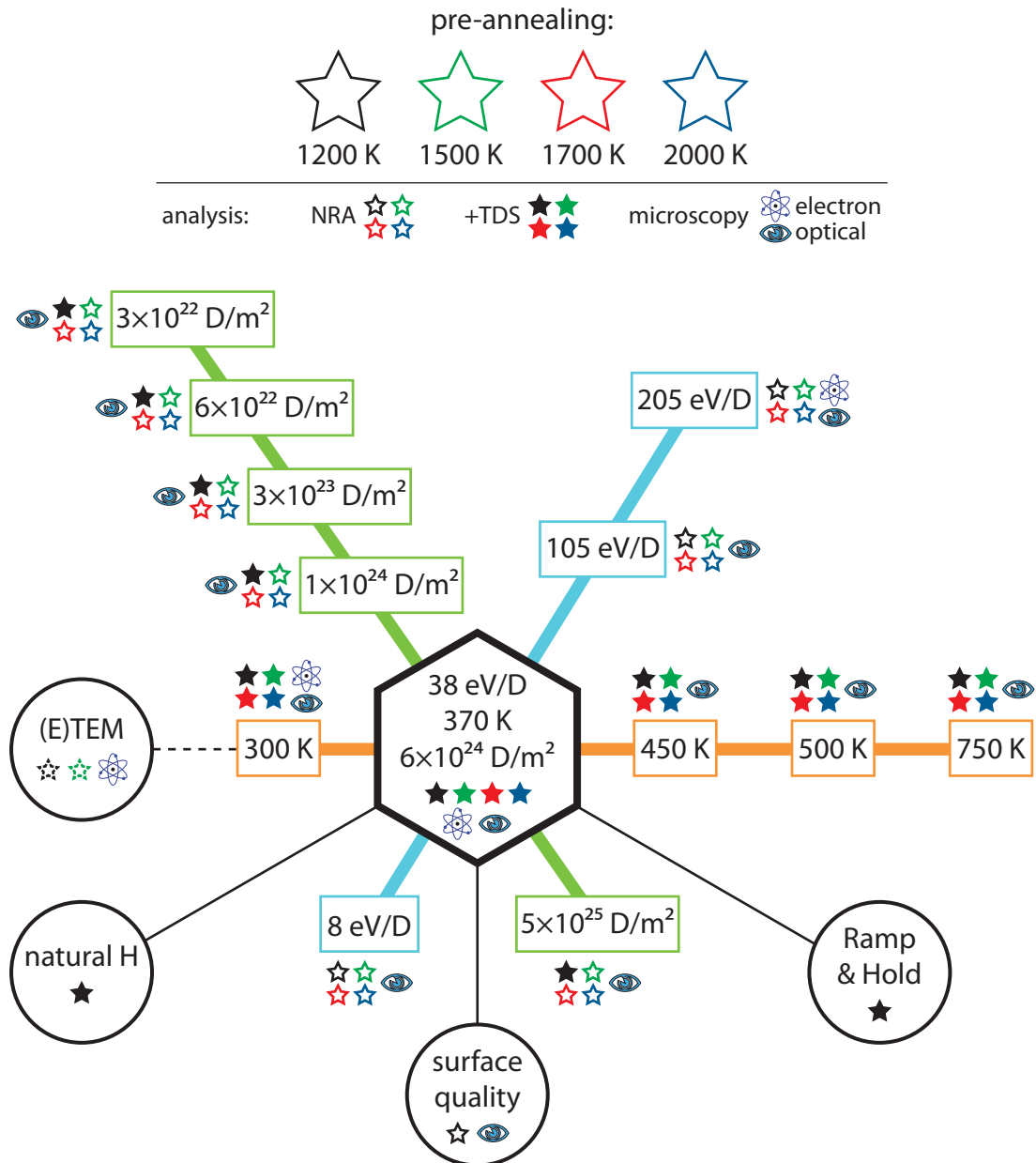
Figure A.4. Schematic representation of the parameter space covered by the experiments presented in this thesis (see chapter 7). Specimens with four different microstructures resulting from pre-annealing at 1200, 1500, 1700 or 2000 K (see chapter 6) were exposed to deuterium plasmas at various ion energies, fluences and temperatures. The crossing point of these parameter variations is an energy of 38 eV/D, a fluence of 6×10^{24} D m^{-2} and a specimen temperature during exposure of 370 K. Under these reference conditions, further investigations such as "Ramp-and-Hold" experiments were performed, mainly for tungsten stress-relieved at 1200 K.

A.6. Energy levels for deuterium in tungsten
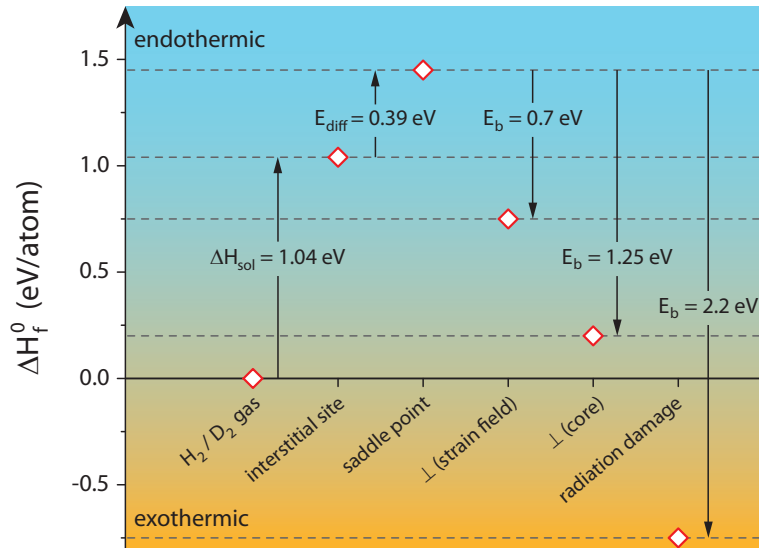
Figure A.5. Overview of energy levels for deuterium in tungsten. As the reference scale, the standard enthalpy of formation ΔH_f^0 — which is 0 for gaseous hydrogen respectively deuterium under standard conditions — is chosen. The values for the enthalpy of solution ΔH_{sol} and the diffusion barrier E_{diff} are those published by Frauenfelder [27]. The detrapping (respectively binding) energy E_b for dislocation cores (and possibly also grain boundaries) was derived in this thesis (see section 8.5). The values of E_b for the strain fields of dislocations and radiation damage at the plasma-exposed surface are estimates used for modelling (see section 3.3).

Bibliography

[1] V. Alimov *et al.* (2008) *Deuterium retention in tungsten exposed to low-energy, high-flux clean and carbon-seeded deuterium plasmas*, J. Nucl. Mater. **375**; pp. 192–201

[2] V. Alimov *et al.* (2012) *Temperature dependence of surface morphology and deuterium retention in polycrystalline ITER-grade tungsten exposed to low-energy, high-flux D plasma*, J. Nucl. Mater. **420 (1–3)**; pp. 519–524

[3] V. K. Alimov, M. Mayer and J. Roth (2005) *Differential cross-section of the $D(^3He, p)^4He$ nuclear reaction and depth profiling of deuterium up to large depths*, Nucl. Instrum. Meth. B **234 (3)**; pp. 169–175

[4] V. K. Alimov and B. M. U. Scherzer (1996) *Deuterium retention and re-emission from tungsten materials*, J. Nucl. Mater. **240**; pp. 75–80

[5] V. K. Alimov *et al.* (2009) *Surface morphology and deuterium retention in tungsten exposed to low-energy, high flux pure and helium-seeded deuterium plasmas*, Phys. Scr. **T138**; p. 014048

[6] V. K. Alimov *et al.* (2011) *Temperature dependence of surface topography and deuterium retention in tungsten exposed to low-energy, high-flux D plasma*, J. Nucl. Mater. **417 (1–3)**; pp. 572–575

[7] V. K. Alimov *et al.* (2011) *Hydrogen isotope exchange in tungsten irradiated sequentially to low-energy deuterium and protium ions*, Phys. Scr. **T145**; p. 014037

[8] M. Balden and J. Roth (2000) *Comparison of the chemical erosion of Si, C and SiC under deuterium ion bombardment*, J. Nucl. Mater. **279 (2–3)**; pp. 351–355

[9] M. Balden *et al.* (2011) *D_2 gas–filled blisters on deuterium-bombarded tungsten*, J. Nucl. Mater. **414 (1)**; pp. 69–72

[10] R. Behrisch *et al.* (2000) *Quantitative analysis of deuterium in a-C:D layers, a Round Robin experiment*, J. Nucl Mater. **281 (1)**; pp. 42–56

[11] G. Benamati, E. Serra and C. H. Wu (2000) *Hydrogen and deuterium transport and inventory parameters through W and W-alloys for fusion reactor applications*, J. Nucl Mater. **283–287 (2)**; pp. 1033–1037

[12] C. Brandmaier, K. R. Spring and M. W. Davidson (2010), *Reflected light DIC microscopy*, Nikon MicroscopyU (online), http://www.microscopyu.com/

[13] R. Causey *et al.* (1999) *Tritium retention in tungsten exposed to intense fluxes of 100 eV tritons*, J. Nucl. Mater. **266–269**; pp. 467–471

[14] R. A. Causey (2002) *Hydrogen isotope retention and recycling in fusion reactor plasma-facing components*, J. Nucl. Mater. **300**; pp. 91–117

[15] R. A. Causey, J. N. Brooks and G. Federici (2002) *Tritium inventory and recovery in next-step fusion devices*, Fusion Eng. Des. **61–62**; pp. 525–536

[16] R. A. Causey *et al.* (2009) *Defects in tungsten responsible for molecular hydrogen isotope retention after exposure to low energy plasmas*, J. Nucl. Mater. **390–391**; pp. 717–720

[17] J. Condon and T. Schober (1993) *Hydrogen bubbles in metals*, J. Nucl Mater. **207**; pp. 1–24

[18] A. M. de Jong and J. W. Niemantsverdriet (1990) *Thermal desorption analysis: Comparative test of ten commonly applied procedures*, Surf. Sci. **233 (3)**; pp. 355–365

[19] R. Doerner (2007) *The implications of mixed-material plasma-facing surfaces in ITER*, J. Nucl. Mater. **363–365**; pp. 32–40

[20] Y. Ebisuzaki and M. O'Keeffe (1967) *The solubility of hydrogen in transition metals and alloys*, Prog. Solid State Chem. **4**; pp. 187–211

[21] W. Eckstein *et al.* (1993) *Sputtering data*, Technical Report 9/82, Max-Planck-Institut für Plasmaphysik, Garching

[22] W. Eckstein *et al.* (2007) *SDTrimSP: A Monte-Carlo code for calculating collision phenomena in randomized targets*, IPP Report 12/3, Max-Planck-Institut für Plasmaphysik, Garching, Germany

[23] W. Espe (1960) *Werkstoffe der Hochvakuumtechnik*, volume I, VEB Deutscher Verlag der Wissenschaften

[24] J. L. Falconer and R. J. Madix (1975) *Flash desorption activation energies: DCOOH decomposition and CO desorption from Ni (110)*, Surf. Sci. **48 (2)**; pp. 393–405

[25] J. R. Fransens, M. S. Abd El Keriem and F. Pleiter (1991) *Hydrogen–vacancy interaction in tungsten*, J. Phys.: Condens. Matter **3 (49)**; p. 9871

[26] P. Franzen *et al.* (1997) *Hydrogen trapping in and release from tungsten: Modeling and comparison with graphite with regard to its use as fusion reactor material*, J. Nucl Mater. **241–243**; pp. 1082–1086

[27] R. Frauenfelder (1969) *Solution and diffusion of hydrogen in tungsten*, J. Vac. Sci. Technol. **6 (3)**; pp. 388–397

[28] Y. Fukai (1984) *Site preference of interstitial hydrogen in metals*, J. Less-Common Met. **101**; pp. 1–16

[29] Y. Fukai (1993) *The metal–hydrogen system: basic bulk properties*, Springer-Verlag, Berlin Heidelberg New York, ISBN 3-540-55637-0

[30] Y. Fukai (2003) *Superabundant vacancies formed in metal–hydrogen alloys*, Phys. Scr. **T103**; p. 11

[31] Y. Fukai and H. Sugimoto (1985) *Diffusion of hydrogen in metals*, Adv. Phys. **34 (2)**; pp. 263–326

[32] C. García-Rosales *et al.* (1996) *Re-emission and thermal desorption of deuterium from plasma sprayed tungsten coatings for application in ASDEX Upgrade*, J. Nucl. Mater. **237**; pp. 803–808

[33] R. Griessen (1988) *Heats of solution and lattice-expansion and trapping energies of hydrogen in transition metals*, Phys. Rev. B **38**; pp. 3690–3698

[34] P. Gumbsch (2003) *Brittle fracture and the brittle-to-ductile transition of tungsten*, J. Nucl Mater. **323 (2–3)**; pp. 304–312

[35] P. Gumbsch *et al.* (1998) *Controlling factors for the brittle-to-ductile transition in tungsten single crystals*, Science **282 (5392)**; pp. 1293–1295

[36] I. Gutierrez-Urrutia, S. Zaefferer and D. Raabe (2009) *Electron channeling contrast imaging of twins and dislocations in twinning-induced plasticity*

steels under controlled diffraction conditions in a scanning electron microscope, Acta Mater. **61 (7)**; pp. 737–740

[37] A. A. Haasz *et al.* (1998) *Deuterium retention in tungsten for fusion use*, J. Nucl. Mater. **258–263**; pp. 889–895

[38] A. A. Haasz *et al.* (2001) *Deuterium retention in single crystal tungsten*, J. Nucl. Mater. **290**; pp. 85–88

[39] S. Hamdi, W. E. Schiesser and G. W. Griffiths (2007) *Method of lines*, Scholarpedia **2 (7)**; p. 2859

[40] K. Heinola and T. Ahlgren (2010) *Diffusion of hydrogen in bcc tungsten studied with first principle calculations*, J. Appl. Phys. **107**; p. 113531

[41] Hiden Analytical Ltd. (2011), *company homepage: cracking patterns*, http://www.hidenanalytical.com/

[42] A. Jablonski, F. Salvat and C. J. Powell (2010) *NIST elastic electron scattering cross-section database (SRD 64)*, National Institute of Standards and Technology, Gaithersburg, MD (USA), version 3.2

[43] A. Kallenbach *et al.* (2009) *Non-boronized compared with boronized operation of ASDEX Upgrade with full-tungsten plasma facing components*, Nucl. Fusion **49 (4)**; p. 045007

[44] A. Kallenbach *et al.* (2010) *Divertor power load feedback with nitrogen seeding in ASDEX Upgrade*, Plasma Phys. Control. Fusion **52 (5)**; p. 055002

[45] R. Kirchheim (1988) *Hydrogen solubility and diffusivity in defective and amorphous metals*, Progress in Materials Science **32**; pp. 261–325

[46] R. Kirchheim (2001) *Solubility and diffusivity of hydrogen in complex metals*, Phys. Scr. **T94**; pp. 58–67

[47] R. Kirchheim (2007) *Reducing grain boundary, dislocation line and vacancy formation energies by solute segregation II. Experimental evidence and consequences*, Acta Mater. **55**; pp. 5139–5148

[48] R. Kirchheim (2007) *Reducing grain boundary, dislocation line and vacancy formation energies by solute segregation. I. Theoretical background*, Acta Mater. **55**; pp. 5129–5138

[49] R. Kirchheim and R. B. McLellan (1980) *Electrochemical methods for mea-*

suring diffusivities of hydrogen in palladium and palladium alloys, J. Electrochem. Soc. **127 (11)**; pp. 2419–2425

[50] R. D. Kolasinski *et al.* (2009) *Characterization of surface morphology and retention in tungsten materials exposed to high fluxes of deuterium ions in the tritium plasma experiment*, Phys. Scr. **T138**; p. 014042

[51] J. Kondo (1976) *Localized atomic states in metals*, Physica B **84 (1)**; pp. 40–49

[52] J. Kondo (1976) *Localized atomic states in metals : II. Resistivity and free energy*, Physica B **84 (2)**; pp. 207–212

[53] J. Kondo (1984) *Adiabatic vs. non-adiabatic state of a heavy particle in a metal*, Physica B **124 (1)**; pp. 25–34

[54] J. Kondo (1984) *Diffusion of light interstitials in metals*, Physica B **125 (3)**; pp. 279–285

[55] J. Kondo (1984) *Diffusion of light interstitials in metals*, Physica B **126 (1–3)**; pp. 377–384

[56] A. H. M. Krom and A. Bakker (2000) *Hydrogen trapping models in steel*, Met. and Mat. Trans. B **31B**; pp. 1475–1482

[57] S. Lindig *et al.* (2009) *Subsurface morphology changes due to deuterium bombardment of tungsten*, Phys. Scr. **T138**; p. 014040 (5pp)

[58] S. Lindig *et al.* (2011) *Sub-surface structures of ITER-grade W (Japan) and re-crystallized W after ITER-similar low-energy and high-flux D plasma loadings*, Phys. Scr. **T145**; p. 014039

[59] J. M. Liu and B.-W. Shen (1982) *Grain boundary fracture in tungsten bi-crystals*, Acta Metall. **30 (6)**; pp. 1197–1202

[60] X. Liu *et al.* (2004) *Glide of edge dislocations in tungsten and molybdenum*, Mat. Sci. Eng. A **365 (1–2)**; pp. 96–100

[61] G. R. Longhurst (1985) *The soret effect and its implications for fusion reactors*, J. Nucl Mater. **131 (1)**; pp. 61–69

[62] G. R. Longhurst (2008) *TMAP7 user manual*, Idaho National Engineering and Environmental Laboratory, Idaho Falls, Idaho 83415, INEEL/EXT-04-02352 Rev. 2

[63] V. Lottner *et al.* (1979) *Study of jump models for the diffusion of hydrogen in NbH0.02 by means of the quasielastic scattering of slow neutrons*, J. Phys. Chem. Solids **40 (7)**; pp. 557–563

[64] J. Luo *et al.* (2011) *Dissolution, diffusion and permeation behavior of hydrogen in vanadium: a first-principles investigation*, J. Phys.: Condens. Matter **23**; p. 135501

[65] A. Manhard, T. Schwarz-Selinger and W. Jacob (2011) *Quantification of the deuterium ion fluxes from a plasma source*, Plasma Sources Sci. Technol. **20**; p. 015010

[66] A. Manhard *et al.* (2011) *Influence of the microstructure on the deuterium retention in tungsten*, J. Nucl. Mater. **415 (1S)**; pp. S632–S635

[67] A. Manhard *et al.* (2011) *Statistical analysis of blister bursts during temperature programmed desorption of deuterium-implanted polycrystalline tungsten*, Phys. Scr. **T145**; p. 014038

[68] M. Maxelon *et al.* (2001) *Interaction of hydrogen and deuterium with dislocations in palladium as observed by small angle neutron scattering*, Acta Mater. **49**; pp. 2625–2634

[69] M. Mayer (1997) *SIMNRA User's Guide*, IPP Report 9/113, Max-Planck-Institut für Plasmaphysik, Garching, Germany, original publication

[70] M. Mayer *et al.* (2009) *Quantitative depth profiling of deuterium up to very large depths*, Nucl. Instrum. Meth. **267**; pp. 506–512

[71] G. E. Moore and F. C. Unterwald (1964) *Thermal dissociation of hydrogen*, J. Chem. Phys. **40**; p. 2639

[72] K. A. Moshkunov *et al.* (2010) *Air exposure and sample storage time influence on hydrogen release from tungsten*, J. Nucl. Mater. **404 (3)**; pp. 174–177

[73] D. Murphy *et al.* (2010), *Differential interference contrast*, Olympus Microscopy Resource Center (online),
http://www.olympusmicro.com/

[74] R. Nazarov, T. Hickel and J. Neugebauer (2010) *First-principles study of the thermodynamics of hydrogen–vacancy interaction in fcc iron*, Phys. Rev. B **82**; p. 224104

[75] D. Nishijima *et al.* (2005) *Suppression of blister formation and deuterium retention on tungsten surface due to mechanical polishing and helium pre-exposure*, Nucl. Fusion **45**; pp. 669–674

[76] J. K. Nørskov (1979) *Electron structure of single and interacting hydrogen impurities in free-electron-like metals*, Phys. Rev. B **20 (2)**; pp. 446–454

[77] G. Nomarski (1955) *Microinterféromètre différentiel à ondes polarisées*, J. Phys. Radium **16**; pp. S9–S13

[78] P. Nordlander, J. K. Nørskov and F. Besenbacher (1986) *Trends in hydrogen heats of solution and vacancy trapping energies in transition metals*, J. Phys. F: Met. Phys. **16**; pp. 1161–1171

[79] O. Ogorodnikova *et al.* (2009) *Deuterium Retention in Different Tungsten Grades*, Phys. Scr. **T138**; p. 014053 (5pp)

[80] O. V. Ogorodnikova, J. Roth and M. Mayer (2003) *Deuterium retention in tungsten in dependence of the surface conditions*, J. Nucl. Mater. **313–316**; pp. 469–477

[81] O. V. Ogorodnikova, J. Roth and M. Mayer (2008) *Pre-implantation and pre-annealing effects on deuterium retention in tungsten*, J. Nucl. Mater. **373 (1–3)**; pp. 254–258

[82] O. V. Ogorodnikova, J. Roth and M. Mayer (2008) *Ion-driven deuterium retention in tungsten*, J. Appl. Phys. **103**; p. 034902 (10pp)

[83] O. V. Ogorodnikova *et al.* (2011) *Effect of nitrogen seeding into deuterium plasma on deuterium retention in tungsten*, Phys. Scr. **T145**; p. 014034

[84] M. J. O'Keefe and J. T. Grant (1996) *Phase transformation of sputter deposited tungsten thin films with A-15 structure*, J. Appl. Phys. **79**; p. 9134

[85] P. Petroff *et al.* (1973) *Microstructure, growth, resistivity, and stresses in thin tungsten films deposited by rf sputtering*, J. Appl. Phys. **44**; p. 2545

[86] J. von Pezold, L. Lymperakis and J. Neugebauer (2011) *Hydrogen–enhanced local plasticity at dilute bulk H concentrations: The role of H–H interactions and the formation of local hydrides*, Acta Mater. **59**; pp. 2969–2980

[87] S. T. Picraux and F. L. Vook (1974) *Deuterium lattice location in Cr and W*, Phys. Rev. Lett. **33 (20)**; pp. 1216–1220

[88] M. Poon, A. A. Haasz and J. W. Davis (2008) *Modelling deuterium release during thermal desorption of D^+-irradiated tungsten*, J. Nucl. Mater. **374 (3)**; pp. 390–402

[89] M. Poon *et al.* (2005) *Effects of background gas impurities during D^+ irradiation on D trapping in single crystal tungsten*, J. Nucl. Mater. **337-39 (1-3)**; pp. 629–633

[90] S. Primig *et al.* (2011) *SEM and TEM investigations of recovery and recrystallization in technically pure molybdenum*, Prakt. Metallogr. **48 (7)**; pp. 345–355

[91] P. A. Redhead (1962) *Thermal desorption of gases*, Vacuum **12 (4)**; pp. 203–211

[92] R. E. Reed-Hill (1973) *Physical Metallurgy Principles*, D. Van Nostrand Company, New York, second edition, ISBN 0-442-26868-8

[93] S. M. Rossnagel, I. C. Noyan and C. Cabral (2002) *Phase transformation of thin sputter-deposited tungsten films at room temperature*, J. Vac. Sci. Technol. B **20**; p. 2047

[94] J. Roth (2006) *Status of knowledge of chemical erosion of carbon and critical issues for extrapolation to ITER*, Phys. Scr. **T124**; pp. 37–43

[95] J. Roth *et al.* (2009) *Recent analysis of key plasma wall interactions issues for ITER*, J. Nucl. Mater. **390–391**; pp. 1–9

[96] L. Ryabchikov (1964) *Mass spectrometric investigation of degasation of molybdenum, tungsten and niobium on heating them in a vacuum*, Ukr. Fiz. Zh. (Ukr. Phys. J.) **9 (3)**; pp. 293–302

[97] R. Sakamoto, T. Muroga and N. Yoshida (1995) *Microstructural evolution induced by low energy hydrogen ion irradiation in tungsten*, J. Nucl Mater. **220–222**; pp. 819–822

[98] E. Salançon *et al.* (2008) *Redeposition of amorphous hydrogenated carbon films during thermal decomposition*, J. Nucl. Mater. **376**; pp. 160–168

[99] K. Schmid and U. v. Toussaint (2012) *Statistically sound evaluation of trace element depth profiles by ion beam analysis*, Nucl. Instrum. Meth. B **281**; pp. 64–71

[100] E. Serra, G. Benamati and O. V. Ogorodnikova (1998) *Hydrogen isotopes*

transport parameters in fusion reactor materials, J. Nucl Mater. **255 (2–3)**; pp. 105–115

[101] B. D. Shanina *et al.* (1999) *Paramagnetic spin resonance in hydrogen-charged stainless austenitic steel*, J. Phys. D: Appl. Phys. **32**; pp. 298–308

[102] Y. G. Shen and Y. W. Mai (2000) *Influences of oxygen on the formation and stability of A15 β-W thin films*, Mat. Sci. Eng. A **284 (1–2)**; pp. 176–183

[103] W. M. Shu, G.-N. Luo and T. Yamanishi (2007) *Mechanisms of retention and blistering in near-surface region of tungsten exposed to high flux deuterium plasmas of tens of eV*, J. Nucl. Mater. **367–370**; pp. 1463–1467

[104] A. Sieverts and E. Jurisch (1912) *Platin, Rhodium und Wasserstoff*, Ber. dtsch. chem. Ges. **45**; pp. 221–229

[105] D. S. Sivia (1996) *Data analysis—a Bayesian tutorial*, Clarendon Press, Oxford, 1st edition

[106] K. Sugiyama *et al.* (2011) *Deuterium retention in bulk tungsten exposed to the outer divertor plasma of ASDEX Upgrade*, Phys. Scr. **T145**; p. 014033

[107] S. Tamura *et al.* (2005) *Damage process of high purity tungsten coatings by hydrogen beam heat loads*, J. Nucl Mater. **337–339**; pp. 1043–1047

[108] J. Toribio and V. Kharin (2000) *A hydrogen diffusion model for applications in fusion nuclear technology*, Fusion Eng. Des. **51–52**; pp. 213–218

[109] B. Tyburska *et al.* (2009) *Deuterium retention in self-damaged tungsten*, J. Nucl. Mater. **395 (1–3)**; pp. 150–155

[110] Y. Ueda *et al.* (2005) *Hydrogen blister formation and cracking behavior for various tungsten materials*, J. Nucl Mater. **337–339**; pp. 1010–1014

[111] A. Van Veen *et al.* (1988) *Hydrogen exchange with voids in tungsten observed with TDS and PA*, J. Nucl. Mater. **155–157 (2)**; pp. 1113–1117

[112] T. J. Venhaus and R. A. Causey (2001) *Analysis of thermal desorption spectra to understand the migration of hydrogen in tungsten*, Fusion Technol. **39 (2)**; pp. 868–873

[113] D. Vergara *et al.* (2005) *Two-dimensional numerical modelling of hydrogen diffusion assisted by stress and strain*, Anales de Mecánica de la Fractura **22**; pp. 87–92

[114] U. von Toussaint *et al.* (2011) *Molecular dynamics study of grain boundary diffusion of hydrogen in tungsten*, Phys. Scr. **T145**; p. 014036

[115] W. Wampler and R. Doerner (2009) *The influence of displacement damage on deuterium retention in tungsten exposed to plasma*, Nucl. Fusion **49**; p. 115023 (9pp)

[116] W. Wampler and R. Doerner (2009) *Deuterium retention in tungsten from exposure to plasma*, Phys. Scr. **T138**; p. 014037 (8pp)

[117] J. Westerhout *et al.* (2007) *PSI research in the ITER divertor parameter range at the FOM PSI-lab*, Phys. Scr. **T128**; p. 18

[118] G. K. Williamson and R. E. Smallman (1956) *III. Dislocation densities in some annealed and cold-worked metals from measurements on the X-ray debye-scherrer spectrum*, Philos. Mag. **1 (1)**; pp. 34–46

[119] H. Wipf (1978) *Electro- and thermotransport of hydrogen in metals*, in: G. Alefeld and J. Völkl (eds.), *Hydrogen in metals II: application-oriented properties*, pp. 272–304, Springer-Verlag, Berlin Heidelberg New York, ISBN 3-540-08883-0

[120] H. Wipf (1997) *Diffusion of hydrogen in metals*, in: H. Wipf (ed.), *Hydrogen in Metals III: properties and applications*, pp. 51–91, Springer-Verlag, Berlin Heidelberg New York, ISBN 3-540-61639-X

[121] H. Wipf (2001) *Solubility and diffusivity of hydrogen in pure metals and alloys*, Phys. Scr. **T94**; pp. 43–51

[122] R. Wisniewski and A. J. Rostocki (1971) *Hall effect in the Pd-H system*, Phys. Rev. B **3 (2)**; pp. 251–252

[123] A. P. Zakharov, V. M. Sharapov and E. I. Evko (1973) *Hydrogen permeability of polycrystalline and monocrystalline molybdenum and tungsten*, Fiz.-Khim. Mekh. Mater. **9 (2)**; pp. 29–33

[124] D. Zamir (1965) *Nuclear-magnetic-resonance study of hydrogen alloying in the early transition metals (Group VB)*, Phys. Rev. **140 (1A)**; pp. A217–A274

Publication history

Articles related to this thesis

- M. Balden, S. Lindig, A. Manhard and Y.-H. You:
  D_2 gas–filled blisters on deuterium-bombarded tungsten. J. Nucl. Mater.
  414(1), pp. 69–72, 2011.

- S. Lindig, M. Balden, V. Kh. Alimov, A. Manhard C. Höschen, T. Höschen,
  B. Tyburska-Püschel, and J. Roth:
  *Sub-surface structures of ITER-grade W (Japan) and re-crystallized W after
  ITER-similar low-energy and high-flux D plasma loadings.* Phys. Scr. **T145**,
  p. 014039, 2011.

- A. Manhard, T. Schwarz-Selinger and W. Jacob:
  Quantification of the deuterium ion fluxes from a plasma source. Plasma
  Sources Sci. Technol. **20**, p. 015010, 2011.

- A. Manhard, K. Schmid, M. Balden and W. Jacob:
  Influence of the microstructure on the deuterium retention in tungsten. J.
  Nucl. Mater. **415(1S)**, pp. S632–S635, 2011.

- A. Manhard, U. v. Toussaint, T. Dürbeck K. Schmid and W. Jacob:
  *Statistical analysis of blister bursts during temperature programmed desorp-
  tion of deuterium-implanted polycrystalline tungsten.*
  Phys. Scr. **T145**, p. 014038, 2011.

- O. V. Ogorodnikova, K. Sugiyama, A. Markin, Yu. Gasparyan, V. Efimov,
  A. Manhard and M. Balden:
  *Effect of nitrogen seeding into deuterium plasma on deuterium retention in
  tungsten.* Phys. Scr. **T145**, p. 014034, 2011.

- U. von Toussaint, S. Gori, A. Manhard, T. Höschen and C. Höschen:
  Molecular dynamics study of grain boundary diffusion of hydrogen in tungsten. Phys. Scr. **T145**, p. 014036, 2011.

Articles on other topics

- S. Brezinsek, R. Pugno, U. Fantz, A. Manhard, H. W. Müller, A. Kallenbach, and Ph. Mertens:
  Determination of photon efficiencies and hydrocarbon influxes in the detached outer divertor plasma of ASDEX Upgrade. Phys. Scr. **T128**, p. 40, 2007.

- S. Brezinsek, A. Pospieszczyk, D. Borodin, M. F. Stamp,R. Pugno, A. G. McLean, U. Fantz, A. Manhard, A. Kallenbach, N. H. Brooks, M. Groth, Ph. Mertens, V. Philipps, U. Samm, TEXTOR, ASDEX Upgrade, DIII-D Teams and JET-EFDA Contributors:
  Hydrocarbon injection for quantification of chemical erosion yields in tokamaks. J. Nucl. Mater. **363–365**, p. 1119–1128, 2007.

- K. Schmid, A. Manhard, Ch. Linsmeier, A. Wiltner, T. Schwarz-Selinger, W. Jacob, and St. Mändl:
  Interaction of nitrogen plasmas with tungsten. Nucl. Fusion **50**, p. 025006, 2010.

- P. Wang, W. Jacob, M. Balden, A. Manhard, and T. Schwarz-Selinger:
  Erosion of tungsten-doped amorphous carbon films in oxygen plasma, J. Nucl. Mater, **420(1–3)**, pp. 101–109, 2012

Curriculum vitae

Armin Michael Manhard

born on February 18th, 1982,
in Augsburg, Germany

2008–2011	PhD student at the Max-Planck-Institute for Plasma Physics, Garching; also enrolled at the University of Augsburg.
2002–2008	University of Augsburg course of studies: physics, degree: *Diplom-Physiker* Diploma thesis: *Spectroscopic studies on positive ion based neutral beam injection systems*
2001–2002	Military service
1999–2001	Maria-Theresia-Gymnasium, Augsburg degree: *Abitur*
1992–1999	Rudolf-Diesel-Gymnasium, Augsburg
1988–1992	Volksschule Hochzoll Nord, Augsburg

Augsburg, December 2011

Acknowledgements